New tensor network methods and studies of criticality in low-dimensional quantum systems

Thesis by
Brenden Carlisle Roberts

In Partial Fulfillment of the Requirements for the
Degree of
Doctor of Philosophy

CALIFORNIA INSTITUTE OF TECHNOLOGY
Pasadena, California

2021
Defended May 25, 2021

Brenden Carlisle Roberts
ORCID: 0000-0002-3107-1878

ACKNOWLEDGEMENTS

I would first like to acknowledge the substantial contributions to the contents of this dissertation by my advisor, Lesik Motrunich. During my time as his student he provided a constant supply of instruction, guidance, support, and patience, equalled only by a seemingly limitless amount of detailed handwritten notes on any topic that ever came to my mind. He invested a substantial amount of his time and energy into working on our projects together, as well as into my professional growth and development.

I learned a great deal from working with our coauthors Thomas Vidick and Shenghan Jiang, who were always willing to share their insight as experts. More generally, I benefited immensely from the environment at Caltech through various discussions with my colleagues Cheng-Ju Lin, Christopher White, Aaron Chew, Matt Fishman, Dave Aasen, and many others.

There are very many friends and fellow students who made the past few years fun. Among them are: Soichi Hirokawa; Matt Orr; Alistair Hayden; Thom Bohdanowicz and the rest of the Fightin' Pinecones; Vatsal Jhalani, who went to Utah with one other man; Mike "Truk" Citrin; Elise Post; Phil Jahelka; dining guys Gabriel Valencia, Jon Webster, and Jaime Reyes; Craig Cahillane; Isaac Fees; Tom Mannion; and of course the very famous Book Club. Without the many wonderful contributions to my life from all of these people, I would likely have been able to graduate last year.

Finally, I am grateful to my family, who have always provided me with every opportunity, and with encouragement too. In particular, its newest member my wife Christine has tirelessly supported me in many ways, both practical and abstract.

ABSTRACT

In this thesis several investigations are presented on the topic of the low-energy properties of models for many-body quantum physics in one dimension (1d).

First we present a novel numerical method based on recent theoretical developments in the understanding of the success of polynomial-time tensor network methods for computing ground states of certain local Hamiltonians. The convergence proof relies on "rigorous renormalization group" (RRG) techniques which differ fundamentally from existing algorithms. Our practical adaptation of the RRG procedure which, while no longer theoretically guaranteed to converge, efficiently finds MPS approximations to the ground spaces and low-lying excited spectra of local Hamiltonians in situations of physical interest. In contrast to other schemes, RRG does not utilize variational methods on tensor networks. Rather, it operates on subsets of the system Hilbert space by constructing approximations to the global ground space in a tree-like manner. We evaluate the algorithm numerically, finding similar performance to DMRG in the case of a gapped nondegenerate Hamiltonian. Even in challenging situations of criticality, large ground-state degeneracy, or long-range entanglement, RRG remains able to identify candidate states having large overlap with ground and low-energy eigenstates, even outperforming DMRG in some cases.

As an application of RRG, we perform a study of the antiferromagnetic XYZ spin chain with quenched randomness. Our focus is on the critical line between localized magnetic phases, which we access by varying the bandwidth of a coupling distribution. In this way one can tune between a free-fermion fixed point and S_3-symmetric multicritical point with identically distributed couplings. The RRG method obtains unbiased numerically exact results targeting the ground state and low-energy physics, allowing us to compute critical indices, which have been proposed to vary continuously based on results of a strong disorder renormalization group (RG) calculation. Our findings support these claims as well as an infinite-randomness fixed point (IRFP), and we furthermore exhibit a perturbative relationship to the critical line connecting the random XX IRFP with U(1) symmetry and the random XY IRFP. Even though the RG equations are not tractable due to the correlations in the distributions, using a formulation in terms of random walks we are able to prove

rigorous bounds establishing continuously varying critical exponents along this line.

We then change topics and perform a numerical study of a spin-$\frac{1}{2}$ model with $\mathbb{Z}_2 \times \mathbb{Z}_2$ symmetry in 1d which demonstrates an interesting similarity to the physics of 2d deconfined quantum critical points (DQCP). Specifically, we investigate the quantum phase transition between Ising ferromagnetic and valence bond solid (VBS) symmetry-breaking phases. Working directly in the thermodynamic limit using uniform MPS, we find evidence for a direct continuous phase transition that lies outside of the Landau–Ginzburg–Wilson paradigm. In our model, the continuous transition is found everywhere on the phase boundary. We find that the magnetic and VBS correlations show very close power law exponents, which is expected from the self-duality of the parton description of this DQCP. Critical exponents vary continuously along the phase boundary in a manner consistent with the predictions of the field theory for this transition. We also find a regime where the phase boundary splits, as suggested by the theory, introducing an intermediate phase of coexisting ferromagnetic and VBS order parameters. Interestingly, we discover a transition involving this coexistence phase which is similar to the DQCP, being also disallowed by Landau–Ginzburg–Wilson symmetry-breaking theory.

Finally we continue the study of examples of deconfined quantum criticality in 1d models by investigating the transition between a $\mathbb{Z}_3$ ferromagnet and a phase with VBS order in a spin chain now with $\mathbb{Z}_3 \times \mathbb{Z}_3$ global symmetry. We study a model with alternating projective representations on the sites of the two sublattices, allowing the Hamiltonian to connect to an exactly solvable point having VBS order with the character of SU(3)-invariant singlets. Such a model does not admit a Lieb–Schultz–Mattis theorem typical of systems realizing deconfined critical points. Nevertheless, we find evidence for a direct transition from the VBS phase to a $\mathbb{Z}_3$ ferromagnet. Finite-entanglement scaling data are consistent with a second-order or weakly first-order transition. We find in our parameter space an integrable lattice model apparently describing the phase transition, with a very long, finite, correlation length of 190878 lattice spacings. Based on exact results for this model, we propose that the transition is extremely weakly first order, and is part of a family of DQCP described by walking of renormalization group flows.

PUBLISHED CONTENT AND CONTRIBUTIONS

[1] B. Roberts, S. Jiang, and O. I. Motrunich, "One-dimensional model for deconfined criticality with $\mathbb{Z}_3 \times \mathbb{Z}_3$ symmetry", Physical Review B 103 (2021), 155143, DOI: 10.1103/PhysRevB.103.155143.
B.R. wrote the bulk of the manuscript and performed the numerics, and contributed to the analysis and results.

[2] B. Roberts, S. Jiang, and O. I. Motrunich, "Deconfined quantum critical point in one dimension", Physical Review B 99 (2019), 165143, DOI: 10.1103/PhysRevB.99.165143.
B.R. wrote the bulk of the manuscript and performed the numerics, and contributed to the analysis and results.

[3] B. Roberts, T. Vidick, and O. I. Motrunich, "Implementation of rigorous renormalization group method for ground space and low-energy states of local Hamiltonians", Physical Review B 96 (2017), 214203, DOI: 10.1103/PhysRevB.96.214203.
B.R. wrote the bulk of the manuscript and the code implementing the new method, and performed the numerical tests.

CONTENTS

LIST OF FIGURES

LIST OF TABLES

Chapter 1

INTRODUCTION

This dissertation presents several projects of varying degrees of independence, which I have chosen to unify under the theme of the low-energy properties of many-body quantum models in one dimension (1d). This particular subject benefits from a rich literature dating back many decades and enjoys a relative abundance of tools and techniques. In fact, so much work has already been done that one may be tempted to think that there are not very many interesting results left here. Indeed, the frontiers of many-body physics include such fascinating topics as topological states, thermalization and nonequilibrium dynamics, and strongly-coupled phenomena in 2d; perhaps in comparison the paths of 1d ground states are well trodden. An implicit argument of this thesis is that its subject is not in fact rendered less interesting but rather more so, and is a useful component of the environment of exciting new topics.

It is evident that the understanding of new and more advanced ideas in physics is often incubated in simpler settings. This is only one pathway however, and in practice insight can of course flow in both directions. That is certainly true of this work, whose motivation arose in a variety of cross-disciplinary settings. The projects presented here were inspired by rigorous proofs from quantum information theory; studies of many-body localization; exotic mechanisms for phase transitions in 2d; and unusual renormalization group flows from high-energy theory. All of these studies were essential for developing interest in the present investigations and, conversely, I hope that this work can contribute meaningfully to the understanding of the related phenomena beyond the strict dimensional requirements of many of the tools we have used.

A very brief summary of these projects and the results is as follows. In this Introduction I provide an overview of the relevant topics, with the later chapters devoted to the work itself and containing a minimum of background material. Ch. 2 introduces and tests a novel numerical method, the *rigorous renormalization group*, which is based on proofs of efficient algorithms for ground and low-energy states of local Hamiltonians in 1d. In Ch. 3 the rigorous renormalization group is used to study the antiferromagnetic XYZ spin chain with

quenched randomness, where we obtain results previously inaccessible to unbiased numerical methods and find evidence for an infinite-randomness fixed point with continuously varying critical exponents. As an extended subtopic, we prove using analytic strong-disorder RG methods that random anisotropy is marginal along the critical line from the random XX to XY fixed points. Chs. 4 and 5 present studies of deconfined quantum criticality in 1d models. First we provide strong evidence supporting an instance of such a phase transition in a concrete spin chain with $\mathbb{Z}_2 \times \mathbb{Z}_2$ symmetry. We then investigate a generalization to a model with $\mathbb{Z}_3 \times \mathbb{Z}_3$ symmetry, which surprisingly appears to be very weakly first-order, with the transition controlled by complex fixed points through walking behavior of the renormalization group flow. Finally, Ch. 6 concludes with some discussion of opportunities for future work based on these projects.

1.1 Rigorous renormalization group method

Whereas the Schrödinger equation, a linear partial differential equation governing the time evolution of a quantum state, can sometimes be solved analytically for a single particle, even few-body systems already do not admit a direct solution due to the exponential scaling of the dimension of Hilbert space. This is the fundamental roadblock which the modern techniques of many-body quantum physics are designed to bypass, via such diverse routes as field theories, phenomenological models, variational states, and the renormalization group, all of which exist alongside and in conjunction with numerical methods. Being linear, the Schrödinger equation permits a very straightforward extension of the single-particle case by numerical exact diagonalization of the Hamiltonian energy operator H, yielding eigenstates of definite energy which fully determine the thermal and nonequilibrium behavior. Exact diagonalization cannot surpass few-body physics, however, and developing numerical methods for larger systems requires much additional structure, some aspects of which have only recently been understood formally.

In order to be able to make further statements, the problem must be specialized; we focus here on algorithms for tensor networks, and have in mind a system of lattice sites in 1d, with a *local Hamiltonian* H that decomposes into spatially local energy terms acting on $k \sim O(1)$ neighboring sites. A tensor network is a strategy for making a controlled assumption about the corresponding spatial locality of a quantum state itself, which one might hope is inherited

from H. In 1d the canonical—though not the only—such representation is the matrix product state (MPS) [1–4], an ansatz suitable for "finitely-correlated" states. Tensor network states are not typical in Hilbert space and in fact the space of MPS evidently has very high codimension; moreover, the locality of H is not enough to prevent nearly all eigenstates from being typical. Instead, the utility of the form derives from the *area law* of entanglement, a result proved by Hastings [5] in 2007 which establishes that any ground state of a 1d local Hamiltonian with a finite excitation gap Δ is in fact an MPS. The area law is a consequence of a finite correlation length $\xi \sim 1/\Delta$ which limits the possible degree of correlations between spatially separated observables (this claim turns out to be correct, data-hiding states notwithstanding [6, 7]), and consequently applies to equilibrium states [8]. Subsequently, MPS were used to classify all gapped phases in 1d [9].

Although tensor networks have inspired time-evolution algorithms [10–12], we focus on the more theoretically well-founded application to eigenstates close to the band edge of H, which determine the low-temperature equilibrium physics of the system. The "gold standard" numerical technique for such problems is the density matrix renormalization group (DMRG) invented by White [13, 14]. Though it was not the case originally, the modern understanding of DMRG is now based on MPS [15]. Essentially, the algorithm performs an iterated optimization over the variational parameters of the MPS, which, up to gauge transformation, are the tensor elements. The iteration manifests as a "sweeping" over the tensors in the 1d chain, where at each step an effective local eigenvalue problem on one or a few sites is solved by the Lanczos algorithm.

Since its introduction, DMRG has seen enormous practical success in a wide range of 1d and quasi-1d models, with extensions for translation invariance [16, 17], finite temperature [18, 19], time dependence [20], and many other applications. However, for some time the effectiveness of the basic algorithm was not well understood. That is, although MPS had been established for ground states, it was not clear that DMRG itself was provably efficient (requiring only polynomially many resources in the system size), or even that such an efficient algorithm existed. It was not until the work of Landau et al. [21] in 2015 that a polynomial-time algorithm was developed for ground states of gapped models, proving that an efficient method is possible in principle.

However, the algorithm exhibited in Ref. [21] bears little resemblance in its

particulars to DMRG, and devising a proof for the DMRG algorithm appears to be challenging; in fact, it is known that the multi-site variants can be NP-hard in the worst case [22]. As a practical matter, in systems with strong disorder DMRG is susceptible to spurious convergence to excited states, an occurrence which cannot be readily diagnosed [23]. This is fundamentally a consequence of performing the iterated local optimization. The rigorous algorithm is distinguished by a reliance on an *approximate ground state projector* (AGSP), an operator derived from the Hamiltonian which was introduced by Arad et al. [24]. The role of the AGSP is to provide global information, ensuring that intermediate states can be efficiently represented and directing the algorithm along a computationally tractable route to the ground state.

AGSP-based methods were generalized in Ref. [25] to low-energy excited states in models with slightly relaxed conditions on the density of states. Based on this work we introduced the *rigorous renormalization group* (RRG), a numerical implementation for low-energy states of local Hamiltonians in one dimension [26]. While the implemented method differs slightly from the proof construction and does not strictly satisfy the conditions of the guarantee—whose parameters are not known *a priori* regardless—it inherits the intuitive benefits of the AGSP and has been seen to be effective in practice for non-trivial low-energy spectra like those of strongly disordered systems, or in the presence of nearly degenerate manifolds [26, 27], where DMRG may be unreliable. In addition, RRG is tuned by two "hyperparameters" (s, D) which provide controllable improvements in the accuracy of the solution.

At the time of its introduction in Ref. [26], the implementation of RRG was not particularly technically sophisticated, and lacked basic features such as the ability to resolve global symmetries. As a result, the comparisons of its performance to DMRG presented there and in Ch. 2 appear to be fairly bleak. The reality is the opposite, however: since then many technical improvements have brought the performance of RRG even with DMRG in its basic setting of gapped 1d Hamiltonians, when multiple low-energy states are required. In addition, symmetries can be exactly realized and more complex situations tackled, with one example of both being the study in Ch. 3.

One way to think about RRG which has emerged from its use in practical settings is a strategy akin to golf. As described above, the goal of RRG is to produce a state having constant overlap with low-energy states, but its output

N	RRG+DMRG time (s)	DMRG time (s)
32	$7 + 3 = 10$	26
64	$20 + 7 = 27$	83
128	$55 + 23 = 78$	205
256	$150 + 114 = 264$	662

Table 1.1: We perform an up-to-date comparison similar to Table 2.1 as an example of the use of RRG, however in a slightly different setting than was considered there. Solution times are shown for the "golf" strategy RRG+DMRG along with DMRG alone for the transverse-field Ising model in the paramagnetic phase close to the critical point ($g/J = 1.1$ in the notation of Eq. (2.7)). Each method obtains 6 eigenstates to accuracy 10^{-10} in units of energy, without resolving the Ising symmetry. The RRG hyperparameters used are $(s, D) = (6, 8)$. All computations used single-threading.

still contains some high-energy contributions; this is nevertheless a favorable initial state for variational optimization. In this way, RRG acts like a driver, a club used from the tee box which is well suited to locating the ball in the vicinity of the hole, avoiding sand traps and water hazards along the way. Once the ball is on the green, the appropriate club is a putter, which allows for precisely following local contours in a gradient descent fashion. This metaphor is not meant to disparage DMRG, whose success is manifest; it simply illustrates how these tools can be used together to accelerate convergence, or to navigate challenging energy landscapes. As an example, in Table 1.1 a comparison is given (similar to Table 2.1 of Ch. 2) between RRG+DMRG, where RRG performs initial state preparation, and DMRG alone for low-energy states of the transverse-field Ising model close to the critical point.

1.2 Strongly disordered quantum spin chains

Many foundational ideas in condensed matter physics rely on a notion of translation invariance, either continuous or discrete. Such useful tools as quasiparticles, effective field theories, and even a standard understanding of quantum phases make use of a clean continuum, or thermodynamic, limit. Gapped phases are stable under weak static, or "quenched," disorder, and in such cases the disorder average of certain quantities can be calculated in a related clean system via either the replica trick [28] or supersymmetry arguments for non-interacting models [29]. These techniques apply to self-averaging observables whose disorder averages are indicative of their typical values, and rely on restoring translation invariance in situations where disorder plays a less

important role than thermal or quantum fluctuations. In cases where disorder is strong or accompanied by interactions, such methods are not effective and a different approach is required. One technique which intuitively seems particularly suitable for directly accounting for spatial inhomogeneity is the real-space renormalization group (RG) [30].

The original development of a real-space RG appropriate for strong-disorder physics in 1d is due to Ma, Dasgupta, and Hu [31, 32]. As is true of all RG procedures, the idea is to introduce effective degrees of freedom associated with a varying scale. The feature distinguishing the *strong-disorder renormalization group* (SDRG) from, e.g., spin blocking, is that the degrees of freedom are explicitly associated with an energy scale rather than with a grouped spatial structure. In this way the disorder realization determines the pattern of integrating out fluctuations.

Such an approach is now understood to be well motivated by the idea of an *infinite-randomness fixed point* (IRFP), a stable solution of the SDRG equations discovered by Fisher in Refs. [33–35] at which the strength of disorder grows with the scale without bound, and where SDRG predictions become asymptotically exact. In an IRFP, disorder dominates the low-energy physics and physical observables are not self-averaging, with average behaviors instead being determined by a small number of "rare regions" within a disorder realization. Interestingly, although such a fixed point has no notion of conformal symmetry, the phenomenology can be similar to that of CFT fixed points: for instance, the scaling of average entanglement follows the conformal form with an effective central charge, which in some cases is related to the central charge of the clean theory but does not obey the same rules under RG [36–38].

Since its introduction, the SDRG has been specialized to a variety of classical and quantum systems, and the original scheme has seen many generalizations [39, 40]. For example, applications in two-dimensional (2d) random models also yield IRFPs in these settings [41]. In another direction, SDRG methods were extended to treat all eigenstates of a quantum Hamiltonian [42–44], in order to assess the possibility of many-body localization (MBL) of excited states. The many-body extended SDRG procedures do not perform an iterative targeting of the low-energy space, but instead tabulate emergent conservation laws corresponding to the local integrals of motion of an MBL phase; nevertheless, the equations are formally quite similar to the original picture based

on a traditional understanding of RG.

One of the extended many-body SDRG procedures, the "spectrum bifurcation renormalization group" (SBRG) developed in Ref. [43] for Hamiltonians comprised of general Pauli strings, was applied to the random XYZ spin chain by Slagle et al. [45]. In this model the RG equations do not simply renormalize the distribution of bare couplings, but generate exponentially many terms (see Sec. 3.2.3 for more details), requiring an uncontrolled approximation. Along a phase boundary between localized Ising antiferromagnets, disorder-averaged spin correlations at infinite temperature were found to decay as power laws with continuously varying critical exponents. Similarly-averaged entanglement entropy scaling exhibits a stable effective central charge that matches the expectation based on the clean case. This phase transition was conjectured to be "marginal MBL," meaning that eigenstates do not thermalize but exhibit a logarithmic violation of the area law.

Such marginal MBL Hamiltonians have recently been argued to be perturbatively unstable to ergodicity at finite energy density due to resonances [46, 47]. As is true of all excited-state SDRG schemes, SBRG relies on MBL for validity, and these recent arguments call this assumption into question. Nevertheless, we find the possibility of continuously varying power laws in the IRFP for the ground state very interesting and worth further study. It is difficult to study even the ground state of the random XYZ spin chain, however. The SDRG for this case requires making an uncontrolled approximation, and in general strongly disordered models are very challenging for numerical methods like DMRG. In fact they are known to be one of the very few cases in which DMRG can spuriously converge to an excited state without any way to diagnose the error [23]. This is related to the "ultra-slow" dynamics in such a phase, which frustrates the local optimization.

There is evidently an opportunity for performing unbiased numerics with RRG for the low-energy properties of the random XYZ spin chain. The benefit of the AGSP is precisely to provide information about the global energy landscape to the local step, presumably escaping spurious convergence. We emphasize that our focus is entirely on low-energy properties, and we will not have anything to say about the existence of MBL physics at finite energy density. In Ch. 3 we preform an RRG study and find that the results are in general agreement with those of Ref. [45] and strongly suggest an IRFP with continuously varying

critical indices. In addition, we find that a more tractable effective XY model with locally correlated couplings reproduces much of the phenomenology of the random XYZ critical line. Although the SDRG equations are difficult to solve directly due to the arbitrary degree of correlation between the distributions, we use a formulation of the analytical SDRG on a classical random walk [39] to prove that local correlations are marginal in the effective model, and find an exact form for a continuously varying critical exponent.

1.3 Deconfined quantum critical points in 1d

Among the great successes of modern physics is the description of interacting continuous phase transitions by the Landau–Ginzburg–Wilson theory [48]. Briefly, in this paradigm one writes a phenomenological theory of an ordering transition in terms of a fluctuating local order parameter. The theory contains all symmetry-allowed terms constructed from the order parameter and its derivatives, and through a perturbative RG analysis properties of the critical fixed point can be computed [49]. An interesting recent line of inquiry is so-called "Landau-forbidden" continuous transitions lying outside of this conventional framework. A number of spiritually similar proposals in this subject have been categorized as a *deconfined quantum critical point* (DQCP). This nomenclature was introduced by Senthil et al. [50, 51], who described a mechanism for a non-Landau continuous phase transition of rotationally symmetric spins on the two-dimensional (2d) square lattice. This particular transition involves conventional phases, one having Néel antiferromagnetic order, and the other lattice symmetry–breaking valence-bond solid (VBS) order.

The order parameter in the magnetic phase is the Néel vector, which undergoes a conventional continuous transition from the ordered phase to a paramagnet through the proliferation of topological defects. Schematically, the ordered phase can instead transition through a DQCP to a paramagnet with VBS order by endowing the topological defects with nontrivial transformation properties under the lattice symmetry. Additionally, this is proposed to lead to RG irrelevance of symmetry-allowed monopole terms at the critical point. The low-energy theory of the Néel-VBS transition is the non-compact CP^1 model of spinons, complex SU(2) spinors coupled to a U(1) gauge field, which fractionalize the Néel order parameter. Its "non-compactness" refers to conservation of the U(1) flux, a symmetry special to the critical point arising from the conjectured irrelevance of monopoles. Away from the critical point in the

paramagnet phase, the spinors are linearly confined as a result of the induced VBS order.

This description inspired a variety of other proposals, which are united by the property that the natural variables for the system at the critical point are confined on either side of the transition. Meanwhile, the original proposal has been extensively tested in numerical studies, which are consistent with either a second-order or very weakly first-order transition [52–69]. Recent interest in this DQCP is a result of new developments in the understanding of the relationship between its symmetries and duality properties [70–73]. Remarkably, quantum Monte Carlo simulations suggested that the IR theory of the model hosts an emergent symmetry, with the Néel and VBS order parameters transforming together as an SO(5) vector [61]. This emergent symmetry, which is realized anomalously, proved to be quite useful for understanding the transition through various dualities to theories appearing on the surface of a three-dimensional symmetry protected topological (SPT) phase [72].

Subsequent conformal bootstrap bounds on unitary CFTs with this SO(5) symmetry turn out to exclude the conformal data measured in numerics, most notably for the SO(5) vector which is too relevant to satisfy consistency conditions [74]. This discovery followed earlier observations of unusual numerical features such as drifting "universal" quantities and inconsistencies in finite-size scaling [55, 56, 60, 63]. The resolution may be that the phase transition is in fact weakly first order (or pseudo-critical), a phenomenon thought to be generically a result of RG walking [75–82]. In this scenario, the transition displays approximate conformal symmetry below some long, but finite, length scale. At intermediate distances the system's properties are governed by non-unitary complex fixed points which can be viewed as analytic continuations of a unitary CFT; however, eventually the theory is trivial. For the DQCP with SU(2) symmetry such a description requires a fixed point with inherent SO(5) symmetry and a tunable parameter providing access to the pseudo-critical regime [72]. Some proposals in this direction have identified as a candidate a nonlinear sigma model with WZW term continued to $d = 2 + \epsilon$ dimensions, with SO$(4 + \epsilon)$ symmetry [83, 84].

A complementary perspective on the above story can be found in 1d, where we again use the language of spin chains. In order to have a symmetry-breaking phase the model must evade the Mermin–Wagner theorem; one way

to do so is through anisotropy breaking global spin-rotation symmetry to a discrete subgroup.[1] In Ref. [87] such a transition was considered between a ferromagnet and a dimerized VBS phase in a 1d system with Ising-like $\mathbb{Z}_2 \times \mathbb{Z}_2$ symmetry. This choice allows nontrivial projective representations, and realizing the global symmetry projectively on the unit cell (a single site) leads to a Lieb–Schultz–Mattis theorem which prohibits a featureless gapped phase from intervening in the transition [88]. There are close parallels between this transition and the easy-plane DQCP in 2d with U(1) symmetry, but the 1d version is more tractable and, in particular, allows a controlled field theory description. This transition therefore is proposed to constitute an example of deconfined quantum criticality in 1d. There are also connections to the web of 1+1 dualities considered in Ref. [89]. The low-energy theory turns out to be a one-component Gaussian theory (a Luttinger liquid) with a single relevant cosine term and continuously varying critical indices. In these variables an emergent $\mathrm{U}(1) \times \mathrm{U}(1)$ symmetry is manifest at the transition.

In Ch. 4 we provide strong evidence that this DQCP in 1d is in fact realized in a concrete spin chain with $\mathbb{Z}_2 \times \mathbb{Z}_2$ symmetry, establishing that many nontrivial aspects of the theory appear. In Ch. 5 we begin to generalize to higher-spin models by considering a case with $\mathbb{Z}_3 \times \mathbb{Z}_3$ symmetry. We find that there is indeed a direct phase transition between magnetic and VBS phases which appears in numerics to be continuous. While straightforward attempts to write a field theory description are not successful, we find an integrable classical 2d vertex model appearing to lie on the phase boundary; surprisingly this model has a finite, but very long, correlation length. Supposing that the integrable model does describe the transition, we develop a picture of the family of $\mathbb{Z}_q \times \mathbb{Z}_q$ critical points in 1d, described by pseudocritical behavior induced by walking RG flows in the vicinity of complex fixed points.

[1] Another method is to use long-ranged interactions; such a model (which can be realized on the boundary of a SPT state in 2d [85]) exhibits a direct transition between a gapless phase with AFM order and a VBS phase [86].

BIBLIOGRAPHY

[1] A. Klümper, A. Schadschneider, and J. Zittartz, "Equivalence and solution of anisotropic spin-1 models and generalized tJ fermion models in one dimension", Journal of Physics A: Mathematical and General 24 (1991), L955.

[2] A. Klümper, A. Schadschneider, and J. Zittartz, "Groundstate properties of a generalized VBS-model", Zeitschrift für Physik B Condensed Matter 87 (1992), 281.

[3] A. Klümper, A. Schadschneider, and J. Zittartz, "Matrix product ground states for one-dimensional spin-1 quantum antiferromagnets", EPL (Europhysics Letters) 24 (1993), 293.

[4] M. Fannes, B. Nachtergaele, and R. F. Werner, "Finitely correlated states on quantum spin chains", Communications in Mathematical Physics 144 (1992), 443.

[5] M. B. Hastings, "An area law for one-dimensional quantum systems", Journal of Statistical Mechanics: Theory and Experiment 2007 (2007), P08024.

[6] F. G. Brandão and M. Horodecki, "An area law for entanglement from exponential decay of correlations", Nature Physics 9 (2013), 721.

[7] F. G. Brandao and M. Horodecki, "Exponential decay of correlations implies area law", Communications in Mathematical Physics 333 (2015), 761.

[8] M. M. Wolf et al., "Area laws in quantum systems: mutual information and correlations", Physical Review Letters 100 (2008), 070502.

[9] X. Chen, Z.-C. Gu, and X.-G. Wen, "Classification of gapped symmetric phases in one-dimensional spin systems", Physical Review B 83 (2011), 035107.

[10] G. Vidal, "Classical Simulation of Infinite-Size Quantum Lattice Systems in One Spatial Dimension", Phys. Rev. Lett. 98 (2007), 070201.

[11] J. Haegeman et al., "Time-Dependent Variational Principle for Quantum Lattices", Phys. Rev. Lett. 107 (2011), 070601.

[12] J. Haegeman et al., "Unifying time evolution and optimization with matrix product states", Phys. Rev. B 94 (2016), 165116.

[13] S. R. White, "Density matrix formulation for quantum renormalization groups", Physical Review Letters 69 (1992), 2863.

[14] S. R. White, "Density-matrix algorithms for quantum renormalization groups", Physical Review B 48 (1993), 10345.

[15] U. Schollwöck, "The density-matrix renormalization group in the age of matrix product states", Annals of Physics 326 (2011), 96.

[16] S. Östlund and S. Rommer, "Thermodynamic limit of density matrix renormalization", Physical review letters 75 (1995), 3537.

[17] V. Zauner-Stauber et al., "Variational optimization algorithms for uniform matrix product states", Physical Review B 97 (2018), 045145.

[18] F. Verstraete, J. J. Garcia-Ripoll, and J. I. Cirac, "Matrix product density operators: Simulation of finite-temperature and dissipative systems", Physical review letters 93 (2004), 207204.

[19] E. Stoudenmire and S. R. White, "Minimally entangled typical thermal state algorithms", New Journal of Physics 12 (2010), 055026.

[20] A. J. Daley et al., "Time-dependent density-matrix renormalization-group using adaptive effective Hilbert spaces", Journal of Statistical Mechanics: Theory and Experiment 2004 (2004), P04005.

[21] Z. Landau, U. Vazirani, and T. Vidick, "A polynomial time algorithm for the ground state of one-dimensional gapped local Hamiltonians", Nature Physics 11 (2015), 566.

[22] J. Eisert, "Computational difficulty of global variations in the density matrix renormalization group", Physical Review Letters 97 (2006), 260501.

[23] P. Schmitteckert, "Disordered one-dimensional fermi systems", *Density-Matrix Renormalization*, Springer, 1999, 345.

[24] I. Arad et al., "An area law and sub-exponential algorithm for 1D systems", arXiv preprint arXiv:1301.1162 (2013).

[25] I. Arad et al., "Rigorous RG algorithms and area laws for low energy eigenstates in 1D", Communications in Mathematical Physics 356 (2017), 65.

[26] B. Roberts, T. Vidick, and O. I. Motrunich, "Implementation of rigorous renormalization group method for ground space and low-energy states of local Hamiltonians", Physical Review B 96 (2017), 214203.

[27] M. Block et al., "Performance of the rigorous renormalization group for first order phase transitions and topological phases", arXiv preprint arXiv:2010.15851 (2020).

[28] M. Mezard, G. Parisi, and M. A. Virasoro, *Spin glass theory and beyond*, World Scientific lecture notes in physics, World Scientific, 1987.

[29] K. Efetov, *Supersymmetry in Disorder and Chaos.* English, Cambridge University Press, 2010.

[30] K. G. Wilson, "The renormalization group: Critical phenomena and the Kondo problem", Reviews of modern physics 47 (1975), 773.

[31] S.-K. Ma, C. Dasgupta, and C.-K. Hu, "Random antiferromagnetic chain", Physical Review Letters 43 (1979), 1434.

[32] C. Dasgupta and S.-K. Ma, "Low-temperature properties of the random Heisenberg antiferromagnetic chain", Physical Review B 22 (1980), 1305.

[33] D. S. Fisher, "Random transverse field Ising spin chains", Physical Review Letters 69 (1992), 534.

[34] D. S. Fisher, "Random antiferromagnetic quantum spin chains", Physical Review B 50 (1994), 3799.

[35] D. S. Fisher, "Critical behavior of random transverse-field Ising spin chains", Physical Review B 51 (1995), 6411.

[36] G. Refael and J. E. Moore, "Entanglement entropy of random quantum critical points in one dimension", Physical Review Letters 93 (2004), 260602.

[37] N. Bonesteel and K. Yang, "Infinite-randomness fixed points for chains of non-Abelian quasiparticles", Physical review letters 99 (2007), 140405.

[38] L. Fidkowski et al., "c-theorem violation for effective central charge of infinite-randomness fixed points", Physical Review B 78 (2008), 224204.

[39] F. Iglói and C. Monthus, "Strong disorder RG approach of random systems", Physics reports 412 (2005), 277.

[40] F. Iglói and C. Monthus, "Strong disorder RG approach–a short review of recent developments", The European Physical Journal B 91 (2018), 1.

[41] O. Motrunich et al., "Infinite-randomness quantum Ising critical fixed points", Physical Review B 61 (2000), 1160.

[42] D. Pekker et al., "Hilbert-glass transition: New universality of temperature-tuned many-body dynamical quantum criticality", Physical review x 4 (2014), 011052.

[43] Y.-Z. You, X.-L. Qi, and C. Xu, "Entanglement holographic mapping of many-body localized system by spectrum bifurcation renormalization group", Physical Review B 93 (2016), 104205.

[44] C. Monthus, "Strong disorder real-space renormalization for the many-body-localized phase of random Majorana models", Journal of Physics A: Mathematical and Theoretical 51 (2018), 115304.

[45] K. Slagle, Y.-Z. You, and C. Xu, "Disordered XYZ spin chain simulations using the spectrum bifurcation renormalization group", Physical Review B 94 (2016), 014205.

[46] S. Moudgalya, D. A. Huse, and V. Khemani, "Perturbative instability towards delocalization at phase transitions between MBL phases", arXiv preprint arXiv:2008.09113 (2020).

[47] B. Ware, D. Abanin, and R. Vasseur, "Perturbative instability of non-ergodic phases in non-Abelian quantum chains", Physical Review B 103 (2021), 094203.

[48] J. L. Cardy, *Scaling and renormalization in statistical physics*, Cambridge lecture notes in physics, Cmabridge ; New York: Cambridge University Press, 1996.

[49] K. G. Wilson and M. E. Fisher, "Critical exponents in 3.99 dimensions", Physical Review Letters 28 (1972), 240.

[50] T. Senthil et al., "Deconfined Quantum Critical Points", Science 303 (2004), 1490.

[51] T. Senthil et al., "Quantum criticality beyond the Landau-Ginzburg-Wilson paradigm", Physical Review B 70 (2004), 144407.

[52] A. W. Sandvik, "Evidence for Deconfined Quantum Criticality in a Two-Dimensional Heisenberg Model with Four-Spin Interactions", Physical Review Letters 98 (2007), 227202.

[53] R. G. Melko and R. K. Kaul, "Scaling in the Fan of an Unconventional Quantum Critical Point", Physical Review Letters 100 (2008), 017203.

[54] J. Lou, A. W. Sandvik, and N. Kawashima, "Antiferromagnetic to valence-bond-solid transitions in two-dimensional SU(N) Heisenberg models with multispin interactions", Physical Review B 80 (2009), 180414.

[55] A. Banerjee, K. Damle, and F. Alet, "Impurity spin texture at a deconfined quantum critical point", Physical Review B 82 (2010), 155139.

[56] A. W. Sandvik, "Continuous quantum phase transition between an antiferromagnet and a valence-bond solid in two dimensions: Evidence for logarithmic corrections to scaling", Physical Review Letters 104 (2010), 177201.

[57] K. Harada et al., "Possibility of deconfined criticality in SU(N) Heisenberg models at small N", Physical Review B 88 (2013), 220408.

[58] F.-J. Jiang et al., "From an antiferromagnet to a valence bond solid: evidence for a first-order phase transition", Journal of Statistical Mechanics: Theory and Experiment 2008 (2008), P02009.

[59] K. Chen et al., "Deconfined Criticality Flow in the Heisenberg Model with Ring-Exchange Interactions", Physical Review Letters 110 (2013), 185701.

[60] A. Nahum et al., "Deconfined Quantum Criticality, Scaling Violations, and Classical Loop Models", Physical Review X 5 (2015), 041048.

[61] A. Nahum et al., "Emergent SO(5) Symmetry at the Néel to Valence-Bond-Solid Transition", Physical Review Letters 115 (2015), 267203.

[62] O. I. Motrunich and A. Vishwanath, "Comparative study of Higgs transition in one-component and two-component lattice superconductor models", arXiv preprint arXiv:0805.1494 (2008).

[63] A. B. Kuklov et al., "Deconfined Criticality: Generic First-Order Transition in the SU(2) Symmetry Case", Physical Review Letters 101 (2008), 050405.

[64] L. Bartosch, "Corrections to scaling in the critical theory of deconfined criticality", Physical Review B 88 (2013), 195140.

[65] D. Charrier, F. Alet, and P. Pujol, "Gauge Theory Picture of an Ordering Transition in a Dimer Model", Physical Review Letters 101 (2008), 167205.

[66] G. Chen et al., "Coulomb gas transitions in three-dimensional classical dimer models", Physical Review B 80 (2009), 045112.

[67] D. Charrier and F. Alet, "Phase diagram of an extended classical dimer model", Physical Review B 82 (2010), 014429.

[68] G. J. Sreejith and S. Powell, "Scaling dimensions of higher-charge monopoles at deconfined critical points", Physical Review B 92 (2015), 184413.

[69] H. Shao, W. Guo, and A. W. Sandvik, "Quantum criticality with two length scales", Science 352 (2016), 213.

[70] A. Karch and D. Tong, "Particle-Vortex Duality from 3D Bosonization", Physical Review X 6 (2016), 031043.

[71] N. Seiberg et al., "A duality web in 2+1 dimensions and condensed matter physics", Annals of Physics 374 (2016), 395.

[72] C. Wang et al., "Deconfined quantum critical points: symmetries and dualities", Physical Review X 7 (2017), 031051.

[73] D. F. Mross, J. Alicea, and O. I. Motrunich, "Symmetry and Duality in Bosonization of Two-Dimensional Dirac Fermions", Physical Review X 7 (2017), 041016.

[74] D. Simmons-Duffin, unpublished.

[75] M. Nauenberg and D. Scalapino, "Singularities and scaling functions at the Potts-model multicritical point", Physical Review Letters 44 (1980), 837.

[76] J. L. Cardy, M. Nauenberg, and D. Scalapino, "Scaling theory of the Potts-model multicritical point", Physical Review B 22 (1980), 2560.

[77] B. Holdom, "Raising the sideways scale", Physical Review D 24 (1981), 1441.

[78] K. Yamawaki, M. Bando, and K.-i. Matumoto, "Scale-invariant hypercolor model and a dilaton", Physical Review Letters 56 (1986), 1335.

[79] T. Appelquist, D. Karabali, and L. Wijewardhana, "Chiral hierarchies and flavor-changing neutral currents in hypercolor", Physical Review Letters 57 (1986), 957.

[80] V. Gorbenko, S. Rychkov, and B. Zan, "Walking, Weak first-order transitions, and Complex CFTs", Journal of High Energy Physics 2018 (2018), 108.

[81] V. Gorbenko, S. Rychkov, and B. Zan, "Walking, Weak first-order transitions, and Complex CFTs II. Two-dimensional Potts model at $Q > 4$", SciPost Physics 5 (2018), 050.

[82] P. Serna and A. Nahum, "Emergence and spontaneous breaking of approximate O(4) symmetry at a weakly first-order deconfined phase transition", Physical Review B 99 (2019), 195110.

[83] A. Nahum, "Note on Wess-Zumino-Witten models and quasiuniversality in $2+1$ dimensions", arXiv preprint arXiv:1912.13468 (2019).

[84] R. Ma and C. Wang, "Theory of deconfined pseudocriticality", Physical Review B 102 (2020), 020407.

[85] C.-M. Jian et al., "Continuous Néel-VBS quantum phase transition in non-local one-dimensional systems with SO(3) symmetry", SciPost Physics 10 (2021), 033.

[86] S. Yang, D.-X. Yao, and A. W. Sandvik, "Deconfined quantum criticality in spin-$\frac{1}{2}$ chains with long-range interactions", arXiv preprint arXiv:2001.02821 (2020).

[87] S. Jiang and O. Motrunich, "Ising ferromagnet to valence bond solid transition in a one-dimensional spin chain: Analogies to deconfined quantum critical points", Physical Review B 99 (2019), 075103.

[88] E. Lieb, T. Schultz, and D. Mattis, "Two soluble models of an antiferromagnetic chain", Annals of Physics 16 (1961), 407.

[89] A. Karch, D. Tong, and C. Turner, "A Web of 2d Dualities: $\mathbb{Z}_2$ Gauge Fields and Arf Invariants", SciPost Physics 7 (2019), 7.

Chapter 2

RIGOROUS RENORMALIZATION GROUP FOR LOCAL HAMILTONIANS

[1] B. Roberts, T. Vidick, and O. I. Motrunich, "Implementation of rigorous renormalization group method for ground space and low-energy states of local Hamiltonians", Physical Review B 96 (2017), 214203.

2.1 Schematic overview

In this chapter we describe in detail how the *rigorous renormalization group* (RRG) operates to solve for the ground and low-energy states of local Hamiltonians in one dimension (1D). The structure of the chapter is as follows. In this section we give a first heuristic overview of RRG and some differences from related existing methods. We then provide a detailed, self-contained description of our algorithm in Sec. 2.2. In Sec. 2.3 is a precise discussion of the differences between the proof and the present work, for the reader familiar with the theoretical RRG paper. An extended presentation of numerical results is contained in Sec. 2.4; while the results are reliable, this study was performed with code which is now out-of-date and **the runtimes quoted in Sec. 2.4 should not be considered currently representative.** For an example of more modern timing, we have performed a comparison similar to Table 2.1 of this chapter using the current code[1] as Table 1.1 in the Introduction. Given its origins as a highly technical theoretical algorithm developed in order to obtain provable guarantees, the RRG method performs surprisingly well, often matching the results of standard DMRG implementations and outperforming them in certain difficult cases exhibiting degenerate ground spaces or highly entangled ground states. Finally, we give an outlook on further work in Sec. 2.5.

Broadly, the RRG strategy is this: partition the system into small initial blocks, and, focusing on the Hilbert space of the blocks individually, identify sets of states that are "extendable" to the rest of the system to create a good approximation to the system-wide ground space. This property is termed

[1] Available at `https://www.github.com/brendenroberts/RigorousRG`.

viability, and formally defined in Eq. (2.1). The identification of viable sets is accomplished with an *approximate ground state projector* (AGSP), an operator approximately filtering out highly excited states on the entire system, whose support is restricted to perform this filtering within each block individually. In this way RRG deviates from a traditional real-space blocking scheme, in which each block does not have access to global information. The next step is to merge the identified viable sets on adjacent blocks, obtaining states supported on blocks of larger size. However, this step and the local application of the AGSP result in an untenable blow-up of the number of states, so a reduction step is performed, returning the number of states per block (now comprising two blocks of the smaller size) to a constant value. This procedure is iterated, merging blocks in a tree-like manner, and at the full system scale, the identified states are shown to closely approximate the low-energy space [1].

In the present work we adapt these techniques to specify a concrete RRG procedure allowing for the explicit computation of ground and low-energy states of local Hamiltonians. This requires making allowance for computational limitations, and generally our modifications operate outside of the regime of rigorous guarantee. Still, our algorithm presents a conceptually new approach to this task. We emphasize that the use of the word "rigorous" is in reference to the title of Arad et al. [1], rather than in order to establish a contrast with other tensor network algorithms.

The main conceptual departure of this algorithm from existing tensor network methods is that RRG operates on viable sets of states supported on blocks, rather than on variational states in the full Hilbert space. Two important features arise from this distinction. First, no local energy minimization on a particular ansatz state is performed. Even though in the RRG procedure described here the basic operations are performed on MPS comprising an approximate basis of the viable sets, the MPS objects themselves are incidental, and the concerns arising from the MPS ansatz (e.g., gauge choice, truncation) are external to the fundamental algorithm.

Second, the physical degrees of freedom are not coarse-grained. The objective of a coarse-graining strategy is to limit the dimensionality of the Hilbert space at increasing scale by the introduction of renormalized degrees of freedom, determined by some local rule, specifying a smaller effective Hilbert space. Instead, RRG achieves this goal by maintaining viable sets of constant dimension

at all levels of the algorithm hierarchy. These processes cannot be considered equivalent, as the RRG step of applying the AGSP operator changes the relationship between scales in a complicated way, and does not match the intuition of an "RG flow" in a small number of parameters. However, this method still allows for fully controllable systematic improvements in accuracy.

2.2 Operation of implemented algorithm

The input is a local Hamiltonian H acting on N qubits, specified by an MPO. Let n, s and D be input parameters.

1. Initialize:
   a) Construct AGSP K from Hamiltonian H.
   b) Partition system into contiguous blocks of length n, denoted J_0^λ for $\lambda = 0, 1, \ldots, N/n - 1$. Obtain s-dimensional low-energy eigenspace V_0^λ of block Hamiltonian H_0^λ for each λ.
2. For $m = 0, 1, \ldots, \log_2(N/n) - 1$, denoting an "RG step" or scale factor:
   a) Expand: for $\lambda = 0, 1, \ldots, N/(2^m n) - 1$:
      i. Extract D^2 operators $\{A_{m,r}^\lambda\}_{r=1,\ldots,D^2}$ from the AGSP K, acting on subsystem J_m^λ. Operate on the viable set, taking $V_m^\lambda \to W_m^\lambda \equiv \{A_{m,r}^\lambda V_m^\lambda\}_r$, where $\dim(W_m^\lambda) \leq sD^2$.
      ii. Compute the restriction of the block Hamiltonian H_m^λ to $W_m^\lambda \subset \mathcal{H}_m^\lambda$.
   b) Reduce: For $\lambda = 0, 2, \ldots, N/(2^m n) - 2$:
      i. (Merge) Obtain the tensor product space $W_m^\lambda \otimes W_m^{\lambda+1} \subset \mathcal{H}_{m+1}^{\lambda/2}$, supported on qubits in $J_{m+1}^{\lambda/2} = J_m^\lambda \cup J_m^{\lambda+1}$. Compute the restriction of $H_{m+1}^{\lambda/2}$ to the tensor product set.
      ii. Obtain s-dimensional low-energy eigenspace of the restriction of $H_{m+1}^{\lambda/2}$ to the tensor product space. Use the eigenstates as a basis for viable set $V_{m+1}^{\lambda/2}$ in iteration $m + 1$.
3. At $m = m^* = \log(N/n)$, the viable set $V_{m^*}^0$ is a candidate for the low-energy space T supported on the full system.

Figure 2.1: Outline of RRG algorithm.

2.2.1 Overview and notation

The steps of RRG as implemented are listed in Fig. 2.1 for reference and are discussed in detail in subsequent sections. A visual schematic is shown in

Fig. 2.2. Our notation is as follows. Let $H = \sum_{i=0}^{N-2} h_i$ be a 2-local Hamiltonian on a chain of N qubits, with term h_i acting on sites i and $i+1$. (The generalization to k-local Hamiltonians and qudits is straightforward.) Denote the Hilbert space of the system by $\mathcal{H}$, and refer to the low-energy eigenspace of H as T. Let n be a parameter specifying the size of initial regions of the system, and assume N/n is a power of 2. For each $m = 0, 1, \ldots, \log_2(N/n)$, partition the N-site system into contiguous blocks of equal length $2^m n$. Call these $J_m^\lambda = \{\lambda 2^m n, \ldots, (\lambda+1)2^m n - 1\}$, for $\lambda = 0, 1, \ldots, N/(2^m n) - 1$. The Hilbert space associated with J_m^λ is denoted $\mathcal{H}_m^\lambda$, and $\mathcal{H} = \bigotimes_\lambda \mathcal{H}_m^\lambda$. Let H_m^λ be the block Hamiltonian on J_m^λ, comprising all terms acting only on sites in J_m^λ and excluding boundary terms. Explicitly, $H_m^\lambda = \sum_{i \in J_m^{\lambda\,*}} h_i$, where $J_m^{\lambda\,*} = \{\lambda 2^m n, \ldots, (\lambda+1)2^m n - 2\}$.

2.2.2 Initialization

The first step is to construct an *approximate ground state projector* (AGSP) K, whose action on states in $\mathcal{H}$ increases overlap with T, the low-energy subspace of H. Many constructions of AGSP are possible. In the interest of efficiency, we use an AGSP obtained as an approximation to a thermal operator at temperature t/k, $K \approx e^{-kH/t}$, $t, k > 0$. Let Q_t denote a matrix product operator (MPO) approximating the thermal operator $e^{-H/t}$ at temperature t; procedures such as a Trotter decomposition [2] or cluster expansion can be used to efficiently compute this MPO. The AGSP is then obtained as a power of Q_t, contracting the product on the physical indices k times.

Because the AGSP must later be divided into operators acting on individual blocks, to compute Q_t requires contraction of the tensor network having terms of the form $e^{-h_i/t}$. After each contraction an SVD is performed between site indices, and the MPO is truncated by eliminating low-weight Schmidt vectors across each bond. Here truncation is meant in the sense of MPS truncation, representing the MPO as a state in a higher-dimensional local Hilbert space. This amounts to using the Frobenius norm to order the terms arising from the SVD, and may not be an optimal way to approximate operators; we address this issue in more detail later.

The second step in the initialization is to identify sets of states $V_0^\lambda \subset \mathcal{H}_0^\lambda$, for $\lambda = 0, 1, \ldots, N/n - 1$, of constant dimension s, where s is a parameter of the algorithm which bounds the dimension of the sets manipulated throughout.

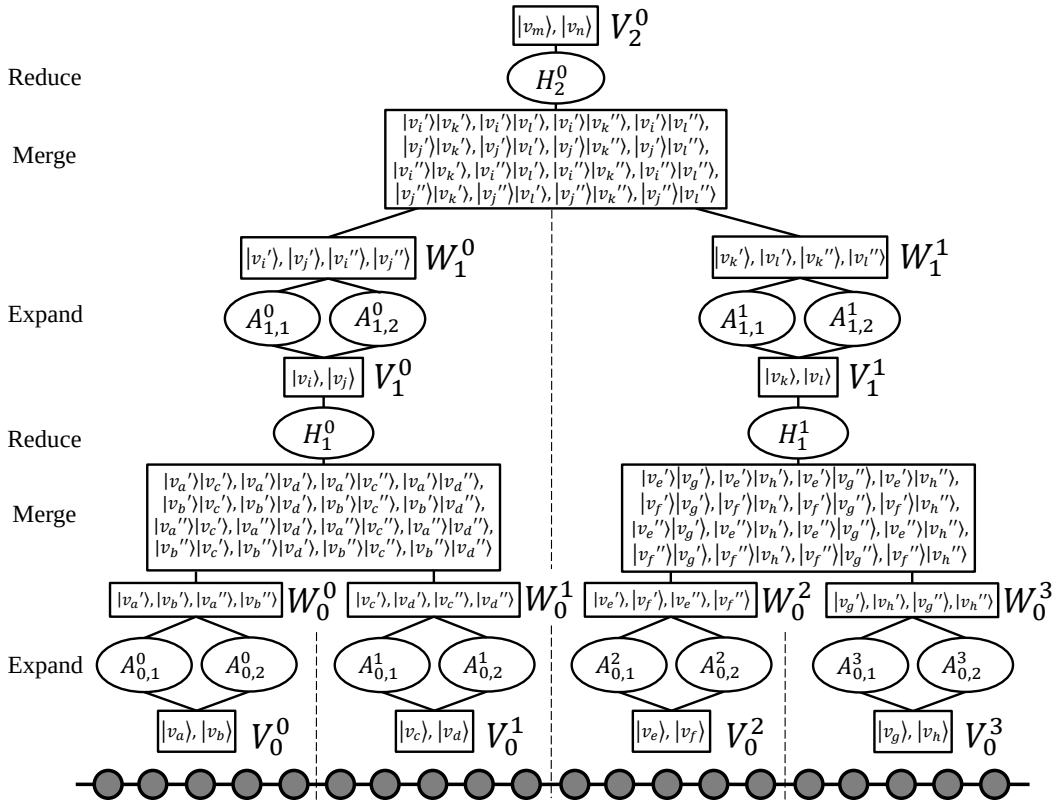

Figure 2.2: Schematic illustration of the RRG algorithm over several length scales $m = 0, 1, 2$. As shown, $(s, D) = (2, 2)$ and block size $n = 5$. Gray dots represent local Hilbert spaces, and the V_0^0, V_0^1, etc., are the viable sets over blocks of sites. The labeled vectors $|v_a\rangle$, etc., are basis states for the viable sets and have no relationship between blocks at a given scale. The action of the projector operators $A_{m,r}^{\lambda}$ on the states is represented by primes and double primes (e.g., $A_{0,1}^0|v_a\rangle = |v_a{}'\rangle$ and $A_{0,2}^0|v_a\rangle = |v_a{}''\rangle$). These generate the expanded viable sets W_0^0, and so on. The Merge procedure obtains tensor product states such as $|v_a{}'\rangle|v_c{}'\rangle$ supported on two blocks, and the tensor product set is reduced in dimension via diagonalizing block Hamiltonians such as H_1^0, producing a viable set supported on two blocks.

We use the term "viable sets" for the V_0^{λ} (generally, for $V_m^{\lambda} \subset \mathcal{H}_m^{\lambda}$) because the intent of the algorithm is that each V_m^{λ} be extendable to include a good approximation to the global low-energy eigenspace T. That is, each set V_m^{λ} is chosen such that if $\mathcal{H} = \mathcal{H}_m^{\lambda} \otimes \overline{\mathcal{H}}_m^{\lambda}$, then $V_m^{\lambda} \otimes \overline{\mathcal{H}}_m^{\lambda}$ contains a subspace which is a good approximation to T. We identify a set V_m^{λ} as *δ-viable* if

$$P_T P_{V_m^{\lambda} \otimes \overline{\mathcal{H}}_m^{\lambda}} P_T \geq (1 - \delta) P_T, \tag{2.1}$$

where P_T is a projector onto a subspace T. More concretely, consider the case of a non-degenerate global ground space $T = \mathrm{Span}\{|\tau\rangle\}, |\tau\rangle \in \mathcal{H}$. The viability

of the set V_m^λ is given by

$$\delta = 1 - \max_{|x\rangle \in V_m^\lambda \otimes \overline{\mathcal{H}}_m^\lambda} |\langle \tau | x \rangle|^2 \ , \tag{2.2}$$

where $|x\rangle = \sum_j a_j |v_j\rangle |\overline{v}_j\rangle$ for a collection of states $\{|v_j\rangle\} \subset V_m^\lambda$ along with coefficients a_j, and states $\{|\overline{v}_j\rangle\}$ arbitrary in the Hilbert space of the sites in the complement. It will be shown in Sec. 2.2.3 that one need never explicitly compute the $\{|\overline{v}_j\rangle\}$. For the case that $\dim(T) > 1$, δ is obtained by taking the smallest value of the maximum in (2.2), over all $|\tau\rangle \in T$. The goal of the algorithm is to construct the viable sets V_m^λ in such a way that they are indeed δ-viable for some constant δ less than 1 for all scales m. Note that a small value of δ corresponds to a better approximation, in contrast with measures like overlap. We emphasize that the viability parameter is not explicitly computed by the algorithm. Instead, it provides a useful metric to evaluate performance, both in terms of the theoretical results and in terms of experimental investigations for cases where we wish to compare with other methods providing estimates for the ground space (such as when exact diagonalization is possible).

If n is chosen to be small enough, generic operators on $\mathcal{H}_0^\lambda$ can be exactly diagonalized. In the initialization step, the initial viable set V_0^λ is specified to be the span of the s eigenvectors of H_0^λ of lowest energy, obtained by exact diagonalization.

2.2.3 Iteration over scale

The algorithm proceeds through a tree-like hierarchy, the levels of which are specified by a scale parameter $m = 0, 1, \ldots, \log_2(N/n)$. At scale m, block J_m^λ consists of $2^m n$ sites and the region index λ runs from 0 to $N/(2^m n) - 1$. Note that although the scale of the algorithm is increasing, we do not eliminate any of the physical degrees of freedom. At each step we assume that the previous level has produced a viable set V_m^λ with basis $\{|v_q\rangle\}_{q=1,\ldots,s}$ represented by MPS, for every λ.

The algorithm performs two steps. The first step is the *expansion* of the viable set, which has the effect of improving the viability parameter δ as defined in Eq. (2.1). This is accomplished using the AGSP constructed in the initialization step as follows. Let $J_{m,L}^\lambda$ denote the qubits to the left of J_m^λ, and $J_{m,R}^\lambda$ those to the right. (Generally J_m^λ has two boundaries with its complement

$J^\lambda_{m,L} \cup J^\lambda_{m,R}$. The system-edge cases follow immediately.) Consider the MPO representation of the AGSP K, whose elementary tensors are collections of operators on the local Hilbert space, as an MPS. The Schmidt decomposition of K across the left boundary, separating $J^\lambda_{m,L}$ from $J^\lambda_m \cup J^\lambda_{m,R}$, produces a virtual index of dimension ζ:

$$K = \sum_{\alpha<\zeta} \sigma_\alpha L_\alpha M_\alpha \ . \tag{2.3}$$

The L_α are the left Schmidt vectors and the M_α the right—which are operators on $J^\lambda_m \cup J^\lambda_{m,R}$—each with a corresponding Schmidt coefficient σ_α. The Schmidt decomposition may then be obtained for each of the M_i across the boundary between J^λ_m and $J^\lambda_{m,R}$, producing a virtual index of dimension ξ. That is,

$$M_\alpha = \sum_{\beta<\xi} \nu_{\alpha\beta} A_{\alpha\beta} R_{\alpha\beta} \ . \tag{2.4}$$

Each $A_{\alpha\beta}$ is an operator on $\mathcal{H}^\lambda_m$, with weight $\gamma_{\alpha\beta} = \sigma_\alpha \nu_{\alpha\beta}$ in the expansion of K. For clarity we make the algorithm variables explicit: $A^\lambda_{m,\alpha\beta}$. Now let $D > 0$ be another parameter of the algorithm. In order to increase the viability of the set V^λ_m, act on it with the D^2 operators $A^\lambda_{m,r}$, $r = (\alpha, \beta)$, having highest weight $\gamma_r = \gamma_{\alpha\beta}$. That is, take $V^\lambda_m \to W^\lambda_m = \mathrm{Span}(\{A^\lambda_{m,r}|v_q\rangle\}_{r,q})$, which we refer to as an *expanded viable set* with dimension bounded by sD^2.

One expects this operation to produce a set W^λ_m of better viability than V^λ_m because the $A^\lambda_{m,r}$ operators together are meant to increase overlap with the global low-energy space T: this is the defining property of the AGSP. More precisely, let $\{|v_j\rangle\}$ be a collection of states in V^λ_m such that there exists $\{|\overline{v}_j\rangle\} \in \overline{\mathcal{H}}^\lambda_m$ such that for some coefficients a_j, the state $|x\rangle = \sum_j a_j |v_j\rangle|\overline{v}_j\rangle$ has good overlap with T. By construction, $K|x\rangle$ has better overlap with T than $|x\rangle$. Using the decomposition of Eqs. (2.3) and (2.4),

$$K|x\rangle = \sum_{\alpha,\beta,j} \gamma^\lambda_{m,\alpha\beta} a_j A^\lambda_{m,\alpha\beta} |v_j\rangle \otimes \overline{A}^\lambda_{m,\alpha\beta} |\overline{v}_j\rangle \ , \tag{2.5}$$

where $\overline{A}^\lambda_{m,\alpha\beta} = L^\lambda_{m,\alpha} R^\lambda_{m,\alpha\beta}$. In this way the viability as defined in Eq. (2.2) of the set V^λ_m can be improved while leaving both the states and the operators supported on the complement $\overline{\mathcal{H}}^\lambda_m$ entirely implicit.

If all operators $A^\lambda_{m,\alpha\beta}$ were applied to V^λ_m, the resulting set would contain the collection of states $\{A^\lambda_{m,\alpha\beta}|v_j\rangle\}$, which has improved viability. However,

instead of applying all $A^{\lambda}_{m,\alpha\beta}$, which would lead to an unmanageable blow-up in the size of the viable set, we introduce an approximation by selecting the D^2 operators $A^{\lambda}_{m,r}$ of highest weight γ_r in order to obtain W^{λ}_m. There is no formal guarantee that this is the best choice, as the Schmidt decomposition is based on the Frobenius rather than the operator norm. In practice we found the choice to be quite reasonable: to observe the increase in viability in a nondegenerate gapped model, compare the V and W points in Fig. 2.3, and in a critical model in Figs. 2.5, 2.6.

The second step performed at each scale m is that of *reduction* of the dimension of the expanded viable sets W^{λ}_m and $W^{\lambda+1}_m$ to generate $V^{\lambda/2}_{m+1}$. At the cost of a loss of viability, this step restores s-dimensionality, resulting in a viable set suitable to use at the next level. One first performs a *merge* operation on disjoint pairs of blocks $(\lambda, \lambda+1)$, with $\lambda = 0, 2, \ldots, N/(2^m n) - 2$. Merging refers to computing the tensor product set $W^{\lambda}_m \otimes W^{\lambda+1}_m$ that has support on sites $J^{\lambda}_m \cup J^{\lambda+1}_m$. One obtains the viable set $V^{\lambda/2}_{m+1}$, a subspace of $\mathcal{H}^{\lambda/2}_{m+1} = \mathcal{H}^{\lambda}_m \otimes \mathcal{H}^{\lambda+1}_m$, from the s-dimensional low-energy eigenspace of the restriction of $H^{\lambda/2}_{m+1}$ to $W^{\lambda}_m \otimes W^{\lambda+1}_m$. We note that this step differs from its counterpart in the theoretical algorithm, which proceeds via random sampling instead of deterministically selecting the lowest-energy eigenvectors of $H^{\lambda/2}_{m+1}$, as we do here. Our choice is based on efficiency considerations described below; see also Sec. 2.3 for further discussion. The effect of the operation on the viability of the reduced subspaces can be seen in Figs. 2.3, 2.5, and 2.6.

The single viable set $V^0_{m^*}$ generated at $m^* = \log_2(N/n)$ after the reduction step at scale $m^* - 1$, is a constant-dimensional δ-viable subspace with support on the full system. The algorithm returns the s lowest-energy eigenvectors of the restriction of H to $W^0_{m^*-1} \otimes W^1_{m^*-1}$, which comprise a basis for this candidate subspace.

2.2.4 Scaling and computational considerations

The accuracy with which RRG approximates low-energy eigenstates of H is controlled primarily by two parameters, s and D. To recapitulate, s bounds the dimension of the reduced viable sets at each step, and D controls the level of approximation in the application of the AGSP via the operators $\{A^{\lambda}_{m,r}\}$, $r = 1, \ldots, D^2$. Both parameters are reflected in the bound on the dimension sD^2 of the expanded viable sets W^{λ}_m.

We review the steps in the algorithm and discuss their complexity scaling based on these parameters. In addition to s and D, important parameters are the system size N and the bond dimensions χ for MPS and η for MPO that are manipulated throughout. For physical Hamiltonians it is reasonable to expect χ and η to be constant in the gapped case, and in gapless systems $\chi, \eta \sim N$. See Schollwöck [3] for a discussion of the scaling of basic MPS operations. Note that the initial block size n only enters this analysis in determining the number of necessary layers $\log(N/n)$.

The initialization requires obtaining viable sets V_0^λ of the Hilbert space $\mathcal{H}_0^\lambda$ on the qubits J_0^λ. For small enough choices of n the complexity of this step will be negligible, so we omit it. Similarly, the computation of the full AGSP $K \approx (e^{-H/t})^k$ can be done efficiently via Trotter decomposition, and is not an important bottleneck. In order to extract the operators $\{A_{m,r}^\lambda\}$, $r = 1, \ldots, D^2$, the AGSP must be obtained as an MPO in canonical form, analogous to that used for MPS. To do so requires a sequence of $O(N)$ SVD operations, each with cost $O(\eta^3)$.

For the steps comprising the iterated procedure we give scaling results applicable at the final computational level $m = m^* - 1$. The first step is to apply K to each V_m^λ by means of the Schmidt decomposition of K across the boundary separating J_m^λ from its complement $\bigcup_{\lambda' \neq \lambda} J_m^{\lambda'}$. This yields a set of operators acting on $\mathcal{H}_m^\lambda$. Applying the D^2 such operators of highest Schmidt weight to a basis of the subspace takes $V_m^\lambda \to W_m^\lambda$, increasing the dimension to sD^2. The total cost of contracting these MPS and MPO is $O(sD^2 N \chi^2 \eta^2)$.

The second step acts on disjoint pairs of neighboring regions, forming the tensor product of expanded viable sets: $W_m^\lambda \otimes W_m^{\lambda+1}$, with dimension $(sD^2)^2$. We compute the matrix elements of the restriction of the block Hamiltonian to the tensor product set. The scaling of this step is $O\left([(sD^2)^2]^2 N \chi^3\right)$. For local Hamiltonians the constant can be improved using the decomposition

$$H_{m+1}^{\lambda/2} = H_m^\lambda + H_m^{\lambda+1} + B_{m+1}^{\lambda/2} = H_m^\lambda + H_m^{\lambda+1} + \sum_p B_{m,p}^\lambda \otimes B_{m,p}^{\lambda+1} \, . \tag{2.6}$$

The operator $B_{m+1}^{\lambda/2}$ contains $O(1)$ terms in H acting across the boundary between J_m^λ and $J_m^{\lambda+1}$.

Exact diagonalization of the restricted block Hamiltonian in the subspace has complexity $O([(sD^2)^2]^3) = O(s^6 D^{12})$. After this, the final step is to explicitly

compute the s lowest-energy eigenstates, which has a total cost $O(s(sD^2)^2 N\chi^3)$. These states are used as a basis for the viable set at the next iteration.

From this coarse analysis it is clear that the limiting step with respect to s and D is the diagonalization of the restricted block Hamiltonian. This step is not part of the original formulation, which specifies instead that the reduction of viable set dimension takes place by randomly selecting states from the tensor product set. The choice of our variant is motivated by its effect on the entanglement of the intermediate basis states: low-energy excited states of a block Hamiltonian may display lower entanglement than states chosen randomly. In practice this lowers χ in some systems. It also demonstrates a different possible interpretation of the parameter s, which during the iteration step implicitly defines an energy scale with respect to the restricted Hamiltonian. States having block excitation energy higher than this scale are inaccessible to the algorithm for the purposes of the expansion step.

2.3 Differences from Arad et al. [1]

Before presenting our numerical results on the performance of the RRG algorithm, we give an account of the main points of departure of our numerical procedure from the theoretically guaranteed algorithm introduced in Arad et al. [1], giving heuristic justification for our choices.

For concreteness we base our comparison on the algorithm presented in Arad et al. [1] for the case of a local Hamiltonian with degenerate gapped ground space (Assumption (DG)). The algorithm is stated as Algorithm 1 in Arad et al. [1]. It consists of two main steps, *Generate* and *Merge*. The two steps together recursively construct a sequence of viable sets V_m^λ for an N-qubit local Hamiltonian, where as in the main text m denotes a scale parameter and λ indexes a subregion.

2.3.1 Generate

The goal of the *Generate* step is to generate an MPO representation for a suitable AGSP. In Arad et al. [1] a fresh AGSP is computed for each scale m and region λ. Given a decomposition $\mathcal{H} = \mathcal{H}_L \otimes \mathcal{H}_m^\lambda \otimes \mathcal{H}_R$, a global AGSP is defined as $K_m^\lambda = T_k(\tilde{H})$, where $\tilde{H}$ is a norm-reduced approximation of H (which depends on the region decomposition) and T_k a suitably scaled Chebyshev polynomial of degree k. The operators $A_{m,r}^\lambda$ are then computed from a specific decomposition of K_m^λ across the left and right boundaries, yielding D^2

terms $A^{\lambda}_{m,r}$ such that the expansion procedure $V^{\lambda}_{m} \to W^{\lambda}_{m}$ described in the main text is guaranteed to have a significant improvement on the viability parameter.

Here we depart from the theoretical algorithm in two important ways. First we use a simpler construction of AGSP, which we expect to exhibit similar behavior but is more efficient to compute. Our AGSP takes the form of an approximation $K \approx e^{-kH/t}$ obtained by Trotter decomposition. (In Arad et al. [1] a similar approach is taken to norm-reduce the parts of the Hamiltonian that lie in the regions L, M, and R but are a distance at least $\ell > 0$ from the boundaries.) In Arad et al. [1] the properties of the Chebyshev polynomial are essential to establish that the AGSP has sufficiently low bond dimension across the boundaries of region M. Considering only the efficiency in terms of improvement in viability, however, the use of $e^{-kH/t}$ over the whole chain gives similar guarantees.

Using our simpler construction implies a loss of theoretical control over the bond dimension D of the AGSP operator across the left and right cuts. This entails a second main point of departure from the theoretical algorithm, as a choice has to be made as to which operators $A^{\lambda}_{m,r}$ to keep. As described in the main text we proceed in a natural way by considering the MPO as an MPS and performing SVD operations to create virtual bonds between sites. We then make the choice of keeping operators associated with the D^2 highest Schmidt weights. This choice is heuristic: the Schmidt weights control the Frobenius norm of the associated term $A^{\lambda}_{m,r}$, rather than the operator norm of the resulting operator, as would be desirable. The heuristic nevertheless proved effective: in practice the magnitude of the Schmidt coefficients often fell off quickly, allowing for a relatively aggressive choice of cutting point.

2.3.2 Merge process

The second step in the algorithm is called *Merge*. The goal of this step is to combine two neighboring viable sets into a single viable set over the union of the two regions, with similar approximation and size guarantees. The procedure is described as *Merge'* in Arad et al. [1]. Merge' is provided as input viable sets W^{λ}_{m} and $W^{\lambda+1}_{m}$ defined over neighboring regions, and returns a viable set $W^{\lambda/2}_{m+1}$ defined over the union of the two regions. Merge consists of three steps: *Tensoring*, *Random Sampling*, and *Error Reduction*.

1. *Tensoring:* This step is the same as in Arad et al. [1].

2. *Random Sampling:* Here as already mentioned in the main text we depart from Arad et al. [1] in an important way. In Arad et al. [1] a family of s vectors lying in $W_m^\lambda \otimes W_m^{\lambda+1}$ is obtained by random sampling within the subspace. In practice this procedure is very inefficient: (i) it requires performing high-weight (random) linear combinations of MPS, a step that is computationally expensive due to the MPS renormalization procedure; (ii) the linear combinations formed tend to be arbitrary, and in particular their MPS representations may have high MPS bond dimension, as each vector may include an "irrelevant" (with respect to the low-energy eigenspace of the Hamiltonian) component that artificially inflates its complexity.

   Here we replace random sampling by a deterministic choice of the s lowest-energy eigenvectors of the restriction of H to $W_m^\lambda \otimes W_m^{\lambda+1}$. The idea is that low-energy eigenstates are likely, due to the local structure of the Hamiltonian, to display less entanglement. Indeed in practice this procedure is much more efficient, and yields MPS with lower bond dimension, than the random sampling proposed in Arad et al. [1].

   However, there is *a priori* no reason for the low-energy eigenstates of the block Hamiltonian to form a viable set for the global low-energy space. A simple heuristic argument can nevertheless be given to argue correctness of our procedure. Recall that the viability criterion Eq. (2.1) guarantees that the initial tensor product space supports a good approximation to any ground state. Considering the Schmidt decomposition of this approximation, each of the Schmidt vectors will have a certain energy with respect to the block Hamiltonian $H_{m+1}^{\lambda/2}$, which may not be minimal. The key is thus to argue that vectors with high energy will not have an important contribution to the Schmidt decomposition of the ground state. In general approximation error and energy difference can scale with the norm of the Hamiltonian, making the argument difficult. However, for the purposes of approximating the ground space of a local Hamiltonian two elements play in our favor: first, locality of H, and second, the area law. The former allows to show that the low-energy space of H is well-approximated by an approximation of H with constant norm, so that the error blow-up mentioned above can be controlled (see Arad et al. [1,

Proposition 3], for a precise statement). The latter establishes that the ground state has low bond dimension, so that few Schmidt vectors need to be considered (see Arad et al. [1, Lemma 15], for details on how this can be used). Together these two properties provide a heuristic argument in favor of our modified procedure.

3. *Error Reduction:* The goal of this step is to improve the approximation quality of the viable set. We follow the procedure described in Arad et al. [1], except that the operators $\{A^{\lambda}_{m,r}\}$ are generated differently, as already described.

The final iteration is performed on two viable sets $V^0_{m^*-1}$ and $V^1_{m^*-1}$, each with support on one half of the system. The algorithm returns the low-lying energies and eigenstates obtained via exact diagonalization of the Hamiltonian restricted to the final viable subspace.

2.4 Numerical tests and performance

We now present results from RRG for some example models with the following goals in mind. We first validate the algorithm in a simple gapped nondegenerate system in Sec. 2.4.1, demonstrating consistency with DMRG as well as previous numerical and perturbation theory results. In this case the states obtained by RRG are of similar accuracy to those of DMRG, with run times a factor of 5–10 slower depending on s, D, and N. However, we emphasize that it is not the objective of RRG to obtain a numerically precise ground state; rather, it is to accurately identify states having constant overlap with the global low-energy subspace. One expects an optimization algorithm to obtain a more precise state in the absence of local energy minima or very flat energy landscapes, and for simple models we take the DMRG ground state to be exact (in particular, using it to measure viability δ). The RRG candidate states may later be variationally optimized in order to achieve a particular accuracy, but we do not modify the states here.

Our next goal is to demonstrate the practical scaling of the algorithm's performance and computational costs associated with the subspace parameters (s, D). We use the familiar case of the Ising model in the transverse field in Sec. 2.4.2, both away from and at criticality. We find that for low values of these parameters, often surprisingly good results can be obtained, with close

to unity overlap between DMRG and RRG ground state candidates. However, neither algorithm scales linearly with system size in the critical regime. Here the slowdown of RRG is no longer a simple numerical factor but becomes a significant cost at larger system sizes (beyond a few hundred sites in our implementation) or for larger values of the algorithm parameters.

Finally, we consider somewhat more challenging models demonstrating areas in which RRG may hold an advantage. In Sec. 2.4.3 we investigate the Bravyi-Gosset model [4], which has $O(N)$ ground state degeneracy, by obtaining a complete basis for the ground space. In Sec. 2.4.4 we consider the XY model with randomly-distributed couplings. The ground state of this model, the random singlet phase, displays long-range entanglement in that it supports algebraic decay of correlations. We compare the correlations present in the candidate states of DMRG and RRG to exact results obtained by the Jordan-Wigner transformation, finding that RRG more accurately reproduces observables measured on the state.

All numerical results were obtained using the tensor network library ITensor [5] for both the DMRG and RRG computations. In all of the following, a Trotter decomposition with 60 steps was used to obtain the tensor network for $Q_t \approx e^{-H/t}$, with $t = 10$, and degree $k = 8$ used to compute the AGSP $K \approx (Q_t)^k$. Thus the effective temperature t/k is of order unity. For reasonable choices of parameters the accuracy of the approximation Q_t is not a limiting factor of the algorithm. Computations were performed on standard hardware on a single node of a computing cluster, with only single threading for the reported run times. A single error parameter τ was used to control MPS truncation in ITensor for both DMRG and RRG (usually $\tau \sim 10^{-9}$–10^{-12}); in most cases a more lenient value would drastically improve run times with little effect on accuracy. DMRG convergence was handled using a fixed number of sweeps ≥ 20 and relying on the internal diagonalization routine included in ITensor without any modifications specific to the individual systems. Excited states were found iteratively in DMRG by adding projectors into previously-found states to the Hamitonian and using random trial wavefunctions. Often the average viability will be used as a metric; this is simply the average over region label λ of the viability δ of each viable set (V_m^λ or W_m^λ) at fixed level m.

2.4.1 Nonintegrable Ising model

This model refers to a spin-1/2 Hamiltonian

$$H = -J \sum_{i=0}^{N-2} \sigma_i^z \sigma_{i+1}^z - g \sum_{i=0}^{N-1} \sigma_i^x - h \sum_{i=0}^{N-1} \sigma_i^z \ . \tag{2.7}$$

For $h \neq 0$ the model is gapped with a nondegenerate ground state, and admits no good quantum numbers due to the longitudinal component of the field. A recent numerical study [6] for the parameters $(J, g, h) = (1, -1.05, 0.5)$ found the ground state energy density to be $\varepsilon_0/N \approx -1.722$ and the gap $\gamma = 3.6401$.

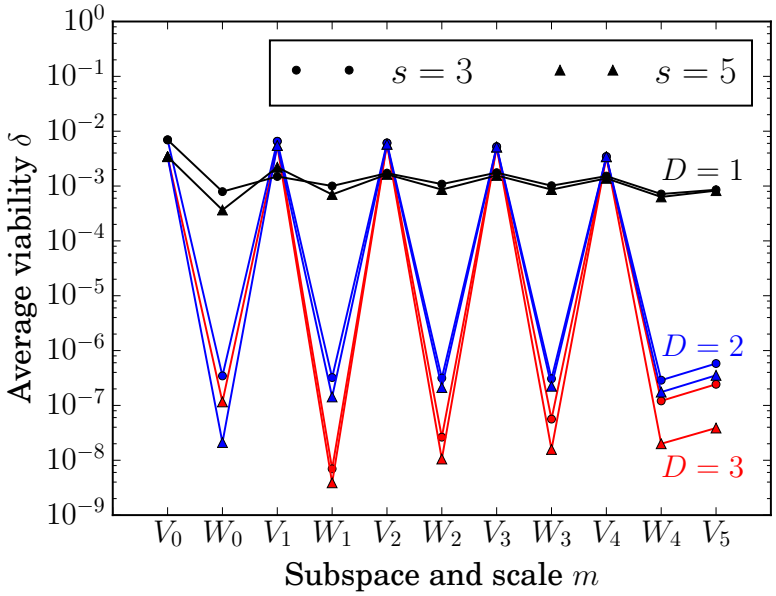

Figure 2.3: Viability of sets V_m^λ, W_m^λ averaged over λ, for nonintegrable Ising model with $N = 256$ spins, obtained as the RRG algorithm progresses through the scale hierarchy. Data are shown for parameter values $s = 3, 5$ and $D = 1, 2, 3$.

We run the RRG algorithm for a fixed system size $N = 256$, initial block size $n = 8$, and track the average viability δ of the viable sets V_m and W_m through the sequence of dimensional expansion and reduction at each scale m (see Fig. 2.2). Each data point shown in Fig. 2.3 is the average over λ at a given length scale m. The parameters (s, D) are varied to demonstrate their influence on the results. For gapped systems of this size both DMRG and RRG have run times scaling linearly with system size, however RRG runs more slowly by a factor of 5–10 compared to DMRG. At $N = 256$, DMRG

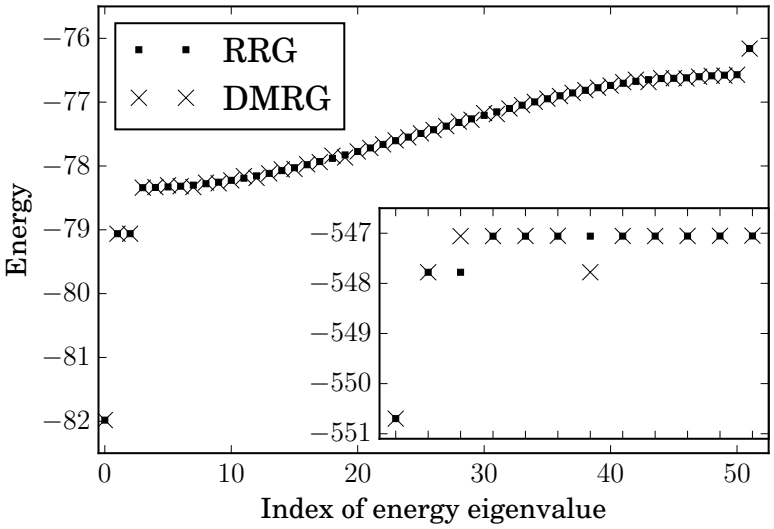

Figure 2.4: Energy eigenvalues of the nonintegrable Ising Hamiltonian for $N = 48$ within the subspace obtained by RRG for $(s, D) = (52, 3)$, along with DMRG results for low-energy states. Inset: the same computation for $N = 320$ and $(s, D) = (12, 3)$. DMRG does not consistently identify both edge states in sequence; see text for details.

took 5 minutes to converge $s = 5$ states (ground and four excited) and RRG ran in 30 minutes with $(s, D) = (5, 3)$.

The large improvement in viability from V to W is attributable to the AGSP, rather than simple increase in dimension. Both $\dim(V) = s$ and $\dim(W) = sD^2$ are constant in m and very small compared to the dimensions of the block Hilbert spaces. Choosing n vectors without bias from an M-dimensional space will produce a subspace whose squared overlap with a specific vector is of order n/M. Since M here is exponentially large, a constant increase in n would not much affect measured viability. Thus, the AGSP is an effective projector even at low values of D, which we expect as the model is gapped.

A consequence is that the accuracy of RRG for the largest (s, D) is comparable to that of DMRG, but we do not expect this to be a general feature. Recall from Sec. 2.2.2 that the criterion the algorithm seeks to maintain is that the measured viability δ of the V_m^λ (and thus the average viability) be bounded for all m by some constant $\delta^* < 1$, rather than approaching unity exponentially in m. The viability of the W_m^λ is not necessarily specified, but should be sufficiently good for the V_{m+1} viable sets at the next level to satisfy the bound. For assessing the performance of RRG, as in Fig. 2.3, one requires that δ be

maintained away from 1 for the V_m averages.

The final s-dimensional viable sets V_{m^*} (V_5 in Fig. 2.3) here and in the following examples display much better average viability than that of the previous V_m. This is generally true: at steps $m < m^*$ the viable set is found by diagonalizing a block Hamiltonian H_m^λ, which omits terms present in H. The low-energy eigenspace of this operator need not be close to T, the global low-energy space. At $m = m^*$, however, the low-energy eigenspace of $H_{m^*}^0 = H$ coincides with T, resulting in minimal loss of viability from the dimensional reduction.

By changing the parameters of RRG, we obtain candidates for low-energy excited states. The ground state of this model is close to a uniform spin-up state, and the excited band contains a spin-flip excitation. Under open boundary conditions two nearly degenerate lower-energy states separate from the first band, corresponding to quasiparticles localized at either edge. We obtain the low-energy spectrum for $N = 48$ with $(s, D) = (52, 3)$, and for $N = 320$ with $(s, D) = (12, 3)$. The results are shown in Fig. 2.4, compared with DMRG states. For small N both methods find the entire first excited band. In the larger system, the localized edge states are more difficult for DMRG, and it does not consistently find the edge states in sequence. The RRG ground state energy density at $N = 320$ is $\varepsilon_0/N = -1.721$ and the gap to the excited band is $\gamma = 3.6402$, in agreement with previous results. We find the half-chain entanglement entropy of the ground state and edge states to be $S = 0.01$ bits, and of the states in the band to be $S \approx 1.01$ bits, consistent with qualitative understanding of these states. For DMRG and RRG, ground states have bond dimension 4 and excited states in the band have bond dimension 31. (The methods do not yield identical bond dimension in all cases.)

2.4.2 Transverse-field Ising model

Consider the same Hamiltonian in the regime $h = 0$; that is, the Ising model in a transverse field. Fig. 2.5 shows the result as we approach the critical point $J = g$ from the paramagnetic phase for $N = 128$, measuring average viability throughout the algorithm. One observes a strong deterioration of the measured viability as the gap closes. Approaching the critical point, RRG takes increasingly more time than DMRG to run: runtimes for $J/g = 0.6$ for both methods are shown in Table 2.1, where, for example, at criticality DMRG takes 800 seconds and RRG takes 17000 seconds.

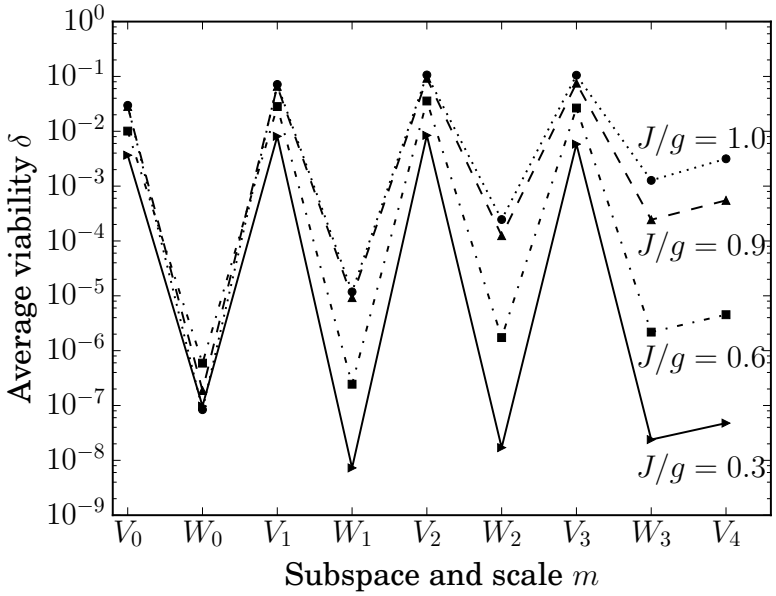

Figure 2.5: Viability of sets V_m^λ, W_m^λ, averaged over λ, for the transverse-field Ising model both away from and at criticality. The number of spins is $N = 128$. All data points were generated using parameter values $(s, D) = (5, 4)$.

N	RRG runtime (s)	DMRG runtime (s)
32	158	94
48	337	132
64	866	208
96	1871	277
128	3912	393

Table 2.1: Runtimes of DMRG and RRG for the transverse-field Ising model with $J/g = 0.6$, using $(s, D) = (5, 4)$. Some randomness is inherent in the DMRG results due to the use of random trial states. $s = 5$ states are found by DMRG.

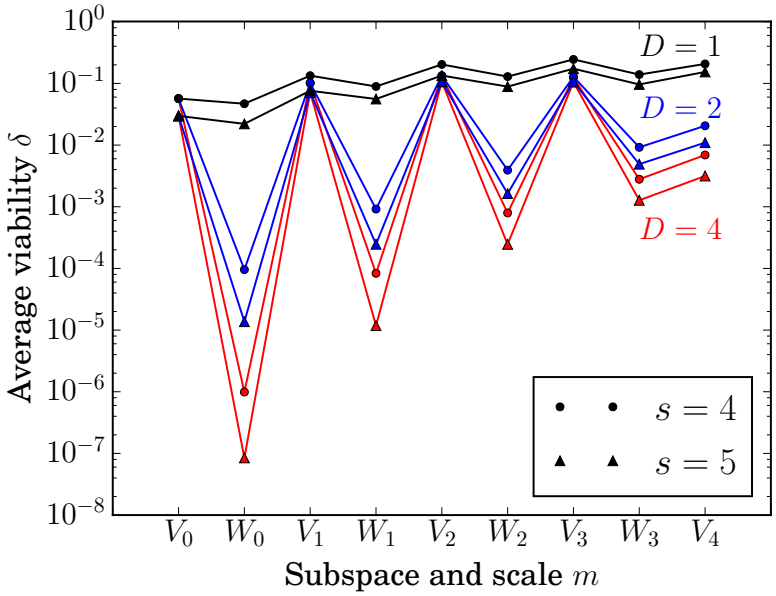

Figure 2.6: Viability of sets V_m^λ, W_m^λ, averaged over λ, for the transverse-field Ising model at criticality, obtained as the RRG algorithm progresses through the scale hierarchy. Data are shown for parameter values $s = 4, 5$ and $D = 1, 2, 4$.

We demonstrate the scaling with parameters s and D at criticality in Fig. 2.6. The improvement in viability with increasing D is less dramatic than seen in Fig. 2.3, corresponding to a flatter spectrum of Schmidt values across the cuts between subsystems. Note in this case that at the critical point, as the algorithm progresses, the average viability of the V_m sets visibly approaches unity, in contrast to the gapped case, which appears to maintain viability bounded away from 1.

2.4.3 Bravyi-Gosset model

This model was initially introduced as a classification scheme for frustration-free 2-local Hamiltonians[4]. The Hamiltonian is

$$H = \sum_{i=0}^{N-2} |\psi\rangle\langle\psi|_{i,i+1}, \tag{2.8}$$

where $|\psi\rangle$ is a generic state on two qubits. Up to a global phase, such a state can be specified in the form $|\psi\rangle = R(\theta)_1 \left(p|00\rangle + \sqrt{1-p^2}|11\rangle\right)$, with $R(\theta)_1$ a rotation performed on the first qubit. As the spectrum is invariant under global rotation, the Hamiltonian is fully specified by the two parameters $\theta \in [0, 2\pi)$, $p \in [0, 1/2]$. Restricting to $\theta = 0$, we may rewrite Eq. (2.8) in a

more familiar notation:

$$H = \sum_{i=0}^{N-2} \left(\frac{\sqrt{p(1-p)}}{2} \left(\sigma_i^x \sigma_{i+1}^x - \sigma_i^y \sigma_{i+1}^y \right) + \frac{1}{4} \sigma_i^z \sigma_{i+1}^z \right) + \sum_{i=0}^{N-1} \left(\frac{1-2p}{4} \sigma_i^z + \frac{1}{8} \right). \tag{2.9}$$

That is, this model is equivalent to a particular XYZ model in a fine-tuned field. For any value of p the system exhibits $(N+1)$-fold ground state degeneracy. Basis states for the ground space can roughly be thought of as having two regions of differing magnetization, with an interface which can be located at any site with ground state energy $\varepsilon_0 = 0$. (Refer to Bravyi et al. [4] for a full description.) Therefore the algorithm choice $s \geq N + 1$ is sufficient to obtain the full ground space.

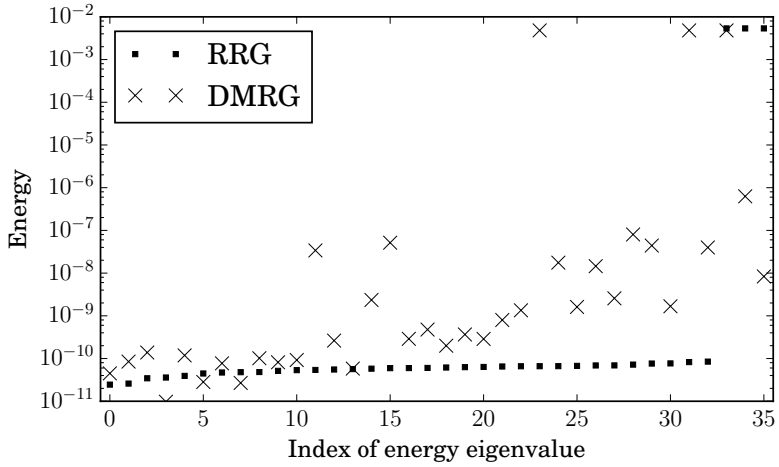

Figure 2.7: Energy eigenvalues of Bravyi–Gosset model with $N = 32$ sites within the subspace obtained by RRG for $(s, D) = (36, 3)$. Also shown are DMRG results for the 36 lowest-energy states.

The low-energy spectrum obtained by RRG for this model at $N = 32$ is shown in Fig. 2.7, along with the DMRG results. We use $p = 1/2$; that is, $|\psi\rangle$ is a Bell state. Using $(s, D) = (36, 3)$, RRG identifies the full zero-energy ground space to within an accuracy determined by τ, the truncation error of the MPS. In contrast, obtaining the full ground space of this model is challenging for DMRG, which becomes hampered by candidate states of very high entanglement, often requiring a bond dimension an order of magnitude larger than those of RRG candidate states in order to achieve similar truncation error. These not only are computationally intensive to optimize, but also present DMRG with difficulty finding further excited states, as the modified

Hamiltonian includes nonlocal projectors. Thus, the candidate states are not accurate eigenstates of the original Hamiltonian. This difficulty is evident in run times as well; to obtain the data shown took 10 hours for RRG and 40 hours for DMRG. Here we use DMRG without taking into account the degenerate ground state manifold, and we consider these results to be only a point of reference. Use of a specialized approach like multiple targeting could improve accuracy, or diagonalization of the original Hamiltonian within the subspace spanned by the DMRG candidate states could recover much of the ground space; however, no such specialized approach is needed for RRG.

2.4.4 Random XY model

The random XY model is an inhomogeneous spin-1/2 system with Hamiltonian

$$H = \sum_{i=0}^{N-2} J_i(\sigma_i^x \sigma_{i+1}^x + \sigma_i^y \sigma_{i+1}^y) \ , \tag{2.10}$$

where the position-dependent coupling constants J_i are drawn from a random distribution. If the logarithm of the distribution is broad, Dasgupta-Ma real-space renormalization group analysis identifies the ground state as the random singlet phase, in which pairs of spins form singlet states at all length scales [7–10]. This model is tractable by the Jordan-Wigner transformation, which maps onto free spinless fermions. We use this system as a benchmark of algorithmic ability to encode long-range correlations in the ground state.

We use the following distribution for the Hamiltonian terms: $p(J_i) = \frac{1}{\Gamma} J_i^{-(1-\frac{1}{\Gamma})}$, $J_i \in (0, 1]$, with Γ controlling the width of the distribution of log-energies [10]. We fix $\Gamma = 2$, which is sufficiently broad that the ground state is composed predominantly of localized singlet states on neighboring sites, along with spatially separated correlated qubits occurring at all length scales. As a metric we use the average two-point correlation function $\overline{\langle \sigma_i^z \sigma_j^z \rangle}$ as a function of separation $r = |i - j|$ in the ground state, which is known to decay algebraically as r^{-2}. This quantity is compared to exact diagonalization results from the inhomogeneous free fermion description in Fig. 2.8.

These results are intended to present a fair comparison between DMRG and RRG. Both methods used unrestricted MPS bond dimension to achieve a truncation error $\tau \leq 10^{-12}$. Typically the ground state bond dimension is similar for both methods. The RRG parameters are $(s, D) = (4, 5)$. DMRG used 20 sweeps per state, and convergence of several "hard" examples (see below) was

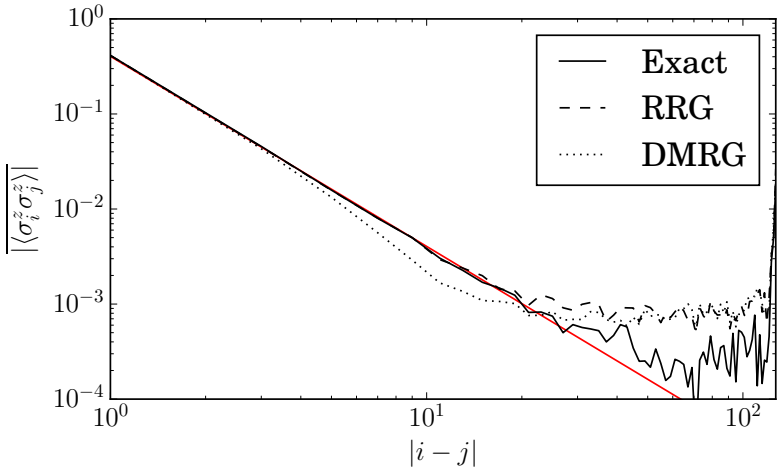

Figure 2.8: Disorder-averaged decay of correlations of candidate ground states of the random XY model for $N = 128$, as compared to exact results obtained through the Jordan-Wigner transformation. The predicted power-law behavior is indicated by the red line.

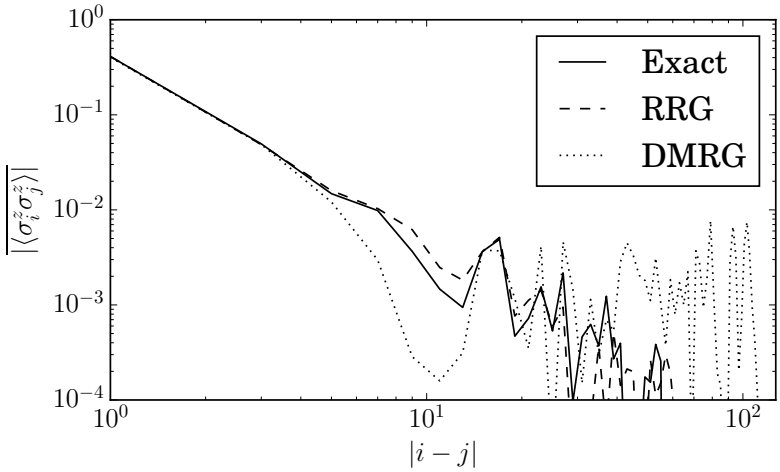

Figure 2.9: A typical "hard" instance contained in the disorder average above, with energy gap $\gamma \approx 10^{-7}$. This is sufficiently large for RRG to track the long-range correlations with $(s, D) = (4, 5)$. DMRG displays a tendency for lower correlations until saturating at the noise floor.

confirmed using 50 sweeps. DMRG typically took 1 hour to converge $s = 4$ states and RRG took 8 hours to complete. The average is over 150 disorder realizations.

The observed "saturation" of the correlations of Fig. 2.8 to a noise floor arises from the structure of the low-energy excited states. For a broad initial distri-

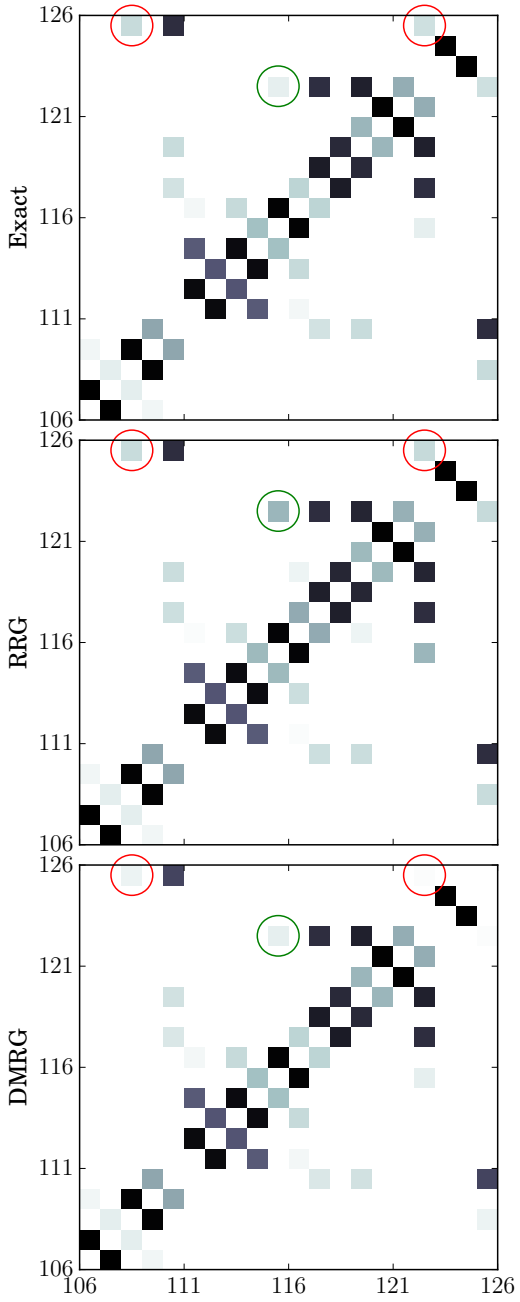

Figure 2.10: Expectation value $\langle \sigma_i^z \sigma_j^z \rangle$, where sites i and j are given by the axes for $i, j \in [106, 125]$. The color scales with $\log |\langle \sigma_i^z \sigma_j^z \rangle|$ and runs from $[-2, 0]$ in all plots, with darker color indicating a higher value. The diagonal is omitted. Circles mark particular sites where differences between exact results and candidate states are evident. This disorder realization is the same "hard" instance shown in Fig. 2.9.

bution, the energy gap of a specific disorder Hamiltonian may be very small. For any method using MPS, a lower limit on the gap in order to distinguish the ground state (at energy ε_0) is $\gamma \sim \tau\varepsilon_0$, below which the MPS truncation procedure will randomly select a vector from the low-lying subspace. However, even for realizations with much larger gaps a candidate ground state may include substantial contributions from low-energy excited states. A singlet of length l has energy scale $\varepsilon \sim e^{-\sqrt{l}}$; thus, the low-lying states involve excitations localized on the long-range entangled sites. Choosing a random superposition of these amounts to white noise at long distances. Instances of such Hamiltonians in the disorder average must necessarily eventually overwhelm the decay of correlations; here the distribution of energy gaps is very broad on a log scale [11], so these cases are frequent. However in all cases the RRG candidate state has $O(1)$ overlap with the true ground state, and typically this overlap is greater than 99%.

For disorder-averaged correlations at short range up to $|i - j| \approx 20$, RRG reproduces algebraic decay of correlations matching the exact results. In contrast, the DMRG candidate states demonstrate stronger decay of correlations. There is no systematic difference in MPS bond dimension between DMRG and RRG, indicating that RRG is not simply using additional resources, but is indeed more sensitive to long-range correlations.

Independent of the saturation due to the energy gap, the disorder average comprises both "easy" and "hard" instances. In easy cases both DMRG and RRG match the exact results closely at all length scales. In the hard cases both algorithms obtain the correlations only approximately, but DMRG appears to consistently underestimate correlations. RRG does not demonstrate a tendency towards either enhanced or reduced correlations. We provide an example of the spatially averaged correlations from a hard disorder realization in Fig. 2.9. Fig. 2.10 shows an example of measured correlations $\langle \sigma_i^z \sigma_j^z \rangle$ for various sites $i, j \in [106, 125]$ in this particular disorder realization. Each square corresponds to a measurement $\langle \sigma_i^z \sigma_j^z \rangle$ where (i, j) are specified by the axes. Darker squares indicate a larger magnitude of correlation between these sites. We show the exact results, RRG, and DMRG, and indicate some particular pairs of sites where either DMRG (red) or RRG (green) differ visibly from exact results. These variations in certain entangled sites tend toward reduced correlations in DMRG candidate ground states; it is unclear how much addi-

tional sweeping is required to compensate. RRG shows similar inaccuracies, but these are random, due to states missing from certain viable sets. Accurate correlations emerge in the disorder-averaged value, and the performance on individual disorder realizations can be controllably improved by tuning the dimension of the viable sets through the parameters s and D.

2.5 Outlook for RRG method

One of the main findings of our initial numerical investigation is that the RRG algorithm, developed for theoretical purposes, can in fact be made quite effective in practice, to the point of providing a potentially viable alternative to DMRG in certain cases of practical interest. We stress that the choices of parameters that we employ in our numerics are not known to be located in the theoretically guaranteed regime, and some of the building blocks required for the proof have been altered in our implementation. Regardless, we find that RRG obtains ground state candidates having large overlap with the true ground state in a variety of physically relevant models, and surpasses existing techniques in obtaining low-energy excited states and ground states of particular models demonstrating large degeneracy or long-range entanglement.

Like another numerical scheme, *time-evolving block decimation* (TEBD), the RRG procedure is a projector method, relying on operators extracted from the AGSP to guide the choice of states between scales. As a result, given a sufficiently accurate AGSP, RRG will not output a part of the spectrum strictly excited above the ground space. This is advantageous relative to variational ansatz methods which may without warning converge to an excited state rather than the ground state [12]. (For example, this can occur if the energy landscape in Hilbert space has local minima or is very flat in the low-energy space, as is the case with the random XY model of Sec. 2.4.4.) The downsides to projector methods are that performance strongly depends on the gap and that a random initial state, even taken from the manifold of low bond dimension MPS, has exponentially small overlap with the ground state. RRG circumvents the latter issue by never choosing a trial wavefunction on the entire system, but rather building global states from wavefunctions supported on blocks which already have good viability; thus the projection step never has to overcome starting with an exponentially small overlap between the initial and the target state.

One advantage of RRG is flexibility to operate independently of a specific rep-

resentation of states in Hilbert space. Here we have described an MPS RRG. In order to translate the logic to subspaces whose basis states are described by MERA—as would be natural for critical phases—one needs only the ability to perform evaluation of observables and addition. The former is a standard contraction which is highly efficient in MERA, and the latter can be seen as a variational process on overlaps, providing a straightforward interpretation as a MERA operation. Systems with periodic boundary conditions also present an interesting generalization, as until the final level the steps of the algorithm are insensitive to the system boundaries, provided an appropriate AGSP is given. On a more speculative note, other tensor network ansatze may also be amenable: although it is not known that the RRG algorithm scales efficiently in higher dimensions, the hierarchical structure does generalize in an evident way and it may be the case that the algorithm gives acceptable results for PEPS representations of some two-dimensional systems.

Our numerical results suggest situations in which RRG may perform well relative to existing algorithms. The first, informed by Sec. 2.4.1, is a case in which localized and delocalized excitations lie close in energy. An optimization algorithm operating on local degrees of freedom in a sweeping pattern may exhibit a bias towards delocalized excitations, which allow for effective optimization on many lattice sites. RRG is largely insensitive to such distinctions. The second case is that of Sec. 2.4.3, exhibiting highly degenerate ground states. The full ground space is more accurately found in its entirety by RRG than DMRG. The iterative DMRG procedure of finding states is susceptible to finding poor or highly entangled candidates, which reduce the accuracy of subsequent candidates. Such a limitation is not fundamental and could likely be eliminated by modification of the procedure; however no such modification is necessary for RRG. Finally, in Sec. 2.4.4 we observe in the random XY model in the random singlet phase that long-range correlations are encoded more precisely in the ground state candidate of RRG than of DMRG, influencing observables computed for the state.

The examples we provide illustrate specific properties indicating that a model may be well suited for RRG. However, very little is known about its more general performance: other systems with disorder, periodic boundary conditions, and higher dimensions all pose interesting challenges and could constitute exciting new directions.

BIBLIOGRAPHY

[1] I. Arad et al., "Rigorous RG algorithms and area laws for low energy eigenstates in 1D", Communications in Mathematical Physics 356 (2017), 65.

[2] M. Suzuki, "Relationship between d-dimensional quantal spin systems and $(d+1)$-dimensional Ising systems equivalence, critical exponents and systematic approximants of the partition function and spin correlations", Progress of theoretical physics 56 (1976), 1454.

[3] U. Schollwöck, "The density-matrix renormalization group in the age of matrix product states", Annals of Physics 326 (2011), 96.

[4] S. Bravyi and D. Gosset, "Gapped and gapless phases of frustration-free spin-12 chains", Journal of Mathematical Physics 56 (2015), 061902.

[5] M. Fishman, S. R. White, and E. M. Stoudenmire, *The ITensor Software Library for Tensor Network Calculations*, 2020.

[6] C.-J. Lin and O. I. Motrunich, "Quasiparticle explanation of the weak-thermalization regime under quench in a nonintegrable quantum spin chain", Phys. Rev. A 95 (2017), 023621.

[7] R. N. Bhatt and P. A. Lee, "Scaling Studies of Highly Disordered Spin-$\frac{1}{2}$ Antiferromagnetic Systems", Phys. Rev. Lett. 48 (1982), 344.

[8] S.-K. Ma, C. Dasgupta, and C.-K. Hu, "Random Antiferromagnetic Chain", Phys. Rev. Lett. 43 (1979), 1434.

[9] C. Dasgupta and S.-K. Ma, "Low-temperature properties of the random Heisenberg antiferromagnetic chain", Phys. Rev. B 22 (1980), 1305.

[10] D. S. Fisher, "Random antiferromagnetic quantum spin chains", Phys. Rev. B 50 (1994), 3799.

[11] D. S. Fisher and A. P. Young, "Distributions of gaps and end-to-end correlations in random transverse-field Ising spin chains", Phys. Rev. B 58 (1998), 9131.

[12] P. Schmitteckert, "Disordered one-dimensional fermi systems", *Density-Matrix Renormalization*, Springer, 1999, 345.

Chapter 3

CONTINUOUSLY VARYING CRITICAL EXPONENTS IN RANDOM XYZ MODEL

3.1 Motivation for study

In this chapter we perform a study of the XYZ model of spins in 1d with quenched randomness. Our motivation is the result of Slagle et al. [1], who investigated the possibility of MBL along a critical line between gapped phases with magnetic order. The previous work found evidence for continuously varying exponents for disorder- and energy-averaged Edwards–Anderson correlators along the critical line.

It is not clear whether their picture is stable to ergodicity at finite energy density [2, 3], and we do not address that question here. Instead, we are interested in the low-energy description of the critical line as an IRFP with continuously varying critical indices. We apply RRG to this problem, as it was already shown to be effective in a related model, the random XY spin chain, in Sec. 2.4.4. Our goals for the unbiased tensor network numerics are both to test the findings of Ref. [1] and to better understand the IRFP associated with the critical line.

The outline of this chapter is as follows. In Sec. 3.2 we present the XYZ spin model and summarize the history of the SDRG in this case, along with explicitly developing the RG rules in the many-body language. In Sec. 3.3 we preform an unbiased numerical study of the ground state. In Sec. 3.4, based on our numerical results, we develop both a Hartree–Fock mean-field theory and a quadratic effective model we describe as "locally correlated." Both theories reproduce aspects of the phenomenology of the XYZ model. In Sec. 3.5, we use a picture of the SDRG acting on random walks to prove continuously varying critical exponents in the locally correlated effective model. Finally in Sec. 3.6 we discuss the implications of these results taken together.

3.2 Random XYZ model and review of previous SDRG results

3.2.1 Spin chain Hamiltonian

As our most general model we consider the antiferromagnetic XYZ spin chain with quenched randomness in all couplings; that is,

$$H = \sum_{j=1}^{N-1} \left(J_j^x \sigma_j^x \sigma_{j+1}^x + J_j^y \sigma_j^y \sigma_{j+1}^y + J_j^z \sigma_j^z \sigma_{j+1}^z \right) \ . \tag{3.1}$$

The couplings $J_j^\alpha > 0$, $\alpha = x, y, z$, are independent. This model generically has a $\mathbb{Z}_2 \times \mathbb{Z}_2$ global symmetry, with generators given by the Ising-type operators $g_x = \prod_{j=1}^N \sigma_j^x$ and $g_y = \prod_{j=1}^N \sigma_j^y$. In particular, local field terms are excluded by this symmetry. This model also respects time reversal on the spins, which we implement as $g_y \mathcal{K}$, where $\mathcal{K}$ is complex conjugation in the z basis.

We impose the same functional form on the disorder distributions for J_j^x, J_j^y, and J_j^z (though delay specification until Sec. 3.3), with bandwidths specified by a set of parameters $\tilde{J}^x, \tilde{J}^y, \tilde{J}^z > 0$. If the value of any one of these is larger than the other two, the ground state of the model displays Ising antiferromagnetic (AFM) order. As we are considering strong disorder, we anticipate that these phases are localized. If two bandwidths are equal and of the largest magnitude, the model lies on a boundary between localized phases with distinct types of magnetic order; we will primarily consider this case. If all three disorder bandwidths are equal, the model has a statistical S_3 permutation symmetry and sits at a tricritical point in the phase diagram [1, 4].

Many exact results are known for phases of the Hamiltonian Eq. (3.1) in certain limits, and we provide a brief recap here. The SDRG was in fact originally introduced in order to study the random Heisenberg antiferromagnet with SU(2) symmetry [5, 6], achieved in the present notation by fixing $J_j^x = J_j^y = J_j^z$ for all bonds j. These works argued for the asymptotic development of a power-law singularity in the distribution of couplings and computed leading contributions to critical indices, which vary slowly along the flow.

Fisher [4] generalized this analysis to account for anisotropy and performed a thorough study of the resulting phase diagram. The SDRG rules for the random XX model ($J_j^x = J_j^y$ and $J_j^z = 0$ for all j), which breaks the SU(2) spin rotation symmetry to a U(1) subgroup, are very similar to those of the isotropic model, and in particular both realize the *random-singlet* (RS) phase. In the ground state, the microscopic spins are paired up into singlets at arbitrarily

long scales. Correlations between the spins in a given singlet are of order unity, and are strongly suppressed with the rest of the system. Thus typical spin correlations are short-ranged, whereas the average correlations are dominated by rare paired spins. This is one hallmark of an IRFP: that a distribution which is broad on a logarithmic scale leads to exponential separation between typical and averaged properties of the state. From the density of paired spins one obtains the power-law decay of average spin correlations scaling as r^{-2} for separation r. The characteristic energy scale of the singlets in the RS phase follows $\log(1/E) \sim L^{\psi}$, where $\psi = \frac{1}{2}$. As a consequence for the density of states, the dynamical exponent is formally infinite.

The random XY chain (i.e., independent J_j^x and J_j^y but with $\tilde{J}^x = \tilde{J}^y$, $\tilde{J}^z = 0$), in contrast, does not realize the RS phase. With the mean anisotropy serving as the quantum control parameter, Fisher [4] computed the critical exponents $\nu = 2$ and $\beta = 3-\sqrt{5}$ for the transition separating Ising x- and y-AFM phases. This is accomplished through a lattice duality mapping to two decoupled copies of the random transverse-field Ising model (RTFIM), whose SDRG equations are also well studied [7–9]. Translating the RTFIM results to the present XY chain, at the phase transition the critical exponent for the decay of x and y components of spin correlations is $\eta_x = \eta_y = 4 - 2\phi$, where $\phi = \frac{1+\sqrt{5}}{2}$ is the golden mean.

Starting from the opposite limit of the XX model, with $J_j^x = J_j^y$ for all j, it was also found by Fisher [4] that weak random anisotropy, which moves along the phase transition toward the XY point, is a marginal perturbation. It was not clear whether this is the case along the entire phase boundary, and we will in fact be led to take up this question in some detail in Sec. 3.5.

The set of exponents for average decay of spin correlations can be completed using the mapping of the XX and XY models to free fermions [10]. For the anisotropic model with S_2 permutation symmetry, $\eta_z = 4$. In a chain with open boundaries, consideration of the form of the surface magnetization leads to the scaling of the end-to-end spin correlations $\eta_x^{\mathrm{e}} = \eta_z^{\mathrm{e}} = 1$ for the XX model and $\eta_x^{\mathrm{e}} = 1$, $\eta_z^{\mathrm{e}} = 2$ for the XY model.

Focusing on a different type of spin chain, Damle et al. [11] studied permutation-symmetric multicritical points arising from effective low-energy theories of partially dimerized spin-S models with SU(2) symmetry. They perform a fixed-point analysis of the SDRG equations for degrees of freedom localized at the

boundaries between distinct domains of $n = 2S + 1$ different types of local order. Their primary result is a generalization of the $n = 2$ random-singlet criticality to a countably infinite set of IRFPs with critical exponents $\psi = \frac{1}{n}$ and $\nu = \frac{2n}{\sqrt{4n+1}-1}$. The permutation symmetry refers to the interchange of distributions for the different types of order, which mediate effective couplings between the domain walls. While the permutation-symmetric tricritical point at $\tilde{J}^x = \tilde{J}^y = \tilde{J}^z$ in our model shares the symmetry of these theories for $n = 3$, its microscopic details are dissimilar and it is not clear whether this category of universality applies.

3.2.2 Majorana representation

Aspects of this problem become more evident in the language of fermions, for which we use the Jordan–Wigner transformation. Eq. (3.1) maps to a spinless p-wave superconductor with density-density interactions:

$$H = \sum_{j=1}^{N-1} (t_j c_j^\dagger c_{j+1} + \Delta_j c_j^\dagger c_{j+1}^\dagger + \text{H.c.}) + J_j^z (2n_j - 1)(2n_{j+1} - 1) \ , \tag{3.2}$$

which has position-dependent hopping $t_j = J_j^x + J_j^y$ and pairing potential $\Delta_j = J_j^x - J_j^y$. Following the idea of Kitaev [12], it is enlightening to introduce two species of Majorana fermion,

$$\eta_j = c_j^\dagger + c_j \ \text{ and } \ \zeta_j = \frac{1}{i}(c_j^\dagger - c_j) \ . \tag{3.3}$$

The η_j and ζ_j are Hermitian, and normalized so that $(\eta_j)^2 = (\zeta_j)^2 = 1$. In terms of these operators the Hamiltonian is written

$$H = \sum_{j=1}^{N-1} i J_j^x \zeta_j \eta_{j+1} - i J_j^y \eta_j \zeta_{j+1} - J_j^z \eta_j \zeta_j \eta_{j+1} \zeta_{j+1} \ . \tag{3.4}$$

The symmetry group of the problem is somewhat more expressive in the Majorana language. In the following we specialize to even system sizes $N \in 2\mathbb{Z}$. The generators of the global symmetry translate to

$$g_x = i^{N/2} \zeta_1 \eta_2 \zeta_3 \cdots \eta_N \ , \tag{3.5}$$

$$g_y = (-i)^{N/2} \eta_1 \zeta_2 \eta_3 \cdots \zeta_N \ . \tag{3.6}$$

The symmetries measure fermion parity on two disjoint sets partitioning the Majorana orbitals. The Hamiltonian Eq. (3.4) takes the form of separate

"imaginary random hopping" problems (see Ref. [13]) on these two chains of Majoranas of length N, which we denote $\mathcal{X} = \{\zeta_1, \eta_2, \zeta_3, \ldots, \eta_N\}$ and $\mathcal{Y} = \{\eta_1, \zeta_2, \eta_3, \ldots, \zeta_N\}$. On each chain the coefficients of the hopping terms—which are fermion parity measurements on adjacent orbitals within a chain—alternate between iJ_j^x and $-iJ_j^y$. There are also inter-chain coupling terms with coefficients J_j^z. A single "rung" term $i\eta_j\zeta_j$ is odd under the parity symmetries, and H instead includes the double-rung interactions $-\eta_j\zeta_j\eta_{j+1}\zeta_{j+1}$.

The generator Θ of time-reversal symmetry acts on the Majoranas as $\{i, \eta_j, \zeta_j\} \mapsto \{-i, \eta_j, -\zeta_j\}$. This symmetry prohibits nonzero expectation values of the form $\langle i\eta_j\eta_k\rangle$ or $\langle i\zeta_j\zeta_k\rangle$, even when these orbitals are included in the same Majorana chain.

Constraining $J_j^z = 0$ for all j, the resulting Hamiltonian $H_{\text{xy}} = H[\tilde{J}^x, \tilde{J}^y, \tilde{J}^z = 0]$ is quadratic in the fermions and can be solved for any particular disorder realization by diagonalization of the auxiliary Bogoliubov–de Gennes (BdG) matrix in the particle-hole basis. The mapping to the Majoranas in Eq. (3.3) transforms the BdG matrix to a purely imaginary and block-off-diagonal form, corresponding to the decoupling of the two Majorana chains $\mathcal{X}$ and $\mathcal{Y}$. This further simplifies the solution for the single-particle eigenstates to diagonalization of a pair of $N \times N$ tridiagonal matrices.

As we are considering boundaries between Ising ordered phases, the natural observables are the corresponding magnetic order parameters σ^α, $\alpha = x, y, z$. Written in terms of fermion operators, the spin correlation functions $C^\alpha(j,k) = \langle\sigma_j^\alpha\sigma_k^\alpha\rangle$ are

$$C^x(j,k) = \langle i\zeta_j(i\eta_{j+1}\zeta_{j+1})\cdots(i\eta_{k-1}\zeta_{k-1})\eta_k\rangle \ , \tag{3.7}$$

$$C^y(j,k) = \langle -i\eta_j(i\eta_{j+1}\zeta_{j+1})\cdots(i\eta_{k-1}\zeta_{k-1})\zeta_k\rangle \ , \tag{3.8}$$

$$C^z(j,k) = \langle -\eta_j\zeta_j\eta_k\zeta_k\rangle \ . \tag{3.9}$$

From Wick's theorem, in the ground state for any specific disorder realization $C^x(j, j+r)$ and $C^y(j, j+r)$—which we collectively refer to as $C^\perp(j, j+r)$—can be computed as Pfaffians of antisymmetric $2r \times 2r$ matrices. We focus on this case and consider the angle brackets $\langle\cdot\rangle$ as denoting expectation values measured in the ground state, although the expressions Eqs. (3.7–3.9) apply more generally.

3.2.3 Strong-disorder renormalization group

Decoupled Majorana chains

Examining the Hamiltonian on Majorana chains $\mathcal{X}$ and $\mathcal{Y}$ also clarifies the form of the analytic SDRG. In the decoupled model H_{xy}, the RG proceeds independently on each of the chains, which are endowed with parity conservation. The SDRG for a single such chain was developed explicitly in the single-particle spectrum language by Motrunich et al. [13] and in the many-body Hamiltonian language by Monthus [14]. We review the result here, specialized to our case, in the many-body language, which naturally extends to the interacting problem [14]. For now we consider only a single Majorana chain, and relabel the orbitals as γ_n, $n = 1, \ldots, N$. The Hamiltonian acting on this chain is $H_{\mathcal{M}} = \sum_{n=1}^{N-1} i h_n \gamma_n \gamma_{n+1}$. Suppose that the largest energy scale is set by $H_0 = i h_k \gamma_k \gamma_{k+1}$ for some $k \in [1, N-1]$. H_0 measures fermion parity on the two orbitals, with eigenvalues $\pm h_k$ associated with the two parity states; denote the splitting by $\Omega = 2h_k$. Accordingly, this term is diagonalized by the complex fermion mode $f_0^\dagger = \frac{1}{2}(\gamma_k + i\gamma_{k+1})$, which has projectors $\pi^+ = f_0 f_0^\dagger$ and $\pi^- = 1 - \pi^+ = f_0^\dagger f_0$ into the even and odd parity sectors, respectively. In terms of the projectors $H_0 = (\Omega/2)(\pi^+ - \pi^-)$.

The rest of the terms in $H_{\mathcal{M}} \equiv H_0 + V$ can be treated as a perturbation if the nearby couplings are much smaller than the local gap $|\Omega|$. Because the SDRG generates an effective disorder distribution with increasingly broad logarithm, although this condition may not be satisfied initially the validity of the assumption improves during the RG flow. The rest of the Hamiltonian can be divided into diagonal and off-diagonal components with respect to H_0; specifically, $V = V_{\mathrm{d}} + V_{\mathrm{od}}$, where

$$V_{\mathrm{d}} = \pi^+ V \pi^+ + \pi^- V \pi^- \ , \tag{3.10}$$

$$V_{\mathrm{od}} = \pi^- V \pi^+ + \pi^+ V \pi^- = \pi^- H_{\mathcal{M}} \pi^+ + \pi^+ H_{\mathcal{M}} \pi^- \ . \tag{3.11}$$

Note that V_{od} contains only a constant number of local terms. We denote the small scale of these terms relative to H_0 by the parameter ϵ. The effective Hamiltonian with emergent good quantum number $\langle f_0^\dagger f_0 \rangle$ is found by a Schrieffer–Wolff transformation eliminating V_{od} up to order $O(\epsilon^2)$ [15–17]. That is, $H'_{\mathcal{M}} = e^{iS} H_{\mathcal{M}} e^{-iS}$, where the Hermitian generator of the rotation can be expanded in powers of ϵ as $S = S^{[1]} + S^{[2]} + \cdots$. The conditions on the rotation are that $S^{[1]}$ is off-diagonal and satisfies $V_{\mathrm{od}} = [H_0, iS^{[1]}]$, and $S^{[2]}$

eliminates off-diagonal terms at order $O(\epsilon^2)$ (but we will not need to write it explicitly); that is,

$$[iS^{[2]}, H_0] + [iS^{[1]}, V] + \frac{1}{2}[iS^{[1]}, [iS^{[1]}, H_0]] = 0 \ . \tag{3.12}$$

A suitable generator is $iS^{[1]} = \frac{1}{\Omega}(\pi^+ H_{\mathcal{M}} \pi^- - \pi^- H_{\mathcal{M}} \pi^+)$,

$$H'_{\mathcal{M}} = e^{iS} H_{\mathcal{M}} e^{-iS} \tag{3.13}$$

$$= H_{\mathcal{M}} + [iS, H_{\mathcal{M}}] + \frac{1}{2}[iS, [iS, H_{\mathcal{M}}]] + \cdots \tag{3.14}$$

$$= H_0 + V_{\rm d} + \frac{1}{2}\sum_{\iota=\pm} \pi^\iota [iS^{[1]}, V_{\rm od}] \pi^\iota + O(\epsilon^3) \tag{3.15}$$

$$\approx H_0 + V_{\rm d} + \frac{1}{\Omega}[\pi^+ H_{\mathcal{M}} \pi^-, \pi^- H_{\mathcal{M}} \pi^+] \ , \tag{3.16}$$

the final line being Eq. (17) of Ref. [14].

The off-diagonal terms are those which share an odd number of Majoranas with H_0 and thus anticommute. Consequently $V_{\rm od} = ih_{k-1}\gamma_{k-1}\gamma_k + ih_{k+1}\gamma_{k+1}\gamma_{k+2}$ and

$$\pi^+ H_{\mathcal{M}} \pi^- = (ih_{k-1}\gamma_{k-1} + h_{k+1}\gamma_{k+2}) f_0 \ , \tag{3.17}$$

$$\pi^- H_{\mathcal{M}} \pi^+ = (ih_{k-1}\gamma_{k-1} - h_{k+1}\gamma_{k+2}) f_0^\dagger \ . \tag{3.18}$$

Finally the rotated Hamiltonian is

$$H'_{\mathcal{M}} = H_0 + V_{\rm d} + \frac{h_{k-1}^2 + h_{k+1}^2}{2h_k}(i\gamma_k\gamma_{k+1}) + i\frac{h_{k-1}h_{k+1}}{h_k}\gamma_{k-1}\gamma_{k+2} + O(\epsilon^3) \ . \tag{3.19}$$

This result includes a renormalization of the strength of the H_0 term which increases the magnitude of the splitting, in addition to a new term $ih'_{k-1}\gamma_{k-1}\gamma_{k+2}$. By projecting into the low-energy sector of H_0 (which depends on the sign of h_k), the Majoranas γ_k and γ_{k+1} are "decimated" into one of the definite parity states of the complex fermion mode, and thereby decoupled from the effective Hamiltonian. The single effective coupling replaces three hopping terms in $H_{\mathcal{M}}$. Because the new term maintains the imaginary random-hopping form, the SDRG is closed in this model space and can be iterated, with the flow acting on the disorder distribution of the couplings $\{h_n\}$. During the RG flow, some of the terms involved in decimations will be themselves renormalized couplings from a prior step; they can be made to fit the present format by

re-indexing the chain after every step in order to remove the decimated Majorana orbitals. In addition, the specific form of the renormalized coupling h'_{k-1} permits a framing of the SDRG in terms of a classical random walk; this approach will be developed in detail in Sec. 3.5.

The many-body Hilbert space is therefore decomposed into a tensor product of non-interacting complex fermions in definite parity states. From the signs of the couplings in Eq. (3.4) one sees that the ground state is even under g_x and g_y if $N \mod 4 = 0$ and odd under g_x and g_y if $N \mod 4 = 2$. The spin correlations in an eigenstate of the Hamiltonian can also be understood from this picture. See Sec. 3.2.4 for a discussion of the ground state correlations.

Majorana problem with inter-chain terms

In the presence of interactions coupling the two Majorana chains, it is necessary to consider the full Hamiltonian Eq. (3.4). In the notation of the present section $H = H_{\mathcal{X}} + H_{\mathcal{Y}} + H_{\text{int}}$, where

$$H_{\mathcal{X}} = \sum_{n=1}^{N-1} i h_n^{\mathcal{X}} \gamma_n^{\mathcal{X}} \gamma_{n+1}^{\mathcal{X}} \ , \tag{3.20}$$

$$H_{\mathcal{Y}} = \sum_{n=1}^{N-1} i h_n^{\mathcal{Y}} \gamma_n^{\mathcal{Y}} \gamma_{n+1}^{\mathcal{Y}} \ , \tag{3.21}$$

$$H_{\text{int}} = \sum_{n=1}^{N-1} K_n (i\gamma_n^{\mathcal{X}} \gamma_{n+1}^{\mathcal{X}})(i\gamma_n^{\mathcal{Y}} \gamma_{n+1}^{\mathcal{Y}}) \ . \tag{3.22}$$

Because all of the terms in H are measurements of fermion parity, the general framework from the previous section—in particular Eq. (3.16)—still applies. Now there are two cases: the largest energy scale can be set by one of either the hopping terms $\{h_n^{\mathcal{M}}\}$ or the interactions $\{K_n\}$. Suppose first that $H_0 = i h_k^{\mathcal{X}} \gamma_k^{\mathcal{X}} \gamma_{k+1}^{\mathcal{X}}$. Now

$$\begin{aligned} V_{\text{od}} = {} & i h_{k-1}^{\mathcal{X}} \gamma_{k-1}^{\mathcal{X}} \gamma_k^{\mathcal{X}} + i h_{k+1}^{\mathcal{X}} \gamma_{k+1}^{\mathcal{X}} \gamma_{k+2}^{\mathcal{X}} \\ & + K_{k-1} (i\gamma_{k-1}^{\mathcal{X}} \gamma_k^{\mathcal{X}})(i\gamma_{k-1}^{\mathcal{Y}} \gamma_k^{\mathcal{Y}}) + K_{k+1} (i\gamma_{k+1}^{\mathcal{X}} \gamma_{k+2}^{\mathcal{X}})(i\gamma_{k+1}^{\mathcal{Y}} \gamma_{k+2}^{\mathcal{Y}}) \ . \end{aligned} \tag{3.23}$$

The components appearing in each off-diagonal block of the Hamiltonian are

$$\begin{aligned}\pi^+ H \pi^- &= \Big(i\left(h^{\mathcal{X}}_{k-1} + K_{k-1}(i\gamma^{\mathcal{Y}}_{k-1}\gamma^{\mathcal{Y}}_{k})\right)\gamma^{\mathcal{X}}_{k-1} \\ &\quad + \left(h^{\mathcal{X}}_{k+1} + K_{k+1}(i\gamma^{\mathcal{Y}}_{k+1}\gamma^{\mathcal{Y}}_{k+2})\right)\gamma^{\mathcal{X}}_{k+2}\Big) f_0 \qquad (3.24)\\ &\equiv (ih^{\mathcal{X},\mathrm{int}}_{k-1}\gamma^{\mathcal{X}}_{k-1} + h^{\mathcal{X},\mathrm{int}}_{k+1}\gamma^{\mathcal{X}}_{k+2}) f_0 \ , \qquad (3.25)\\ \pi^- H \pi^+ &= \Big(i\left(h^{\mathcal{X}}_{k-1} + K_{k-1}(i\gamma^{\mathcal{Y}}_{k-1}\gamma^{\mathcal{Y}}_{k})\right)\gamma^{\mathcal{X}}_{k-1} \\ &\quad - \left(h^{\mathcal{X}}_{k+1} + K_{k+1}(i\gamma^{\mathcal{Y}}_{k+1}\gamma^{\mathcal{Y}}_{k+2})\right)\gamma^{\mathcal{X}}_{k+2}\Big) f_0^\dagger \qquad (3.26)\\ &\equiv (ih^{\mathcal{X},\mathrm{int}}_{k-1}\gamma^{\mathcal{X}}_{k-1} - h^{\mathcal{X},\mathrm{int}}_{k+1}\gamma^{\mathcal{X}}_{k+2}) f_0^\dagger \ . \qquad (3.27)\end{aligned}$$

The effect of the interactions in perturbation theory is simply to modify the couplings into operators which we refer to as "interacting couplings" $h^{\mathcal{X}}_{k\pm1} \to h^{\mathcal{X},\mathrm{int}}_{k\pm1}$. This is a reasonable shorthand because the interacting couplings commute with each other and all fermion operators appearing in the formula. From the result Eq. (3.19) of the previous section, then,

$$H' = H_0 + V_\mathrm{d} + \frac{(h^{\mathcal{X},\mathrm{int}}_{k-1})^2 + (h^{\mathcal{X},\mathrm{int}}_{k+1})^2}{2h^{\mathcal{X}}_k}(i\gamma^{\mathcal{X}}_k\gamma^{\mathcal{X}}_{k+1}) + i\frac{h^{\mathcal{X},\mathrm{int}}_{k-1}h^{\mathcal{X},\mathrm{int}}_{k+1}}{h^{\mathcal{X}}_k}\gamma^{\mathcal{X}}_{k-1}\gamma^{\mathcal{X}}_{k+2} + O(\epsilon^3) \qquad (3.28)$$

$$\begin{aligned}&= H_0 + V_\mathrm{d} + (i\gamma^{\mathcal{X}}_k\gamma^{\mathcal{X}}_{k+1})\Bigg(\frac{(h^{\mathcal{X}}_{k-1})^2 + (h^{\mathcal{X}}_{k+1})^2 + K^2_{k-1} + K^2_{k+1}}{2h^{\mathcal{X}}_k} \\ &\qquad + i\frac{h^{\mathcal{X}}_{k-1}K_{k-1}}{h^{\mathcal{X}}_k}\gamma^{\mathcal{Y}}_{k-1}\gamma^{\mathcal{Y}}_k + i\frac{h^{\mathcal{X}}_{k+1}K_{k+1}}{h^{\mathcal{X}}_k}\gamma^{\mathcal{Y}}_{k+1}\gamma^{\mathcal{Y}}_{k+2}\Bigg) \\ &\quad + i\frac{h^{\mathcal{X}}_{k-1}h^{\mathcal{X}}_{k+1}}{h^{\mathcal{X}}_k}\gamma^{\mathcal{X}}_{k-1}\gamma^{\mathcal{X}}_{k+2} + \frac{K_{k-1}h^{\mathcal{X}}_{k+1}}{h^{\mathcal{X}}_k}(i\gamma^{\mathcal{X}}_{k-1}\gamma^{\mathcal{X}}_{k+2})(i\gamma^{\mathcal{Y}}_{k-1}\gamma^{\mathcal{Y}}_k) \\ &\quad + \frac{h^{\mathcal{X}}_{k-1}K_{k+1}}{h^{\mathcal{X}}_k}(i\gamma^{\mathcal{X}}_{k-1}\gamma^{\mathcal{X}}_{k+2})(i\gamma^{\mathcal{Y}}_{k+1}\gamma^{\mathcal{Y}}_{k+2}) \\ &\quad + \frac{K_{k-1}K_{k+1}}{h^{\mathcal{X}}_k}(i\gamma^{\mathcal{Y}}_{k-1}\gamma^{\mathcal{Y}}_k)(i\gamma^{\mathcal{X}}_{k-1}\gamma^{\mathcal{X}}_{k+2})(i\gamma^{\mathcal{Y}}_{k+1}\gamma^{\mathcal{Y}}_{k+2}) + O(\epsilon^3) \ . \qquad (3.29)\end{aligned}$$

Projecting into the low-energy sector sets $i\gamma^{\mathcal{X}}_k\gamma^{\mathcal{X}}_{k+1} \to \pm 1$ and again decouples the Majorana operators $\gamma^{\mathcal{X}}_k$ and $\gamma^{\mathcal{X}}_{k+1}$ from the rest of the system, decimating them by creating a complex fermion mode with definite parity. As in the non-interacting case, the magnitude of the splitting is increased by renormalization of H_0, and a new hopping term $h^{\mathcal{X}\prime}_{k-1}$ is added to the $\mathcal{X}$ chain. However the leading-order effect at $O(\epsilon)$ arises from V_d, where the "degradation" of interaction term $K_k(i\gamma^{\mathcal{X}}_k\gamma^{\mathcal{X}}_{k+1})(i\gamma^{\mathcal{Y}}_k\gamma^{\mathcal{Y}}_{k+1})$ renormalizes $h^{\mathcal{Y}\prime}_k = h^{\mathcal{Y}}_k - \mathrm{sgn}(h^{\mathcal{X}}_k) \times K_k$. As

a result, correlations develop between the hopping terms on the same bond. (This aspect of the perturbation will constitute the basis of a mean-field study of the interacting system, presented in Sec. 3.4.) The effective Hamiltonian also includes renormalized couplings $h^{\mathcal{Y}\prime}_{k-1}$ and $h^{\mathcal{Y}\prime}_{k+1}$, as well as new four-fermion terms which change the structure of the lattice graph, and a six-fermion term. The appearance of these terms breaking the form of H, along with the generation of correlations between terms, is an indication that the RG flow cannot be tracked exactly in the interacting model. However, if the interaction terms already tend to be weak compared to the hopping, the higher-order terms generated by this process will accordingly be weaker still. This is the situation, at least initially, in the random XYZ model with small $\tilde{J}^z$; however there is no guarantee that the relative strengths of the different types of couplings are maintained asymptotically.

Now if instead the dominant energy scale is set by an interaction term, the high- and low-energy eigenspaces of $H_0 = K_k(i\gamma^{\mathcal{X}}_k\gamma^{\mathcal{X}}_{k+1})(i\gamma^{\mathcal{Y}}_k\gamma^{\mathcal{Y}}_{k+1})$, for some k, again correspond to sectors of definite fermion parity, now measured on four Majoranas rather than two. Accordingly, with only some modifications the result Eq. (3.16) applies. We specify two complex fermion modes $d^\dagger_0 = \frac{1}{2}(\gamma^{\mathcal{X}}_k + i\gamma^{\mathcal{X}}_{k+1})$ and $f^\dagger_0 = \frac{1}{2}(\gamma^{\mathcal{Y}}_k + i\gamma^{\mathcal{Y}}_{k+1})$. As before, associate with the complex fermions projectors into the single-particle parity sectors $\pi^\pm_d$ and $\pi^\pm_f$. In contrast with the previous cases, these fermions are only aids for performing the algebra and by themselves do not necessarily describe emergent conserved quantities in the effective Hamiltonian. Now the projectors into the overall H_0 sectors are

$$\pi^+ = \pi^+_d\pi^+_f + \pi^-_d\pi^-_f \ , \tag{3.30}$$

$$\pi^- = \pi^+_d\pi^-_f + \pi^-_d\pi^+_f \ . \tag{3.31}$$

All interaction terms commute, and are contained in the diagonal part of H. The terms anticommuting with H_0 are

$$V_{\text{od}} = ih^{\mathcal{X}}_{k-1}\gamma^{\mathcal{X}}_{k-1}\gamma^{\mathcal{X}}_k + ih^{\mathcal{X}}_{k+1}\gamma^{\mathcal{X}}_{k+1}\gamma^{\mathcal{X}}_{k+2} + ih^{\mathcal{Y}}_{k-1}\gamma^{\mathcal{Y}}_{k-1}\gamma^{\mathcal{Y}}_k + ih^{\mathcal{Y}}_{k+1}\gamma^{\mathcal{Y}}_{k+1}\gamma^{\mathcal{Y}}_{k+2} \ . \tag{3.32}$$

The off-diagonal blocks of the Hamiltonian are given by

$$\begin{aligned}\pi^\pm H\pi^\mp = {} & (ih^{\mathcal{X}}_{k-1}\gamma^{\mathcal{X}}_{k-1} - h^{\mathcal{X}}_{k+1}\gamma^{\mathcal{X}}_{k+2})d^\dagger_0\pi^\mp_f + (ih^{\mathcal{X}}_{k-1}\gamma^{\mathcal{X}}_{k-1} + h^{\mathcal{X}}_{k+1}\gamma^{\mathcal{X}}_{k+2})d_0\pi^\pm_f \\ & + (ih^{\mathcal{Y}}_{k-1}\gamma^{\mathcal{Y}}_{k-1} - h^{\mathcal{Y}}_{k+1}\gamma^{\mathcal{Y}}_{k+2})f^\dagger_0\pi^\mp_d + (ih^{\mathcal{Y}}_{k-1}\gamma^{\mathcal{Y}}_{k-1} + h^{\mathcal{Y}}_{k+1}\gamma^{\mathcal{Y}}_{k+2})f_0\pi^\pm_d \ .\end{aligned} \tag{3.33}$$

Returning to Eq. (3.16) to compute the rotated Hamiltonian, we find

$$H' = H_0 + V_{\rm d} + \frac{1}{\Omega}[\pi^+ H \pi^-, \pi^- H \pi^+] + O(\epsilon^3) \tag{3.34}$$

$$\begin{aligned} &= H_0 + V_{\rm d} + \frac{(h^{\mathcal{X}}_{k-1})^2 + (h^{\mathcal{X}}_{k+1})^2 + (h^{\mathcal{Y}}_{k-1})^2 + (h^{\mathcal{Y}}_{k+1})^2}{2K_k}(i\gamma^{\mathcal{X}}_k \gamma^{\mathcal{X}}_{k+1})(i\gamma^{\mathcal{Y}}_k \gamma^{\mathcal{Y}}_{k+1}) \\ &\quad + \frac{h^{\mathcal{X}}_{k-1} h^{\mathcal{X}}_{k+1}}{K_k}(i\gamma^{\mathcal{Y}}_k \gamma^{\mathcal{Y}}_{k+1})(i\gamma^{\mathcal{X}}_{k-1} \gamma^{\mathcal{X}}_{k+2}) + \frac{h^{\mathcal{Y}}_{k-1} h^{\mathcal{Y}}_{k+1}}{K_k}(i\gamma^{\mathcal{X}}_k \gamma^{\mathcal{X}}_{k+1})(i\gamma^{\mathcal{Y}}_{k-1} \gamma^{\mathcal{Y}}_{k+2}) \\ &\quad - \frac{1}{K_k}\left(h^{\mathcal{X}}_{k-1}(i\gamma^{\mathcal{X}}_{k-1}\gamma^{\mathcal{X}}_{k+1}) - h^{\mathcal{X}}_{k+1}(i\gamma^{\mathcal{X}}_k \gamma^{\mathcal{X}}_{k+2})\right) \\ &\qquad\qquad \times \left(h^{\mathcal{Y}}_{k-1}(i\gamma^{\mathcal{Y}}_{k-1}\gamma^{\mathcal{Y}}_{k+1}) - h^{\mathcal{Y}}_{k+1}(i\gamma^{\mathcal{Y}}_k \gamma^{\mathcal{Y}}_{k+2})\right) + O(\epsilon^3)\ . \end{aligned} \tag{3.35}$$

The Schrieffer–Wolff transformation for an interaction term does not decouple the Majoranas involved from the rest of the system. Instead, a two-dimensional degree of freedom, known as a "spin cluster" [7, 8], remains in the low-energy space. Generally all symmetry-allowed couplings are generated between the spin cluster and its neighbors. The twofold degeneracy is split at order $O(\epsilon)$ by the terms commuting with H_0:

$$\begin{aligned} V_{\rm d} - (\#)\mathbb{I} = {} & K_{k-1}(i\gamma^{\mathcal{X}}_{k-1}\gamma^{\mathcal{X}}_k)(i\gamma^{\mathcal{Y}}_{k-1}\gamma^{\mathcal{Y}}_k) + K_{k+1}(i\gamma^{\mathcal{X}}_{k+1}\gamma^{\mathcal{X}}_{k+2})(i\gamma^{\mathcal{Y}}_{k+1}\gamma^{\mathcal{Y}}_{k+2}) \\ & + i h^{\mathcal{X}}_k \gamma^{\mathcal{X}}_k \gamma^{\mathcal{X}}_{k+1} + i h^{\mathcal{Y}}_k \gamma^{\mathcal{Y}}_k \gamma^{\mathcal{Y}}_{k+1}\ , \end{aligned} \tag{3.36}$$

where we have removed an extensive quantity proportional to the identity arising from terms sharing no Majorana operators with H_0. If the magnitude of the hopping terms dominates—that is, $h^{\mathcal{X}}_k, h^{\mathcal{Y}}_k \gg K_{k-1}, K_{k+1}$—then the Majorana orbitals indeed decimate into the complex fermions f_0 and d_0, with each associated with a definite parity state depending on the signs of the couplings (because all $K_n > 0$ in our model and $h^{\mathcal{X}}_k$ and $h^{\mathcal{Y}}_k$ have opposite sign, in the ground state the d_0 and f_0 fermions have opposite parity). If instead the interaction terms dominate, the energy splitting will be associated with emergent quantities $i\gamma^{\mathcal{X}}_k \gamma^{\mathcal{Y}}_k$ and $i\gamma^{\mathcal{X}}_{k+1}\gamma^{\mathcal{Y}}_{k+1}$. These onsite measurements of fermion parity are associated with a magnetic z-ordered phase. In our model the four-Majorana odd parity state is preferred and the ground state displays Ising AFM order, as expected for the region of the model Eq. (3.1) with $\tilde{J}^z > \tilde{J}^x, \tilde{J}^y$.

3.2.4 XY model spin correlations in SDRG

From the controlled SDRG for the random XY model one can deduce that average correlations in the ground state follow power laws—even though typical correlations are short-ranged—and even calculate the exponents. One

also obtains a more qualitative picture of the behavior of the spin correlation functions.

Expanding Eq. (3.9) in the ground state at separation r,

$$C^z(j, j+r) = \langle i\eta_j\zeta_{j+r}\rangle\langle i\zeta_j\eta_{j+r}\rangle \ . \tag{3.37}$$

Other terms vanish due to symmetry. One sees immediately that $C^z(j, j+r) = 0$ if r is even. For odd r, $C^z(j, j+r)$ assumes a large value if and only if the sites j and $j+r$ were decimated together on both Majorana chains, in which case both expectation values $\langle i\eta_j\zeta_{j+r}\rangle$ and $\langle i\zeta_j\eta_{j+r}\rangle$ have approximately unit magnitude and opposite sign. Otherwise if this decimation did not occur on either or both of the Majorana chains the contribution is suppressed, arising only from higher-order terms in the perturbation theory. Consider the correlations averaged over sites j as well as over disorder realizations, which we denote $C^z(r)$. Nearly all terms will be vanishingly small, with rare terms of roughly unit magnitude occurring with some density; these dominate the average. It is a result of Ref. [4] for the RS phase that at sufficiently large separation the likelihood of such a decimation scales as r^{-2}; thus for two independent Majorana chains $\eta_z = 4$.

The transverse correlations Eqs. (3.7) and (3.8), summarized as $C^\perp(j, j+r)$, are the expectation values of strings of $2r$ Majoranas. Such operators are evaluated as the sum of r-fold products of expectation values of symmetry-allowed bilinear contractions, with signs arising from the signature of each permutation. A term in the sum has a large value if and only if it contracts all Majoranas with their decimation partners in the SDRG. This will be the case for exactly one term if all decimations of the Majoranas appearing in the string expectation value are "internal"; that is, if all decimation partners are also included. If any Majoranas were decimated with orbitals which do not appear, the expectation value will be small. We again define $C^\perp(r)$ as the average over sites and disorder realizations.

If on both chains $\mathcal{X}$ and $\mathcal{Y}$ the sites j and $j+r$ are decimation partners, then as described above, this pair contributes a large value to $C^z(r)$. The pair also necessarily contributes a large value to $C^\perp(r)$, as pairing of the extremal Majorana orbitals in a string implies that all decimations are internal to the string. Thus, the critical exponent $\eta_\perp$ lower-bounds η_z. For the random XY

model $\eta_\perp = 3 - \sqrt{5} \approx 0.764$, however the bound is saturated in the XX model where $\eta_\perp = \eta_z = 2$ [4].

Finally, the SDRG picture also tells us about the end-to-end correlations of transverse spin components in the XX and XY models. The expectation value $C^\perp(1, L) \equiv C^\perp_{\rm e}(L)$ includes all Majorana orbitals on one chain, and all but those at sites 1 and L on the other. This string has a large expectation value if all of these Majoranas are paired internally, which is to say that the two excluded Majoranas are decimated together. This is a property of a single chain only, and so is the same in both the random XX and XY models. Indeed, $\eta^{\rm e}_\perp = 1$ in both cases [10].

3.3 Unbiased RRG study

3.3.1 Details of numerical study

In the following sections, we perform a numerical study of the line $\tilde{J}^z \in [0, 1]$, $\tilde{J}^x = \tilde{J}^y = 1$, in the phase diagram of Eq. (3.1), using RRG. Our objective is primarily to verify by unbiased numerics the observation of continuously varying critical exponents in the SDRG method of Slagle et al. [1], and then to shed additional light on the nature of the low-energy theory. (Here we focus solely on the ground state properties and low-energy physics, rather than the question of MBL.) For concreteness, we use the disorder distribution described in Eqs. (3) and (4) of Ref. [1], namely,

$$p(J_i^\alpha) = \frac{1}{\Gamma \tilde{J}^\alpha} (J_i^\alpha)^{1/\Gamma - 1} \ , \quad J_i^\alpha \in [0, (\tilde{J}^\alpha)^\Gamma] \ . \tag{3.38}$$

We use a milder disorder strength $\Gamma = 2$, as compared to $\Gamma = 4$ for the previous work [1]. Both choices lead to strong disorder physics and the specific value should have little effect on the universal low-energy physics for large enough systems. However, we find that the logarithm of the distribution of the energy gaps depends significantly on Γ, with smaller values tending to lead to larger gaps; this eases the challenge to the numerics which in any case are limited by double-precision floating-point errors on the order of 10^{-16}. In RRG we are capable of accurately resolving energy scales down to $\log_{10}(\Omega/\epsilon) \sim -12$, and validate our results against the free-fermion solution at the soluble point $\tilde{J}^z = 0$.

To construct the AGSP for RRG we use a Trotter approximation to a thermal operator $K \approx e^{-\beta H}$. The output of the RRG algorithm is a subspace

$\tilde{J}^z$	0.0	0.2	0.4	0.6	0.8	1.0
(s, D)	(8,14)	(8,14)	(6,10)	(6,10)	(5,8)	(5,8)

Table 3.1: RRG hyperparameters are shown for values of $\tilde{J}^z$ studied numerically. As described in the text, we optimize the output of RRG using DMRG, and for finite $\tilde{J}^z$ take as a measure of accuracy the number of sweeps required for convergence. These values of s and D were chosen in order to accurately converge approximately 99% of disorder realizations on $N = 80$ spins. For the small fraction of more difficult realizations which are not solved by the hyperparameters above we repeat the algorithm with increased values, finding that convergence is achieved this way.

of constant dimension approximating the low-energy states of the model. We use an implementation based on ITensor [18], in which we explicitly realize the $\mathbb{Z}_2 \times \mathbb{Z}_2$ symmetry and solve for the lowest two eigenstates in each of the four symmetry sectors.[1] In each case the MPSs generated by RRG are then further optimized using DMRG in order to minimize the overlap with high-energy states. The RRG "hyperparameters" s and D (see Ch. 2 or Ref. [19] for details) are chosen so that for the majority of disorder realizations DMRG can optimize the RRG output in a small number of sweeps. For approximately the most challenging 1% of realizations, DMRG requires many sweeps to converge. In these instances we repeat the calculation, increasing the RRG hyperparameters, and find that the improved RRG states are easily converged by DMRG. From comparison with exact free-fermion results for $\tilde{J}^z = 0$ obtained by numerical matrix diagonalization, we find that if RRG produces states which are successfully converged by DMRG and the excitation gap is larger than the target threshold 10^{-12}, the ground state energy and gap are numerically exact in $\gtrsim 99.5\%$ of realizations. As we will show in the following section, at $\tilde{J}^z > 0$ the finite-size gaps tend to be larger than those at $\tilde{J}^z = 0$ and should be easier for RRG; thus we believe our results are even more reliable for these points.

3.3.2 Projective realization of symmetry and site pairing

The $\mathbb{Z}_2 \times \mathbb{Z}_2$ symmetry of the general model, while Abelian, is problematic for exact numerical implementation because it is projectively represented on a single site. A tensor network algorithm which exactly conserves these quantum numbers can be easily realized by pairing up neighbors into doubled sites with

[1] The RRG code used in this work is available online at `https://www.github.com/brendenroberts/RigorousRG`.

total spin 0 or 1, so that the local terms in the symmetry generators commute instead. Upon performing this pairing all of the relevant operators must be translated into the new language. Instead of using the symmetry generators g_x and g_y, we implement the equivalently valid generators g_x and $g_z = -ig_xg_y$, which turn out to be simpler. The basis for a paired site m, $m = 0, \ldots, L/2$, on the original sites $(2m, 2m+1)$ will be

$$\left\{ |0\rangle = \frac{1}{\sqrt{2}}\left(|\uparrow\uparrow\rangle + |\downarrow\downarrow\rangle\right) \ , \ |1\rangle = \frac{1}{\sqrt{2}}\left(|\uparrow\uparrow\rangle - |\downarrow\downarrow\rangle\right) \ , \right.$$
$$\left. |2\rangle = \frac{1}{\sqrt{2}}\left(|\uparrow\downarrow\rangle + |\downarrow\uparrow\rangle\right) \ , \ |3\rangle = \frac{1}{\sqrt{2}}\left(|\uparrow\downarrow\rangle - |\downarrow\uparrow\rangle\right) \right\} . \tag{3.39}$$

The states $|0\rangle$, $|1\rangle$, $|2\rangle$ form the vector subspace and $|3\rangle$ the singlet. More importantly, these basis states are eigenstates of the local symmetry terms, which have the form

$$\sigma^x_{2m}\sigma^x_{2m+1} = |0\rangle\langle 0| - |1\rangle\langle 1| + |2\rangle\langle 2| - |3\rangle\langle 3| \tag{3.40}$$
$$\sigma^z_{2m}\sigma^z_{2m+1} = |0\rangle\langle 0| + |1\rangle\langle 1| - |2\rangle\langle 2| - |3\rangle\langle 3| \ . \tag{3.41}$$

Thus, exact conservation of the two $\mathbb{Z}_2$ quantum numbers can be implemented for operators in this basis.

3.3.3 Translation of Hamiltonian into paired basis

Under the site pairing, some terms in Eq. (3.1) become onsite terms, and some remain pairing terms. Very explicitly, the symmetry flux of an operator in this basis (under $\mathbb{Z}_2$ addition) is

$$O = \begin{bmatrix} (0_x, 0_z) & (1_x, 0_z) & (0_x, 1_z) & (1_x, 1_z) \\ (1_x, 0_z) & (0_x, 0_z) & (1_x, 1_z) & (0_x, 1_z) \\ (0_x, 1_z) & (1_x, 1_z) & (0_x, 0_z) & (1_x, 0_z) \\ (1_x, 1_z) & (0_x, 1_z) & (1_x, 0_z) & (0_x, 0_z) \end{bmatrix} . \tag{3.42}$$

Thus the onsite terms must be diagonal, and both operators in the tensor comprising each pairing term must occupy the same symmetry sector, in order to have no net flux.

The unitary rotating the basis $\{|\uparrow\uparrow\rangle, |\uparrow\downarrow\rangle, |\downarrow\uparrow\rangle, |\downarrow\downarrow\rangle\}$ to $\{|0\rangle, |1\rangle, |2\rangle, |3\rangle\}$ is

easily read off from Eq. (3.39):

$$U = \frac{1}{\sqrt{2}} \begin{bmatrix} 1 & 0 & 0 & 1 \\ 1 & 0 & 0 & -1 \\ 0 & 1 & 1 & 0 \\ 0 & 1 & -1 & 0 \end{bmatrix} . \tag{3.43}$$

It is straightforward to rotate important operators like Hamiltonian terms using U. First we observe that the transformation induced by exchanging the sites $2m \leftrightarrow 2m+1$ is

$$|0\rangle \mapsto |0\rangle \ , \ |1\rangle \mapsto |1\rangle \ , \ |2\rangle \mapsto |2\rangle \ , \ |3\rangle \mapsto -|3\rangle \ . \tag{3.44}$$

Now we find that

$$\sigma^x_{2m}\sigma^x_{2m+1} = +|0\rangle\langle 0| - |1\rangle\langle 1| + |2\rangle\langle 2| - |3\rangle\langle 3| \ , \tag{3.45}$$
$$\sigma^y_{2m}\sigma^y_{2m+1} = -|0\rangle\langle 0| + |1\rangle\langle 1| + |2\rangle\langle 2| - |3\rangle\langle 3| \ , \tag{3.46}$$
$$\sigma^z_{2m}\sigma^z_{2m+1} = +|0\rangle\langle 0| + |1\rangle\langle 1| - |2\rangle\langle 2| - |3\rangle\langle 3| \ , \tag{3.47}$$
$$\mathbb{I}_{2m}\sigma^x_{2m+1} = +|0\rangle\langle 2| + |2\rangle\langle 0| + |1\rangle\langle 3| + |3\rangle\langle 1| \ , \tag{3.48}$$
$$\sigma^x_{2m}\mathbb{I}_{2m+1} = +|0\rangle\langle 2| + |2\rangle\langle 0| - |1\rangle\langle 3| - |3\rangle\langle 1| \ , \tag{3.49}$$
$$\mathbb{I}_{2m}\sigma^y_{2m+1} = -i|0\rangle\langle 3| - i|1\rangle\langle 2| + i|2\rangle\langle 1| + i|3\rangle\langle 0| \ , \tag{3.50}$$
$$\sigma^y_{2m}\mathbb{I}_{2m+1} = +i|0\rangle\langle 3| - i|1\rangle\langle 2| + i|2\rangle\langle 1| - i|3\rangle\langle 0| \ , \tag{3.51}$$
$$\mathbb{I}_{2m}\sigma^z_{2m+1} = +|0\rangle\langle 1| + |1\rangle\langle 0| - |2\rangle\langle 3| - |3\rangle\langle 2| \ , \tag{3.52}$$
$$\sigma^z_{2m}\mathbb{I}_{2m+1} = +|0\rangle\langle 1| + |1\rangle\langle 0| + |2\rangle\langle 3| + |3\rangle\langle 2| \ . \tag{3.53}$$

As expected, all onsite terms are diagonal and the individual operators in the pairing terms live in the following symmetry sectors: σ^x in $(0_x, 1_z)$, σ^y in $(1_x, 1_z)$, and σ^z in $(1_x, 0_z)$.

3.3.4 Results from RRG study

Critical spin correlations

We measure spin correlations in the RRG ground state of $H[\tilde{J}^x = 1, \tilde{J}^y = 1, \tilde{J}^z]$ with $\tilde{J}^z$ ranging from 0 to 1 and microscopic disorder strength $\Gamma = 2$ throughout. Bulk correlations in an open chain of length N are measured for $r \leq \frac{N}{2}$ including only sites $j = \frac{N}{4}, \ldots, \frac{3N}{4}$, in order to distinguish the power law from the end-to-end correlations closer to the boundaries. We show disorder-averaged correlations data measured in chains of length $N = 80$ sites in Fig. 3.1, which

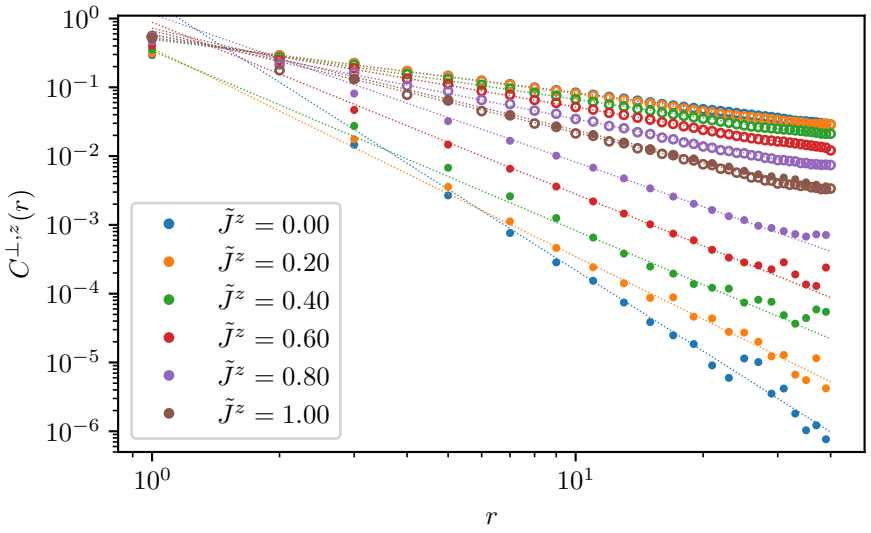

Figure 3.1: Bulk spin correlations data from RRG are shown for the random XYZ model with varying bandwidth $\tilde{J}^z$, up to separation $r = 40$ lattice spacings, from systems of length $N = 80$. Filled circles indicate $C^z(r)$ data, while open circles mark $C^\perp(r)$. The disorder averages for each value of $\tilde{J}^z$ are taken over 1200–1500 realizations. In the average we include only the middle half of the spin chain—that is, excluding sites $1, \ldots, N/4 - 1$ and $3N/4 + 1, \ldots, N$—in order to separate the bulk correlations from the ends, which exhibit different scaling laws. See Fig. 3.3 for the critical power law decay exponents extracted from this data.

includes slices at values of $\tilde{J}^z$ moving along the phase boundary from the free-fermion model to the tricritical point.

End-to-end spin correlations are measured only between the single pair of sites 1 and N for each disorder realization, and exhibit correspondingly larger statistical fluctuations. In addition, reproducing $C^z_{\rm e}(N)$ correlations presents a singular challenge for the RRG algorithm. As discussed in Sec. 3.2.4, in the SDRG the likelihood of a nonzero value of $\langle \sigma^z_1 \sigma^z_N \rangle$ at the free-fermion point is the square of the probability of a singlet of length N in the RS phase. That is, the distribution is broad on a logarithmic scale, with the average being dominated by a very small tail. More importantly, the disorder realizations located in the tail—of outsize importance in the average—are those on which sites 1 and N were decimated together on both Majorana chains, which correlate with the smallest excitation gaps in the low-energy spectrum and are the most difficult realizations for the method to solve accurately. Accordingly, we do not include data for $C^z_{\rm e}(N)$ measured in chains of length $N = 80$ sites in

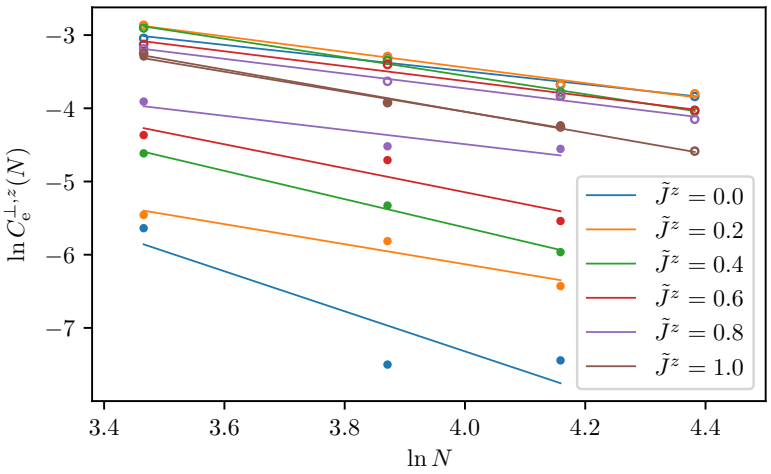

Figure 3.2: RRG end-to-end correlations data are shown for the random XYZ model with varying bandwidth $\tilde{J}^z$. System sizes $N = 32, 48, 64, 80$ are included for $C_e^{\perp}(N)$ (open circles). Due to the special difficulty of measuring the quantity $C_e^{z}(N)$ (filled circles) in RRG, as described in the text, chains of length $N = 80$ are not included in these fits. See Fig. 3.3 for the critical power law decay exponents extracted from this data.

Fig. 3.2.

Our unbiased numerical results for the bulk correlations are in broad agreement with the finding of Slagle et al. [1] of critical exponents governing the decay of spin correlations that vary continuously with $\tilde{J}^z$. In contrast to the previous approach, we perform direct measurements in optimized MPS for the ground state. We estimate the critical index for the permutation-symmetric point to be $\eta_z = \eta_\perp \approx 1.5$.

Entanglement structure

We also study measures of entanglement in the RRG ground states for varying $\tilde{J}^z$. The average bipartite entanglement entropy of a connected subsystem of length ℓ adjacent to the system boundary is known to scale according to the conformal field theory result $S_b(\ell) = \frac{\tilde{c}}{6} \ln \ell$, with a universal constant $\tilde{c}$. In some cases the "effective central charge" $\tilde{c}$ seems to be related to the central charge of the clean model [20]; for example, in the critical phase of a single Majorana chain $\tilde{c} = \frac{\ln 2}{2} = c \ln 2$, where $c = \frac{1}{2}$ is the central charge of a clean Majorana chain. Accordingly, the XY fixed point has $\tilde{c} = \ln 2$, being equivalent to two decoupled copies of the critical random Majorana

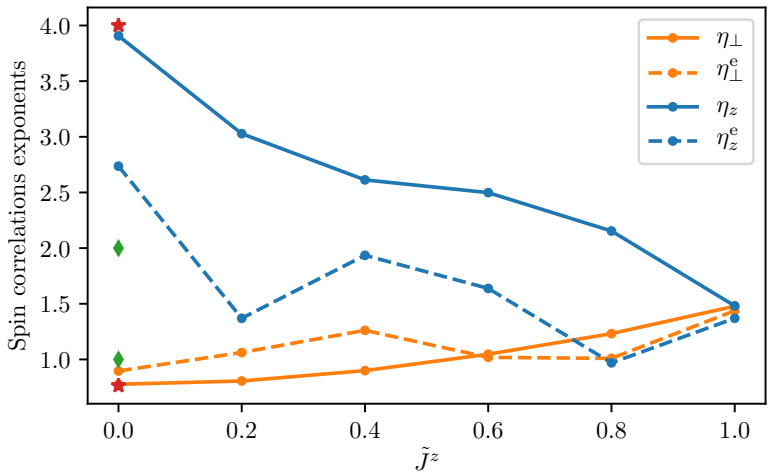

Figure 3.3: Critical exponents governing spin correlations in the RRG ground states are shown, extracted from the data in Figs. 3.1 and 3.2. Both end-to-end and bulk exponents are included, with known results for the bulk correlations in the free-fermion model at $\tilde{J}^z = 0$ indicated by red stars and for the end-to-end correlations by green diamonds. An increase in statistical noise is evident in the end-to-end correlations as compared to the bulk. The reason for the difficulty of these computations, particularly $C^z_{\rm e}(N)$, is discussed in the text.

chain. From finite-size scaling of the disorder-averaged half-system bipartite entanglement entropy $S_b(N/2)$ we find with fair precision that $\tilde{c}$ is stable at this value for any interaction strength $\tilde{J}^z$ along the critical line, in agreement with Ref. [1].

We also measure long-range mutual information (LRMI) between disconnected regions; the formula for this entropic quantity in terms of the entanglement entropy of a subsystem is $I(A : B) = S(A) + S(B) - S(A \cup B)$. We will take A and B to be single spins separated by a distance r; Ref. [1] found that up to appropriate rescaling, the lengths of the subsystems do not affect the asymptotic behavior. The disorder-averaged LRMI we denote $I(r)$, and this quantity will decay no faster than the slowest observable. That is, in a symmetry-breaking phase $I(r)$ will exhibit long-range order, in a phase without order one expects exponential decay, and at a critical point the associated exponent ρ, $I(r) \sim r^{-\rho}$, lower-bounds the power-law decay exponent of any local observable. We show disorder-averaged LRMI data in the upper panel of Fig. 3.4. The exponent ρ varies continuously with $\tilde{J}^z$, as is the case with the other critical indices measured, and is very close to the exponent $\eta_\perp$, suggesting

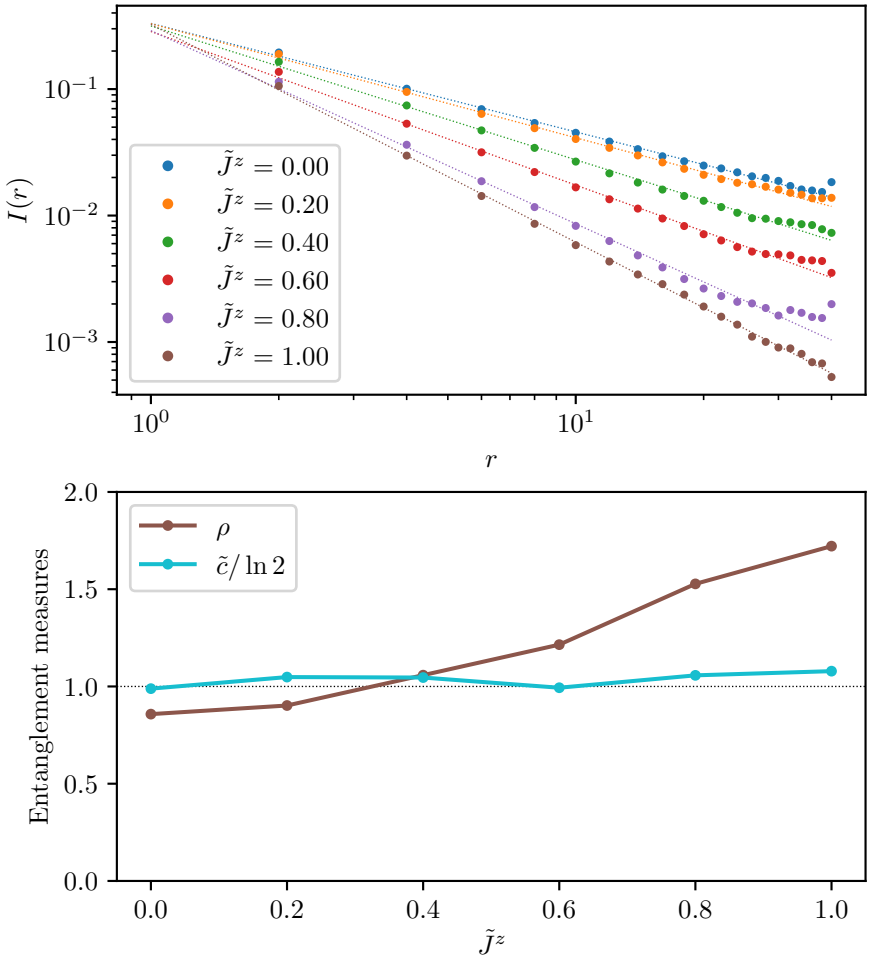

Figure 3.4: Characterizations of the entanglement structure of the ground state are shown. We include the power-law exponent ρ for decay of average long-range mutual information $I(r)$, based on the raw data shown in the upper panel. The subsystems considered in this case consist of two spins separated by a distance r, and the average is taken over sites in the middle half of the chain. Also shown is the effective central charge $\tilde{c}$, found from finite-size scaling of the half-chain entanglement entropy. While $\tilde{c}$ appears to be insensitive to the coupling between the two Majorana chains, the LRMI exponent varies continuously.

that the correlations of the order parameters for the adjacent phases saturate the lower bound everywhere along the boundary. Our RRG results for ρ as well as the effective central charge $\tilde{c}$ are shown in the lower panel of Fig. 3.4.

Scaling of excitation gap

Because RRG produces not only an MPS representation of the ground state but a constant number of low-energy states, it is possible in principle to study spectral properties as well. We focus primarily on the simplest of these, the energy gap to the lowest excitation in a finite system. From the SDRG for the free-fermion point one observes that this excitation consists of flipping the parity of the complex fermion associated with the lowest-energy (i.e., the last decimated) singlet pairing on either Majorana chain. As we consider chains with lengths that are multiples of 4, the ground state is found in the $(g_x, g_y) = (+1, +1)$ sector of the global $(\mathbb{Z}_2)^2$ symmetry and the first excited state will be found in either the $(+1, -1)$ or $(-1, +1)$ sector.

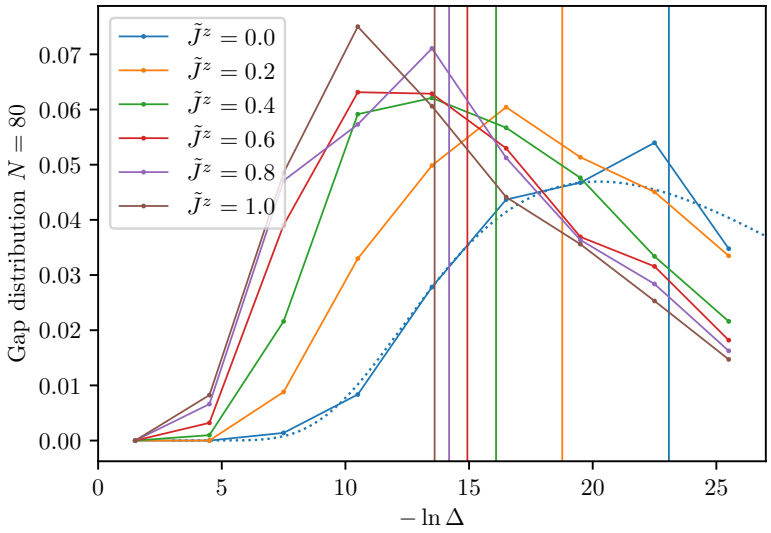

Figure 3.5: Histograms of excitation gaps are shown for the disordered XYZ model at system size $N = 80$ sites. Vertical lines indicate the median of each distribution. The medians include long tails that are not shown, as they contain excitation gaps too small to be accurately measured by the RRG algorithm; however the estimate of the median is not sensitive to these uncertainties. The trace for each value of $\tilde{J}^z$ contains between 1200–1500 disorder realizations.

The distribution of excitation gaps is known exactly via the mapping to two

decoupled copies of the RTFIM, where the universal form of the gap distribution is known [9]. The gap in the random XY model is the minimum of two independent random variables sampled from the distribution of Fisher et al. [9]. In Fig. 3.5 we show histograms of the (logarithmic) excitation gaps for the random XYZ model with varying $\tilde{J}^z$ for chains of length $N = 80$. The exact distribution for the $\tilde{J}^z = 0$ point is indicated with a dotted line.

Indicated on Fig. 3.5 by vertical lines are the medians of the histograms; these are provided as a characterization of the tails, where the energy gaps are near the limit of what is possible to resolve using MPS due to accumulation of numerical errors. While the precise tails are not available this way, it is rare for RRG to make an error which would move a disorder realization out of the tail into the bulk of the distribution. Thus, the median provides an accurate characterization of the gap distribution even when the mean cannot be reliably estimated. In Fig. 3.6 the scaling with chain length of the median of the gap distribution is shown with varying $\tilde{J}^z$. This allows an estimate of the exponent ψ controlling the length-energy relationship, which has the value $\psi = \frac{1}{2}$ at the free-fermion point. The RRG scaling data suggest that ψ does not drift systematically as $\tilde{J}^z$ is varied, even up to the permutation-symmetric point $\tilde{J}^z = 1$. This result would exclude the $n = 3$ Damle–Huse universality for this tricritical point.

3.4 Mean field theory of interaction

Turning on $\tilde{J}^z > 0$ introduces four-fermion interaction terms to the quadratic Hamiltonian H_{xy}. These terms couple the Majorana chains $\mathcal{X}$ and $\mathcal{Y}$ in such a way that the ground state is no longer analytically tractable under SDRG, which generates a quantity of multi-fermion terms in the effective Hamiltonian that grows exponentially with the RG scale. However, as mentioned in Sec. 3.2.3, if at some point in the RG the interaction terms are typically weaker than the hopping terms, the effective higher-order descendants will be even weaker. One might hope, then, that by beginning with a bandwidth $\tilde{J}^z \ll \tilde{J}^x, \tilde{J}^y$ the strength of these terms may be suppressed at all scales, leading to only a minimal effect on the criticality. Moreover, this hope is supported by some numerical evidence: namely, the absence of a systematic drift of either the effective central charge $\tilde{c}$ or the length-energy scaling exponent ψ away from their characteristic values in the decoupled RS phase.

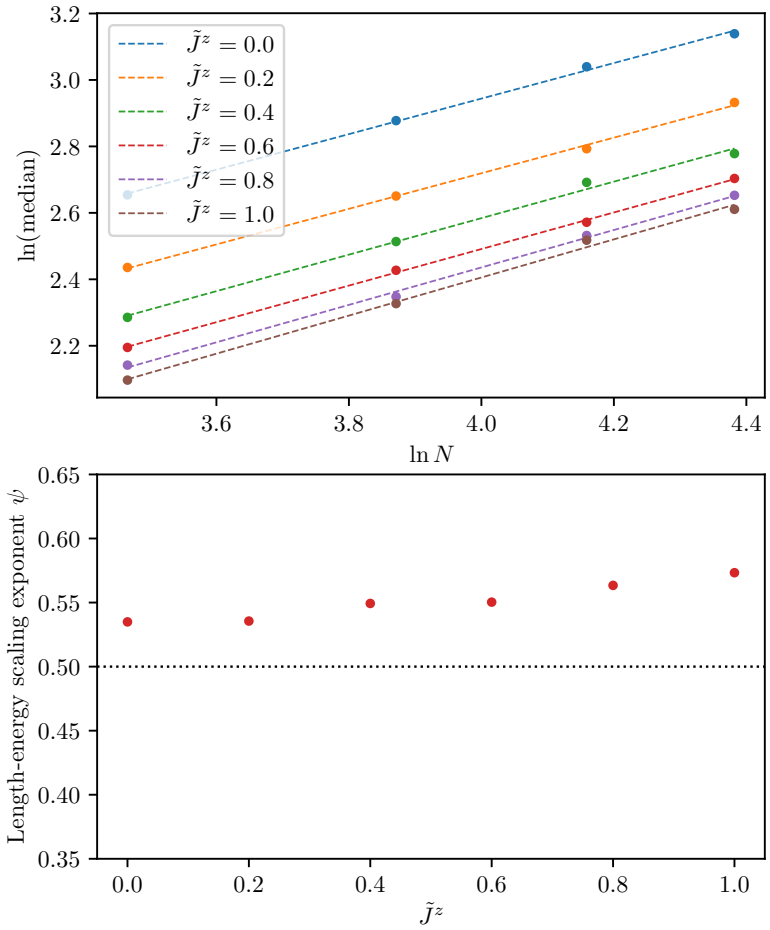

Figure 3.6: The value of the length-energy scaling exponent ψ extracted from finite-size scaling of the lowest excitation gaps in RRG is shown. While the exact value displays statistical noise, there does not appear to be a significant trend along the critical line, and the exponent is stable near $\psi = \frac{1}{2}$, the free-fermion value, for all values of $\tilde{J}^z$ including at the tricritical point $\tilde{J}^z = 1$. The systematic deviation from the exact value is likely due to finite-size corrections to the universal behavior.

Based on this understanding, we consider the mean field theory by "expanding" the interaction into fermion bilinear terms. In the Majorana language, the mean-field structure is particularly transparent; here the only symmetry-allowed bilinear terms act internally on the chains. For $J_j^z \ll 1$,

$$J_j^z (i\eta_j\zeta_j)(i\eta_{j+1}\zeta_{j+1}) \approx J_j^z \left(i\eta_j\zeta_{j+1}\langle i\zeta_j\eta_{j+1}\rangle + i\zeta_j\eta_{j+1}\langle i\eta_j\zeta_{j+1}\rangle\right). \tag{3.54}$$

This can also be seen in terms of the original spins, where the mean field

theory takes the form

$$J_j^z \sigma_j^z \sigma_{j+1}^z = -J_j^z \sigma_j^x \sigma_{j+1}^x \sigma_j^y \sigma_{j+1}^y$$
$$\approx -J_z \left(\sigma_j^x \sigma_{j+1}^x \langle \sigma_j^y \sigma_{j+1}^y \rangle + \langle \sigma_j^x \sigma_{j+1}^x \rangle \sigma_j^y \sigma_{j+1}^y \right) . \tag{3.55}$$

The effect of the allowed terms is to renormalize the existing couplings in the following way:

$$(J_j^x)^{\mathrm{mf}} = J_j^x + J_j^z \langle i\eta_j \zeta_{j+1} \rangle = J_j^x - J_j^z \langle \sigma_j^y \sigma_{j+1}^y \rangle \ , \tag{3.56}$$
$$(J_j^y)^{\mathrm{mf}} = J_j^y - J_j^z \langle i\zeta_j \eta_{j+1} \rangle = J_j^y - J_j^z \langle \sigma_j^x \sigma_{j+1}^x \rangle \ . \tag{3.57}$$

Because the Majorana chains remain decoupled, the mean-field theory can be solved in the analytic SDRG, at least in principle, by accounting for the distributions of effective J_j^x and J_j^y couplings no longer being independent. In the following subsections we numerically investigate the universal behavior of this mean-field theory. We continue using the disorder distribution Eq. (3.38). We present exact results from the analytic SDRG for an effective model based on the mean-field theory in Sec. 3.5.

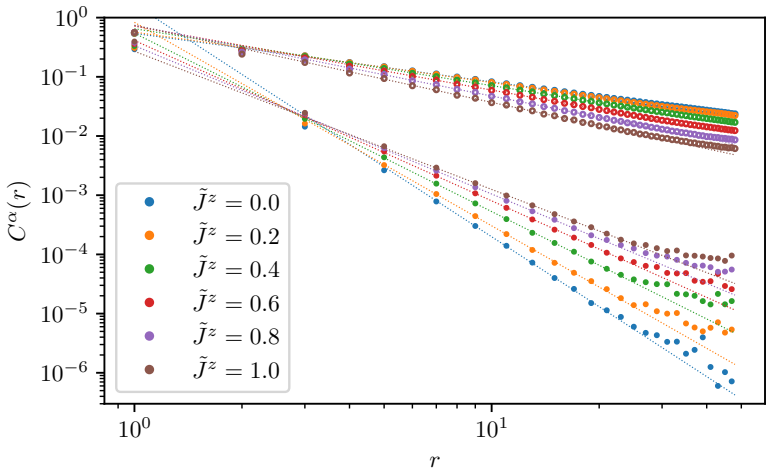

Figure 3.7: Bulk correlations data from the self-consistent Hartree–Fock mean-field theory are shown with varying bandwidth $\tilde{J}^z$, up to separation $r = 48$ in chains of length $L = 96$. Filled circles indicate $C^z(r)$ data, while open circles mark $C^\perp(r)$. The disorder averages for each value of $\tilde{J}^z$ are taken over 25000 realizations and include only the middle half of the spin chain, as described in the caption to Fig. 3.1.

3.4.1 Self-consistent Hartree–Fock treatment of interaction terms

We first perform a self-consistent numerical study of the interaction term in the Gaussian mean-field theory by directly implementing Eqs. (3.56) and (3.57)

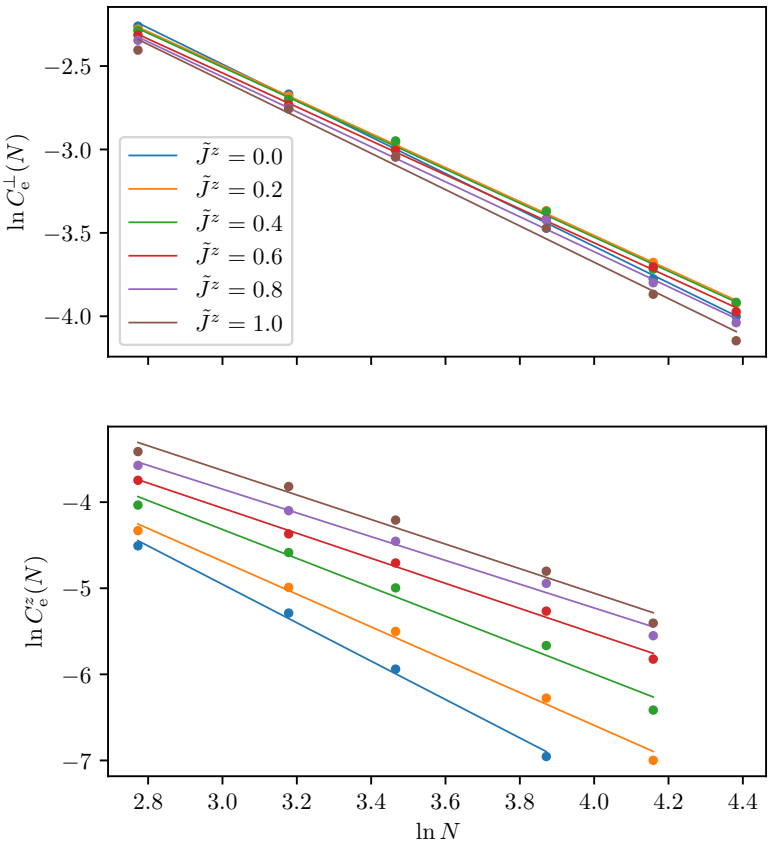

Figure 3.8: End-to-end correlations data from the self-consistent Hartree–Fock mean-field theory are shown with varying bandwidth $\tilde{J}^z$. Each data point is the average end-to-end correlations from 25000 disorder realizations. Because for small $\tilde{J}^z$ the likelihood of simultaneous end-to-end decimations is very low, in computing $C_{\mathrm{e}}^{z}(L)$ we are restricted to shorter systems in order to have reasonable statistics. For example, $25000 \times e^{-7} \approx 23$ important "events" only.

in the BdG Hamiltonian, iteratively performing exact diagonalization and updating the mean-field couplings until convergence is reached. The bulk correlations data are shown in Fig. 3.7, end-to-end correlations in Fig. 3.8, and a summary of the critical exponents in Fig. 3.9. In the mean field model the exponents are indeed perturbed in a manner consistent with our observations for the interacting model. Here $\tilde{J}^z = 1$ is not necessarily special, so there is no reason to expect the equivalence of exponents seen in the RRG case.

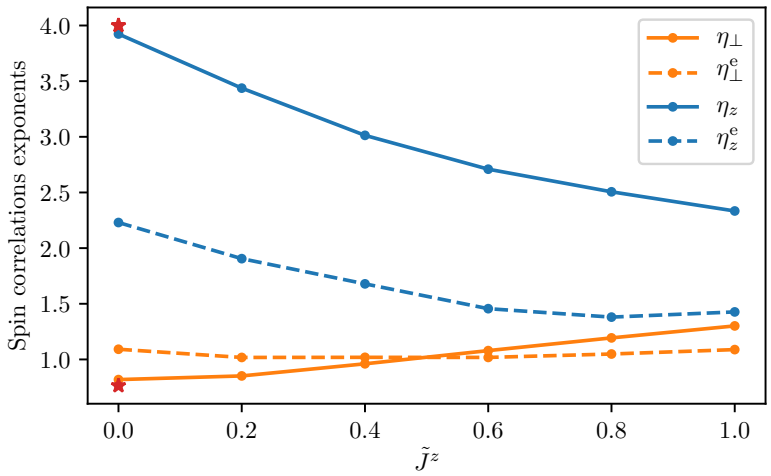

Figure 3.9: Critical exponents are shown for the self-consistent Hartree–Fock mean-field theory with varying bandwidth $\tilde{J}^z \in [0, 1]$. Filled circles indicate $C^z(r)$ data, while open circles mark $C^\perp(r)$. The disorder averages for each value of $\tilde{J}^z$ are taken over 25000 realizations and the bulk correlations include only the middle half of the system, as described in the caption to Fig. 3.1.

3.4.2 Numerical study of random XY chain with locally correlated couplings

The rules Eqs. (3.56) and (3.57) for the mean-field couplings modify bonds on one Majorana chain based on expectation values across the same bond on the other chain. As a result, recalling that $J_j^z > 0$ for all j, the terms on a given bond (which at the mean-field level are strengthened by the interactions) develop correlations among themselves; however terms on separate bonds remain independent. We refer to such an effective model as having "local correlations," in order to distinguish from spatial correlations between terms on separated bonds. One can mimic the behavior of the mean field theory and explore the entire space of correlations using the following parameterization of the couplings: for A_j, B_j independent random variables and $\delta \in [0, 1]$, let

$$J_j^x = \left(1 - \frac{\delta}{2}\right) A_j + \frac{\delta}{2} B_j \ , \tag{3.58}$$

$$J_j^y = \frac{\delta}{2} A_j + \left(1 - \frac{\delta}{2}\right) B_j \ . \tag{3.59}$$

Tuning δ from 0 to 1 interpolates between fully independent couplings and the perfectly correlated case with U(1) symmetry. That is, the parameterization runs along the line between the random XY and XX spin chains. As mentioned in Sec. 3.2.1, Fisher [4] found that weak random anisotropy is marginal

around the XX point, which is in the RS phase. However it was not clear there whether this perturbation is truly marginal, marginally relevant, or marginally irrelevant. The mean-field numerical results in this section provide an investigation into this question, a topic which will be discussed in more detail within the analytic SDRG in Sec. 3.5.

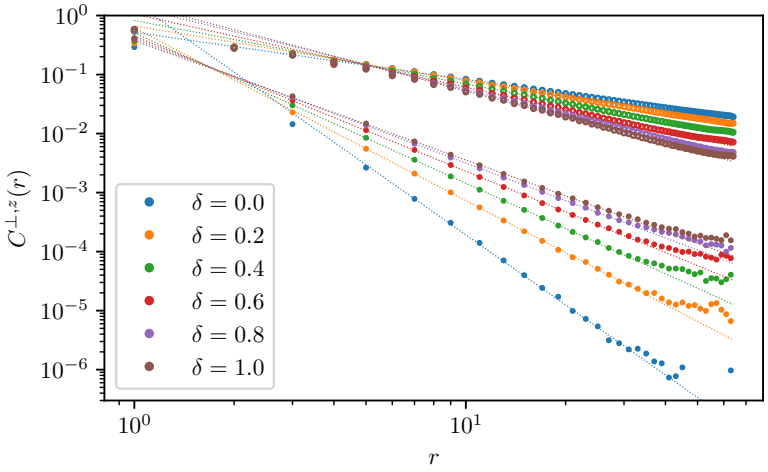

Figure 3.10: Bulk spin correlations data from the locally-correlated mean-field theory are shown for the random XYZ model with varying bandwidth $\tilde{J}^z$, up to separation $r = 64$. Filled circles indicate $C^z(r)$ data, while open circles mark $C^{\perp}(r)$. The disorder averages for each value of $\tilde{J}^z$ are taken over 25000 realizations. In the average we include only the middle half of the spin chain (excluding sites $1, \ldots, N/4 - 1$ and $3N/4 + 1, \ldots, N$) in order to separate the bulk correlations from the surface, which exhibits different scaling laws.

It is not immediately clear to what extent the locally-correlated free fermion effective model specified by Eqs. (3.58) and (3.59) shares the qualitative features of the XYZ model, or indeed the self-consistent mean field theory. We investigate this by repeating the measurements of bulk and end-to-end spin correlations in chains of similar length to the previous studies, now varying the coupling correlation parameter δ. Figs. 3.10, 3.11, and 3.12 demonstrate that these critical indices do vary continuously in a similar way to the interacting case. Our observation that this mean-field approach indeed exhibits many of the qualitative features of the original case suggests that at least for small $\tilde{J}^z$, the primary effect of the interactions is to correlate the coefficients of the hopping terms on the two Majorana chains. However, we emphasize that although the η_z and $\eta_\perp$ converge to similar values at the XX point $\delta = 1$ and the tricritical XYZ point $\tilde{J}^z = 1$, the reasons for this are not necessarily

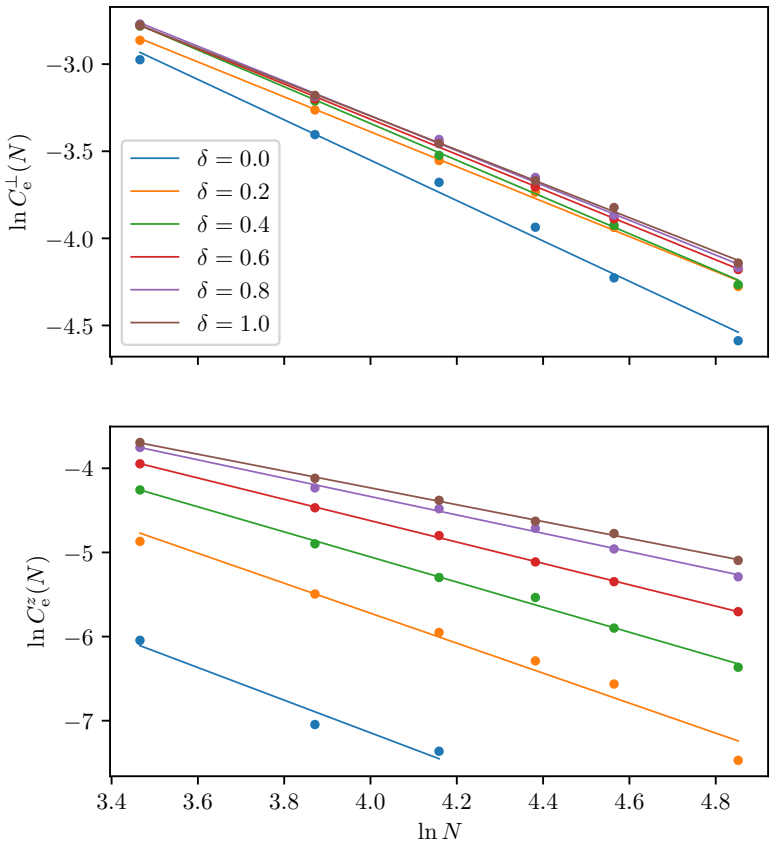

Figure 3.11: End-to-end spin correlations data are shown from exact diagonalization of the locally-correlated mean field with varying coupling correlations δ. System sizes $N = 32, 48, 64, 80, 96, 128$ are included. See Fig. 3.12 for the critical power law decay exponents extracted from this data.

the same. The mean field should not be taken too seriously as a picture of the interacting phase away from the perturbative regime.

3.5 Locally correlated XY model in the random walk formalism

Some disordered quantum Hamiltonians can be associated uniquely with a classical random walk (RW), and a picture of the SDRG developed acting on these objects. This mathematical connection can be useful for understanding the properties of IRFP phases. The RW formulation has been applied to both the RTFIM [21, 22] and AFM quantum spin chains [10, 23]. In this section we first review the RW picture for a single Majorana chain in the RS phase, based on the SDRG procedure of Sec. 3.2.3. While all results for correlation functions in this case are known from Fisher's analytic solutions for flows approaching the RS fixed point, we demonstrate how to obtain power law exponents from

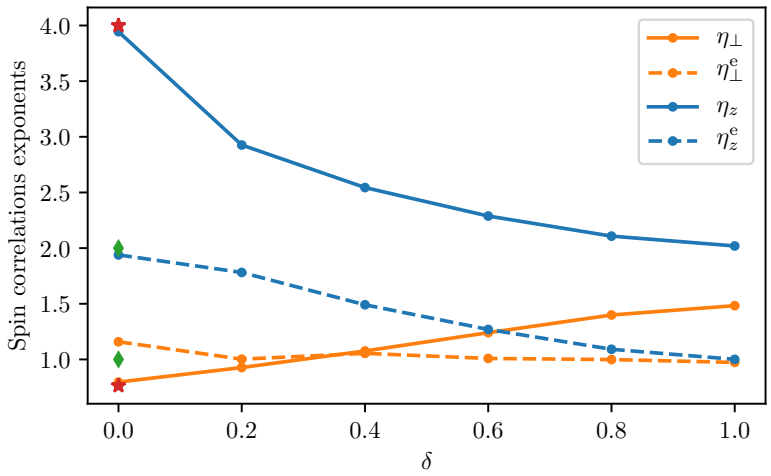

Figure 3.12: Critical exponents governing spin correlations are shown, extracted from data shown in Figs. 3.10 and 3.11. Both end-to-end and bulk exponents are shown, with known results for the bulk correlations in the free-fermion model at $J^z = 0$ indicated by red stars.

different arguments, which will generalize to the locally correlated XY chain where we do not have analytic flows. We first obtain rigorous bounds in the continuum limit on the asymptotic scaling of the Majorana pairing probability (which gives the dominant contribution to the correlations of the z component of spin in the XX chain) based on the RW survival probability, a connection which had previously been noted in Ref. [10]. We then consider the problem of two locally correlated RWs (one for each Majorana chain) following the mean-field approximation developed in Sec. 3.4.2. It turns out that this model is represented as an anisotropic RW in a two-dimensional space. We again rigorously bound the spin decay of correlations using the RW survival probability, where we find that the power law exponent varies continuously with the local correlations parameter. As a result, we are able to rigorously establish the continuously varying critical indices in the locally-correlated effective model.

3.5.1 RW formulation of SDRG for the Majorana chain

Returning to the notation of Sec. 3.2.3, define the logarithm of the energy associated with each bond in the Majorana chain Hamiltonian $\mathcal{H}_\mathcal{M}$ to be $u_n = \ln(\tilde{J}/|h_n|)$, $n = 1, \ldots, N-1$. Here $\tilde{J}$ is a bandwidth for the bare coupling terms, meant to evoke the parameters of the Hamiltonian Eq. (3.1). From Eq. (3.4) one sees that if $\tilde{J}^x = \tilde{J}^y$, in a single Majorana chain the hopping terms

are identically distributed. Note that the signs of h_n are not important for the discussion of probabilities of site pairings below, and are only needed to fix sign factors for the spin correlation functions, as discussed earlier. We consider the specific disorder distribution Eq. (3.38) with $\tilde{J}^x = \tilde{J}^y = \tilde{J} = 1$. Then the distribution of log-energies is exponential, with distribution parameter Γ:

$$\tau(u) = \frac{1}{\Gamma} e^{-u/\Gamma} \ , \quad u \in (0, \infty) \ , \tag{3.60}$$

which has mean $\langle u \rangle = \Gamma$ and variance $\mathrm{Var}(u) = \Gamma^2$. The Majorana model $H_{\mathcal{M}}$ on N sites is associated with a 1d RW $\mathfrak{m}$, a Markov chain with state variables (x_n, σ_n), $n = 1, \ldots, N$, where $x_n \in \mathbb{R}$ is a cumulative log-energy defined below and $\sigma_n = (-1)^{n-1}$ is an internal variable determining the sign of the next step to be taken. (That is, the RW takes alternating positive and negative steps depending on the sublattice of site n. This is distinct from the alternating signs of the couplings in Eq. (3.4), which are not invariant under a unitary rotation on the spins.) The discrete RW time n is the spatial index of the quantum chain. A given disorder distribution $\{h_j\}_{1 \le j < N}$ corresponds to the RW step sequence $\{\sigma_n u_n\}_{1 \le j < N}$. Its value at time n is given by

$$\mathfrak{m}[n] = \sum_{j=1}^{n-1} \sigma_j u_j \ , \tag{3.61}$$

where we have left the σ_n state variable implicit. Let $\rho(x, \sigma, n)$ be the distribution of $\mathfrak{m}[n]$; its master equation is

$$\rho(x, \sigma, n+1) = \int_0^\infty du \, \tau(u) \, \rho(x + \sigma u, -\sigma, n) \ . \tag{3.62}$$

We now consider the behavior under the SDRG of a RW $\mathfrak{m}$ associated with a Majorana chain $\mathcal{H}_{\mathcal{M}}$. The largest local energy scale $|h_k|$, for some k, corresponds to the smallest log-energy u_k. The effect of the Schrieffer–Wolff transformation up to second order is to eliminate the following hopping terms:

$$i h_{k-1} \gamma_{k-1} \gamma_k + i h_k \gamma_k \gamma_{k+1} + i h_{k+1} \gamma_{k+1} \gamma_{k+2} \ , \tag{3.63}$$

and to introduce the renormalized bond term

$$i h'_{k-1} \gamma_{k-1} \gamma_{k+2} \ , \quad h'_{k-1} = \frac{h_{k-1} h_{k+1}}{h_k} \ . \tag{3.64}$$

(There is also a shift of the leading energy scale, but this will not be important here.) Suppose that $h_k > 0$; then the SDRG rule replaces three consecutive

steps with log-energies u_{k-1}, u_k, and u_{k+1} by a single step with log-energy $u'_{k-1} = u_{k-1} - u_k + u_{k+1}$. For the RW the new step is

$$\sigma_{k-1}u'_{k-1} = \sigma_{k-1}u_{k-1} + \sigma_k u_k + \sigma_{k+1}u_{k+1} \ . \tag{3.65}$$

In this way the SDRG transformation simply corresponds to a sequential "smoothing" of the RW, in which the step of smallest magnitude and its neighbors are removed, and replaced by a treble step directly connecting $\mathfrak{m}[k-1]$ and $\mathfrak{m}[k+2]$. For an illustration, the reader is referred to Fig. 8 in App. B of the arXiv version of Ref. [23], or Fig. 1 of Ref. [24].

From the above description a precise statement can be made about the decimation of a site k, which we suppose without loss of generality to be a local minimum. First define right and left "partial RWs:" for $m < n$,

$$\mathfrak{m}_R[m,n] = \sum_{j=0}^{(n-m)-1} \sigma_{m+j}t_{m+j} \ , \tag{3.66}$$

$$\mathfrak{m}_L[m,n] = \sum_{j=1}^{n-m} -\sigma_{n-j}t_{n-j} \ . \tag{3.67}$$

Now the necessary and sufficient conditions for a site k to be partnered in the SDRG with a site k', $k' - k = r$, where $\mathfrak{m}_R[k,k'] \equiv \Delta > 0$, are the following:

1. The right partial RW $\mathfrak{m}_R[k,l]$, $k < l \leq k'$ attains a maximum Δ at $l = k' = k + r$ without reaching 0;

2. The right partial RW $\mathfrak{m}_R[k',l]$, $l > k'$, reaches the value $-\Delta$ before crossing 0;

3. The left partial RW $\mathfrak{m}_L[l,k]$ for decreasing $l < k$ reaches Δ before crossing 0.

These conditions are independent, once Δ is specified, and relate the likelihood of a decimation pairing (k,k') to the survival probability of the partial RWs on the bounded interval $(0,\Delta)$. The physical interest of this quantity follows from the strong correlations shared by sites paired in the SDRG; the asymptotic scaling of the decimation probability with r determines the decay of average spin correlations in the RS phase.

Focusing on the asymptotic scaling (i.e., $n, r \gg 1$) allows a description of the RW in continuous time, passing from $n \to t$. The central limit theorem specifies that the distribution of a sum of random variables like $\mathfrak{m}[n]$ for sufficiently large n approaches a Gaussian, independent of the individual details of the random variables, provided only that the moments of the constituent distributions are bounded. The variance of the continuum distribution $\rho(x,t)$ is $\mathrm{Var}(\rho) = \mathrm{Var}(u)\, t$. The effect of the internal state variable σ can be accounted for by noting that sites which decimate together necessarily inhabit distinct sublattices. This means that, assuming k to be a minimum, one additional $\sigma = +1$ step is always taken. The mean of the distribution, then, should be taken to be the expectation value for this step: $x_0 \equiv \langle u \rangle = \langle \tau \rangle$. So the asymptotic density in free space is simply

$$\rho(x,t) = \frac{1}{\sqrt{2\pi \mathrm{Var}(u)\, t}} \exp\left[-\frac{(x-x_0)^2}{2\mathrm{Var}(u)\, t} \right] \ . \tag{3.68}$$

(Sec. 3.A.2 contains an explicit derivation of Eq. (3.68) from the master equation Eq. (3.62).)

Now the continuum limit of Eq. (3.62) is the diffusion equation [25]

$$\frac{\partial}{\partial t}\rho(x,t) = D \frac{\partial^2}{\partial x^2}\rho(x,t) \ , \tag{3.69}$$

with diffusion constant $D = \mathrm{Var}(u)/2$. The central limit form of $\rho(x,t)$ in Eq. (3.68) is the Green's function of Eq. (3.69) on $x \in \mathbb{R}$ with initial condition $\rho(x, t=0) = \delta(x - x_0)$. This illustrates that the continuous writing of the RW can be treated as a particle initially localized at $x = x_0$ diffusing over a domain. Accordingly, in the following sections we use the language of the diffusion problem, referring to the counterparts of discrete RWs associated with particular Majorana Hamiltonians as "paths," "histories," or "trajectories." We also sometimes write the initial condition explicitly, as $\rho(x, t; x_0)$.

3.5.2 Rigorous bounds on critical exponents from RW survival

The diffusion equation on the bounded interval $(0, \Delta)$, i.e., with absorbing boundary conditions at $x = 0$ and $x = \Delta$, can be straightforwardly solved by harmonic expansion. From the full time-dependent solution one can calculate the scaling of the asymptotic decimation probability and obtain critical exponents for the RS phase this way. However, in Sec. 3.5.4 the geometry for two locally correlated case Majorana chains will be too complicated to allow a full

solution. Instead we employ a different approach for the likelihood of end-to-end decimation, in which we prove upper and lower bounds exhibiting the same power-law scaling, based on the survival probability in a semi-infinite domain. This simplification is enough that a similar method will work for both the single Majorana chain and the locally correlated effective model with arbitrary degree of correlation.

First consider the survival probability of a RW in the semi-infinite interval at time t. As in the free case Eq. (3.68), the initial condition on the constrained density $\rho_c(x,t)$ is $\rho_c(x,t=0) = \delta(x-x_0)$, with $x_0 = \langle u \rangle$, but now an absorbing boundary is present at $x = 0$, restricting the solution domain to $x \in (0,\infty)$ and terminating trajectories that reach $x = 0$. The boundary condition $\rho_c(x=0,t) = 0$ is accounted for by placing an "image charge" at $x = -x_0$ and superposing the distributions: $\rho_c(x,t) = \rho(x,t;x_0) - \rho(x,t;-x_0)$. In this geometry the survival probability at time $t > 0$ is

$$S(t) = \int_0^\infty dx\, \rho_c(x,t) \tag{3.70}$$

$$= \frac{1}{\sqrt{4\pi D t}} \int_0^\infty dx \left(e^{-(x-x_0)^2/4Dt} - e^{-(x+x_0)^2/4Dt} \right) \tag{3.71}$$

$$= \operatorname{erf}\left[\frac{x_0}{\sqrt{4Dt}} \right] \approx \frac{x_0}{\sqrt{\pi D t}} \,. \tag{3.72}$$

In the last line we replace the exact solution with the first-order term in the series expansion. At late times, when the argument is small, this gives the leading power-law behavior in $1/t$.

Now consider the SDRG problem on a finite RW $\mathfrak{m}[t = L]$. The end-to-end spin correlations in the Majorana model are determined by the likelihood that sites 1 and L decimate together. From conditions 1 and 2, one sees that the survival probability $S(L)$ gives the likelihood that in $\mathfrak{m}$ the left end site 1 is not decimated until the very last step, i.e., belongs to the lowest-energy singlet pair. However, in this calculation the partner is allowed to be any site on the chain, while for the end-to-end correlations we are interested in, we require that its partner be precisely the right end site L. In order for this to occur, it must additionally be the case that $\mathfrak{m}_R[1,L] = \mathfrak{m}[L]$ reaches a maximum at $t = L$.

The intuition we rely on is this: a simple calculation shows that the surviving histories at a given time are likely to be located increasingly far from the

absorbing boundary [26]. As a result, we will treat the two ends of the chain separately despite the correlations generated in the RG. Applying an inversion $\mathfrak{I} : (x, t) \mapsto (-x, -t)$ to $\mathfrak{m}$, one sees that the requirement at the right end that the RW reach a maximum at $t = L$ takes the same form as the absorbing boundary condition $x = 0$ at the left end in the RW without inversion. Consequently to establish bounds on the probability of the $(1, L)$ decimation we consider two chains of length $t = L/2$, applying $\mathfrak{I}$ to one, and use a "gluing" procedure to construct suitable RWs of length L.

To be more concrete, we first give an upper bound on the end-to-end $(1, L)$ decimation probability $p_{\mathrm{e}}(L)$. Note that any RW $\mathfrak{m}[L]$ can be viewed as two independent "half-RWs" up to time $t = L/2$, one starting from site 1 and going to site $L/2$, and the other starting from site L and going to site $L/2$, with the two RWs properly glued at their respective time $t = L/2$. It may be the case that these "half-RWs" never reach the absorbing boundary, and thus each is considered a surviving RW in the semi-infinite geometry. Any RW instance of length L producing the $(1, L)$ pairing in the SDRG, i.e., satisfying condition 1, will indeed decomposes into two independent surviving RWs up to time $t = L/2$ with only one absorbing boundary in each case. The opposite is not true, because when such two surviving trajectories are joined, we cannot guarantee that the full walk satisfies the condition 1. Thus, the desired probability $p_{\mathrm{e}}(L) \leq S(L/2)^2 \sim 1/L$.

Now to prove a lower bound on p_{e} we construct a subset of all of the paths satisfying condition 1 through an explicit gluing procedure of half-chains of length $t = L/2$ which when combined satisfy the criterion. Essentially we will bound the density of surviving trajectories which have drifted sufficiently far away from the absorbing boundary, but have not deviated so far as to preempt the end-to-end decimation. Again, in the present case we can solve this problem using two absorbing boundaries, but we want to demonstrate how to extract the behavior using the semi-infinite solution, where the geometry is simpler, as this will be the only option for the locally correlated model.

For two positive constants α and β, $\alpha < \beta \leq 2\alpha$, define the *target window* $x \in [\alpha\sqrt{Dt}, \beta\sqrt{Dt}]$, where $t > 0$ is a time. In the problem with one absorbing boundary at $x = 0$, the fraction of surviving trajectories contained in the

target window at t is

$$p_{\rm w}(\alpha,\beta) = \frac{1}{S(t)}\int_{\alpha\sqrt{Dt}}^{\beta\sqrt{Dt}} dx\,\rho_c(x,t) \tag{3.73}$$

$$= \frac{1}{S(t)}\left(\int_{\alpha\sqrt{Dt}}^{\beta\sqrt{Dt}} dx\,\rho(x,t;x_0) - \int_{\alpha\sqrt{Dt}}^{\beta\sqrt{Dt}} dx\,\rho(x,t;-x_0)\right) \tag{3.74}$$

$$= \frac{1}{S(t)}\frac{1}{2}\left(\mathrm{erf}\left[\frac{\alpha}{2}+\frac{x_0}{\sqrt{4Dt}}\right] - \mathrm{erf}\left[\frac{\alpha}{2}-\frac{x_0}{\sqrt{4Dt}}\right] - \mathrm{erf}\left[\frac{\beta}{2}+\frac{x_0}{\sqrt{4Dt}}\right] + \mathrm{erf}\left[\frac{\beta}{2}-\frac{x_0}{\sqrt{4Dt}}\right]\right) \tag{3.75}$$

$$\approx e^{-\alpha^2/4} - e^{-\beta^2/4}\ . \tag{3.76}$$

In the final line we again take the leading behavior for large t. Then a constant fraction $p_{\rm w}(\alpha,\beta)$ of the surviving density is located within the target window.

However, using the density $\rho_c(x,t)$ defined in the semi-infinite region for the fraction Eq. (3.76) leads to an overcounting of the number of valid paths for the purposes of end-to-end correlations by gluing as described above, because it includes "dangerous" histories which take an excursion to large values of x before returning to the target window at time t. When glued to a trajectory for the other end of the chain these histories may cross the eventual decimation log-energy scale Δ prematurely and would spoil the lower bound. To account for the dangerous cases, we exclude from our counting those histories which ever cross $x = \beta\sqrt{Dt}$ and then return to the target window.

The way we achieve the exclusion is the following. Suppose that a history $\mathfrak{m}[t']$, $t' \in [0,t]$, performs q crossings of the line $x = \beta\sqrt{Dt}$ at times $\{t_1, t_2, \ldots, t_q\}$ before returning to the target window at $t' = t$. Immediately after t_q, the history must travel downwards and remain below $x = \beta\sqrt{Dt}$ until $t' = t$. We apply a transformation to $\mathfrak{m}[t']$ by reflecting the partial RW $\mathfrak{m}_R[t_q, t]$ about the line $x = \beta\sqrt{Dt}$ and fixing the remainder. Because $\mathfrak{m}[t] \in [\alpha\sqrt{Dt}, \beta\sqrt{Dt}]$, the transformed path $\tilde{\mathfrak{m}}$ necessarily ends in a "shadow window" $x \in [\beta\sqrt{Dt}, (2\beta - \alpha)\sqrt{Dt}]$ at $t' = t$. Moreover, the probability of the trajectory is unaffected by the transformation $\mathfrak{m} \mapsto \tilde{\mathfrak{m}}$. Now for every dangerous path with $q \geq 1$ crossings we can identify a transformed partner terminating in the shadow window which has the same probability. Thus the density in the shadow

window at time t is an upper bound on the contribution to the density in the target window arising from dangerous histories. (The upper bound is not saturated, because a trajectory included in the shadow window could deviate above $x = 2\beta\sqrt{Dt}$ for some $t' \in (t_q, t]$, and this RW would have no inverse-transformed counterpart due to the absorbing boundary at $x = 0$.)

From the previous calculation, the fraction of the surviving density contained in the shadow window is $p_{\rm sw}(\alpha, \beta) = e^{-\beta^2/4} - e^{-(2\beta-\alpha)^2/4}$. Therefore a lower bound on the valid density of surviving histories in the target window at time t is given by

$$\tilde{p}_{\rm w}(\alpha, \beta) = p_{\rm w}(\alpha, \beta) - p_{\rm sw}(\alpha, \beta) \tag{3.77}$$

$$= e^{-\alpha^2/4} - 2e^{-\beta^2/4} + e^{-(2\beta-\alpha)^2/4} \ . \tag{3.78}$$

There is an extended region of (α, β) for which the coefficient is positive; for example, $\tilde{p}_{\rm w}(\alpha = 2, \beta = 4) \approx 0.33$.

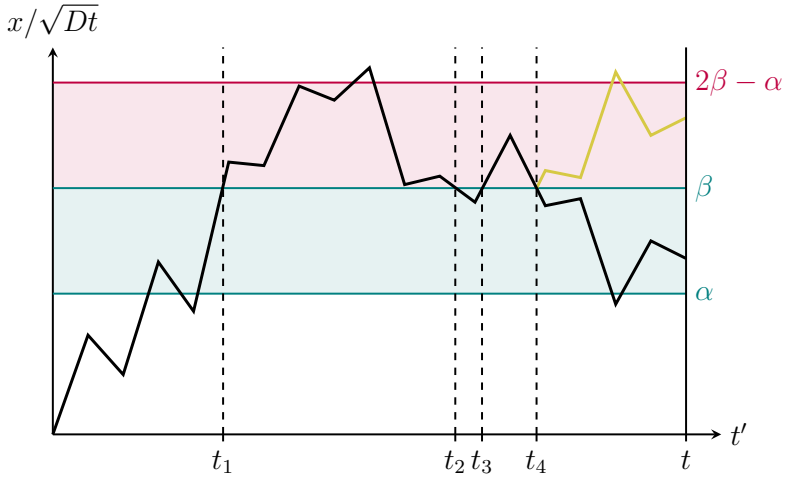

Figure 3.13: A dangerous trajectory contributing to the counting $p_{\rm w}$ of the density in the target window, drawn in blue, is illustrated. The shadow window used to eliminate these trajectories is also shown, drawn in purple. The particular history shown has $q = 4$ crossings of the upper limit of the target window and the reflected partial path on $(t_q, t]$, terminating in the shadow window, is shown in yellow. Because the diffusion is unbiased, both the black and black+yellow paths have the same probability, and as any such dangerous trajectory has a counterpart under the transformation, the density in the shadow window upper-bounds the associated contribution to the density in the target window.

Now take $t = L/2$. One can combine two such RWs satisfying the criteria above to create a RW of length L by inverting one instance via $\mathfrak{I}$ as $(x, t) \mapsto (-x, -t)$

and gluing the endpoints at $t = \pm L/2$. The result is a trajectory of length L reaching a maximum at $t = L$ without crossing $x = 0$. Not all RWs of length L which generate the $(1, L)$ decimation in SDRG can be constructed this way, only those with $\mathfrak{m}[L/2]$ lying in the target window, but every RW coming from this construction evidently satisfies condition 1. Thus this probability is a lower bound on $p_{\mathrm{e}}(L) \geq [\tilde{p}_{\mathrm{w}}(\alpha, \beta)S(L/2)]^2 \sim 1/L$.

Together with the upper bound, this lower bound establishes the scaling for end-to-end decimation probability—and thus the power law for end-to-end correlations in the RS phase—as $1/L$. Interestingly, this result is in agreement (up to constants) with the naive guess assuming the independence of the decimations of the two end spins.

3.5.3 Locally-correlated Majorana chains as a two-dimensional RW

In order to address the locally correlated Majorana chains it is necessary to deal simultaneously with two RWs (returning for the moment to the discrete formulation) $\mathfrak{x}[n]$ and $\mathfrak{y}[n]$. In the general case, the steps taken at time n by the RWs $\mathfrak{x}$ and $\mathfrak{y}$ are not independent, and are drawn from a joint distribution $\mu(u, v)$. If the full state of the system is specified by variables (x_n, y_n, n), the master equation for the probability distribution $\rho(x, y, n)$ is

$$\rho(x, y, n + 1) = \int du \int dv\, \mu(u, v)\, \rho(x - u, y - v, n) \ . \tag{3.79}$$

This is however just the master equation for a RW in two dimensions (2d). In the natural 2d vector notation,

$$\rho(\boldsymbol{x}, n + 1) = \int d^2\boldsymbol{u}\, \mu(\boldsymbol{u})\rho(\boldsymbol{x} - \boldsymbol{u}, n),\ \boldsymbol{x} = \begin{bmatrix} x \\ y \end{bmatrix},\ \boldsymbol{u} = \begin{bmatrix} u \\ v \end{bmatrix}. \tag{3.80}$$

The continuum limit of such a master equation is again diffusion, however the correlation between x and y results in anisotropic diffusion coefficients. As a remedy we first transform the problem into isotropic diffusion.

The correlation coefficient is $\mathrm{corr}(u, v) = \frac{\mathrm{cov}(u,v)}{\mathrm{std}(u)\,\mathrm{std}(v)} \equiv \delta \in [0, 1]$, where $\mathrm{Var}(u) = \mathrm{Var}(v) = 2D$. (The value of δ here is related to, but not necessarily the same as, the bare δ defined in Sec. 3.4.2.) The eigenvalue decomposition of the covariance matrix Σ is

$$\frac{\Sigma}{2D} = \begin{bmatrix} 1 & \delta \\ \delta & 1 \end{bmatrix} \equiv U\Lambda U^{\dagger} = \left((1 - \delta)\hat{e}_-\hat{e}_-^{\top} + (1 + \delta)\hat{e}_+\hat{e}_+^{\top}\right), \tag{3.81}$$

with eigenvectors $\hat{e}_- = \frac{1}{\sqrt{2}}(1,-1)^\top$ and $\hat{e}_+ = \frac{1}{\sqrt{2}}(1,1)^\top$. The transformation of the plane under which the 2d RW diffuses isotropically with coefficient D sets $\Sigma' = 2D\,\mathbb{I}$:

$$W(\delta) = [\Lambda(\delta)]^{-1/2}\,U^\dagger = [\Lambda(\delta)]^{-1/2}\,R\left[\frac{\pi}{4}\right]. \tag{3.82}$$

This transformation consists of a rotation about the origin by $\pi/4$, followed by a δ-dependent anisotropic rescaling. It acts as $\mathcal{W}(\delta) : A \mapsto A' = W(\delta) A\, W^\dagger(\delta)$. There is a divergence at $\delta = 1$, where Σ is rank-deficient; this reflects that the line $y = x$ cannot be mapped onto the plane in this way, and the RW in the perfectly correlated case is fundamentally one-dimensional. We will refer to the (x, y) plane of the original problem as the "physical geometry," and the image of the mapping $\mathcal{W}(\delta)$ as the "solution geometry," where the governing equation is isotropic diffusion:

$$\frac{\partial}{\partial t}\rho = D\left(\frac{\partial^2}{\partial x'^2} + \frac{\partial^2}{\partial y'^2}\right)\rho\ . \tag{3.83}$$

3.5.4 Rigorous bounds on critical exponents in the locally-correlated model

Investigating the $(1, L)$ decimation likelihood directly in the exact solution for the fully bounded geometry would necessitate solving the diffusion equation in a parallelogram. A harmonic decomposition is not directly accessible here, and as far as we are aware the solution would require a prohibitively complicated Schwarz–Christoffel conformal transformation [27] and likely only be possible numerically. Thus, an analytic treatment of the SDRG for the Majorana chains with arbitrary local correlations requires the connection to the semi-infinite RW survival probability, and the simpler geometry involved there.

As was the case for the single Majorana chain, we will make use of the solution in a semi-infinite domain, now bounded by the lines $x = 0$ and $y = 0$. The origin is evidently fixed by $\mathcal{W}(\delta)$, and for any δ the boundaries map to the lines $y' = \pm\sqrt{\frac{1-\delta}{1+\delta}}x'$, where x' lies in the $\hat{e}_-$ direction and y' along $\hat{e}_+$. These boundaries delimit an absorbing wedge geometry with opening angle $\cos\Theta = -\delta$, which runs from $\Theta = \pi/2$ at $\delta = 0$ to $\Theta = \pi$ at $\delta = 1$.

The Green's function in the infinite wedge can be found from the free-space distribution by the method of images for opening angles $\Theta = \pi/m$, with m a positive integer. This entails $2m - 1$ image charges with alternating sign arranged symmetrically around the wedge apex. However, writing the

distribution in this form turns out to be very complicated, and for our case $\frac{\pi}{2} \leq \Theta < \pi$ so this solution is of limited use. Fortunately the Green's function is in fact known exactly for arbitrary angles Θ. In polar coordinates with the wedge apex at $r = 0$ and solution domain bounded by absorbing walls $\rho(r, \theta = 0, t) = \rho(r, \theta = \Theta, t) = 0$, the Green's function is [28]

$$\rho(r, \theta, t; r_0, \theta_0) = \frac{e^{-(r^2+r_0^2)/4Dt}}{\Theta Dt} \sum_{l=1}^{\infty} I_{l\nu}\Big(\frac{rr_0}{2Dt}\Big) \sin(l\nu\theta) \sin(l\nu\theta_0) \ , \tag{3.84}$$

where $\nu = \pi/\Theta$ and $I_{l\nu}$ is a modified Bessel function of the first kind:

$$I_s(x) = \sum_{z=0}^{\infty} \frac{(x/2)^{s+2z}}{z!\,\Gamma(s+z+1)} \ , \tag{3.85}$$

which arises from the equation for the radial coordinate. The initial condition is $(x_0, y_0) = (\langle u \rangle, \langle v \rangle)$, where in our case $\langle u \rangle = \langle v \rangle$. In the solution geometry this point maps to $r_0 \hat{e}_+$, where $r_0 = \langle u \rangle \sqrt{\frac{2}{1+\delta}}$. In polar coordinates the source point is $(r_0, \theta_0 = \frac{\Theta}{2})$. As a result, in Eq. (3.84), the factor $\sin(l\nu\theta_0)$ vanishes for even l, and for odd l is equal to a phase $(-1)^{(l-1)/2}$.

The survival probability is determined from the Green's function by integration over the solution region. To determine its asymptotic scaling we take the contribution at leading order at late times t; even though the integration domain extends $r \to \infty$, the integral is regulated by the exponential, which decays fast enough to suppress errors arising at large r. Because $\nu \in (1, 2]$ the leading behavior requires only the $l = 1$, $z = 0$ term in the double sum, and sets $e^{-r_0^2/4Dt} \to 1$. Explicitly,

$$\begin{aligned}
S(t) &= \int r\,dr\,d\theta\,\rho(r, \theta, t; r_0, \theta_0) && (3.86)\\
&\approx \frac{\int_0^{\Theta} d\theta \sin(\nu\theta)}{\Theta\Gamma(\nu+1)Dt} \int_0^{\infty} r\,dr\,e^{-r^2/4Dt} \left(\frac{rr_0}{4Dt}\right)^{\nu} && (3.87)\\
&= \frac{2}{\pi\Gamma(\nu+1)Dt} \left(\frac{r_0}{\sqrt{4Dt}}\right)^{\nu} \int_0^{\infty} r\,dr\,e^{-r^2/4Dt} \left(\frac{r}{4Dt}\right)^{\nu} && (3.88)\\
&= \frac{8}{\pi\Gamma(\nu+1)\sqrt{4Dt}} \left(\frac{r_0}{\sqrt{4Dt}}\right)^{\nu} \int_0^{\infty} dr\,e^{-r^2/4Dt} \left(\frac{r}{\sqrt{4Dt}}\right)^{\nu+1} && (3.89)\\
&= \frac{8}{\pi\Gamma(\nu+1)} \left(\frac{r_0}{\sqrt{4Dt}}\right)^{\nu} \int_0^{\infty} du\,e^{-u^2} u^{\nu+1} && (3.90)\\
&= \frac{4\,\Gamma(\frac{\nu}{2}+1)}{\pi\Gamma(\nu+1)} \left(\frac{r_0}{\sqrt{4Dt}}\right)^{\nu} . && (3.91)
\end{aligned}$$

We find that the survival probability exponent depends on the opening angle as $S(t) \sim t^{-\pi/2\Theta}$. This result for a RW in a 2d wedge is in fact well known [26, 29, 30]. As Θ is a function of the correlation coefficient δ, continuously varying behavior of this type is in agreement with the numerical observations in Sec. 3.4.2. Specifically, again relying on the naive assumption that the two ends of the chain decimate independently, the likelihood of this pairing scales as $[S(L)]^2 \sim L^{-\pi/\Theta}$, which matches the known end-to-end scaling exponents $\eta_z^{\mathrm{e}} = 2$ for the uncorrelated model at $\delta = 0$ and $\eta_z^{\mathrm{e}} = 1$ for $\delta = 1$.

Our strategy for bounding the probability of the decimation $(1, L)$ occurring on both chains is analogous to that of Sec. 3.5.2. From the Green's function we establish that at late times a constant fraction of surviving RWs are valid and found in a target window, using a shadow window to exclude dangerous trajectories. Then by gluing together the ends of two RWs of length $t = L/2$ we establish bounds on the power law.

In particular, we can write the upper bound immediately. Any 2d RW corresponding to a locally correlated pair of Majorana chains can be decomposed into half-chains, one with time coordinate running from $t = 1$ to $t = L/2$ and the other from $t = L$ to $t = L/2$, which are properly glued at their respective times $t = L/2$. Each of these half-chains may be valid surviving trajectories in their semi-infinite wedge, and of that set some will produce $(1, L)$ decimations on both Majorana chains. Trajectories that do not decompose into surviving half-chains will not satisfy criterion 1. However because not every pair of surviving trajectories at $t = L/2$ will do so either, the probability $p_{\mathrm{e}}(L) \leq S(L/2)^2 \sim L^{-\pi/\Theta}$.

Now in order to prove a lower bound, let α and β be positive constants, $\alpha < \beta \leq 2\alpha$, and define the target window for a 2d RW at time t by $x, y \in [\alpha\sqrt{Dt}, \beta\sqrt{Dt}]$. In the physical geometry the window is a square, however mapped to the solution geometry it becomes a parallelogram. The corners $\{a, b, c, d\}$ map to

$$\{a', b', c', d'\} = \Big\{ \frac{2\alpha\sqrt{Dt}}{\sqrt{2(1+\delta)}}\hat{e}_+ \ , \ \frac{(\alpha-\beta)\sqrt{Dt}}{\sqrt{2(1-\delta)}}\hat{e}_- + \frac{(\alpha+\beta)\sqrt{Dt}}{\sqrt{2(1+\delta)}}\hat{e}_+ \ , \\ \frac{(\beta-\alpha)\sqrt{Dt}}{\sqrt{2(1-\delta)}}\hat{e}_- + \frac{(\alpha+\beta)\sqrt{Dt}}{\sqrt{2(1+\delta)}}\hat{e}_+ \ , \ \frac{2\beta\sqrt{Dt}}{\sqrt{2(1+\delta)}}\hat{e}_+ \Big\}. \quad (3.92)$$

Treating this exact shape in the polar coordinates of Eq. (3.84) is not simple; instead we define an integration volume that is a subset of the target window,

with the same t scaling, but which leads to a simpler result. Consider the midpoints of the edges of the target window in the physical geometry:

$$\{e,f,g,h\} = \left\{ \left(\frac{\alpha+\beta}{2}\sqrt{Dt}, \alpha\sqrt{Dt}\right), \left(\frac{\alpha+\beta}{2}\sqrt{Dt}, \beta\sqrt{Dt}\right), \right. \\ \left. \left(\alpha\sqrt{Dt}, \frac{\alpha+\beta}{2}\sqrt{Dt}\right), \left(\beta\sqrt{Dt}, \frac{\alpha+\beta}{2}\sqrt{Dt}\right) \right\}. \tag{3.93}$$

These map to

$$\{e',f',g',h'\} = \\ \left\{ \frac{(\beta-\alpha)\sqrt{Dt}}{2\sqrt{2(1-\delta)}}\hat{e}_- + \frac{(3\alpha+\beta)\sqrt{Dt}}{2\sqrt{2(1+\delta)}}\hat{e}_+ \ , \ \frac{(\alpha-\beta)\sqrt{Dt}}{2\sqrt{2(1-\delta)}}\hat{e}_- + \frac{(\alpha+3\beta)\sqrt{Dt}}{2\sqrt{2(1+\delta)}}\hat{e}_+ \ , \right. \\ \left. \frac{(\alpha-\beta)\sqrt{Dt}}{2\sqrt{2(1-\delta)}}\hat{e}_- + \frac{(3\alpha+\beta)\sqrt{Dt}}{2\sqrt{2(1+\delta)}}\hat{e}_+ \ , \ \frac{(\beta-\alpha)\sqrt{Dt}}{2\sqrt{2(1-\delta)}}\hat{e}_- + \frac{(\alpha+3\beta)\sqrt{Dt}}{2\sqrt{2(1+\delta)}}\hat{e}_+ \right\}. \tag{3.94}$$

They describe the four corners of a rectangle in the solution geometry, symmetric about the line $\theta = \frac{\Theta}{2}$, with edges in the directions $\hat{e}_-$ and $\hat{e}_+$. We define an integration domain bounded by the two distinct radial values r_+ (of points f' and h') and r_- (of e' and g'), and the angular deviation ψ of points f' and h' from the midline $\theta = \frac{\Theta}{2}$. The proof that this "sector" geometry is indeed a subvolume of the target domain for any opening angle $\Theta \in (0,\pi)$ can be seen by drawing a picture. The specific integration bounds can be found straightforwardly from Eq. (3.94), but the crucial property is their scaling with t. Denote the radial limits by $r_\pm = C_\pm(\alpha,\beta,\delta)\sqrt{Dt}$; the angular half-width $\psi = \psi(\alpha,\beta,\delta)$ turns out to be purely geometric, with no t dependence. Again extracting the leading behavior for late times t, the density of surviving paths

in the integration window is

$$p_{\rm w}(\alpha,\beta,\delta) = \frac{1}{S(t)}\int_{r_-}^{r_+} r\,dr\int_{\frac{\Theta}{2}-\psi}^{\frac{\Theta}{2}+\psi} d\theta\,\rho(r,\theta,t;r_0,\theta_0) \tag{3.95}$$

$$\approx \frac{1}{S(t)}\frac{1}{\Theta\Gamma(\nu+1)Dt}\int_{r_-}^{r_+} r\,dr\,e^{-r^2/4Dt}\left(\frac{rr_0}{4Dt}\right)^{\nu}\int_{\frac{\Theta}{2}-\psi}^{\frac{\Theta}{2}+\psi} d\theta\sin(\nu\theta) \tag{3.96}$$

$$= \frac{1}{S(t)}\frac{1}{\Theta\Gamma(\nu+1)Dt}\left(\frac{2}{\nu}\sin(\nu\psi)\right)\int_{r_-}^{r_+} r\,dr\,e^{-r^2/4Dt}\left(\frac{rr_0}{4Dt}\right)^{\nu} \tag{3.97}$$

$$= \frac{1}{S(t)}\frac{8\sin(\nu\psi)}{\pi\Gamma(\nu+1)}\left(\frac{r_0}{\sqrt{4Dt}}\right)^{\nu}\int_{C_-/2}^{C_+/2} du\,e^{-u^2}u^{\nu+1} \tag{3.98}$$

$$= \frac{1}{S(t)}\frac{8\sin(\nu\psi)}{\pi\Gamma(\nu+1)}\mathcal{I}(\alpha,\beta,\delta)\left(\frac{r_0}{\sqrt{4Dt}}\right)^{\nu} \tag{3.99}$$

$$= \frac{2\sin(\nu\psi)}{\Gamma(\frac{\nu}{2}+1)}\mathcal{I}(\alpha,\beta,\delta)\ , \tag{3.100}$$

where

$$\mathcal{I}(\alpha,\beta,\delta) = \int_{C_-/2}^{C_+/2} du\,e^{-u^2}u^{\nu+1}\ . \tag{3.101}$$

So $p_{\rm w}$ is indeed a constant, determined only by the correlation coefficient δ and the constants α and β.

As was the case for the 1d RW, the density calculation above includes a "dangerous" contribution which should be subtracted in order to lower-bound the decimation probability by gluing. Again we upper-bound this contribution by calculating the density in a shadow window. We consider those paths dangerous which ever cross the lines $x = \beta\sqrt{Dt}$ or $y = \beta\sqrt{Dt}$ in the physical space before returning to the target window at time t. In the solution geometry these lines map to

$$R:\ \sqrt{2(1-\delta)}x' + \sqrt{2(1+\delta)}y' - 2\beta\sqrt{Dt} = 0\ , \tag{3.102}$$

$$L:\ -\sqrt{2(1-\delta)}x' + \sqrt{2(1+\delta)}y' - 2\beta\sqrt{Dt} = 0\ . \tag{3.103}$$

On the "right" half-wedge defined by $0 < \theta \le \frac{\Theta}{2}$, the boundary for dangerous trajectories is R, the image of $x = \beta\sqrt{Dt}$. On the "left" half wedge $\frac{\Theta}{2} < \theta < \Theta$, the boundary is L, the image of $y = \beta\sqrt{Dt}$. Suppose a trajectory with time parameter t' makes q crossings at times $\{t_1,\ldots,t_q\}$ of the combined boundary at various points $\{(r_1,\theta_1),\ldots,(r_q,\theta_q)\}$ before returning to the target window

at time $t' = t$. After its last crossing at (r_q, θ_q), it must stay within the allowed region for times $(t_q, t]$. We transform the trajectory by reflecting the partial RW for times $t' \in (t_q, t]$ about the boundary that was crossed at $t' = t_q$, either R if $\theta_q \in (0, \frac{\Theta}{2}]$ or L if $\theta_q \in (\frac{\Theta}{2}, \Theta)$. Because the distribution of steps in the solution geometry is isotropic, the transformed path has the same probability as the dangerous original. (The reflection must be performed in the solution geometry, and does not commute with $\mathcal{W}(\delta)$.) The shadow window in this case has two components, which are disconnected for $\Theta < \frac{2\pi}{3}$ but overlap for $\Theta > \frac{2\pi}{3}$.

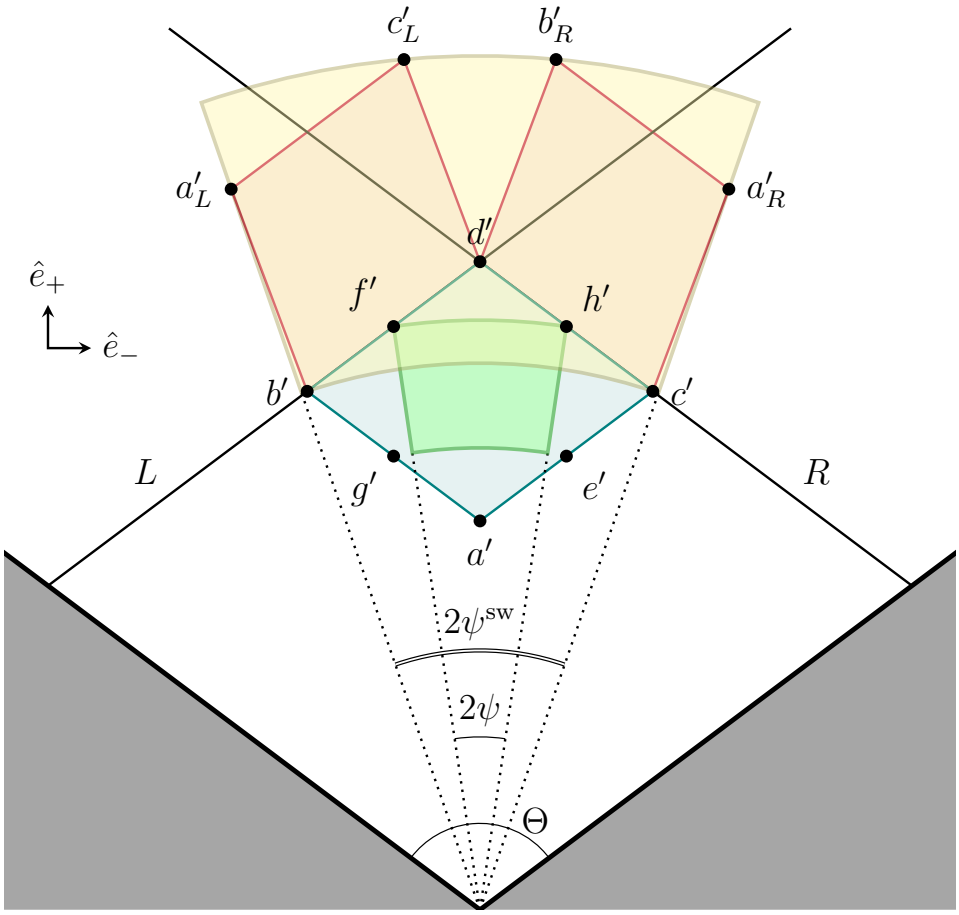

Figure 3.14: The solution geometry is illustrated for the 2d RW problem in the wedge with opening angle Θ, found from the correlation coefficient by $\cos\Theta = -\delta$. The exact target window is drawn in blue, and the sector defining the integration region for the target in green. The two components of the shadow window are found by reflecting the exact target window across the lines L and R and are drawn in purple, with the bounding shadow integration region, which necessarily covers these areas, in yellow.

The corners c' and d' of the target window lie on line R, and b' and d' on line L. Thus we need only reflect a' and b' about R, and a' and c' about L. The coordinates of these points reflected about R are

$$\begin{aligned}
&\{a'_R, b'_R\} = \\
&\Bigg\{(\beta-\alpha)\sqrt{Dt}\sqrt{2(1-\delta)}\hat{e}_- + \left((\beta-\alpha)\sqrt{Dt}\sqrt{2(1+\delta)} + \frac{2\alpha\sqrt{Dt}}{\sqrt{2(1+\delta)}}\right)\hat{e}_+ \ , \\
&\quad \left((\beta-\alpha)\sqrt{Dt}\sqrt{2(1-\delta)} + \frac{(\alpha-\beta)\sqrt{Dt}}{\sqrt{2(1-\delta)}}\right)\hat{e}_- \\
&\qquad\qquad + \left((\beta-\alpha)\sqrt{Dt}\sqrt{2(1+\delta)} + \frac{(\alpha+\beta)\sqrt{Dt}}{\sqrt{2(1+\delta)}}\right)\hat{e}_+\Bigg\}, \qquad (3.104)
\end{aligned}$$

and about L,

$$\begin{aligned}
&\{a'_L, c'_L\} = \\
&\Bigg\{(\alpha-\beta)\sqrt{Dt}\sqrt{2(1-\delta)}\hat{e}_- + \left((\beta-\alpha)\sqrt{Dt}\sqrt{2(1+\delta)} + \frac{2\alpha\sqrt{Dt}}{\sqrt{2(1+\delta)}}\right)\hat{e}_+ \ , \\
&\quad \left((\alpha-\beta)\sqrt{Dt}\sqrt{2(1-\delta)} + \frac{(\beta-\alpha)\sqrt{Dt}}{\sqrt{2(1-\delta)}}\right)\hat{e}_- \\
&\qquad\qquad + \left((\beta-\alpha)\sqrt{Dt}\sqrt{2(1+\delta)} + \frac{(\alpha+\beta)\sqrt{Dt}}{\sqrt{2(1+\delta)}}\right)\hat{e}_+\Bigg\}. \qquad (3.105)
\end{aligned}$$

The four-sided figures described by the exact shadow window are evidently complicated. As with the target window, we bound the area using a sector which scales in the same way, however in this case we need an upper bound. The upper limit $r_+^{\rm sw}$ is the radial coordinate of points c'_L and b'_R, and the lower limit $r_-^{\rm sw}$ that shared by the corners b' and c'. The angular half-width is the maximum of the half-width of points c' and a'_R; this depends on the specific value of Θ. Again we find that the integration limits $r_\pm^{\rm sw} = C_\pm^{\rm sw}(\alpha,\beta,\delta)\sqrt{Dt}$, and $\psi^{\rm sw} = \psi^{\rm sw}(\alpha,\beta,\delta)$.

Then based on the previous calculation, $p_{\rm sw}(\alpha,\beta,\delta) = \frac{2\sin(\nu\psi^{\rm sw})}{\Gamma(\frac{\nu}{2}+1)}\mathcal{I}^{\rm sw}(\alpha,\beta,\delta)$ and the corrected fraction is

$$\begin{aligned}
\tilde{p}_{\rm w}(\alpha,\beta,\delta) &= p_{\rm w}(\alpha,\beta,\delta) - p_{\rm sw}(\alpha,\beta,\delta) \qquad (3.106)\\
&= \frac{2}{\Gamma(\frac{\nu}{2}+1)}\big(\sin(\nu\psi)\mathcal{I} - \sin(\nu\psi^{\rm sw})\mathcal{I}^{\rm sw}\big)\ . \qquad (3.107)
\end{aligned}$$

By working explicitly through the algebra, we determine that $\tilde{p}_{\rm w}$ is positive for all values of $\delta \in [0,1)$ for $\alpha = 1$, $\beta = 2$.

Now, taking $t = L/2$, for any two valid trajectories in the target window we can apply an inversion $(x, y, t) \mapsto (-x, -y, -t)$ to one and glue the endpoints at $t = \pm L/2$ in order to construct a RW which satisfies condition 1 for end-to-end decimation in the quantum chain. Therefore a lower bound on the simultaneous $(1, L)$ decimation probability is given by $p_{\mathrm{e}} \geq [\tilde{p}_{\mathrm{w}} S(L/2)]^2 \sim L^{-\pi/\Theta}$. In combination with the upper bound, this shows that the power law exponent controlling end-to-end decimation probability (and consequently η_z^{e}) varies continuously with δ as

$$\eta_z^{\mathrm{e}} = \pi / \arccos(-\delta) \ . \tag{3.108}$$

3.6 Discussion of results

In the preceding sections, motivated by the observations of Ref. [1], we have performed a study of the low-energy properties of the random XYZ model using RRG, developed in Ref. [19] and Ch. 2, for unbiased numerically exact results at low energies. At all points allowing comparison, our results are in general agreement with the previous findings measured at infinite temperature in SBRG, and strongly suggest that—regardless of the behavior of highly excited states—the critical line is an IRFP with continuously varying critical exponents. Perhaps surprisingly, a Hartree–Fock mean-field theory treating the J^z interaction terms as a perturbation around the random XY fixed point yields results from diagonalization of the Majorana Hamiltonian that are qualitatively rather consistent with the full interacting model. This is in contrast to the clean case, where the mean field model is not qualitatively accurate due to divergences in the perturbation theory [31].

Continuously varying critical exponents were previously observed in IRFPs associated with correlated disorder in Ref. [32], however this is in a qualitatively different setting than ours. Specifically, the RTFIM disordered fixed point perturbed by the introduction of long-range correlations $\sim r^{-a}$ was argued to exhibit critical indices varying continuously with a. In addition to being dependent on spatial correlations, the disorder in this model is of the "random-temperature" type, as opposed to the random anisotropy of the present case. The distinction can be seen sharply in the Harris criterion for correlated disorder, which applies to random-temperature disorder and stipulates that long-range correlations are irrelevant in an RG sense if $a > 2/\nu$, where ν is the correlation length critical exponent [33, 34]. This criterion is evidently violated by our locally correlated effective model.

The locally-correlated effective model, introduced with the idea of distilling the essential feature of the mean field theory, again exhibits continuously varying critical exponents. Because of the simple form of this quadratic effective model, we were able to treat it analytically in the SDRG using the random walk formulation in two dimensions. By making use of a connection between survival probability and the structure of decimation in the RG, we showed that a critical exponent for end-to-end spin correlations varies continuously as the coupling correlation parameter is tuned. This result proves one of the scenarios of Fisher [4], that random anisotropy is marginal along the critical line connecting the random XX and random XY fixed points. It should be the case that the proof can be extended to other critical exponents without too much difficulty, in particular that governing simultaneous decimation in the bulk (which is also our η_z); this is because the additional conditions required to ensure decimation do not involve time-dependent quantities but only time-averaged "eventual" hitting probabilities.

3.A Random-walk results for the microscopic disorder distribution

3.A.1 Eventual absorption on the bounded interval

In order to treat the parts of the RW to the left of A and to the right of A' it suffices to look for a set of steady-state functions $a_L^\sigma(x) \equiv a_L(x,\sigma)$ and $a_R^\sigma(x) \equiv a_R(x,\sigma)$, denoting the eventual probability of absorption by crossing the boundary at 0 or Δ, respectively, for the system in state (x,σ). We can treat this question directly using the microscopic disorder distribution. Based on the transition rule of the RW, we have the following self-consistency condition for these functions:

$$a_d^\pm(x) = \int_0^\infty du\, \tau(u)\, a_d^\mp(x \pm u) \ , \quad d = L, R \ . \tag{3.109}$$

By symmetry under $x \to \Delta - x$ (this relies on the statistical symmetry between J^x and J^y),

$$a_L^\pm(x) = a_R^\mp(\Delta - x) \ \text{ and } \ a_R^\pm(x) = a_L^\mp(\Delta - x) \ . \tag{3.110}$$

Finally, we know with certainty that the RW will cross one or the other boundary, so $a_L^\pm(x) + a_R^\pm(x) = 1$ for all $x \in \mathbb{R}$. Using this fact along with plugging Eq. (3.110) into Eq. (3.109) obtains the condition for a single distribution, which is

$$a_d^\pm(x) = 1 - \int_0^\infty du\, \tau(u)\, a_d^\pm(\Delta - x \mp u) \ . \tag{3.111}$$

Define the probabilities piecewise:

$$a_L^\sigma(x) = \begin{cases} 1, & x \le 0 \\ \tilde{a}_L^\sigma(x), & 0 < x < \Delta \\ 0, & x \ge \Delta \end{cases} \quad \text{and} \quad a_R^\sigma(x) = \begin{cases} 0, & x \le 0 \\ \tilde{a}_R^\sigma(x), & 0 < x < \Delta \\ 1, & x \ge \Delta \end{cases} . \tag{3.112}$$

The functions may not be continuous at $x = 0$ or Δ, but we expect that

$$\lim_{\epsilon\to 0} \tilde{a}_R^-(\epsilon) = \lim_{\epsilon\to 0} \tilde{a}_L^+(\Delta - \epsilon) = 0, \text{ and } \lim_{\epsilon\to 0} \tilde{a}_L^-(\epsilon) = \lim_{\epsilon\to 0} \tilde{a}_R^+(\Delta - \epsilon) = 1 . \tag{3.113}$$

Consider the RW to the right of A'. The situation here is a boundary set at Δ followed by a single downward step of size $x \sim \tau(u)$. The likelihood that the RW will return to the initial level 0 Δ is then simply $\tilde{a}_L^-(x = \Delta)$.

It seems the way to proceed is by trying to guess terms which could satisfy Eq. (3.111). Specifically, consider the case of $\tilde{a}_R^-(x)$, which is convenient because we expect its limiting value as $x \to 0$ to be 0, and its limiting value as $x \to \Delta$ to be some number less than 1. Then we have

$$\tilde{a}_R^-(x) = 1 - \int_0^x du\, \tau(u)\, \tilde{a}_R^-((\Delta - x) + u) - \int_x^\infty du\, \tau(u) \tag{3.114}$$

$$= 1 - e^{-x/\Gamma} - \frac{1}{\Gamma} \int_0^x du\, e^{-u/\Gamma}\, \tilde{a}_R^-((\Delta - x) + u) . \tag{3.115}$$

This looks pretty challenging, however really all of this should just be some sort of notationally obscured Poisson equation. For the case of diffusion—which should also be applicable here—the solution is quite simple, being linear in x. So, trying a variational form $\tilde{a}_R^-(x) = c_1 x$,

$$c_1 x \triangleq 1 - e^{-x/\Gamma} - \frac{1}{\Gamma} \int_0^x du\, e^{-u/\Gamma}\, \kappa((\Delta - x) + u) \tag{3.116}$$

$$= 1 - e^{-x/\Gamma} - c_1 \left((\Delta + \Gamma)(1 - e^{-x/\Gamma}) - x\right) , \tag{3.117}$$

which is solved by $c_1 = \frac{1}{\Delta+\Gamma}$. One can show that the coefficient of a quadratic term vanishes. The likelihood of eventually exiting via the "far" boundary (satisfying condition 2 or 3 of Sec. 3.5.1) is

$$p_{\text{far}}(\Delta) = 1 - \frac{\Delta}{\Delta + \Gamma} = \frac{\Gamma}{\Delta + \Gamma} \approx \frac{\Gamma}{\Delta} \quad \text{for} \quad \Gamma/\Delta \ll 1 . \tag{3.118}$$

3.A.2 Time-dependent free-space density

Steady-state methods do not suffice to determine the probability that the RW will reach a maximum Δ at a specific time t. It is natural to apply the continuum diffusion picture on an interval, to which end we work explicitly through

the derivation of the free-space probability density. This is just reproducing a result already well known from the central limit theorem, from which we know that the distribution of the sum of a large number of random variables is Gaussian, as long as the component distributions have finite moments. In the present case it essentially constrains our result for the free-space density to be Gaussian with variance $\Gamma^2 t$. However because the alternation of step directions, accounted for by an internal state, introduces an interesting modification we follow the derivation despite knowing the answer in advance. We use RW-appropriate symbols, maintaining $x \in \mathbb{R}$ for log-energy density and $t = r \in \mathbb{Z}$ for RW time, which we will later also treat as continuous.

The master equation, using the condensed notation $\rho^{\pm}(x,t) = \rho(x,\pm 1,t)$, is

$$\rho^{\pm}(x,t+1) = \int_0^\infty du\, \tau(u)\, \rho^{\mp}(x \pm u, t)\ . \tag{3.119}$$

Following the standard procedure for solving these types of problems, as in Ref. [26], we want to change variables using the generating function for t (the discrete counterpart to the Laplace transform) and Fourier transform in x:

$$\rho^{\pm}(k,z) = \int_{\mathbb{R}} dx\, e^{ikx} \sum_{t=0}^{\infty} z^t \rho^{\pm}(x,t) \tag{3.120}$$

Now Eq. (3.119) is equivalently written

$$\sum_{t=0}^{\infty} z^{t+1} \int_{\mathbb{R}} dx\, e^{ikx} \rho^{\pm}(x,t+1) = z \sum_{t=0}^{\infty} z^t \int_{\mathbb{R}} dx\, e^{ikx} \int_0^\infty du\, \tau(u)\, \rho^{\mp}(x \pm u, t) \tag{3.121}$$

$$\rho^{\pm}(k,z) - \rho^{\pm}(k,t=0) = z \int_0^\infty du\, \tau(u)\, e^{\mp iku} \sum_{t=0}^{\infty} z^t \int_{\mathbb{R}} dx\, e^{ik(x\pm u)} \rho^{\mp}(x \pm u, t) \tag{3.122}$$

$$= z\rho^{\mp}(k,z) \int_0^\infty du\, \tau(u)\, e^{\mp iku} \tag{3.123}$$

$$= \frac{z\rho^{\mp}(k,z)}{1 \pm i\Gamma k}\ . \tag{3.124}$$

The initial conditions are $\rho^{+}(x, t=0) = \delta(x)$ and $\rho^{-}(x, t=0) = 0$. This reflects that $\rho^{+}(x)$ is really only defined for even times t and $\rho^{-}(x)$ for odd times. (Though if we had $\rho^{-}(x, t=0) = \delta(x)$ we'd get the same result, only by more complicated math.) Now we concatenate the two equations in

Eq. (3.124) to solve for the distribution in (k, z)-space:

$$\rho^+(k,z) - 1 = \frac{z^2\rho^+(k,z)}{1+\Gamma^2k^2} \implies \rho^+(k,z) = \frac{1}{1-\frac{z^2}{1+\Gamma^2k^2}} \,. \tag{3.125}$$

By expanding the Taylor series of Eq. (3.125) in z we undo the generating function and restore t dependence:

$$\rho^+(k,t) = \left(\frac{1}{\sqrt{1+\Gamma^2k^2}}\right)^t \equiv \left(\frac{1}{1+\Gamma^2k^2}\right)^{t/2} \,. \tag{3.126}$$

Where $t/2 \in \mathbb{Z}$, as we evaluate this function only at even times t. Now, to second order in the Taylor series expansion, $\frac{1}{1+\Gamma^2k^2} = 1 - \Gamma^2k^2 + \cdots \approx e^{-\Gamma^2k^2}$. The inverse Fourier transform is evaluated by completing the square:

$$\rho^+(x,t) \approx \frac{1}{2\pi}\int_{\mathbb{R}} dk\, e^{-ikx-\Gamma^2k^2(t/2)} \tag{3.127}$$

$$= \frac{1}{2\pi}\int_{\mathbb{R}} dk\, \exp\left[-\frac{\Gamma^2 t}{2}\left(k + \frac{ix}{\Gamma^2 t}\right)^2 - \frac{x^2}{2\Gamma^2 t}\right] \tag{3.128}$$

$$= \frac{1}{\Gamma\sqrt{2\pi t}}\exp\left[-\frac{x^2}{2\Gamma^2 t}\right] . \tag{3.129}$$

So, as anticipated from the central limit theorem, the asymptotic distribution is a Gaussian having $\mathrm{Var}[\rho^+(x,t)] = \Gamma^2 t = \mathrm{Var}[\tau]t$, and mean 0. The $\sigma = -1$ density can be found by applying the master equation:

$$\rho^-(x,t+1) = \int_0^\infty du\, \tau(u)\, \rho^+(x-u,t) \tag{3.130}$$

$$= \frac{1}{\Gamma^2\sqrt{2\pi t}}\int_0^\infty du\, \exp\left[-\frac{(x-u)^2}{2\Gamma^2 t} - \frac{u}{\Gamma}\right] \tag{3.131}$$

$$= \frac{1}{2\Gamma}\exp\left[\frac{\Gamma^2t^2 - 2\Gamma tx}{2\Gamma^2 t}\right]\mathrm{erfc}\left[\frac{\Gamma t - x}{\Gamma\sqrt{2t}}\right] \tag{3.132}$$

$$\approx \sqrt{\frac{t}{2\pi}}\frac{1}{\Gamma t - x}\exp\left[\frac{\Gamma^2t^2 - 2\Gamma tx}{2\Gamma^2 t} - \left(\frac{\Gamma t - x}{\Gamma\sqrt{2t}}\right)^2\right] \tag{3.133}$$

$$= \sqrt{\frac{t}{2\pi}}\frac{1}{\Gamma t - x}\exp\left[-\frac{x^2}{2\Gamma^2 t}\right] \tag{3.134}$$

$$\approx \frac{1}{\Gamma\sqrt{2\pi t}}\left(1 + \frac{x}{\Gamma t}\right)\exp\left[-\frac{x^2}{2\Gamma^2 t}\right] \tag{3.135}$$

$$\approx \frac{1}{\Gamma\sqrt{2\pi t}}\exp\left[-\frac{x^2}{2\Gamma^2 t} + \frac{x}{\Gamma t}\right] \tag{3.136}$$

$$= \frac{e^{1/2t}}{\Gamma\sqrt{2\pi t}}\exp\left[-\frac{(x-\Gamma)^2}{2\Gamma^2 t}\right] \,. \tag{3.137}$$

Above we used the first term in the asymptotic expansion of erfc:

$$\mathrm{erfc}(x) = \frac{2}{\sqrt{\pi}} \int_x^\infty e^{-t^2} dt \approx \frac{e^{-x^2}}{x\sqrt{\pi}} \ . \tag{3.138}$$

So at late times the $\sigma = -1$ distribution is approximately a shifted Gaussian with mean $\mu = \Gamma = \langle \tau \rangle$, reflecting that one more positive step than negative has been taken at odd times t. Collecting the two results, in the long-time limit (using t versus $t+1$ in the second case has a negligible effect),

$$\rho^+(x,t) = \frac{1}{\Gamma\sqrt{2\pi t}} \exp\left[-\frac{x^2}{2\Gamma^2 t} \right] \ , \tag{3.139}$$

$$\rho^-(x,t) = \frac{1}{\Gamma\sqrt{2\pi t}} \exp\left[-\frac{(x-\Gamma)^2}{2\Gamma^2 t} \right] . \tag{3.140}$$

BIBLIOGRAPHY

[1] K. Slagle, Y.-Z. You, and C. Xu, "Disordered XYZ spin chain simulations using the spectrum bifurcation renormalization group", Physical Review B 94 (2016), 014205.

[2] S. Moudgalya, D. A. Huse, and V. Khemani, "Perturbative instability towards delocalization at phase transitions between MBL phases", arXiv preprint arXiv:2008.09113 (2020).

[3] B. Ware, D. Abanin, and R. Vasseur, "Perturbative instability of non-ergodic phases in non-Abelian quantum chains", Physical Review B 103 (2021), 094203.

[4] D. S. Fisher, "Random antiferromagnetic quantum spin chains", Physical Review B 50 (1994), 3799.

[5] S.-K. Ma, C. Dasgupta, and C.-K. Hu, "Random antiferromagnetic chain", Physical Review Letters 43 (1979), 1434.

[6] C. Dasgupta and S.-K. Ma, "Low-temperature properties of the random Heisenberg antiferromagnetic chain", Physical Review B 22 (1980), 1305.

[7] D. S. Fisher, "Random transverse field Ising spin chains", Physical Review Letters 69 (1992), 534.

[8] D. S. Fisher, "Critical behavior of random transverse-field Ising spin chains", Physical Review B 51 (1995), 6411.

[9] D. S. Fisher and A. Young, "Distributions of gaps and end-to-end correlations in random transverse-field Ising spin chains", Physical Review B 58 (1998), 9131.

[10] F. Iglói, R. Juhász, and H. Rieger, "Random antiferromagnetic quantum spin chains: Exact results from scaling of rare regions", Physical Review B 61 (2000), 11552.

[11] K. Damle and D. A. Huse, "Permutation-symmetric multicritical points in random antiferromagnetic spin chains", Physical Review Letters 89 (2002), 277203.

[12] A. Y. Kitaev, "Unpaired Majorana fermions in quantum wires", Physics-Uspekhi 44 (2001), 131.

[13] O. Motrunich, K. Damle, and D. A. Huse, "Griffiths effects and quantum critical points in dirty superconductors without spin-rotation invariance: One-dimensional examples", Physical Review B 63 (2001), 224204.

[14] C. Monthus, "Strong disorder real-space renormalization for the many-body-localized phase of random Majorana models", Journal of Physics A: Mathematical and Theoretical 51 (2018), 115304.

[15] J. R. Schrieffer and P. A. Wolff, "Relation between the anderson and kondo hamiltonians", Physical Review 149 (1966), 491.

[16] S. Bravyi, D. P. DiVincenzo, and D. Loss, "Schrieffer–Wolff transformation for quantum many-body systems", Annals of Physics 326 (2011), 2793.

[17] C.-J. Lin and O. I. Motrunich, "Quasiparticle explanation of the weak-thermalization regime under quench in a nonintegrable quantum spin chain", Physical Review A 95 (2017), 023621.

[18] M. Fishman, S. R. White, and E. M. Stoudenmire, *The ITensor Software Library for Tensor Network Calculations*, 2020.

[19] B. Roberts, T. Vidick, and O. I. Motrunich, "Implementation of rigorous renormalization group method for ground space and low-energy states of local Hamiltonians", Physical Review B 96 (2017), 214203.

[20] G. Refael and J. E. Moore, "Entanglement entropy of random quantum critical points in one dimension", Physical Review Letters 93 (2004), 260602.

[21] F. Iglói and H. Rieger, "Random transverse Ising spin chain and random walks", Physical Review B 57 (1998), 11404.

[22] F. Iglói and H. Rieger, "Anomalous diffusion in disordered media and random quantum spin chains", Physical Review E 58 (1998), 4238.

[23] O. Motrunich, K. Damle, and D. A. Huse, "Dynamics and transport in random quantum systems governed by strong-randomness fixed points", Physical Review B 63 (2001), 134424.

[24] F. Iglói and C. Monthus, "Strong disorder RG approach of random systems", Physics reports 412 (2005), 277.

[25] B. D. Hughes, *Random walks*, vol. 1, Random walks and random environments, Clarendon Press, 1995.

[26] S. Redner, *A guide to first-passage processes*, Cambridge University Press, 2001.

[27] T. A. Driscoll and L. N. Trefethen, *Schwarz-Christoffel Mapping*, vol. 8, Cambridge monographs on applied and computational mathematics, Cambridge University Press, 2002.

[28] H. S. Carslaw and J. C. Jaeger, *Conduction of heat in solids*, 2nd ed, Clarendon Press; Oxford University Press, 1986.

[29] M. E. Fisher and M. P. Gelfand, "The reunions of three dissimilar vicious walkers", Journal of Statistical Physics 53 (1988), 175.

[30] A. J. Bray, S. N. Majumdar, and G. Schehr, "Persistence and first-passage properties in nonequilibrium systems", Advances in Physics 62 (2013), 225.

[31] T. Giamarchi, *Quantum physics in one dimension*, The international series of monographs on physics, Clarendon ; Oxford University Press, 2004.

[32] H. Rieger and F. Iglói, "Random quantum magnets with long-range correlated disorder: Enhancement of critical and Griffiths-McCoy singularities", Physical Review Letters 83 (1999), 3741.

[33] A. Weinrib and B. I. Halperin, "Critical phenomena in systems with long-range-correlated quenched disorder", Physical Review B 27 (1983), 413.

[34] A. Weinrib, "Long-range correlated percolation", Physical Review B 29 (1984), 387.

Chapter 4

DECONFINED QUANTUM CRITICAL POINT IN ONE DIMENSION

[1] B. Roberts, S. Jiang, and O. I. Motrunich, "Deconfined quantum critical point in one dimension", Physical Review B 99 (2019), 165143.

4.1 Introduction

In this chapter, we numerically study a version of the deconfined quantum critical point (DQCP) realized in 1d, following the recent theoretical proposal [1] of a continuous quantum phase transition in a particular 1d model having Ising-type $\mathbb{Z}_2 \times \mathbb{Z}_2$ symmetry as well as translation symmetry. The transition is between an Ising ferromagnet and a Valence Bond Solid (VBS); as is the case for the 2d DQCP, the phases on either side break different symmetries and a continuous phase transition is disallowed in Landau–Ginzburg–Wilson theory.

Here, we present strong numerical evidence supporting the 1d proposal in a concrete model. We use matrix product states (MPS), working directly in the thermodynamic limit, and develop a specialized "finite-entanglement scaling" protocol that allows us to study this transition with high precision. A non-trivial aspect of the infinite-volume MPS study of the DQCP is that the MPS ground state at fixed bond dimension undergoes a first-order transition, which turns out to be advantageous for accessing properties of the true continuous DQCP via scaling in finite bond dimension. Our numerical study confirms key predictions of the 1d DQCP theory, thus providing a definitive example of such a phase transition. We note that non-Landau continuous transitions were found previously in 1d fermionic models, in Refs. [2–7].

The chapter is organized as follows. In Sec. 4.2, we give an overview of the system and symmetries, summarize field theory predictions for the transition, and introduce our concrete model and its phase diagram. In Sec. 4.3, we describe the numerical study of the ferromagnet to VBS transition, including details of our finite-entanglement scaling protocol which leads to an accurate determination of the critical indices, and study the variation along the phase

boundary. In Sec. 4.4, we study the regime where the transition splits into two, with an intervening phase of coexistence of magnetic and VBS orders. We conclude in Sec. 4.5 with a summary of our results. We also include three appendices: Appendix 4.A provides a basic mean-field description of the phase diagram using pictures of the ground states described by separable wavefunctions. Appendix 4.B resolves some questions arising from the separable-state mean-field picture by representation of model ground states for the phases as analytic MPS of bond dimension two. Finally, Sec. 4.C develops a field theory description of another phase transition encountered in this model beyond the LGW symmetry-breaking paradigm.

4.2 Description of model

Here we summarize the key results of Ref. [1], which contains a number of descriptions of the model at hand. Briefly, a second-order phase transition was proposed at the phase boundary of an Ising ferromagnet and valence bond solid (VBS). Because these states break different symmetries, a continuous phase transition between them falls outside of the Landau–Ginzburg–Wilson paradigm.

4.2.1 General model and symmetries

Our general Hamiltonian is the following spin model, with nearest- and next-nearest-neighbor terms:

$$H = \sum_j \left(-J_x \sigma_j^x \sigma_{j+1}^x - J_z \sigma_j^z \sigma_{j+1}^z + K_{2x} \sigma_j^x \sigma_{j+2}^x + K_{2z} \sigma_j^z \sigma_{j+2}^z \right) \ . \tag{4.1}$$

We take J_x, J_z, K_{2x}, K_{2z} nonnegative, that is, with ferromagnetic nearest-neighbor and antiferromagnetic next-nearest-neighbor interactions. H respects two Ising-like symmetries as well as time reversal:

$$g_x = \prod_j \sigma_j^x \ : \quad \sigma_j^x \mapsto \sigma_j^x \ , \ \sigma_j^{y,z} \mapsto -\sigma_j^{y,z} \ ; \tag{4.2}$$

$$g_z = \prod_j \sigma_j^z \ : \quad \sigma_j^z \mapsto \sigma_j^z \ , \ \sigma_j^{x,y} \mapsto -\sigma_j^{x,y} \ ; \tag{4.3}$$

$$\mathcal{T} = \left(\prod_j i\sigma_j^y \right) \mathcal{K} \ : \quad \sigma_j^\alpha \mapsto -\sigma_j^\alpha \ , \ i \mapsto -i \ . \tag{4.4}$$

Here $\mathcal{K}$ is complex conjugation in the σ^z basis. The model also has translation symmetry, $T_1 : \sigma_j^\alpha \mapsto \sigma_{j+1}^\alpha$, as well as inversion symmetry $I : \sigma_j^\alpha \mapsto \sigma_{-j+1}^\alpha$, which we take to be about a bond center.

In the regime where J_z is dominant, the spins order as a ferromagnet in the σ^z direction; we call this phase "zFM." For intermediate $K_{2x} \sim K_{2z}$, the spins are disordered (all on-site symmetries are preserved) and instead form dimers on alternating bonds; we call this phase "VBS-I," to distinguish from other specific dimer states which we encounter. A fixed-point picture of this particular VBS phase is a product state of dimers on, say, all $(2m-1, 2m)$ bonds, where each dimer is an entangled state of two spins of the form

$$\begin{aligned} |D_{12}^{(I)}\rangle &= \frac{|+\hat{z}\rangle_1|+\hat{z}\rangle_2 + |-\hat{z}\rangle_1|-\hat{z}\rangle_2}{\sqrt{2}} \\ &= \frac{|+\hat{x}\rangle_1|+\hat{x}\rangle_2 + |-\hat{x}\rangle_1|-\hat{x}\rangle_2}{\sqrt{2}} \\ &= \frac{|+\hat{y}\rangle_1|-\hat{y}\rangle_2 + |-\hat{y}\rangle_1|+\hat{y}\rangle_2}{\sqrt{2}} \ . \end{aligned} \tag{4.5}$$

Note that the spins in the dimer have ferromagnetic zz and xx correlations and antiferromagnetic yy correlations. This state is expected from the ferromagnetic J_z and J_x couplings. Most of the time, we will focus on the VBS-I phase and will frequently refer to it as simply VBS where it does not cause confusion.

The above fixed-point VBS wavefunction is an exact ground state at the Majumdar–Ghosh point: $J_x = J_z = J$, $K_{2x} = K_{2z} = K_2$, and $K_2/J = 0.5$ [8–11]. Our primary focus is on the phase transition between the zFM and VBS-I phases.

4.2.2 Summary of field theory for the zFM to VBS transition

The field theory description of the zFM to VBS transition in Ref. [1] has a Luttinger liquid–like form and is written in terms of conjugate fields $\tilde{\phi}$ and $\tilde{\theta}$, with velocity $\tilde{v}$ and Luttinger parameter $\tilde{g}$:

$$\begin{aligned} S[\tilde{\phi},\tilde{\theta}] = &\int \mathrm{d}\tau\, \mathrm{d}x \left[\frac{\mathrm{i}}{\pi} \partial_\tau \tilde{\phi} \partial_x \tilde{\theta} + \frac{\tilde{v}}{2\pi} \left(\frac{1}{\tilde{g}} (\partial_x \tilde{\theta})^2 + \tilde{g} (\partial_x \tilde{\phi})^2 \right) \right] \\ &+ \int \mathrm{d}\tau\, \mathrm{d}x \left[\lambda \cos(2\tilde{\theta}) + \lambda' \cos(4\tilde{\theta}) + \kappa \cos(4\tilde{\phi}) \right] . \end{aligned} \tag{4.6}$$

The notation here matches that in Ref. [1] (see Sec. VII there); in particular, tildes over the fields signify that they are not simply related to a naive bosonization of spins in the xz plane.

As written, the fields have periodicities $\tilde{\phi} + \pi \equiv \tilde{\phi}$ and $\tilde{\theta} + 2\pi \equiv \tilde{\theta}$, which follows from their partonic origin (see Sec. VII in Ref. [1] for details and

also App. E there for another perspective on this theory). The second line shows the leading symmetry-allowed cosine terms of the fields. Taking the Luttinger parameter in the range $\tilde{g} \in (1/2, 2)$ arranges that the λ' and κ terms are irrelevant and the λ term is the only relevant cosine. The zFM to VBS transition occurs when the relevant coupling λ changes sign, hence the critical theory is Gaussian. The correlation length exponent follows from the scaling dimension of the relevant cosine perturbation and is given by

$$\nu = \frac{1}{2 - \tilde{g}} \ , \tag{4.7}$$

which can vary in the range $\nu \in (2/3, \infty)$ for $\tilde{g} \in (1/2, 2)$.

The most important observables are the zFM and VBS order parameters, which are given by

$$M_z^{\mathrm{FM}} \sim \sin(\tilde{\theta}) \ , \qquad \Psi_{\mathrm{VBS}} \sim \cos(\tilde{\theta}) \ . \tag{4.8}$$

At the critical point, they have the same scaling dimension

$$\dim[M_z^{\mathrm{FM}}] = \dim[\Psi_{\mathrm{VBS}}] = \frac{\tilde{g}}{4} \ , \tag{4.9}$$

which can vary in the range $(1/8, 1/2)$. The scaling dimension of an observable O determines the power law decay of the critical correlations: if $\langle O(x) O(0) \rangle \sim 1/x^{p_O}$, then $p_O = 2 \dim[O]$. General scaling arguments also yield the order parameter onset exponent $\beta = \nu p/2$.

We also mention the next most prominent observables, namely the xFM and yAFM order parameters

$$M_x^{\mathrm{FM}} \sim \cos(2\tilde{\phi}) \ , \qquad M_y^{\mathrm{AFM}} \sim \sin(2\tilde{\phi}) \ , \tag{4.10}$$

with scaling dimensions

$$\dim[M_x^{\mathrm{FM}}] = \dim[M_y^{\mathrm{AFM}}] = \frac{1}{\tilde{g}} \ , \tag{4.11}$$

which can vary between 2 and 1/2. Note that the dominant σ^x correlations are ferromagnetic while the dominant σ^y correlations are antiferromagnetic. This is tied to the fact that this theory describes the transition from the zFM phase to the VBS-I phase with the fixed-point elementary dimer given by Eq. (4.5); see also the discussion following that equation.

To summarize, the critical exponents vary continuously and depend on a single parameter $\tilde{g}$. When $\tilde{g}$ drops below 1/2, the λ' term becomes relevant and destabilizes the above picture for the direct transition between the zFM and VBS phases. Analysis in Ref. [1] suggests that for $\lambda' > 0$, an intermediate phase with coexisting zFM and VBS order parameters appears between the pure zFM and pure VBS phases. We will also examine this scenario in our study of the specific model below.

4.2.3 Specific model and expected phase behavior

In order to study the phase transition between the Ising ferromagnet and VBS phases, we restrict in parameter space to a two-dimensional slice given by $K_2 = K_{2x} = K_{2z}$ and $\delta = (J^z - J^x)/(J^z + J^x)$; that is, $J^z = J(1+\delta)$ and $J^x = J(1-\delta)$, where we will take $J = 1$. The $U(1)$ symmetry of rotations in the xz plane is broken only by the nearest-neighbor couplings, and is restored for anisotropy $\delta = 0$. The point $\delta = K_2 = 0$ is the XX model, which maps to free fermions and belongs to the quasi–long-range-ordered (QLRO) phase present on the $\delta = 0$ axis up to some critical $K_{2,\mathrm{KT}}$. Along this axis at $K_{2,\mathrm{KT}}$, the model undergoes a Kosterlitz–Thouless transition [12–14] to the VBS phase described earlier. Additional phases occur at significantly larger K_2 and were studied in Refs. [10, 11] but are not considered in the present work. For any $|\delta| > 0$, at small values of K_2 the ground state is an Ising ferromagnetic state. At intermediate K_2 the VBS phase is stable to introducing spin anisotropy and extends to non-zero δ. At fixed finite δ, we therefore expect that increasing the K_2 term from small values will drive a transition from the Ising ferromagnet to the VBS phase.

It is sufficient to consider $\delta \geq 0$, as the Hamiltonian with parameters $\{-\delta, K_2\}$ is equivalent to that with $\{\delta, K_2\}$ up to a local unitary rotation, $\sigma_j^x \mapsto \sigma_j^z, \sigma_j^z \mapsto -\sigma_j^x$, which takes the zFM phase to an Ising x ferromagnet ("xFM"), and vice versa. This transformation leaves the VBS-I dimer of Eq. (4.5) invariant, thus the same phase appears for both positive and negative δ.

We may also restrict our focus to models with $\delta \leq 1$ due to another relationship—namely, that models having parameters $\{\delta, K_2\}$ and $\{\delta', K_2'\} = \{1/\delta, K_2/\delta\}$ are related by local unitary $\prod_m \sigma_{2m}^z$, taking $\sigma_{2m}^z \mapsto \sigma_{2m}^z$ and $\sigma_{2m}^x \mapsto -\sigma_{2m}^x$. Indeed, the primed model has parameter values $J^{z\prime} = 1 + \delta' = (1+\delta)/\delta$, $J^{x\prime} = 1 - \delta' = -(1-\delta)/\delta$, and the given rotation relates it to the first model

up to an overall energy scale. Note that under this unitary transformation, the elementary dimer wavefunction Eq. (4.5) maps to

$$\begin{aligned} |D_{12}^{(II)}\rangle &= \frac{|+\hat{z}\rangle_1|+\hat{z}\rangle_2 - |-\hat{z}\rangle_1|-\hat{z}\rangle_2}{\sqrt{2}} \\ &= \frac{|+\hat{x}\rangle_1|-\hat{x}\rangle_2 + |-\hat{x}\rangle_1|+\hat{x}\rangle_2}{\sqrt{2}} \\ &= \frac{|+\hat{y}\rangle_1|+\hat{y}\rangle_2 + |-\hat{y}\rangle_1|-\hat{y}\rangle_2}{\sqrt{2}} \ . \end{aligned} \tag{4.12}$$

Hence, at values $\delta > 1$ one finds another dimer state, which we denote "VBS-II," as it is a distinct phase from the previously described VBS-I provided the on-site symmetries are not broken [1]. The precise distinction between the phases is that on a periodic system with an odd number of dimers, the ground states in VBS-I have quantum numbers $(g_x, g_y, g_z) = (1, -1, 1)$, whereas the quantum numbers in VBS-II are $(g_x, g_y, g_z) = (-1, 1, 1)$.

Naively, one may expect a phase transition between VBS-I and VBS-II at $\delta = 1$. As we discuss in Sec. 4.4.2, the actual situation in this model is somewhat more complicated: in a particular region of the phase diagram close to the zFM phase, the spin system also develops zFM order on top of VBS-I or VBS-II, and this coexisting broken on-site symmetry allows a continuous connection between the two dimer states. Finally, for larger K_2, another phase—which does not appear in the field theory—arises in our model intervening between the two dimer phases. This is the so-called "up-up-down-down" state in the σ^x basis, or "xUUDD." The ground state of this phase breaks T_1 and g_z and has the following fixed-point wavefunction:

$$|x\text{UUDD}\rangle = \otimes_n |+\hat{x}\rangle_{4n-3} |+\hat{x}\rangle_{4n-2} |-\hat{x}\rangle_{4n-1} |-\hat{x}\rangle_{4n} \ . \tag{4.13}$$

In App. 4.A, we give fixed-point pictures and mean field energetics for all phases encountered in our window of study, thus providing some intuition for the observed phase diagram.

4.3 Study of zFM to VBS phase transition

We make use of the recently-developed numerical method "variational uniform matrix product states" (VUMPS), which is similar to infinite-system DMRG (IDMRG) but has been demonstrated to achieve superior convergence in some cases [15]. Like IDMRG, this method optimizes over MPS in the thermodynamic limit; that is, the ansatz is specified by a finite set of tensors comprising

the unit cell of the wavefunction, which contain the variational parameters of the infinite state. The understanding of VUMPS is geometrical: one searches within the manifold of uniform MPS of fixed bond dimension for the point $|\psi^*\rangle$ at which the energy residual $(H - E)|\psi^*\rangle$ is orthogonal to the manifold. This optimization can be formulated in the "post-MPS" tangent space language [16], but turns out to be similar to IDMRG.

The uniform MPS ansatz actually provides a dressed mean-field description of the phase transition [17]. Because the mean-field treatment in the present case exhibits a first-order phase transition, one expects the VUMPS method to encounter metastability effects near the phase transition arising from competing orders. We describe our protocol to address this challenge below; we are in fact able to utilize the first-order behavior of the finite bond dimension MPS to make very accurate determinations of the phase boundary. We first show in Fig. 4.1 our result for the phase diagram outlined in Sec. 4.2.3, and in the following sections we provide a methodological description.

4.3.1 Representative study along $\delta = 0.5$ cut

We illustrate our method of studying this phase transition by discussing in detail a concrete cut through the phase diagram, namely along the line $\delta = 0.5$ generated by varying the parameter K_2. Afterward, we will generalize to obtain a full description of the phase boundary by repeating the same process for multiple slices at constant δ. The line at $\delta = 0.5$ is generic, having no symmetries additional to those specified in Sec. 4.2. This slice is indicated in Fig. 4.1.

Broad description of phase transition

One can attain a basic understanding of the phase transition via simple analysis of the optimized MPS ground states. Using ansatz trial states originating within each phase, we tune K_2 through the critical point and observe the evolution of certain properties of the trial state wavefunction. The most evident indication of the phase transition is the order parameter for each phase acquiring a finite expectation value. Because the numerical method preferentially selects states of low entanglement, it finds everywhere a representative of the ground state manifold with spontaneously broken symmetry. As both phases break $\mathbb{Z}_2$ symmetries (g_x in the zFM phase and T_1 in the VBS phase), both

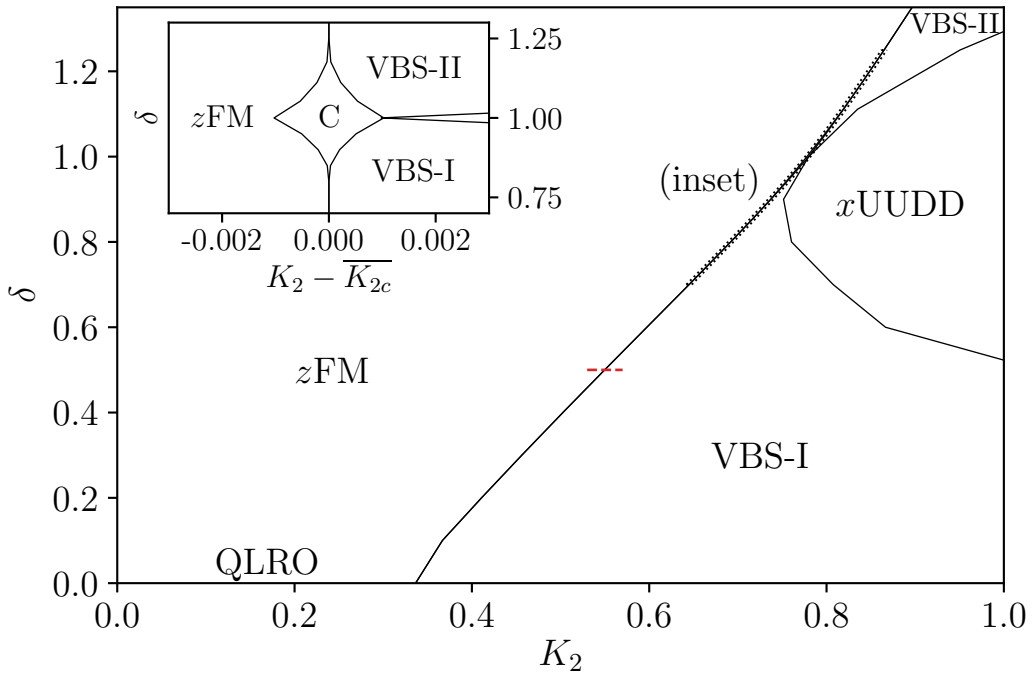

Figure 4.1: The phase diagram in the K_2-δ plane includes the zFM, VBS-I, VBS-II, and xUUDD phases. Inset shows a centered view of the coexistence region, denoted "C," appearing between the zFM and VBS-I or VBS-II phases for δ close to 1. While the distinction between the VBS-I and VBS-II phases is protected by the on-site symmetries, the VBS-I+zFM and VBS-II+zFM coexistence phases are not distinct and there is no transition inside the C region. The cut indicated at $\delta = 0.5$ will be investigated in detail in Sec. 4.3.1 as an example case.

ground state degeneracies are two and the symmetry breaking manifests as a sign in the expectation value of the corresponding order parameters. The order parameter for the zFM phase is

$$\langle M_z^{\mathrm{FM}} \rangle = \langle \sigma_0^z \rangle \ , \tag{4.14}$$

where the site label 0 indicates the first tensor in the unit cell, which in this case has only a single site. For the VBS phase, the order parameter is

$$\langle \Psi_{\mathrm{VBS}} \rangle = \langle \boldsymbol{\sigma}_0 \cdot \boldsymbol{\sigma}_1 - \boldsymbol{\sigma}_1 \cdot \boldsymbol{\sigma}_2 \rangle \ , \tag{4.15}$$

where $\boldsymbol{\sigma}_j$ denotes the Pauli vector acting at site j. The ground state of this phase has a two-site unit cell. We ignore the sign in both order parameters, always implicitly taking the absolute value.

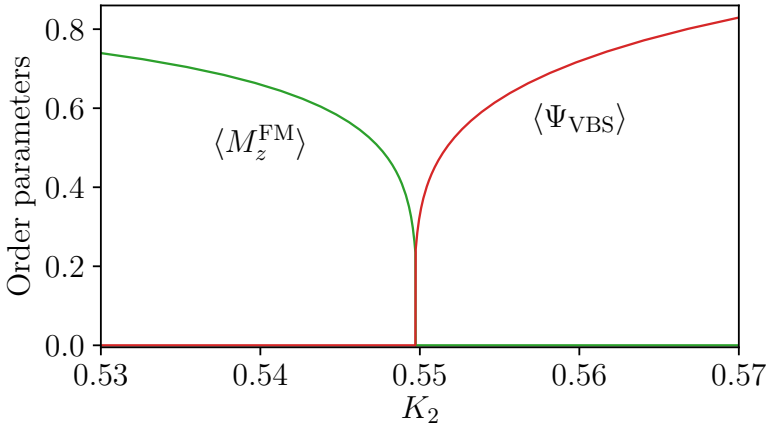

Figure 4.2: Transition between the zFM and VBS phases, as detected by the corresponding order parameters. This scan is taken at fixed $\delta = 0.5$ using bond dimension $\chi = 192$. We observe that at fixed χ, the MPS ground state shows a first-order transition; the discontinuities in the order parameters decrease towards zero with increasing χ, as studied in detail in Fig. 4.7.

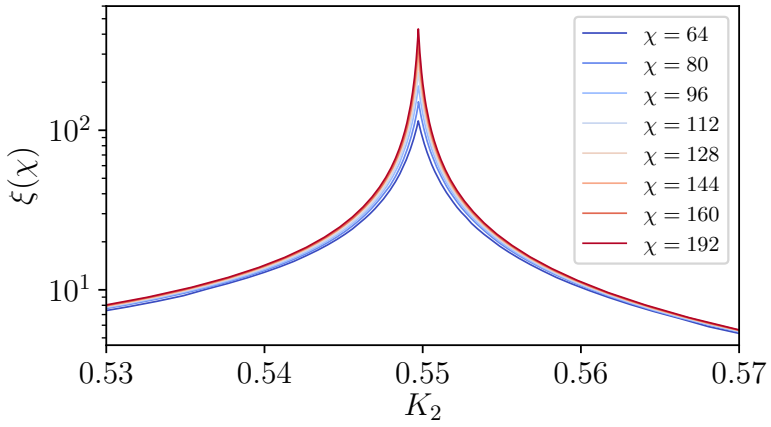

Figure 4.3: The divergence of the correlation length in the exact ground state at the critical point manifests as a χ-dependent cusp in the MPS correlation length $\xi(\chi)$; specifically, the height grows as a power law with χ, as studied in detail in Fig. 4.6. This feature is indicative of a continuous phase transition.

The order parameters are shown in Fig. 4.2 for a large bond dimension $\chi = 192$. As suggested by the mean field analysis, we do in fact find a discontinuous transition, with sizable jumps in both order parameters. However, we argue that the true transition in the $\chi \to \infty$ limit is continuous. Moreover, we use the first-order nature of the finite-χ approximants to our advantage: in particular, we will understand how the size of the order parameter discontinuity scales to

zero with increasing χ.

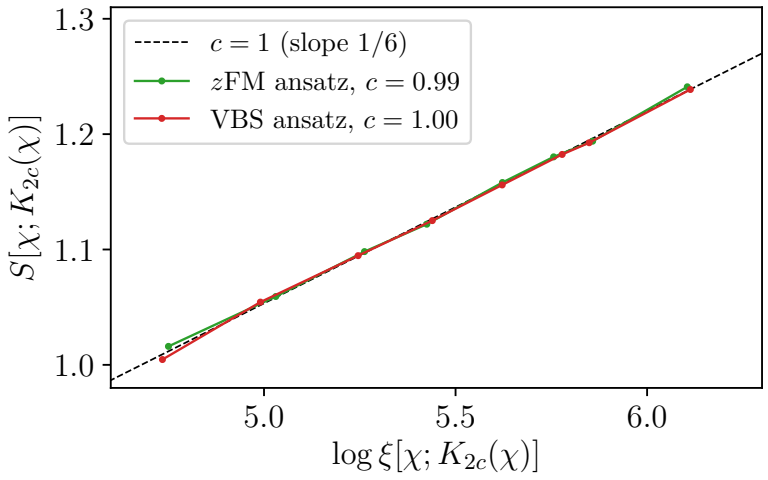

Figure 4.4: The scaling of the critical entanglement entropy $S[\chi; K_{2c}(\chi)]$ is nearly linear in $\log \xi[\chi; K_{2c}(\chi)]$, with the slope in good agreement with predicted central charge $c = 1$. Data shown is taken at parameter $\delta = 0.5$, and the dashed line is provided as a guide to the eye. The pseudocritical point $K_{2c}(\chi)$ is defined later in the text and included here only for specificity; it is important insofar as it is particular to the MPS of bond dimension χ.

Another fundamental characterization of the phase transition is the behavior of the correlation length $\xi(\chi)$ of the minimum-energy state on the manifold of MPS of bond dimension χ. This quantity is a property of the spectrum of the MPS transfer matrix T. In the simplest case of a single-site unit cell, $T = \sum_\sigma A^{\dagger\sigma} \otimes A^\sigma$, where σ runs over a basis of the local Hilbert space. Normalization constrains the largest eigenvalue to be unity; the MPS correlation length is set by the second-largest eigenvalue, which dictates the slowest decay possible in the state. Specifically, if T spans a unit cell of n sites, then $\lambda_2/\lambda_1 = e^{-n/\xi(\chi)}$, or $\xi(\chi) = -n/\log \lambda_2$.

We use ξ without an argument to refer to the correlation length of the ground state and use $\xi(\chi)$ for the MPS correlation length. At a continuous phase transition, the true correlation length ξ diverges; however $\xi(\chi)$ remains finite, as $\lambda_2 < \lambda_1$ by injectivity. Nevertheless, inside a gapped phase $\xi(\chi) \to \xi$, and where ξ diverges $\xi(\chi)$ exhibits a cusp with χ-dependent height. We discuss this relationship further in Sec. 4.3.1. The MPS correlation length at the zFM to VBS phase transition is shown in Fig. 4.3, and indeed displays a strong χ-dependent cusp at the critical point. At our largest $\chi = 192$, $\xi(\chi)$ already

exceeds 400 lattice spacings, with consistent growth in χ (see our later study in Fig. 4.6). This is the first strong evidence of a second-order transition, despite the order parameter discontinuity observed at this χ.

As further evidence for a second-order transition, Fig. 4.4 shows the entanglement entropy in the optimized MPS versus the logarithm of the MPS correlation length near criticality. For each χ we show two data points, measured in both the ansatz originating in the zFM and VBS phases, each tuned to a point still in the phase but very close to the MPS transition at this χ. The relationship is consistent with the finite-entanglement scaling form [18]

$$S(\chi) = \frac{c}{6} \log \xi(\chi) \ , \tag{4.16}$$

where c is the central charge of the critical system. The central charge estimates from fits to the above form are given in the figure and are consistent with the expected $c = 1$ from the theory of the zFM to VBS transition.

Precise identification of critical point

In principle, MPS methods are not well suited for describing ground states of quantum systems tuned to critical points, as the high degree of entanglement places a strong constraint on the accuracy of MPS ("classical") approximations. In contrast, ground states of gapped phases are well represented by MPS; however, in practice one can hope only to approach sufficiently close to a continuous phase transition to observe its true critical behavior. Beyond some crossover point set by the bond dimension, the MPS ground state instead flows to the phase transition described by the mean field theory of the model [17].

While MPS are unable to directly access critical states, it turns out that in the present case we can take advantage of the fact that the mean field phase transition is discontinuous, as described in App. 4.A, to accurately estimate the location of the critical point. Until the crossover point the system exhibits the behavior of the true continuous phase transition, but in tuning the system through the critical point one instead observes a level crossing of states connected to the fixed-point descriptions of each phase. In this regime the near-degeneracy of these dissimilar states leads to increased influence of the initial trial wavefunction in the VUMPS method, making convergence to the true ground state difficult when employing random initial states. To circum-

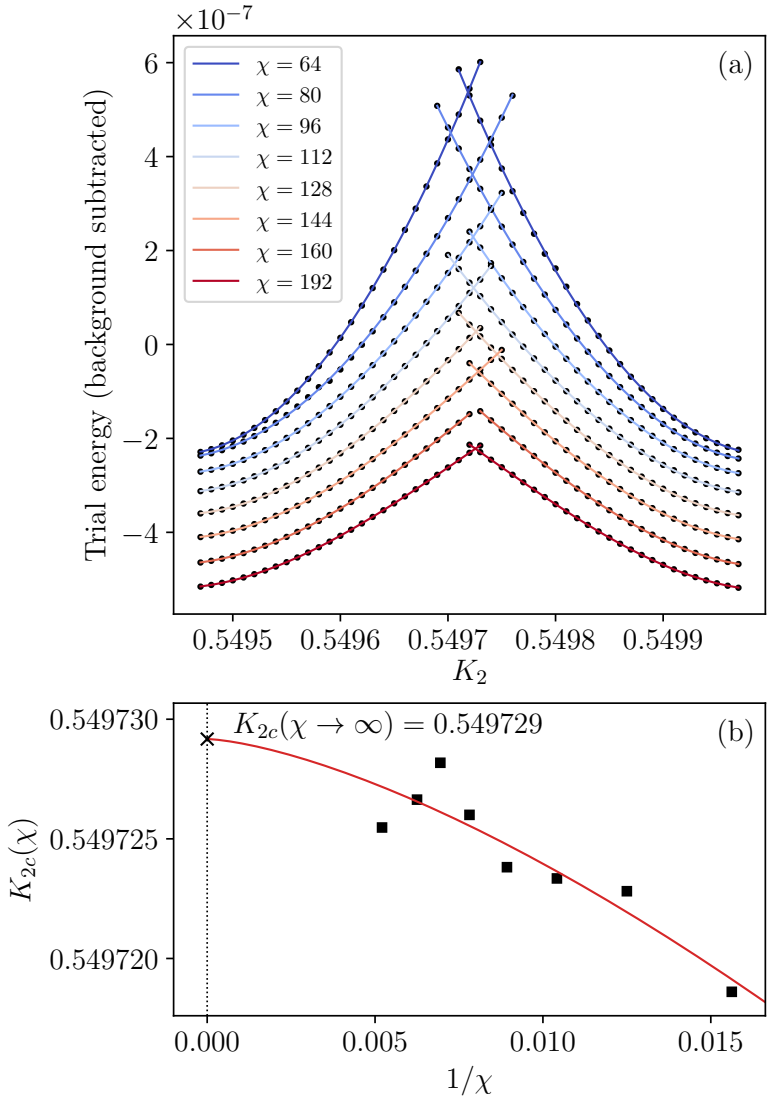

Figure 4.5: Illustration of the process of locating the critical point from finite-entanglement scaling at $\delta = 0.5$. (a) The energies of both trial wavefunctions from the zFM and VBS phases (fully optimized at each K_2) follow smooth curves, which determine the level crossing for a given bond dimension χ to a finer resolution than the scan in parameter K_2 via interpolation. Due to hysteresis, in many cases we directly observe the crossing using the adiabatic protocol described in the text. (b) Using the finite-entanglement scaling form Eq. (4.19), we extrapolate from the extracted pseudocritical $K_{2c}(\chi)$ to estimate the location of the critical point at $\chi \to \infty$. The scatter in data points is not noise from the variational algorithm, but rather may be a consequence of the uneven spacing of the entanglement spectrum.

vent this, we use an "adiabatic" protocol, first obtaining the MPS ground state in each phase far from the transition and slowly tuning the system to criticality in a series of discrete jumps, at each step allowing the state to converge fully. Due to metastability effects, hysteresis develops very close to the critical point; however, we are always able to identify the true ground state from comparison of the trial state energies. Because for MPS all energy levels are analytic functions of the Hamiltonian parameters, performing this scan in both phases allows one to identify the level crossing with a high degree of accuracy, in fact with a greater resolution than is used to tune the Hamiltonian.

This process is illustrated in Fig. 4.5 for a range of χ, where in panel (a) we show the trial energies tracked from each side and in panel (b) we show the extracted locations of the level crossings as a function of $1/\chi$. Note that the range of K_2 values is already very narrow, and the accuracy in the extrapolated crossings is better than 10^{-6}. Note also that the differences in the trial energies are enhanced by subtracting some smooth polynomial background (chosen for each χ), and that the vertical scale is very small; the slope discontinuity in the VUMPS trial energy decreases towards zero with increasing χ.

The above protocol applies to a uniform MPS having a fixed bond dimension χ. In fact, for any such ansatz with finite entanglement, the observed phase transition will occur not at the true critical point $K_{2c,\mathrm{true}}$ but at some *pseudocritical* point $K_{2c}(\chi)$. We expect that in the limit $\chi \to \infty$ the pseudocritical points converge to the true value. Pollmann et al. [18] determined that for a critical system with infinite correlation length ξ, the correlation length of the minimum-energy MPS at fixed bond dimension scales as

$$\xi(\chi) \sim \chi^{\kappa} \tag{4.17}$$

with exponent

$$\kappa = \frac{6}{c\left(\sqrt{\frac{12}{c}}+1\right)} , \tag{4.18}$$

which depends on the central charge of the critical system.

In order to describe the dependence of the pseudocritical point on bond dimension, we adapt an argument from finite-size scaling in statistical mechanics, which is commonly used in Monte Carlo studies. Denote the control parameter driving the transition as h, with the true critical point at $h_{c,\mathrm{true}}$. In a system

of finite length L the transition is smeared, but one can often identify a pseudocritical point $h_c(L)$ from some feature in the observables, such as peaks in susceptibilities, Binder ratio crossings, etc. Finite-size scaling predicts that the pseudocritical points approach the true critical point as $h_c(L) - h_{c,\text{true}} \sim L^{-1/\nu}$, which follows from comparing the true correlation length at $h_c(L)$ with the length scale L imposed by the system size. We conjecture that similar relation holds for the infinite-system variational MPS study, by replacing L with the length scale $\xi(\chi)$ imposed by the bond dimension:

$$K_{2c}(\chi) - K_{2c,\text{true}} \sim \xi(\chi)^{-1/\nu} \sim \chi^{-\kappa/\nu} \ . \tag{4.19}$$

One can also imagine using this relation to extract the correlation length exponent ν.[1]

Unfortunately, one observes in Fig. 4.5(b) significant scatter in the values of $K_{2c}(\chi)$ on top of some smooth behavior. This is not noise or evidence that the trial MPS is not energetically optimal, but rather a reproducible feature of the finite-χ results, which we conjecture arises from the nonuniformity of the gaps in the entanglement spectrum of the state. The plotted curve and value of $K_{2c}(\chi \to \infty)$ was fitted by fixing the value of the correlation length exponent to $\nu \approx 0.914$ extracted from later analysis, and is presented primarily as a consistency check. In any case, $K_{2c}(\chi)$ varies over a very small range, and as our scaling analysis below involves only the pseudocritical points $K_{2c}(\chi)$, the uncertainty in $K_{2c}(\chi \to \infty)$ is irrelevant for our subsequent characterizations of the critical point.

Correlation length and order parameter onset exponents

Using the precise estimates of the finite-entanglement pseudocritical points from Sec. 4.3.1, we are able to determine critical scaling exponents of the transition. Specifically, we consider the correlation length exponent ν and the order parameter exponents for both phases $\beta_{z\text{FM}}$ and β_{VBS}. The most straightforward way to determine ν is through its definition: $\xi \sim |K_2 - K_{2c}|^{-\nu}$. In Fig. 4.6 we show $\xi(\chi)$ as a function of $K_2 - K_{2c}(\chi)$. Sufficiently far from the critical point, $\xi(\chi)$ rapidly converges to ξ with increasing χ. In this regime

[1] In the 1d quantum Ising model studied in Ref. [17], the infinite-system MPS at fixed χ has a continuous mean field transition, and (4.19) provides a fairly accurate description of the approach of the corresponding pseudocritical points to the true critical point, with central charge $c = 1/2$ and correlation length exponent $\nu = 1$ for the Ising transition.

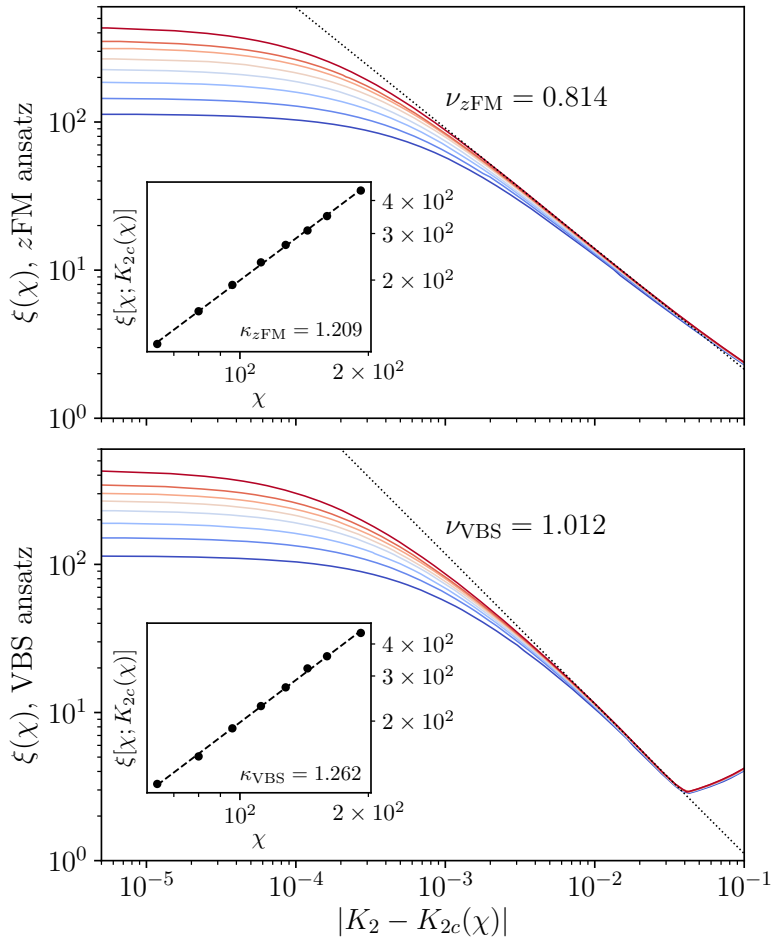

Figure 4.6: The MPS correlation length $\xi(\chi)$ exhibits power-law behavior in an intermediate region around $K_{2c}(\chi)$, here shown in the zFM phase in the top panel and VBS in the bottom. Close to the pseudocritical point, the correlation length saturates to a maximum value dependent on the bond dimension, whereas farther away it approaches a constant in the gapped phase. In the case of the VBS phase, a nearby critical point (the transition to the xUUDD phase) affects the behavior of $\xi(\chi)$. In the insets, we show the dependence of the maximum correlation length $\xi[\chi; K_{2c}(\chi)]$ extrapolated to the pseudocritical point $K_{2c}(\chi)$ as a function of χ. A fit to the scaling form Eq. (4.17) is shown (note that the axes are logarithmic), along with extracted values of κ.

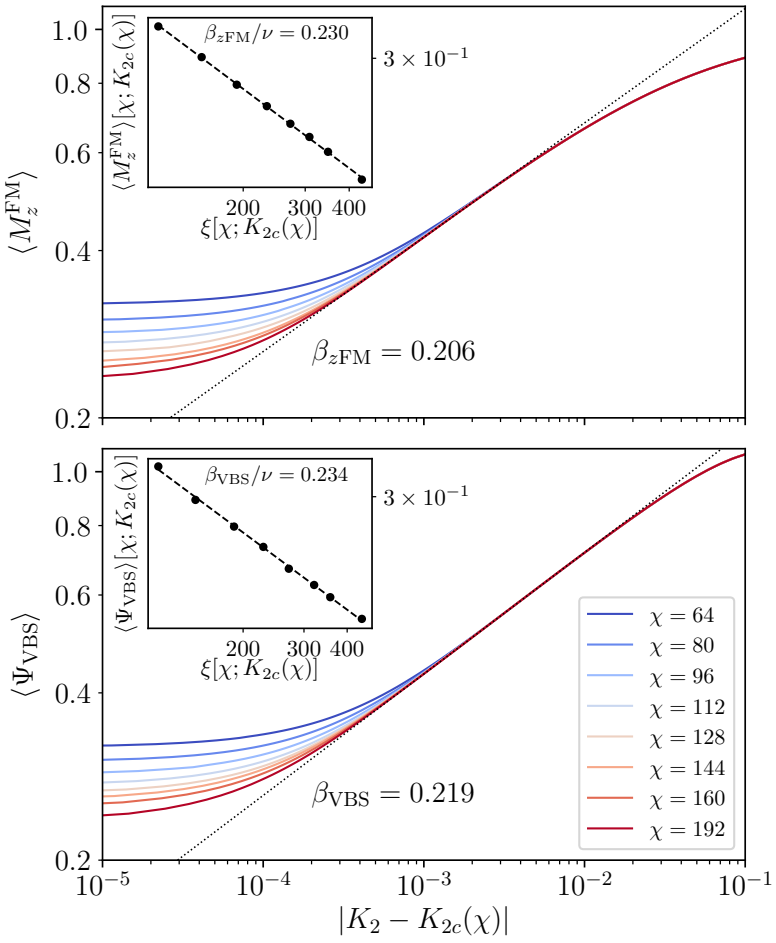

Figure 4.7: Expectation values of the zFM and VBS order parameters on the slice $\delta = 0.5$ show a region of power-law dependence in an intermediate range near the critical point which extends closer to the transition with increasing bond dimension. Far from the critical point, the order parameters approach their maximal values, whereas very close to $K_{2c}(\chi)$ at fixed χ, they saturate due to the discontinuous mean-field description of the transition. The top panel shows K_2 in the zFM phase, and the bottom panel K_2 in the VBS phase; in both panels, we give K_2 relative to the pseudocritical $K_{2c}(\chi)$ determined for each bond dimension as in Fig. 4.5. The dashed line in each panel shows the fitted power-law onset form with exponent $\beta_{z\mathrm{FM}}$ or β_{VBS} in this intermediate range, using the largest bond dimension data, which is essentially already converged to the infinite-χ values. Insets show the limiting values of the corresponding order parameters at $K_{2c}(\chi)$ as a function of the limiting $\xi[\chi, K_{2c}(\chi)]$, and a power law fit to Eq. (4.20). Note that inset axes use logarithmic scaling.

the MPS correlation length is independent of χ, and the power-law behavior of this quantity is indicative of the true critical exponent. By comparing data for different χ, we can visually determine where $\xi(\chi)$ is already sufficiently converged to the infinite-χ limit, and use only this region. The extracted correlation length exponents on both sides of the transition are given in Fig. 4.6. Note that the convergence of the correlation length with bond dimension is relatively gradual, thus we find a somewhat limited dynamical range of converged data $\xi(\chi \to \infty)$, presumably causing the differing values of ν on the two sides of the transition. In addition, it is particularly evident on the VBS side that the correlation length is affected by proximity to the second-order transition to the xUUDD phase. For this reason we will not use the values of ν extracted from this method in the following discussion, but rather rely on another way of determining the exponent, described below and in Fig. 4.7.

At fixed χ, the MPS correlation length $\xi(\chi)$ saturates near the pseudocritical point $K_{2c}(\chi)$. The extrapolated values from either side of the transition, denoted $\xi[\chi; K_{2c}(\chi)]$, are plotted vs χ in the insets in the corresponding panels. Fitting to (4.17) gives similar estimates of κ from both sides which are in rough agreement with $\kappa \approx 1.344$ expected for $c = 1$.

Considering now the order parameters, in Fig. 4.7 we show $\langle M_z^{\mathrm{FM}} \rangle$ (top panel) and $\langle \Psi_{\mathrm{VBS}} \rangle$ (bottom panel) as a function of $|K_2 - K_{2c}(\chi)|$, each within its ordered phase. In the main plot in each, we extract the corresponding order parameter exponent over the range where we see convergence to the $\chi \to \infty$ limit. We appear to have wider dynamical ranges for the power law fitting here compared to the correlation length data in Fig. 4.3. The extracted order parameter exponents are roughly equal for the two order parameters, supporting one of the key predictions of the theory of the 1d DQCP.

As the order parameter scaling behavior appears to be relatively more robust compared to that of the MPS correlation length, we can try to determine the critical exponent ν via the finite-entanglement scaling of the order parameters. Specifically, we again appeal to analogy to finite-size scaling in statistical mechanics, where in a system of length L an order parameter m remains finite at a critical (or pseudocritical) point and scales to zero as $L^{-\beta/\nu}$. We conjecture that in our infinite-system MPS setup, where the bond dimension sets the cutoff length $\xi(\chi)$, the discontinuity in the order parameters at the pseudocritical

point scales as

$$m_{\text{jump}} \sim \xi(\chi)^{-\beta/\nu} \sim \chi^{-\kappa\beta/\nu} \ . \tag{4.20}$$

The last expression gives the predicted scaling with bond dimension, but we will focus on m_{jump} vs $\xi(\chi)$ which is independent of exponent κ. For both the zFM and VBS order parameters, the value in the optimized MPS is strictly zero on one side and non-zero on the other side of the pseudocritical point $K_{2c}(\chi)$. Hence we obtain m_{jump} by fitting and extrapolation of the corresponding order parameter curves $\langle M_z^{\text{FM}}\rangle[\chi; K_2]$ or $\langle \Psi_{\text{VBS}}\rangle[\chi; K_2]$ from their respective ordered sides to the pseudocritical point determined earlier. Insets in both panels in Fig. 4.7 show the corresponding m_{jump} versus similarly obtained limiting correlation lengths at the pseudocritical points for the values of χ used in the main panels, and also show fits to the scaling form Eq. (4.20).

The extracted values of β/ν are fairly close for both order parameters, in agreement with the DQCP theory prediction that $\beta_{z\text{FM}} = \beta_{\text{VBS}}$. These are also roughly consistent with the estimates of β in the main panels in Fig. 4.7 and ν in Fig. 4.6 made from regions where the data is converged nearest to the $\chi \to \infty$ limit, although as discussed earlier, these estimates of ν are not very accurate. Since the extracted values of β from the order parameter scaling appear to be more accurate than the extracted values of ν from the correlation length scaling, we can use the estimates of β and β/ν to provide a more accurate estimate of $\nu \approx 0.914 \pm 0.035$.

Power law decay of correlations

We also measure correlation functions in our MPS in order to establish bounds on the critical decay of the important correlators in the theory introduced in Sec. 4.2.2. These are $p_{z\text{FM}}$ for $\langle M_z^{\text{FM}} M_z^{\text{FM}}\rangle$ and p_{VBS} for $\langle \Psi_{\text{VBS}} \Psi_{\text{VBS}}\rangle$, in addition to exponents $p_{x\text{FM}}$ and $p_{y\text{AFM}}$ for $\langle M_x^{\text{FM}} M_x^{\text{FM}}\rangle$ and $\langle M_y^{\text{AFM}} M_y^{\text{AFM}}\rangle$. Note that the latter two correlators decay exponentially both in the zFM and VBS phases and only at the critical point show slower power law decay. Examples of the correlation functions at criticality for our representative cut at $\delta = 0.5$ and the resulting bounds on the exponents are given in Fig. 4.8.

The top panel shows the correlations at the pseudocritical point $K_{2c}(\chi)$, measured in the zFM ansatz using our largest bond dimension $\chi = 192$. More precisely, we measure the correlations by using the adiabatic process described previously, beginning with a state well within each phase and tuning the Hamil-

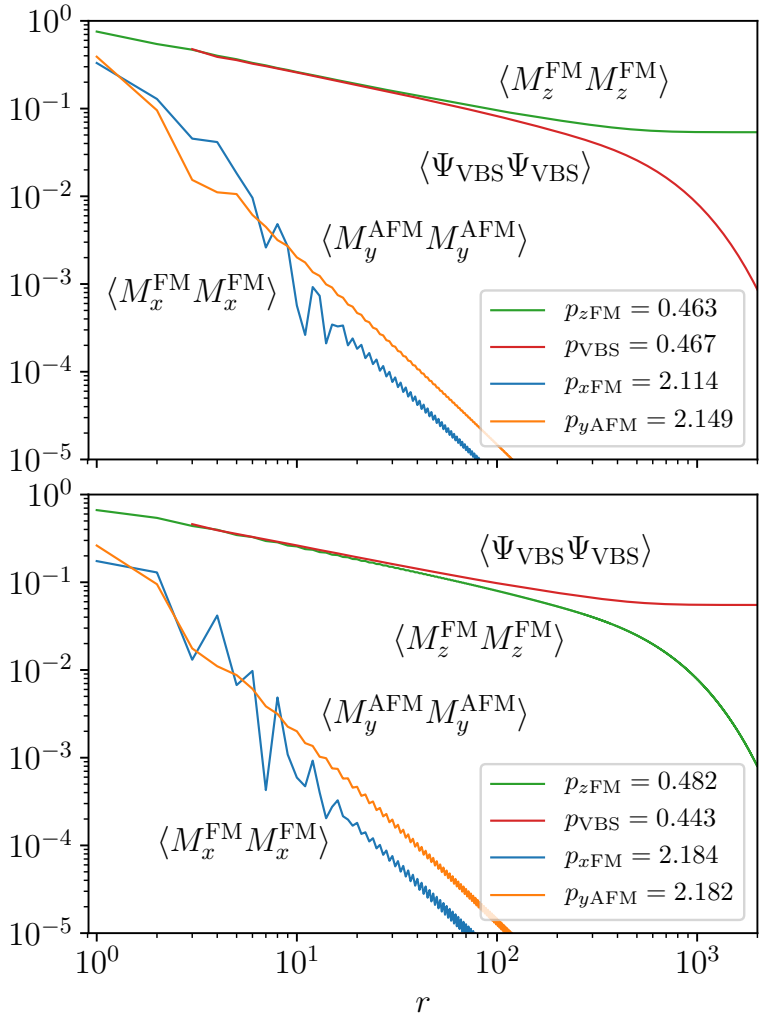

Figure 4.8: Top panel shows measurements of important correlation functions (for example, $\langle M_z^{\mathrm{FM}} M_z^{\mathrm{FM}} \rangle \sim \langle \sigma_0^z \sigma_r^z \rangle$) in the zFM ansatz state tuned to the pseudocritical point $K_{2c}(\chi = 192)$. This data is taken at $\delta = 0.5$. All correlators show a region of critical power-law behavior before reaching a constant or decaying exponentially, as they eventually must in a finitely entangled state. The correlation length in this state is ~ 425. The bottom plot shows the same correlation functions, but measured in the VBS ansatz MPS tuned to the pseudocritical point.

tonian up to a very small distance $\lesssim 10^{-6}$ away from the estimated $K_{2c}(\chi)$. In this case, the M_z^{FM} correlations eventually saturate to a finite value while the Ψ_{VBS} correlations eventually decay exponentially (the latter is also true of the M_x^{FM} and M_y^{AFM} correlators). The bottom panel shows similar measurements coming from the VBS side, where it is now the M_z^{FM} correlations that eventually decay exponentially while the Ψ_{VBS} correlations eventually saturate.

However, in both panels, there is a large window $r < \xi(\chi)$ where all correlators show power law decay, and we list the extracted power law exponents in each case.

Notably, we can tell even visually that the critical M_z^{FM} correlations and Ψ_{VBS} correlations have very similar power laws, and the extracted numerical values of the exponents confirm this. For these correlators, it is natural to take the values of the exponents extracted from the two sides as bounds on the true critical exponent; these are already fairly close, and thus provide informative bounds. We also note that we can tell visually that the critical M_x^{FM} and M_y^{AFM} correlations have very close power laws; for each quantity, the extracted exponents from both sides are very close, and are also close between the two observables.

4.3.2 Continuously varying critical exponents

We repeat the analysis presented above in Sec. 4.3.1 for multiple cuts along fixed δ which exhibit a direct zFM to VBS phase transition. We conclude that this transition exists for all $\delta \leq 0.7$, with a tricritical point lying within $\delta = (0.7, 0.8)$ where the transition branches, allowing an intervening phase. We discuss this region in Sec. 4.4.

Our findings for all critical exponents are summarized in Table 4.1. We first observe that they vary continuously with δ, a general trend which is in agreement with the description of the field theory in Sec. 4.2.2. Additionally, we have several specific predictions of nontrivial relationships between critical exponents which apply to any point on the phase boundary. We test these on our cuts of constant δ, finding good agreement in all cases between the predictions and observations.

Because the critical exponents in the field theory are functions of a single variable—the Luttinger parameter $\tilde{g}$, which varies along the critical line—they can be readily manipulated to obtain relationships between measurable quantities. For example, we have the basic predictions that $p_{z\mathrm{FM}} = p_{\mathrm{VBS}}$ and $p_{x\mathrm{FM}} = p_{y\mathrm{AFM}}$, as well as the relationship

$$p_{z\mathrm{FM}}\, p_{x\mathrm{FM}} = p_{z\mathrm{FM}}\, p_{y\mathrm{AFM}} = 1 \ . \tag{4.21}$$

We find that the data are generally in good agreement with these conditions, as shown in Fig. 4.9, with some deviations for the largest δ. In this regime, the

δ	K_{2c}	$\beta_{z\mathrm{FM}}$	$\beta_{z\mathrm{FM}}/\nu$	β_{VBS}	β_{VBS}/ν	ν	$p_{z\mathrm{FM}}$	p_{VBS}	$p_{x\mathrm{FM}}$	$p_{y\mathrm{AFM}}$
0.1	0.36674	0.653	0.391	0.773	0.388	1.831 ± 0.161	0.759	0.777–0.779	1.290	1.289
0.2	0.41087	0.452	0.279	0.501	0.361	1.503 ± 0.115	0.669–0.674	0.676–0.680	1.485	1.485
0.3	0.45630	0.345	0.295	0.374	0.301	1.205 ± 0.035	0.598–0.605	0.593–0.602	1.70	1.71
0.4	0.502630	0.269	0.265	0.282	0.263	1.045 ± 0.029	0.531–0.540	0.519–0.533	1.87	1.89
0.5	0.549729	0.206	0.234	0.219	0.230	0.916 ± 0.034	0.463–0.482	0.443–0.467	2.15	2.17
0.6	0.597341	0.156	0.200	0.167	0.200	0.808 ± 0.027	0.389–0.422	0.364–0.403	2.44	2.54
0.7	0.644979	0.113	0.163	0.126	0.163	0.733 ± 0.040	0.305–0.369	0.287–0.347	3.08	3.15

Table 4.1: Extracted critical points and exponents on slices of fixed δ exhibiting a direct phase transition between zFM and VBS. Quoted values for β are extracted from near-critical scaling of the $\chi \to \infty$ converged order parameters, while values for β/ν are obtained from the finite-entanglement scaling of the order parameters at the precise pseudocritical points, measuring in both zFM and VBS ansatz states; from these, we obtain the quoted bounds on ν. Similarly, the bounds on $p_{z\mathrm{FM}}$ and p_{VBS} are determined from measurements made in each ansatz state tuned to the pseudocritical point.

correlations feel the influence of the many other nearby critical lines, including the transitions described below which continue after the zFM to VBS critical line terminates. From the power law decay exponents, we can also easily read off the Luttinger parameter: in particular, $p = \tilde{g}/2$ for the (dominant) correlations of the order parameters. From this, we see that $\tilde{g}$ varies inside the expected range $(1/2, 2)$.

From general scaling behavior we have the relationship $\beta/\nu = p/2$ for the zFM and VBS order parameters. We measure both β/ν and p directly in our MPS wavefunctions, and referring to Table 4.1 one observes that this relationship indeed holds fairly accurately. We also have the following nontrivial prediction from the field theory:

$$2\nu(1-p) = 2\nu(1-2\beta/\nu) = 1 \ , \tag{4.22}$$

where β and p apply to the zFM or VBS order parameters. We examine this prediction in Fig. 4.10, finding good agreement of the measurements with the predicted value for large $\delta > 0.3$. However, the data at low δ exhibit some deviations from the expected behavior. This arises from inaccuracy in our estimates of the critical exponents ν and β, which rely on convergence to the infinite-χ limit in a region near enough to the critical point to find a power-law exponent. For low δ, the state is near the quasi–long range ordered phase at $\delta = 0$ and contains a high degree of entanglement; hence, our finite-entanglement scaling is comparatively less accurate.

Despite the influence of various other nearby phases and phase transitions on our results, we have observed several nontrivial predictions from the field theory in our measurements of the continuously varying critical exponents along the zFM to VBS phase boundary. This constitutes further strong evidence that this critical line is indeed an example of the DQCP described in Sec. 4.2.2.

4.4 Study of order parameter coexistence

4.4.1 Evidence for coexistence regime

Returning to the action functional in Eq. (4.6), one expects the destabilization of the zFM to VBS transition due to the emergence of a second relevant cosine at a critical value of the Luttinger parameter $\tilde{g}^* = 1/2$. Here the phase transition is predicted to branch into two distinct critical lines, introducing an intermediate region where both g_x and T_1 are broken, leading to coexistence of both order parameters. It is not easy to relate $\tilde{g}$ to the microscopic parameters,

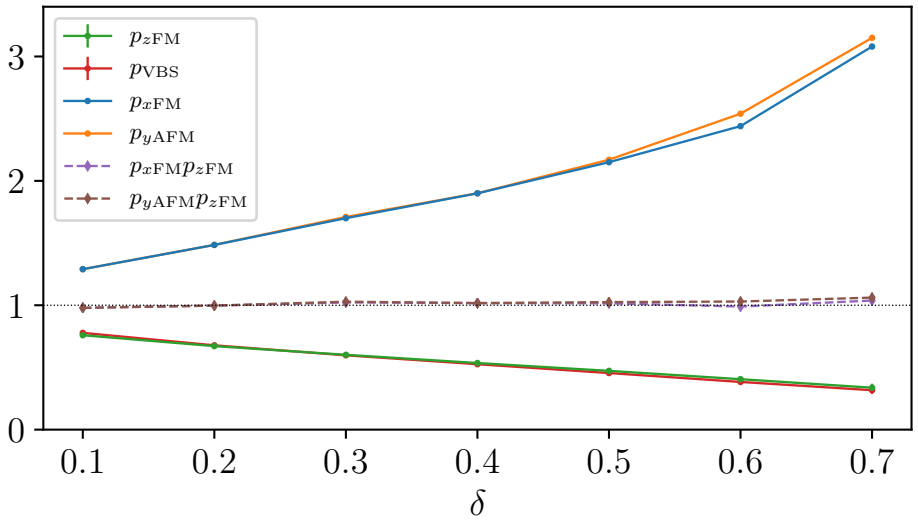

Figure 4.9: The measured power law decay exponents are in good agreement with the predicted behavior $p_{z\mathrm{FM}} = p_{\mathrm{VBS}}$ and $p_{x\mathrm{FM}} = p_{y\mathrm{AFM}}$, as well as with Eq. (4.21). At the larger values of δ, the state begins to feel the tricritical point, which affects the more quickly decaying M_x^{FM} and M_y^{AFM} correlation functions.

but we can read off the values of the critical exponents very close to this tricritical point, finding $\nu^* = 2/3$, $p^*_{z\mathrm{FM}} = p^*_{\mathrm{VBS}} = 1/4$, $\beta^*_{z\mathrm{FM}} = \beta^*_{\mathrm{VBS}} = 1/12$, and $p^*_{x\mathrm{FM}} = p^*_{y\mathrm{AFM}} = 4$.

We observe the branching of the phase transition at some value $\delta \in (0.7, 0.8)$, which is consistent with the description of the critical exponents given above. The appearance of the intermediate phase is illustrated in Fig. 4.11 for the slice $\delta = 0.9$, where the state acquires VBS order on top of the zFM order at $K_{2c,\mathrm{VBS}}(\chi = 144) = 0.73691$ and the zFM order vanishes at $K_{2c,z\mathrm{FM}}(\chi = 144) = 0.73738$. These phase transitions are not described by the DQCP theory; rather, because in each case a single $\mathbb{Z}_2$ symmetry is broken, we expect the critical points to be in the Ising universality. We explore mean field pictures of the phases in Apps. 4.A.2 and 4.B.1, finding support for this expectation.

The analysis of the boundary of the coexistence region does not follow straightforwardly from the protocol used in Sec. 4.3.1. Because the mean field theory of these transitions is not discontinuous, we cannot exploit the level crossings of MPS trial states to accurately determine the locations of the critical points. Similarly, we are unable to use the finite values of the order parameters at the pseudocritical points to determine critical exponents, as we do for the direct

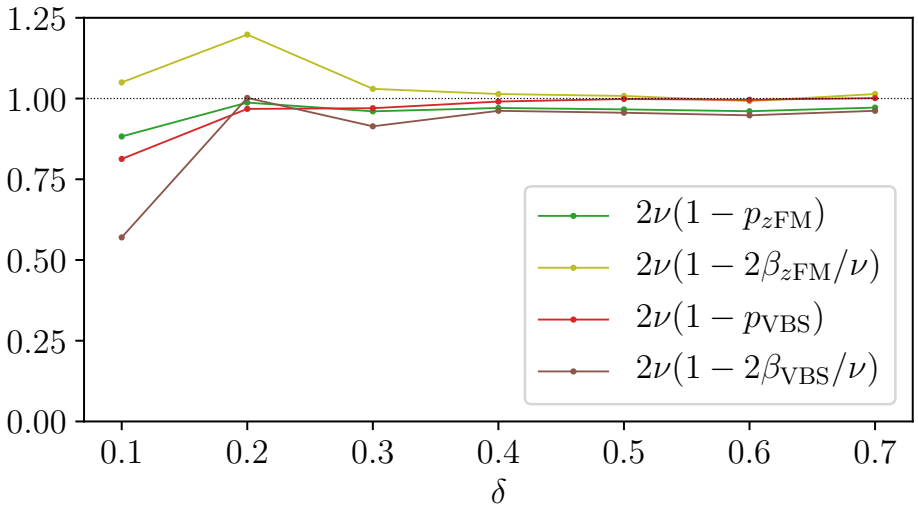

Figure 4.10: We find good agreement with Eq. (4.22), particularly for the larger values of δ on the critical line. The states at small δ are near to the $\delta = 0$ QLRO phase and thus are relatively highly entangled, which makes it difficult to reach the limit $\chi \to \infty$ near enough to the critical point to extract the ν and β critical exponents.

zFM to VBS phase transition. In addition, as the coexistence region is very narrow and located fairly close to the xUUDD phase, we do not have access to a very large dynamical range. Instead, we identify the pseudocritical points by using a power-law fit to the vanishing of the order parameters. Also, we are able to obtain only rough estimates of the critical exponents.

We list our estimates of the transition points for $\delta = 0.8, \ldots, 1.0$ in Table 4.2. Note that the $\delta > 1$ regime can be related to $\delta < 1$ by the map described in Sec. 4.2.3 (which related the VBS-I and VBS-II phases), so numerical studies are required only for $\delta \leq 1$. Also, while for $\delta \neq 1$ the zFM-ordering transition $K_{2c,z\mathrm{FM}}$ involves a strictly VBS ordered phase, for $\delta = 1$ the situation is more complex and the coexistence phase actually transitions to the xUUDD phase. (See the inset in Fig. 4.1 for an image of the coexistence region.) We first focus on $\delta < 1$ and consider the $\delta = 1$ case later.

Figure 4.11 shows the correlation length and expectation values of the order parameters in the coexistence region. We observe cusps in the correlation length at both transitions, with height which increases with increasing χ. However, our data are not of sufficient granularity to perform definitive finite-entanglement scaling at these critical points, and we do not have suffi-

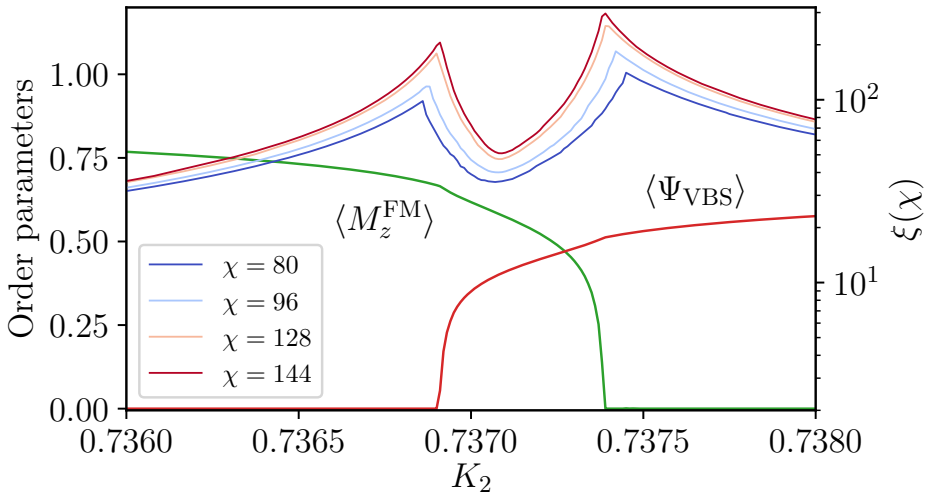

Figure 4.11: The slice at $\delta = 0.9$ clearly exhibits a region of coexistence of order parameters (measurements shown use the bond dimension $\chi = 144$ MPS), and the correlation length displays χ-dependent cusps at both boundaries. However, we do not have good χ-converged properties inside of this phase, as the correlation length does not saturate for the bond dimensions shown here.

cient dynamical range between the two critical points to extract the correlation length exponent at either transition. On the VBS side, we are also close to the xUUDD phase boundary. We can attempt to find ν looking at the pure zFM side; however, the width of the crossover region where the correlation length saturates in χ is significantly wider than the distance between $K_{2c,\mathrm{VBS}}$ and $K_{2c,z\mathrm{FM}}$. In this case, the extracted ν likely does not cleanly correspond to just one transition but instead combines information about all nearby phase transitions and even the tricritical point. Thus, in the top panels of Figs. 4.13 and 4.14, we focus only on the data from the coexistence region, with the understanding that they will hardly be conclusive. The extracted values of κ are quite far from the expectation for this $c = 1/2$ critical point. In the bottom panels of these figures, we have attempted to extract the order parameter onset exponents at each critical point. By the same argument, we clearly should restrict attempts at fitting power-law onset forms to be within the coexistence region. However, we see that the apparent slopes continue to vary visibly for our range of bond dimensions χ. In particular, these measurements are likely to be influenced by some mixture of the actual Ising criticality as well as the mean-field phase transition in the MPS at the pseudocritical point, and indeed we find values for the critical exponents that lie between these two.

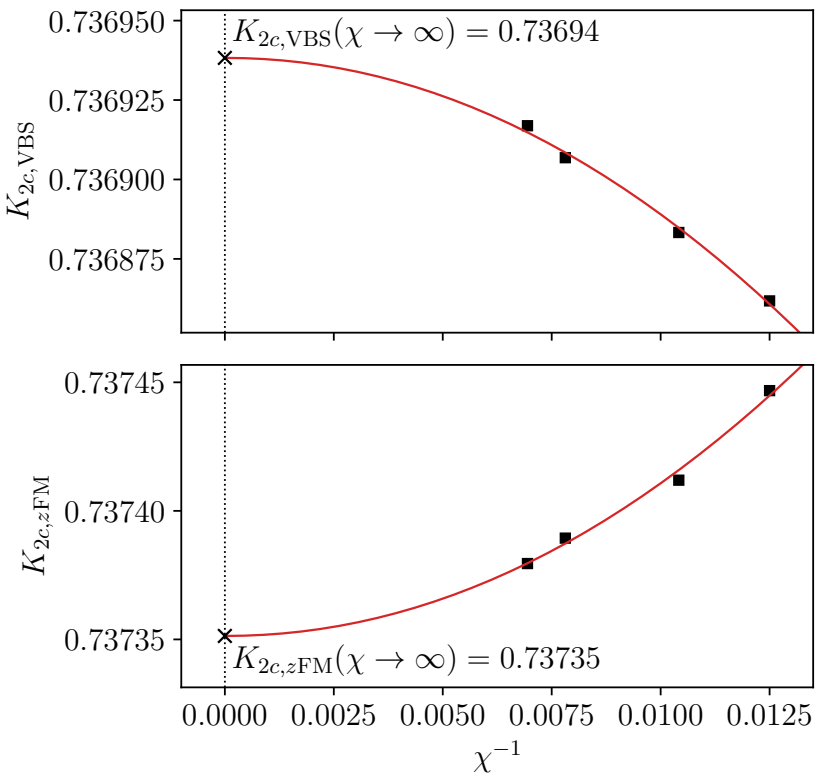

Figure 4.12: Illustration of the process of locating the critical point for each order parameter from finite-entanglement scaling in the coexistence regime at $\delta = 0.9$. Here the data points are found via fits to the power law onset behavior shown in Fig. 4.11. Again, using the finite-entanglement scaling form Eq. (4.19), we extrapolate from pseudocritical $K_{2c,\mathrm{VBS}}(\chi)$ and $K_{2c,z\mathrm{FM}}(\chi)$ to estimate the width of the coexistence region in the limit $\chi \to \infty$.

Table 4.2 summarizes our estimates of the critical indices for the transitions on the slices $\delta = 0.9$ and 0.95. These are rather inaccurate, as explained above, and are shown to emphasize our limitations when studying the transitions involving the coexistence phase. We also quote estimates of the power law correlation decay exponents extracted from fits at the corresponding pseudo-critical points for our largest $\chi = 144$. These estimates also differ somewhat from the exponent $p = 1/4$ expected at each Ising transition, but the accuracy may be a bit better than for the extracted ν and β values.

4.4.2 Higher-symmetry line at $\delta = 1$

The line $\delta = 1$ admits an additional symmetry of the Hamiltonian:

$$g_{z,\mathrm{even}} = \prod_m \sigma^z_{2m} \quad : \quad \sigma^z_{2m} \mapsto \sigma^z_{2m},\ \sigma^{x,y}_{2m} \mapsto -\sigma^{x,y}_{2m}\ . \tag{4.23}$$

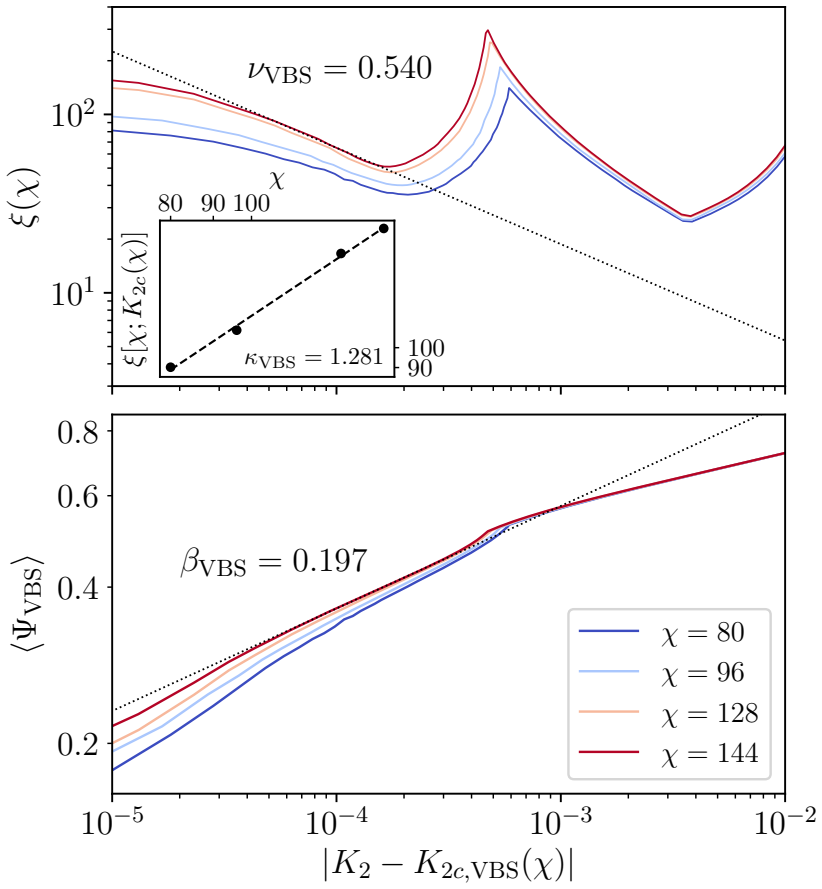

Figure 4.13: Our study of the VBS ordering transition in the coexistence region is impeded by the narrow width of the phase, here shown at $\delta = 0.9$. The top panel shows correlation length along with our best fit, though the MPS results are not reflective of the $\chi \to \infty$ limit and the exponent is far from the Ising $\nu = 1$. The feature seen near 3×10^{-4} on the x-axis is the zFM order transition on the boundary of the coexistence region with the VBS-I phase (this transition is studied in Fig. 4.14). Further from the critical point, one sees the effect of the transition to the xUUDD phase. The bottom panel shows the onset of the VBS order parameter, which is roughly consistent with a continuous phase transition but does not agree with the Ising $\beta = 1/8$. Data here do not use the adiabatic protocol; every point is independent.

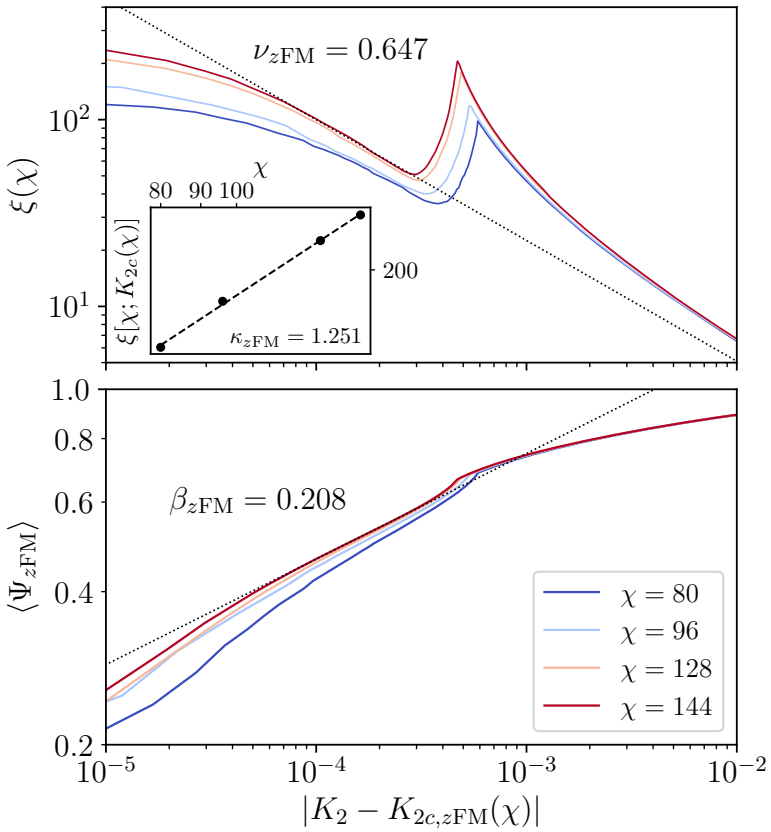

Figure 4.14: Similarly to Fig. 4.13, we provide only a rough study of the zFM ordering transition in the coexistence region, here shown at $\delta = 0.9$. The top panel shows correlation length along with our best fit, though the MPS results are not reflective of the $\chi \to \infty$ limit and the exponent is far from the Ising $\nu = 1$. The feature seen near 3×10^{-4} on the x-axis is the VBS order transition on the boundary of the coexistence region with the zFM phase (this transition is studied in Fig. 4.13). The bottom panel shows the onset of the zFM order parameter, which is roughly consistent with a continuous phase transition but does not agree with the Ising $\beta = 1/8$. Data here do not use the adiabatic protocol; every point is independent.

This is the same symmetry which takes VBS-I to VBS-II, and vice versa. As we stated previously, one possibility for these two phases along this cut is a first-order transition, but this turns out not to be the case in our model. Instead, inside of the coexistence region where g_x is broken the VBS-I and VBS-II orders are in fact the same. This was pointed out in Ref. [1], and we provide a demonstration in Apps. 4.A.2 and 4.B.1 by writing fixed-point wavefunctions for the coexistence which smoothly interpolate between VBS-I and VBS-II in the presence of g_x symmetry breaking. The onset of the VBS

δ	$K_{2c,\mathrm{VBS}}$	ν_{VBS}	β_{VBS}	p_{VBS}	$K_{2c,z\mathrm{FM}}$	$\nu_{z\mathrm{FM}}$	$\beta_{z\mathrm{FM}}$	$p_{z\mathrm{FM}}$
0.8	0.691922	·	·	0.29	0.691927	·	·	0.30
0.85	0.71481	·	·	0.30	0.71486	·	·	0.28
0.9	0.73693	0.54	0.20	0.33	0.73735	0.65	0.21	0.26
0.95	0.75798	0.63	0.19	0.40	0.75936	0.68	0.20	0.28

Table 4.2: Critical properties at the VBS ordering transition $K_{2c,\mathrm{VBS}}$ between the zFM and coexistence phases, and at the zFM ordering transition $K_{2c,z\mathrm{FM}}$, between the VBS and coexistence phases. All data is measured within the coexistence region, in order to reduce the effects of other nearby criticalities. The transition is too narrow for $\delta < 0.9$ to allow for the determination of the correlation length and order parameter onset critical exponents.

order—the boundary between the zFM and coexistence phases—is thus no different from the case for other δ.

On the other hand, at the zFM ordering transition (that is, the transition out of the coexistence phase at which the zFM order disappears), the g_x symmetry is restored. Here we find a transition not to a state with pure VBS character, but rather to the xUUDD phase. Because the phases on either side break different $\mathbb{Z}_2$ symmetries yet we observe a direct phase transition, this criticality in fact bears a resemblance to the zFM to VBS DQCP studied in the preceding sections. (Here the direct transition between the coexistence and xUUDD phases is enforced by the additional $\mathbb{Z}_2$ symmetry $g_{z,\mathrm{even}}$ which apparently remains unbroken in our model.) In fact, in Sec. 4.C we develop a theory of this transition which turns out to be similar to the critical line at $\delta = 0$ separating the zFM and xFM phases but placed on top of a translation symmetry–breaking background.

We are able to study this transition using the methods of Sec. 4.3, where now instead of the VBS order parameter Ψ_{VBS} (which remains ordered throughout the transition) we measure

$$\langle M_x^{\mathrm{UUDD}} \rangle = \langle \sigma_0^x \rangle \ , \tag{4.24}$$

where, as was the case for the previous order parameters, there is a sign ambiguity which we ignore. In a more precise sense, the order parameter in the xUUDD phase has two Ising-like components, $\left(\sum_j (-1)^{j(j-1)/2} \sigma_j^x, \ \sum_j (-1)^{j(j+1)/2} \sigma_j^x \right)$, where in each case j runs over the unit cell. However, because the MPS ground state always has spontaneously broken symmetry—that is, the "UUDD" pattern or its partners related by translation—it suffices to confirm this pattern

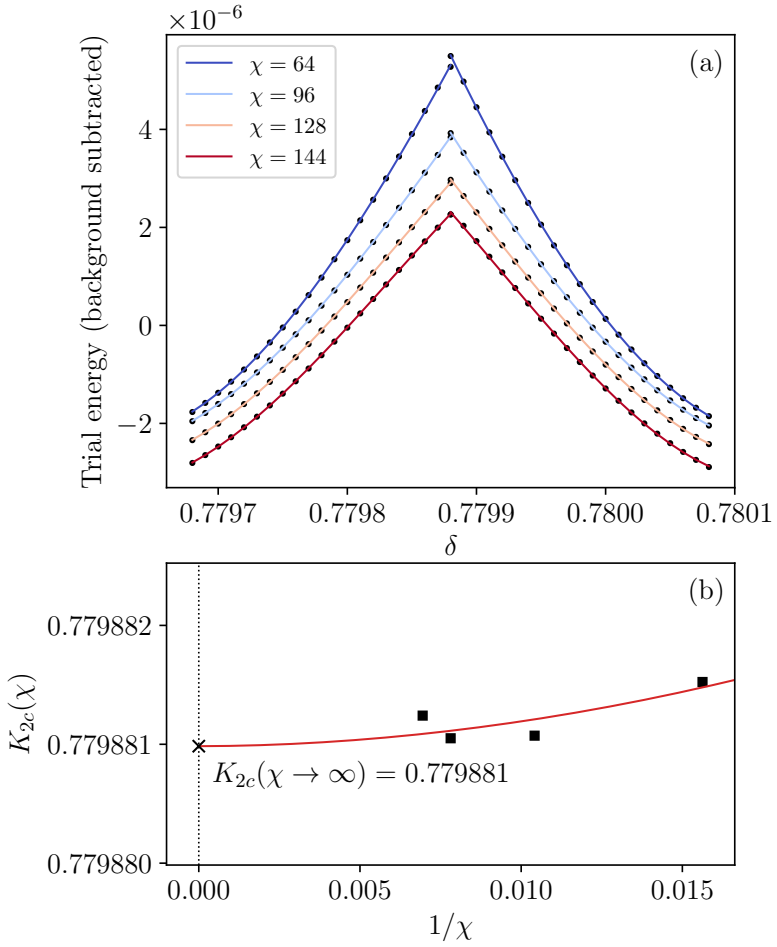

Figure 4.15: Illustration of determining the critical point between zFM+VBS coexistence and xUUDD from finite-entanglement scaling at $\delta = 1$, performed using the same procedure used in Fig. 4.5. (a) The energies of both the coexistence and xUUDD phases follow smooth curves which determine the level crossing, but here happen to not display hysteresis. This does not present a problem, as the smoothness of the evolution of the trial state energies permits extrapolation. (b) Using a fit to the finite-entanglement scaling form Eq. (4.19), we extrapolate the pseudocritical $K_{2c,\mathrm{zFM}}(\chi)$ to estimate the location of the critical point at $\chi \to \infty$. As was the case for the DQCP, the scatter in data points is again not noise from the variational algorithm, but a reproducible feature of the ground state at each bond dimension.

and measure just $\langle \sigma_0^x \rangle$. Because of the relatively slow convergence in ξ exhibited by the correlation length in Sec. 4.3.1 as well as the limited dynamical range within the coexistence region, we focus only on measurements of the order parameter in the xUUDD phase to characterize this transition. This study is shown in Fig. 4.16, where we find that $\beta_{x\mathrm{UUDD}} = 0.117$ and $\nu = 0.69$. We

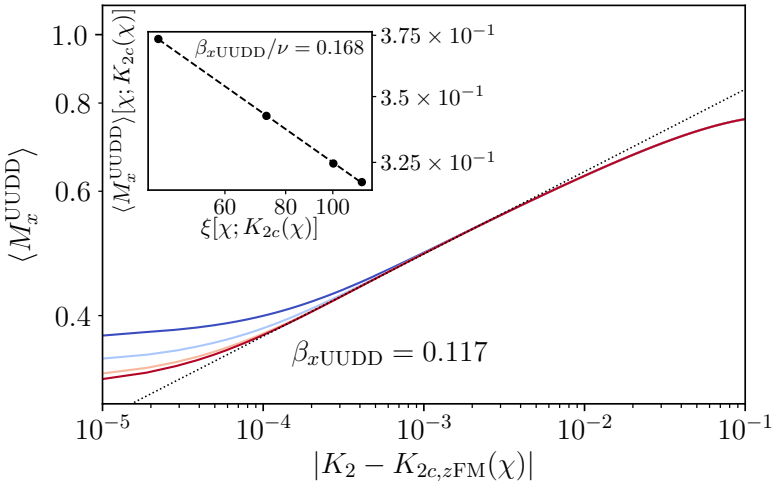

Figure 4.16: Analysis of the phase transition from the zFM+VBS coexistence phase to the xUUDD phase along the cut $\delta = 1$, using the discontinuous VUMPS (generalized mean field) procedure. Because we cannot make an accurate determination of $\beta_{z\mathrm{FM}}$ using measurements arising from inside the coexistence phase, we consider only measurements of M_x^{UUDD}, within the xUUDD phase. However we can perform finite-entanglement scaling analysis of M_z^{FM} extrapolated to the pseudocritical points. Doing so, we find a value $\beta_{z\mathrm{FM}}/\nu = 0.167$ which is quite similar to $\beta_{x\mathrm{UUDD}}/\nu$ shown in the inset.

also find from measurement of the power-law decaying correlation functions that $p_{x\mathrm{FM}} \approx 0.39$ and $p_{z\mathrm{FM}} \approx 0.37$. These values provide some point of reference relative to the other phase transitions studied in this work but are not significant by themselves, as this critical point lies on a line exhibiting continuously varying exponents. Because this line crosses our phase diagram plane only at one point, in the present study we cannot observe continuously varying exponents but we do check that the expected relationships are approximately satisfied: $p_{x\mathrm{FM}} \approx p_{z\mathrm{FM}}$ and $2\nu(1 - p_{x\mathrm{FM}}) \approx 0.86$ (compared to the expected value 1).

4.5 Summary of results

We performed a detailed numerical study of the ferromagnet to VBS transition in a spin-1/2 chain with $\mathbb{Z}_2 \times \mathbb{Z}_2$ symmetry and confirmed key predictions of the 1d DQCP theory of Ref. [1]. Namely, the zFM and VBS order parameters have equal scaling dimensions, and the xFM and yAFM correlations of secondary importance also have equal power law exponents at the zFM to VBS-I transition (the fact that the next-most important observables are the

ferromagnetic component of σ^x and the antiferromagnetic component of σ^y is related to the crystalline SPT–like property of the VBS-I phase that distinguishes it from the VBS-II phase, which is also realized in our model). All exponents vary continuously along the phase boundary but are controlled by a single parameter; this implies relationships among the various exponents, which we confirmed in our numerics. The observed range of the variation of the critical indices is consistent with the regime of validity of the proposed field theory, and we also found the predicted splitting of the transition and appearance of the VBS+zFM coexistence phase at one end of this range. Interestingly, we also found an instance of a new Landau-forbidden transition between the VBS+zFM and xUUDD phases along the line $\delta = 1$ with the additional $\mathbb{Z}_2$ symmetry $g_{z,\text{even}}$.

In our study of the 1d DQCP, we found that VUMPS at fixed bond dimension shows a discontinuous transition at a χ-dependent pseudocritical point, and argued that this is related to the non-Landau nature of the transition which gives first-order behavior in the mean field. We used this discontinuous nature to our advantage to find the pseudocritical points very accurately and for subsequent "finite-entanglement" scaling. We propose that this protocol can be very useful at all transitions described by DQCP, and indeed we have already used it at the new direct continuous VBS+zFM to xUUDD transition enforced by the additional $g_{z,\text{even}}$ symmetry. To accurately locate pseudocritical points is more difficult at conventional continuous transitions where the mean field is also continuous [17], but it can be a powerful systematic approach in such cases as well.

4.A Mean-field study of phase diagram with separable states

In this appendix, we present caricature ("fixed-point") wavefunctions for the phases of interest in our model and use these as simple trial states to find a mean-field phase diagram of the model. Besides developing basic intuition about the phases and their competing energetics, we demonstrate that in the mean field treatment the zFM to VBS transition is first-order, while the VBS to zFM+VBS and also the VBS to xUUDD transitions are second-order. This provides some understanding of the observed "pseudocritical" behavior of VUMPS at fixed bond dimension χ, i.e., behavior very close to $K_{2c}(\chi)$.

4.A.1 Trial states without variational parameters

The zFM fixed-point state is simply

$$|z\mathrm{FM}\rangle = \otimes_j |\uparrow\rangle_j \tag{4.25}$$

or its counterpart $g_x|z\mathrm{FM}\rangle$, with average energy per site

$$\epsilon_{z\mathrm{FM}} = -J_z + K_{2z} = -(1+\delta) + K_2 \ . \tag{4.26}$$

In the right-hand side above, as well as in other trial energy expressions below, we specialize to the slice in the parameter space used in the main text, namely $J_z = 1+\delta$, $J_x = 1-\delta$, $K_{2z} = K_{2x} = K_2$. Note that this wavefunction is an exact ground state at $\delta = 1$, $K_2 = 0$.

The VBS-I fixed-point state is

$$|\text{VBS-I}\rangle = \otimes_m |D^{(I)}_{2m-1,2m}\rangle \tag{4.27}$$

or its counterpart $T_1|\text{VBS-I}\rangle$, where the elementary dimer state of two spins is given in Eq. (4.5). The average energy per site is

$$\epsilon_{\text{VBS-I}} = -(J_z + J_x)/2 = -1 \ . \tag{4.28}$$

This wavefunction is an exact ground state at the Majumdar–Ghosh point $\delta = 0$, $K_2 = 0.5$ [8–11].

The VBS-II fixed point state is

$$|\text{VBS-II}\rangle = \otimes_m |D^{(II)}_{2m-1,2m}\rangle \tag{4.29}$$

or its counterpart $T_1|\text{VBS-II}\rangle$, where the corresponding dimer state of two spins is given in Eq. (4.12). The average energy per site is

$$\epsilon_{\text{VBS-II}} = -(J_z - J_x)/2 = -\delta \ . \tag{4.30}$$

This wavefunction becomes an exact ground state for $\delta \to \infty$, $K_2/\delta = 0.5$.

The xUUDD fixed-point state is

$$|x\mathrm{UUDD}\rangle = \otimes_n |+\hat{x}\rangle_{4n-3} |+\hat{x}\rangle_{4n-2} |-\hat{x}\rangle_{4n-1} |-\hat{x}\rangle_{4n} \tag{4.31}$$

along with its symmetry counterparts $T_1|x\mathrm{UUDD}\rangle$, $(T_1)^2|x\mathrm{UUDD}\rangle = g_z|x\mathrm{UUDD}\rangle$, $(T_1)^3|x\mathrm{UUDD}\rangle$. The average energy per site is

$$\epsilon_{x\mathrm{UUDD}} = -K_{2x} = -K_2 \ . \tag{4.32}$$

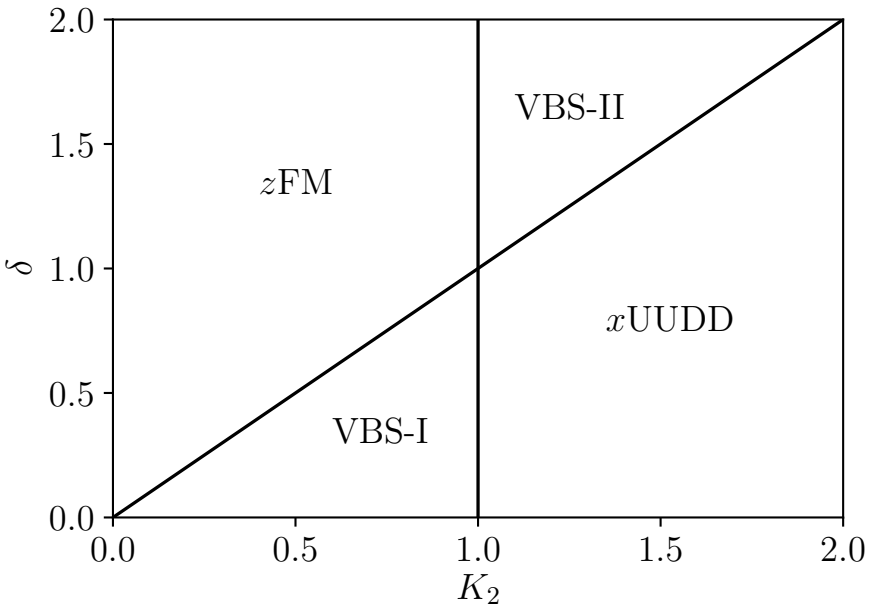

Figure 4.17: Comparing the energies of the separable trial wavefunctions of App. 4.A.1 results in a phase diagram which is broadly similar to the actual behavior of the model, but renders all phase transitions first order.

This wavefunction is an exact ground state for the general model at $J_z = 0$, $K_{2z} = 0$, $K_{2x} > J_x/2$, while it does not occur as a ground state on our slice through the parameter space with $K_{2z} = K_{2x}$. Note that our definition of this phase is that it breaks the g_z and T_1 symmetries but preserves g_x and $g_z(T_1)^2$; hence, the ground state degeneracy is four. The above wavefunction is the only product state that satisfies these symmetries. The above ground state manifold has an additional symmetry $T_1 g_{z,\text{even}}$, which is not a symmetry of the Hamiltonian and is hence spurious, except at $\delta = 1$; in App. 4.A.3 below we write improved variational wavefunctions without this spurious symmetry.

Comparing the trial energies $\epsilon_{z\text{FM}}$, $\epsilon_{\text{VBS-I}}$, $\epsilon_{\text{VBS-II}}$, and $\epsilon_{x\text{UUDD}}$, we obtain the mean field phase diagram in Fig. 4.17. All solid lines in this figure represent "level crossings" and are first-order phase boundaries. The positioning of the phases is roughly similar to the actual phase diagram in the main text, but, of course, this simple mean field is not quantitatively accurate and fails qualitatively about the nature of the zFM to VBS transition.

4.A.2 Dimer product states for the zFM and VBS coexistence

We can also allow for coexistence between the zFM and VBS order parameters, for example by using a trial state of the form

$$|\text{VBS} + z\text{FM}\rangle = \otimes_m \left[\cos\frac{\alpha}{2}\,|\uparrow\uparrow\rangle + \sin\frac{\alpha}{2}\,|\downarrow\downarrow\rangle\right]_{2m-1,2m} . \tag{4.33}$$

Clearly, at $\alpha = \pi/2$ and $-\pi/2$ the wavefunction reduces to $|\text{VBS-I}\rangle$ and $|\text{VBS-II}\rangle$ respectively, and $\alpha = 0$ gives $|z\text{FM}\rangle$; for generic α the state has both VBS and zFM order. The trial energy per site is

$$\begin{aligned}\epsilon_{\text{VBS}+z\text{FM}} &= \frac{-J_z(1+\cos^2\alpha) - J_x\sin\alpha}{2} + K_{2z}\cos^2\alpha \\ &= -J_z + K_{2z} - \frac{J_x}{2}t + \left(\frac{J_z}{2} - K_{2z}\right)t^2 ,\end{aligned} \tag{4.34}$$

where $t \equiv \sin\alpha$, $|t| \le 1$. For $K_{2z} > J_z/2 - |J_x|/4$, the lowest energy is achieved at $t = \text{sign}(J_x)$, which corresponds to pure VBS-I or VBS-II order. Thus, large K_2 prefers the pure dimer states.

Conversely, for $K_{2z} < J_z/2 - |J_x|/4$, this mean field finds it favorable to have coexistence of the VBS and zFM orders, with the optimal $t = J_x/[2(J_z - 2K_{2z})]$ and the trial energy $\epsilon_{\text{VBS}+z\text{FM}} = -J_z + K_{2z} - J_x^2/[8(J_z - 2K_{2z})]$ that is always lower than the product state zFM trial energy Eq. (4.26) except at $J_x = 0$. (See Fig. 4.18, which also includes competition with improved xUUDD states.) We know that this feature is not found in our model beyond mean field, where in fact it is the pure zFM phase that wins over the coexistence phase for small K_2. This artifact arises from the fact that for the pure zFM phase we used a trial state with zero entanglement, whereas for the coexistence phase we allowed entanglement on alternating bonds, which apparently always lowers the energy. This lowering of the energy while simultaneously breaking the translation symmetry is undesirable in the true ground state for small K_2: For example, for $K_2 = 0$ and small J_x the second-order perturbation theory on top of the fixed-point zFM state lowers the energy by $-J_x^2/(4J_z)$ per site—which is better than $\epsilon_{\text{VBS}+z\text{FM}}$—but to capture this lowering one needs to allow entanglement on all bonds.

On the large K_2 side, the mean field transition between either of the VBS phases and VBS+zFM is continuous. We thus expect that numerics at fixed bond dimension χ will show a continuous mean field–like transition at the pseudocritical point $K_{2c,z\text{FM}}(\chi)$, which is indeed what we observe and use to

locate $K_{2c,z\mathrm{FM}}(\chi)$ and extrapolate to the true $K_{2c,z\mathrm{FM}}(\chi \to \infty)$. Of course, the true VBS to VBS+zFM transition is characterized by the onset of the zFM order on top of "inert" background VBS order and is expected to be in the Ising universality class. We also expect that the true zFM to VBS+zFM transition is in the Ising universality. While our primitive mean field does not realize this transition, we expect that VUMPS using fixed χ will have a continuous mean field–like zFM to VBS+zFM transition at the corresponding pseudocritical $K_{2c,\mathrm{VBS}}(\chi)$, which is again borne out in the numerics.

Finally, we note that the trial state Eq. (4.33) can interpolate between the VBS-I+zFM and VBS-II+zFM coexistence phase regimes occurring near the corresponding pure dimer phases. However, during this interpolation it passes through the pure zFM state, which is formally a different phase. Based on general arguments, we expect that the VBS-I+zFM and VBS-II+zFM should be in the same phase; that is, there should be a connection between the two regimes without closing the gap, and in particular with the translation symmetry broken throughout. In App. 4.B.1, we will show that this is indeed possible, but we need to go beyond separable states and consider wavefunctions with entanglement across all cuts, which is achieved using an analytic MPS.

4.A.3 Improved mean field states for the xUUDD phase

Our study in App. 4.A.1 simply compares trial energies of states with no variational parameters that cannot connect to each other, and in this setting the VBS to xUUDD transition is first order. A careful consideration of symmetries reveals that the true transition between either of the VBS phases and the xUUDD phase should be Ising-like: both VBS phases preserve g_x, g_z, and T_1^2 (or, equivalently, $g_z T_1^2$), while the xUUDD phase preserves g_x and $g_z T_1^2$. The two phases thus differ only by a broken $\mathbb{Z}_2$ symmetry, and we expect an Ising-like transition.

We can better reflect this in the mean field treatment by replacing the site-product state in Eq. (4.31) by dimer-product states connected to the VBS wavefunctions. Specifically, starting from the VBS-I state, we can construct

the following period-4 trial state, which is invariant under g_x and $g_z T_1^2$:

$$|x\text{UUDD}'\rangle = \bigotimes_n \left[\cos\frac{\beta}{2}\,|+\hat{x},+\hat{x}\rangle + \sin\frac{\beta}{2}\,|-\hat{x},-\hat{x}\rangle\right]_{4n-3,4n-2} \otimes \left[\cos\frac{\beta}{2}\,|-\hat{x},-\hat{x}\rangle + \sin\frac{\beta}{2}\,|+\hat{x},+\hat{x}\rangle\right]_{4n-1,4n} . \quad (4.35)$$

One observes that $\beta = \pi/2$ gives the pure VBS-I state, while $\beta = 0$ gives the xUUDD product state from Eq. (4.31). The ground state manifold in the xUUDD phase is four-dimensional and is spanned by the above state with generic β and its counterparts $T_1|x\text{UUDD}'\rangle$, $T_1^2|x\text{UUDD}'\rangle = g_z|x\text{UUDD}'\rangle$, and $T_1^3|x\text{UUDD}'\rangle$. The trial energy per site is

$$\epsilon_{x\text{UUDD}'} = -K_{2x} + \left(K_{2x} - \frac{J_x}{2}\right)\sin^2\beta - \frac{J_z}{2}\sin\beta\ . \quad (4.36)$$

For $K_{2x} < J_x/2 + |J_z|/4$, the optimal $\sin\beta = \text{sign}(J_z)$, and assuming $J_z > 0$ the state reduces to the pure VBS-I state. For $K_{2x} > J_x/2 + |J_z|/4$, the energy is minimized by $\sin\beta = J_z/(2(2K_{2x} - J_x))$ and is given by $\epsilon_{x\text{UUDD}'} = -K_{2x} - J_z^2/(8(2K_{2x} - J_x))$; this describes a generic xUUDD phase near the VBS-I phase. The mean field transition between the two phases is continuous, which explains our observation of continuous pseudocritical behavior in VUMPS at the VBS-I to xUUDD transition. However, we do not report any details of this study since it is outside our main interest.

We can also start from the VBS-II state and construct another period-4 trial state for the xUUDD phase that is invariant under g_x and $g_z T_1^2$:

$$|x\text{UUDD}''\rangle = \bigotimes_n \left[\cos\frac{\gamma}{2}\,|+\hat{x},-\hat{x}\rangle + \sin\frac{\gamma}{2}\,|-\hat{x},+\hat{x}\rangle\right]_{4n-3,4n-2} \otimes \left[\cos\frac{\gamma}{2}\,|-\hat{x},+\hat{x}\rangle + \sin\frac{\gamma}{2}\,|+\hat{x},-\hat{x}\rangle\right]_{4n-1,4n} . \quad (4.37)$$

Clearly, $\gamma = \pi/2$ gives the pure VBS-II state, while $\gamma = 0$ gives the primitive xUUDD state in Eq. (4.31). The trial energy per site is

$$\epsilon_{x\text{UUDD}''} = -K_{2x} + \left(K_{2x} + \frac{J_x}{2}\right)\sin^2\gamma - \frac{J_z}{2}\sin\gamma\ . \quad (4.38)$$

Comparing with Eq. (4.36), we see that $\epsilon_{x\text{UUDD}''}$ has the same form as $\epsilon_{x\text{UUDD}'}$ except for the sign of the J_x term. Hence, the variational energy minimization

and mean-field transition between the VBS-II and xUUDD$''$ state is similar to that between the VBS-I and xUUDD$'$ state discussed above.

We also see that for $J_x > 0$ we have $\epsilon_{x\text{UUDD}'} < \epsilon_{x\text{UUDD}''}$, and the opposite for $J_x < 0$. As we vary J_x across $J_x = 0$, since the optimal $\sin\beta = \sin\gamma = J_z/(4K_{2x}) \neq 0$, the two trial energies cross with opposite non-zero slopes; that is, we find a first-order transition between the xUUDD$'$ and xUUDD$''$ states, which are different at the transition. One exception is the limit $K_{2x} \to \infty$ where $\beta = \gamma = 0$ and both states reduce to the site-product xUUDD state in Eq. (4.31) (up to a translation).

Figure 4.18 shows our final mean field phase diagram combing results in this section and in Sec. 4.A.2. It includes competition between the VBS+zFM and xUUDD phases, which have incompatible symmetries and hence are separated by first-order transitions.

Regarding the first-order transition between the xUUDD$'$ and xUUDD$''$ states found in this mean field, we believe that these states are representatives of the same phase coming from different regimes, one near the VBS-I phase and the other near VBS-II. That is, while the VBS-I and VBS-II phases are distinct phases protected by the g_x and g_z symmetries, xUUDD$'$ and xUUDD$''$ break g_z and are not distinct phases. One can still have a first-order transition between xUUDD$'$ and xUUDD$''$ states originating from the respective different regimes, as happens in the above mean field and is akin to a liquid-gas first-order transition. While this may be realized in some Hamiltonians, this does not happen in the true ground states of the model studied in this paper. Instead we find a smooth evolution across the $\delta = 1$ line where $J_x = 0$.

As described in the main text, the $\delta = 1$ line has an additional symmetry $g_{z,\text{even}}$. The generic xUUDD$'$ and xUUDD$''$ states considered away from this line of course do not have this symmetry but are in fact related by the action of $g_{z,\text{even}}$. The above mean field where the two states meet discontinuously at $\delta = 1$ would correspond to spontaneously breaking the additional $\mathbb{Z}_2$ symmetry and hence would imply eight-fold ground state degeneracy. In our Hamiltonian, instead it appears that the system on the $\delta = 1$ line preserves the additional $\mathbb{Z}_2$ symmetry, and the ground state degeneracy is four everywhere in the xUUDD phase. As we show in App. 4.B.2, this scenario can be also realized at the level of improved wavefunctions connected to the above xUUDD$'$ and xUUDD$''$ states but requires allowing entanglement between all sites.

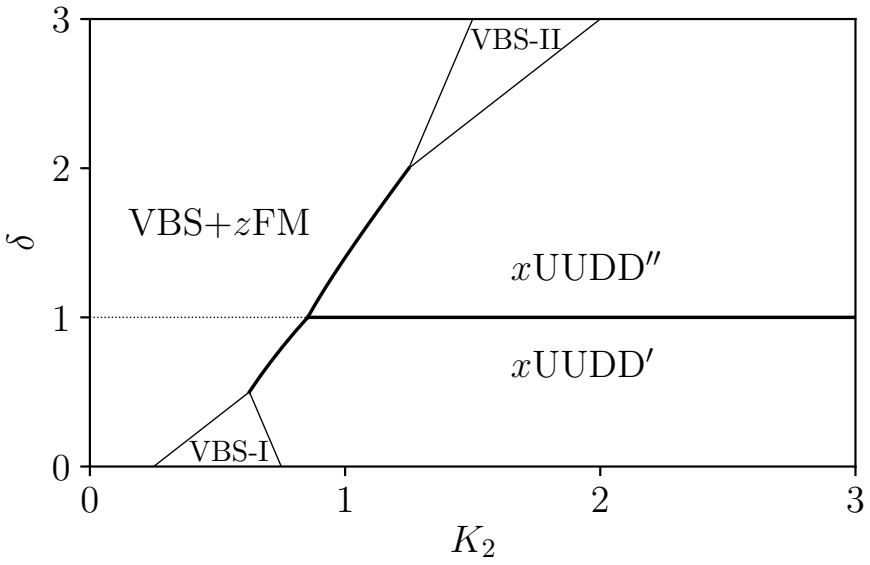

Figure 4.18: The phase diagram of the improved mean-field trial states described in Apps. 4.A.2 and 4.A.3 provides a somewhat more realistic picture, in particular with continuous phase transitions for all boundaries of the VBS-I and VBS-II phases. There is an extended boundary between the coexistence and xUUDD phases, which is first order, as well as a first-order transition between xUUDD′ and xUUDD″. Along the dotted line at $\delta = 1$ the VBS+zFM ansatz coincides with the simple product zFM state from App. 4.A.1; however, the wider zFM phase is not represented, as away from this special line the simple zFM wavefunction is always energetically unfavorable. In App. 4.B we show how some of the unphysical features can be fixed using more entangled wavefunctions.

4.B Simple analytic MPS for phases

In this appendix we add on to our mean-field treatment to address inconsistencies between the study in the main text and the mean field phase diagram obtained using only separable wavefunctions. Specifically, in App. 4.B.1 we write an MPS of bond dimension 2 describing the coexistence region VBS+zFM and matching the symmetries observed in the numerical study, which in particular can connect smoothly across the $\delta = 1$ line with the additional symmetry $g_{z,\text{even}}$. In App. 4.B.2 we write another MPS of bond dimension 2 which interpolates smoothly between the improved states for the xUUDD phase given in Eqs. (4.35) and (4.37) without a phase transition, maintaining the observed ground state degeneracy of 4 throughout.

4.B.1 $\chi = 2$ MPS wavefunction for coexistence phase

In order to write a wavefunction for the VBS and zFM coexistence phase, we require invariance under g_z, $(T_1)^2$, and inversion I about a bond center, and allow breaking of g_x and T_1. At special values of the internal parameters, our wavefunction will also be invariant under $T_1 g_{z,\text{even}}$, which is an additional symmetry present in our model at $\delta = 1$ as described in Sec. 4.4.2. We use an MPS of bond dimension 2 with a two-site unit cell, having the following form:

$$|\text{MPS}_{\text{VBS}+z\text{FM}}\rangle = \sum_{\{\sigma\}} \text{Tr}[\cdots A^{\sigma_{2m-1}} B^{\sigma_{2m}} \cdots]|\{\sigma\}\rangle \ . \tag{4.39}$$

The choice of the unit cell enforces $(T_1)^2$ symmetry, and we can impose invariance under g_z and I as follows. A symmetry O induces on the MPS matrices an action $M_O : (A^{|\sigma\rangle}, B^{|\sigma\rangle}) \mapsto (A_O^{|\sigma\rangle}, B_O^{|\sigma\rangle})$. Choosing a particular representation of the projective symmetry group on the virtual indices, we can guarantee invariance of the state under O by specifying invertible matrices X_O and Y_O such that $A_O^{|\sigma\rangle} = X_O A^{|\sigma\rangle} Y_O^{-1}$, $B_O^{|\sigma\rangle} = Y_O B^{|\sigma\rangle} X_O^{-1}$.

Now, g_z is expressed as an action on the matrices by

$$A_{g_z}^{|\sigma\rangle} = \sigma A^{|\sigma\rangle} \ , \quad B_{g_z}^{|\sigma\rangle} = \sigma B^{|\sigma\rangle} \ , \tag{4.40}$$

while for bond inversion I,

$$A_I^{|\sigma\rangle} = (B^{|\sigma\rangle})^T \ , \quad B_I^{|\sigma\rangle} = (A^{|\sigma\rangle})^T \ . \tag{4.41}$$

As we will show, the specific choice of matrices $(X_{g_z}, Y_{g_z}) = (\sigma^z, \sigma^z)$ and $(X_I, Y_I) = (\sigma^z, 1)$ allows us to connect the MPS state to the product VBS+zFM state (4.33) considered earlier. Using this choice, we find that the most general form of the MPS matrices is given by

$$\begin{aligned} A^{|\uparrow\rangle} &= \begin{bmatrix} a & 0 \\ 0 & b \end{bmatrix} \ , & A^{|\downarrow\rangle} &= \begin{bmatrix} 0 & c \\ d & 0 \end{bmatrix} \ , \\ B^{|\uparrow\rangle} &= \begin{bmatrix} a & 0 \\ 0 & -b \end{bmatrix} \ , & B^{|\downarrow\rangle} &= \begin{bmatrix} 0 & -d \\ c & 0 \end{bmatrix} \ . \end{aligned} \tag{4.42}$$

Of the four parameters a, b, c, d, only three are independent, as the overall scale only affects the wavefunction normalization.

For parameters $b = d = 0$, we have $A^{|\uparrow\rangle} B^{|\uparrow\rangle} = \text{diag}(a^2, 0)$, $A^{|\downarrow\rangle} B^{|\downarrow\rangle} = \text{diag}(c^2, 0)$ and $A^{|\uparrow\rangle} B^{|\downarrow\rangle} = A^{|\downarrow\rangle} B^{|\uparrow\rangle} = 0$. Then it is easy to see that the MPS wavefunction

reduces to a form matching the separable VBS+zFM wavefunction (4.33) with dimers on the $(2m-1, 2m)$ bonds. This state is natural near the VBS-I phase (if $c^2 \neq a^2$, it clearly breaks the g_x symmetry, and approaches the VBS-I phase as $c^2 \to a^2$). On the other hand, for $b = c = 0$ we have $B^{|\uparrow\rangle}A^{|\uparrow\rangle} = \mathrm{diag}(a^2, 0)$, $B^{|\downarrow\rangle}A^{|\downarrow\rangle} = \mathrm{diag}(-d^2, 0)$ and $B^{|\uparrow\rangle}A^{|\downarrow\rangle} = B^{|\downarrow\rangle}A^{|\uparrow\rangle} = 0$. In this case, the wavefunction reduces to a form matching the separable VBS+zFM wavefunction with dimers on the $(2m, 2m+1)$ bonds. This state is natural near the VBS-II phase.

Furthermore, we can connect the two regimes while staying within the same VBS+zFM phase. For example, we can fix $a = 1$, $b = 0$, and vary between the two regimes on a path $(c, d) = (\gamma(1-\ell), \gamma\ell)$, $\ell \in [0, 1]$, with fixed $\gamma < 1$. One can check that both g_x and T_1 remain broken everywhere on this path. By straightforward diagonalization of the transfer matrix one also sees that the MPS remains injective throughout the range $\ell \in [0, 1]$. We thus conclude that the VBS-I and VBS-II orders are not distinguished in the presence of zFM order, where g_x is broken; that is, there is only one VBS+zFM phase.

Finally, if $c = d$ with arbitrary a, b, the MPS wavefunction is invariant under $S = T_1 g_{z,\mathrm{even}}$, which is the additional symmetry present in our model on the $\delta = 1$ line. Indeed, the action of S on the above MPS induces the following action on the matrices

$$A_S^{|\sigma\rangle} = \sigma B^{|\sigma\rangle} \ , \quad B_S^{|\sigma\rangle} = A^{|\sigma\rangle} \ . \tag{4.43}$$

The new matrices are gauge-equivalent to the originals under $(X_S, Y_S) = (\sigma^z, 1)$. On the path discussed above interpolating between the VBS-I+zFM and VBS-II+zFM regimes, the midpoint $\ell = 1/2$ gives $c = d$ and has this symmetry. Thus, we have also constructed candidate wavefunctions for the VBS+zFM coexistence phase on the $\delta = 1$ line that respect the additional symmetry present in our Hamiltonian on this line, and that appear to capture qualitative features of the true ground states of our Hamiltonian.

4.B.2 $\chi = 2$ MPS for the xUUDD phase

We can write down the desired wavefunction interpolating smoothly between the separable mean field states $|x\mathrm{UUDD}'\rangle$ of Eq. (4.35) and $|x\mathrm{UUDD}''\rangle$ of Eq. (4.37) as a period-4 MPS with bond dimension 2 as follows:

$$|\mathrm{MPS}_{x\mathrm{UUDD}}\rangle = \sum_{\{\sigma\}} \mathrm{Tr}[\cdots A^{\sigma_{4n-3}} B^{\sigma_{4n-2}} C^{\sigma_{4n-1}} D^{\sigma_{4n}} \cdots] |\{\sigma\}\rangle \ . \tag{4.44}$$

Here we use the σ^x eigenbasis, and the MPS matrices are

$$A^{|+\hat{x}\rangle} = \begin{bmatrix} r & 0 \\ 0 & s \end{bmatrix} , \quad A^{|-\hat{x}\rangle} = \begin{bmatrix} 0 & u \\ v & 0 \end{bmatrix} ;$$
$$B^{|\sigma\rangle} = (A^{|\sigma\rangle})^T ; \quad C^{|\sigma\rangle} = A^{|-\sigma\rangle} ; \quad D^{|\sigma\rangle} = B^{|-\sigma\rangle} .$$

By construction, the state is invariant under inversion in the bond center between sites $4n-3$ and $4n-2$, and also under $g_z T_1^2$. Furthermore, the state is invariant under g_x. As an action on the matrices, we have

$$M_{g_x}^{|\sigma\rangle} = \sigma M^{|\sigma\rangle} , \tag{4.45}$$

and the new matrices are gauge-equivalent to the old matrices by noting that $M_{g_x}^{|\sigma\rangle} = \pm\sigma^z M^{|\sigma\rangle}\sigma^z$, where the plus sign is for $M = A, B$ and the minus sign is for $M = C, D$. Thus, the state has the desired symmetry properties for a ground state in the generic xUUDD phase.

It is easy to check that when $s = 0$ and $v = 0$, the state reduces to the dimer-product state $|x\text{UUDD}'\rangle$ in Eq. (4.35). Similarly, when $s = 0$ and $u = 0$, the state reduces to $|x\text{UUDD}''\rangle$ in Eq. (4.37) (more precisely, the MPS yields $T_1|x\text{UUDD}''\rangle$).

It is also easy to check that $T_1 g_{z,\text{even}}$ acts on this MPS wavefunction by interchanging u and v. Hence, when $u = v$, the state is invariant under $T_1 g_{z,\text{even}}$ and is a candidate ground state for the xUUDD phase along the $\delta = 1$ slice that does not break the additional $\mathbb{Z}_2$ symmetry present on this line.

4.C Direct phase transition at $\delta = 1$

In this appendix, we propose a field theory description which allows direct phase transition between the VBS+zFM coexistence phase and the xUUDD phase on the $\delta = 1$ line.

As we pointed out in the main text, $\delta = 1$ line admits an additional symmetry $g_{z,\text{even}} = \prod_m \sigma^z_{2m}$. This additional symmetry plays an essential role for the direct phase transition between these two phases at $\delta = 1$. For $\delta \neq 1$ where we do not have the $g_{z,\text{even}}$ symmetry, these two phases are either connected by a first order phase transition or by an intermediate VBS phase.

To see this, we first analyze the symmetry properties of these two phases at $\delta = 1$. The total symmetry group at $\delta = 1$ is generated by $\{g_z, g_x, g_{z,\text{even}}, T_1, I, \mathcal{T}\}$.

For our purposes here, it is enough to focus on the symmetry group generated by $\{g_z, g_x, g_{z,\text{even}}, T_1\}$. We notice that both phases break $g_{z,\text{even}}$ and T_1 but preserve the combination $T_1 g_{z,\text{even}}$.[2] The VBS+zFM coexistence phase additionally breaks g_x, and the remaining symmetry group is generated by $\{g_z, T_1 g_{z,\text{even}}\}$, whereas the xUUDD phase breaks g_z, with the remaining symmetry group generated by $\{g_x, T_1 g_{z,\text{even}}\}$. The ground state degeneracy is four for either of these two phases.

Since the remaining symmetry groups of these two phases are not subgroups of each other, if there is a direct phase transition, this transition must be beyond the Landau–Ginzburg symmetry-breaking paradigm. To develop a theory for this transition, we start from a background configuration that breaks $g_{z,\text{even}}$ and T_1, but preserves $T_1 g_{z,\text{even}}$. For a concrete example of such a background-locking term, we can consider adding to the Hamiltonian a term $\Delta H = J_{x,\,\text{stagg}} \sum_j (-1)^j S^x_j S^x_{j+1}$. In this background configuration, the VBS+zFM coexistence phase breaks g_x, and thus can be viewed as a "z-ordered" phase on the background. Similarly, the xUUDD breaks g_z, and can be viewed as an "x-ordered" phase. Hence, the phase transition can be viewed as the transition between the z-ordered and x-ordered phases on this background configuration.

Motivated by the above discussion, we can now present a hydrodynamic description for this transition. We first define a new set of spin variables as

$$\begin{aligned} &S'^{x/y}_{4n-3} = S^{x/y}_{4n-3} \ , \quad S'^{x/y}_{4n-2} = S^{x/y}_{4n-2} \ , \\ &S'^{x/y}_{4n-1} = -S^{x/y}_{4n-1} \ , \quad S'^{x/y}_{4n} = -S^{x/y}_{4n} \ ; \\ &S'^{z}_{j} = S^{z}_{j} \ . \end{aligned} \tag{4.46}$$

$T_1 g_{z,\text{even}}$ acts as a conventional translation symmetry on the new spin variables. (For example, the specified concrete background-locking term becomes simply $\Delta H = -J_{x,\,\text{stagg}} \sum_j S'^{x}_j S'^{x}_{j+1}$.) We then apply standard bosonization techniques on the new spins:

$$\begin{aligned} &S'^{z}_j \sim \cos\phi'_j \ , \quad S'^{x}_j \sim \sin\phi'_j \ , \\ &S'^{y}_j \sim \frac{\theta'_{j+1/2} - \theta'_{j-1/2}}{\pi} \ , \end{aligned} \tag{4.47}$$

[2] More precisely, both the VBS+zFM and xUUDD phases have ground state degeneracy equal to four. In the VBS+zFM phase, all four ground states are invariant under $T_1 g_{z,\text{even}}$. On the other hand, in the xUUDD phase, two of the ground states preserve $T_1 g_{z,\text{even}}$ while the other two preserve $T_1 g_{z,\text{odd}}$.

where $\phi' \in [0, 2\pi)$ and $\theta' \in [0, \pi)$ are conjugate phase and phonon variables.

The symmetry transformations of ϕ' and θ' read

$$g_x \ : \quad \phi' \to \pi - \phi' \ , \quad \theta' \to -\theta' \ ; \tag{4.48}$$

$$g_z \ : \quad \phi' \to -\phi' \ , \quad \theta' \to -\theta' \ ; \tag{4.49}$$

$$T_1 g_{z,\text{even}} \ : \quad \phi' \to \phi' \ , \quad \theta' \to \theta' + \frac{\pi}{2} \ . \tag{4.50}$$

Thus, the symmetry-allowed scattering (i.e., cosine) terms are $\cos(2m\phi')$ and $\cos(4n\theta')$.

The action for the field theory is

$$\begin{aligned} S = &\int \mathrm{d}\tau \, \mathrm{d}x \left[\frac{\mathrm{i}}{\pi} \partial_\tau \phi' \partial_x \theta' + \frac{v'}{2\pi} \left(\frac{1}{g'} (\partial_x \theta')^2 + g' (\partial_x \phi')^2 \right) \right] \\ &+ \int \mathrm{d}\tau \, \mathrm{d}x \left[\lambda_2 \cos(2\phi') + \lambda_4 \cos(4\phi') + \kappa_4 \cos(4\theta') + \cdots \right] , \end{aligned} \tag{4.51}$$

where the Luttinger parameter g' and velocity v' depend on microscopic details, and $\cdots$ denotes higher order scattering terms. The scaling dimensions for the scattering terms read

$$\dim \left[\cos(2m\phi') \right] = \frac{m^2}{g'} \ , \quad \dim \left[\cos(4n\theta') \right] = 4n^2 g' \ .$$

In particular, when $1/2 < g' < 2$, there is only one relevant cosine operator, which is $\cos(2\phi')$.

For $\lambda_2 > 0$, ϕ' gets pinned at $\pi/2$ or $3\pi/2$, and thus $\langle S'^x \rangle \sim \langle \sin \phi' \rangle \neq 0$, which gives the xUUDD phase. On the other hand, for $\lambda_2 < 0$, ϕ' gets pinned at 0 or π, and thus $\langle S'^z \rangle \sim \langle \cos \phi' \rangle \neq 0$, which gives the VBS+$z$FM coexistence phase. (Recall that we are working on top of a background that breaks T_1, which is why the ground state degeneracy is two in each case here.) The continuous phase transition happens when $\lambda_2 = 0$, which is described by a free Luttinger liquid theory with $c = 1$ and varying critical exponents depending on g'.

Finally, we mention that in the absence of $T_1 g_{z,\text{even}}$, $\cos(2\theta')$ is allowed by symmetry, which becomes relevant when $g' < 2$. It is easy to check that there are always multiple relevant or marginal operators for any g'. Thus, the above field theory loses applicability for the transition between the VBS+zFM and xUUDD phases.

BIBLIOGRAPHY

[1] S. Jiang and O. Motrunich, "Ising ferromagnet to valence bond solid transition in a one-dimensional spin chain: Analogies to deconfined quantum critical points", Physical Review B 99 (2019), 075103.

[2] M. Nakamura, "Mechanism of CDW-SDW transition in one dimension", Journal of the Physical Society of Japan 68 (1999), 3123.

[3] M. Nakamura, "Tricritical behavior in the extended Hubbard chains", Physical Review B 61 (2000), 16377.

[4] P. Sengupta, A. W. Sandvik, and D. K. Campbell, "Bond-order-wave phase and quantum phase transitions in the one-dimensional extended Hubbard model", Physical Review B 65 (2002), 155113.

[5] M. Tsuchiizu and A. Furusaki, "Phase Diagram of the One-Dimensional Extended Hubbard Model at Half Filling", Physical Review Letters 88 (2002), 056402.

[6] M. Tsuchiizu and A. Furusaki, "Ground-state phase diagram of the one-dimensional half-filled extended Hubbard model", Physical Review B 69 (2004), 035103.

[7] A. W. Sandvik, L. Balents, and D. K. Campbell, "Ground state phases of the half-filled one-dimensional extended Hubbard model", Physical review letters 92 (2004), 236401.

[8] C. K. Majumdar and D. K. Ghosh, "On Next-Nearest-Neighbor Interaction in Linear Chain. I", Journal of Mathematical Physics 10 (1969), 1388.

[9] C. K. Majumdar and D. K. Ghosh, "On Next-Nearest-Neighbor Interaction in Linear Chain. II", Journal of Mathematical Physics 10 (1969), 1399.

[10] S. Furukawa, M. Sato, and A. Furusaki, "Unconventional Néel and dimer orders in a spin-$\frac{1}{2}$ frustrated ferromagnetic chain with easy-plane anisotropy", Physical Review B 81 (2010), 094430.

[11] S. Furukawa et al., "Ground-state phase diagram of a spin-$\frac{1}{2}$ frustrated ferromagnetic XXZ chain: Haldane dimer phase and gapped/gapless chiral phases", Physical Review B 86 (2012), 094417.

[12] J. M. Kosterlitz and D. J. Thouless, "Ordering, metastability and phase transitions in two-dimensional systems", Journal of Physics C Solid State Physics 6 (1973), 1181.

[13] J. M. Kosterlitz, "The critical properties of the two-dimensional xy model", Journal of Physics C Solid State Physics 7 (1974), 1046.

[14] F. D. M. Haldane, "Spontaneous dimerization in the $S = \frac{1}{2}$ Heisenberg antiferromagnetic chain with competing interactions", Physical Review B 25 (1982), 4925.

[15] V. Zauner-Stauber et al., "Variational optimization algorithms for uniform matrix product states", Physical Review B 97 (2018), 045145.

[16] J. Haegeman, T. J. Osborne, and F. Verstraete, "Post-matrix product state methods: To tangent space and beyond", Physical Review B 88 (2013), 075133.

[17] C. Liu et al., "Symmetry breaking and criticality in tensor-product states", Physical Review B 82 (2010), 060410.

[18] F. Pollmann et al., "Theory of finite-entanglement scaling at one-dimensional quantum critical points", Physical review letters 102 (2009), 255701.

Chapter 5

ONE-DIMENSIONAL MODEL FOR DECONFINED CRITICALITY WITH $\mathbb{Z}_3 \times \mathbb{Z}_3$ SYMMETRY

5.1 Introduction

One may wonder to what extent the lessons learned about the $\mathbb{Z}_2 \times \mathbb{Z}_2$-symmetric DQCP in 1d, presented in Ch. 4, are representative of a more general class as opposed to being somehow special. In the present chapter we begin to address this question through detailed studies of a concrete lattice model with $\mathbb{Z}_3 \times \mathbb{Z}_3$ symmetry. We will end up arguing that the evidence suggests that a family of DQCP in $\mathbb{Z}_q \times \mathbb{Z}_q$-symmetric models in 1d in fact exhibits pseudo-critical behavior due to RG walking, a situation reminiscent of the current status of the canonical DQCP with SU(2) symmetry in 2d. The putative transition in our $\mathbb{Z}_q \times \mathbb{Z}_q$-symmetric DQCP appears to be described by an integrable model with very long correlation length, and the availability of analytical results makes it a particularly appealing candidate for controlled studies of the RG walking scenario for a very weakly first-order DQCP.

This chapter is organized as follows. In Secs. 5.2, 5.3, and 5.4 we introduce our lattice Hamiltonian and present numerical results from MPS on the phase diagram and evidence for a DQCP. In Sec. 5.5 we develop some low-energy continuum theories related to the lattice model and calculate supporting results in a fine-tuned two-component Gaussian theory that appears to capture many (but not all) aspects of the numerical results. In Sec. 5.6 we provide details on exact results for an integrable model suggested by numerics to describe the DQCP, which leads us to conclude the transition is very weakly first order. In Sec. 5.7 we use exact diagonalization studies to identify some light primary fields in the complex CFTs associated with the RG walking conjecture. Finally, in the appendices we expand on background information and further technical details related to various aspects of this work.

5.2 Review of SU(3) and SU(3)-symmetric Hamiltonians

5.2.1 Basics of SU(3)

The Lie algebra $\mathfrak{su}(3)$ has 8 generators t^a, $a = 1, \ldots, 8$, which in the defining representation **3** are represented by the Gell-Mann matrices λ^a. We use the

alternative convention $T^a = \lambda^a/2$, so the Lie algebra structure constants f_{abc} are determined by $[T^a, T^b] = i f_{abc} T^c$. The T^a are traceless Hermitian matrices, normalized according to $\mathrm{tr}(T^a T^b) = \frac{1}{2}\delta^{ab}$. In the conjugate representation $\overline{\mathbf{3}}$ the generators are represented by $\overline{T}^a = -(T^a)^*$.

For SU(q), $q \geq 2$, one can write a quadratic Casimir invariant

$$C_2 = \sum_a t^a t^a \ . \tag{5.1}$$

By construction C_2 commutes with all of the t^a. Thus, by Schur's lemma, in an irreducible representation C_2 is proportional to the identity. This operator is familiar from SU(2), where $C_2 = \boldsymbol{S}^2$ and the eigenvalue in an irreducible representation of spin l is $l(l+1)$. More generally, in a q-dimensional representation of SU(q), $C_2 = \frac{q^2-1}{2q}$.

5.2.2 SU(3)-invariant Hamiltonians

In the 1d DQCP with $\mathbb{Z}_2 \times \mathbb{Z}_2$ symmetry studied previously [1, 2], a spin Hamiltonian was considered which connects to the solvable Majumdar–Ghosh model. This ensured the appearance of a phase with VBS order. That construction generalizes straightforwardly to SU(q). The Majumdar–Ghosh Hamiltonian is the $q = 2$ case of

$$H_{\mathrm{Cas}} = \sum_j \left(C_{2;j,j+1,j+2} - (C_{2;j} + C_{2;j+1} + C_{2;j+2}) \right), \tag{5.2}$$

where $C_{2;j,j+1,j+2}$ is C_2 acting on the tensor product space of three neighboring sites, and $C_{2;j}$ is simply a constant on each site individually, as sites host irreducible representations of SU(q). For $q = 2$, the fact that the ground states are translation symmetry–breaking products of singlets is a consequence of the irrep decomposition $\mathbf{2} \otimes \mathbf{2} = \mathbf{1} \oplus \mathbf{3}$. The appearance of the singlet $\mathbf{1}$ is particular to $n = 2$; in general, enforcing SU(q) invariance requires as many single-particle orbitals as internal states.

For $q = 3$, Eq. (5.2) can be used by treating the sites on one sublattice as hosting the conjugate representation $\overline{\mathbf{3}}$. Then one decomposes $\mathbf{3} \otimes \overline{\mathbf{3}} = \mathbf{1} \oplus \mathbf{8}$, so neighboring sites favor an SU(3) singlet. (A similar statement is true for any q, and in fact because $\overline{\mathbf{2}} = \mathbf{2}$ as irreps of SU(2), that case is also included.) The analysis then follows in the same way as for $q = 2$.

A local term of H_{Cas} is

$$h_{j,j+1,j+2} = \overline{T}^a_j T^a_{j+1} + T^a_{j+1} \overline{T}^a_{j+2} + T^a_j T^a_{j+2} \ , \tag{5.3}$$

independently of the parity of j, as $\overline{T}^a_j T^a_{j+1} = T^a_j \overline{T}^a_{j+1}$. The action of each of these terms can be understood through the action of C_2 on tensor products of representations. Consider

$$C_2(\mathbf{3} \otimes \overline{\mathbf{3}}) = \sum_a (T^a_j + \overline{T}^a_{j+1})^2 = 2\overline{T}^a_j T^a_{j+1} + \frac{8}{3} \ , \tag{5.4}$$

$$C_2(\mathbf{3} \otimes \mathbf{3}) = \sum_a (T^a_j + T^a_{j+1})^2 = 2T^a_j T^a_{j+1} + \frac{8}{3} \ . \tag{5.5}$$

In Eq. (5.4) we see that $\overline{T}^a_j T^a_{j+1}$ distinguishes the singlet and the eight-dimensional adjoint representations on sites j, $j+1$. A rank-one projector onto the singlet subspace can thus be written using this term. Explicitly,

$$\overline{T}^a_j T^a_{j+1} - \frac{1}{6} = -\frac{3}{2}(\Pi_{\mathrm{s}})_{j,j+1} = -\frac{3}{2}|\psi_{\mathrm{s}}\rangle\langle\psi_{\mathrm{s}}|_{j,j+1} \ , \tag{5.6}$$

where $|\psi_{\mathrm{s}}\rangle_{j,j+1} = \frac{1}{\sqrt{3}}\Big(|00\rangle_{j,j+1} + |11\rangle_{j,j+1} + |22\rangle_{j,j+1}\Big)$. Similarly, $\mathbf{3}\otimes\mathbf{3} = \overline{\mathbf{3}}\oplus\mathbf{6}$, where $\overline{\mathbf{3}}$ is the antisymmetric subspace and $\mathbf{6}$ the symmetric subspace. Thus, Eq. (5.5) tells us that

$$T^a_j T^a_{j+1} + \frac{2}{3} = \Big(\Pi_{\bigvee^2}\Big)_{j,j+1} \ , \tag{5.7}$$

which is the rank-6 projector onto the symmetric subspace of sites j, $j+1$. (Similar statements apply for general q.) As a result, H_{Cas} admits the same arguments that show the ground state manifold of the Majumdar–Ghosh Hamiltonian is spanned by tensor products of SU(2) singlet dimers, with instead twofold degenerate ground states spanned by products of SU(q) singlet dimers.

Conveniently, there is a simpler Hamiltonian than Eq. (5.2) for $q = 3$ which exhibits VBS order. The following nearest-neighbor Hamiltonian was known to Barber et al. [3] and Affleck [4]:

$$H_{\mathrm{bQ}} = \sum_j \overline{T}^a_j T^a_{j+1} \ . \tag{5.8}$$

This Hamiltonian still respects the full SU(3), and turns out to map exactly to the pure biquadratic SU(2) spin-1 model. It is also integrable. Through its Temperley–Lieb operator algebra this Hamiltonian is related to the XXZ spin-1/2 chain for a particular anisotropy $\Delta = -3/2$ and to the 9-state self-dual Potts model [3, 5]. The latter equivalence can be seen more directly via a two-step duality procedure which we present in App. 5.D. Eq. (5.8) turns out to be gapped, with twofold degenerate ground state and finite dimerization

order parameter. Although the ground states are finitely correlated and not a Majumdar–Ghosh-like separable product of dimers, because the ground states respect the SU(3) symmetry we surmise that this Hamiltonian lies in the same phase as H_{Cas}. Thus, we consider the local term in H_{bQ} to be one favoring a lattice symmetry–breaking but internally symmetric VBS phase.

5.3 Model with $\mathbb{Z}_3 \times \mathbb{Z}_3$ symmetry

A quantum chain respecting an internal $\mathbb{Z}_3 \times \mathbb{Z}_3$ symmetry is most naturally realized using a three-dimensional local Hilbert space, placed on the sites of a 1d lattice.

5.3.1 Lattice Hamiltonian

We choose the following generators of the global internal symmetry group:

$$g_x = \prod_j g_{x,j} = \prod_j X_j, \quad g_z = \prod_j g_{z,j} = \prod_k Z_{2k}^\dagger Z_{2k+1} \ , \tag{5.9}$$

which are written using the $\mathbb{Z}_3$ clock operators

$$X = \begin{bmatrix} 0 & 0 & 1 \\ 1 & 0 & 0 \\ 0 & 1 & 0 \end{bmatrix}, \quad Z = \begin{bmatrix} 1 & 0 & 0 \\ 0 & \omega & 0 \\ 0 & 0 & \omega^{-1} \end{bmatrix}, \tag{5.10}$$

with $\omega = e^{\mathrm{i}\,2\pi/3}$ being the primitive cubic root of unity. Because of the commutation relation $ZX = \omega XZ$ the $\mathbb{Z}_3^z \times \mathbb{Z}_3^x$ symmetry is realized projectively on a single lattice site. The projective representations are classified by $H^2[\mathbb{Z}_3 \times \mathbb{Z}_3, \mathrm{U}(1)] = \mathbb{Z}_3$ and labeled by $\{[0],[1],[2]\}$, where for class $[r]$ we have $g_{z,j} g_{x,j} = \omega^r g_{x,j} g_{z,j}$. The sublattice of odd-numbered (even-numbered) sites hosts the [1] ([2]) projective representation of $\mathbb{Z}_3 \times \mathbb{Z}_3$.

The general lattice Hamiltonian we consider is

$$\begin{aligned} H &= H[J^x, J^z, K] \\ &= -\sum_j \Big((J^x X_j X_{j+1} + J^z Z_j^\dagger Z_{j+1} + \mathrm{H.c.}) \\ &\qquad + K(1 + X_j X_{j+1} + \mathrm{H.c.})(1 + Z_j^\dagger Z_{j+1} + \mathrm{H.c.}) \Big) \qquad (5.11) \\ &= -\sum_j \Big(J^x X_j X_{j+1} + J^z Z_j^\dagger Z_{j+1} + \mathrm{H.c.} \Big) + 6K \sum_j \left(\sum_a \overline{T}_j^a T_{j+1}^a - \frac{1}{6} \right). \qquad (5.12) \end{aligned}$$

In the final line the K term is written using standard SU(3) spin operators connecting to an integrable model with VBS ground state, as reviewed in Sec. 5.2. We generally restrict all coupling constants to be real and non-negative.

Other internal symmetries of Eq. (5.11) include time reversal Θ, which we implement as complex conjugation in the Z eigenbasis, and charge conjugation symmetry $\mathcal{C} : |n\rangle \to |3 - n \mod 3\rangle$. Together $\mathcal{C}$ and g_x generate the S_3 permutation symmetry of the local basis state labels. With periodic boundaries on the lattice, the model is invariant under the generator of translation T_1, as well as spatial inversion $\mathcal{I}$ about a site. While T_1 is a symmetry of H, it does exchange the projective symmetry groups on the sublattices. The action of the symmetries on the clock operators is

$$g_x : \ (X_j, Z_j) \ \mapsto \ (X_j, \omega^{-1} Z_j) \ , \tag{5.13}$$

$$g_z : \ (X_j, Z_j) \ \mapsto \ (\omega^{2p_j - 1} X_j, Z_j) \ , \tag{5.14}$$

$$\Theta : \ (X_j, Z_j) \ \mapsto \ (X_j, Z_j^\dagger), \ \mathrm{i} \mapsto -\mathrm{i} \ , \tag{5.15}$$

$$\mathcal{C} : \ (X_j, Z_j) \ \mapsto \ (X_j^\dagger, Z_j^\dagger) \ , \tag{5.16}$$

$$T_1 : \ (X_j, Z_j) \ \mapsto \ (X_{j+1}, Z_{j+1}) \ , \tag{5.17}$$

$$\mathcal{I} : \ (X_j, Z_j) \ \mapsto \ (X_{-j}, Z_{-j}) \ , \tag{5.18}$$

where we use p_j to denote the parity of j:

$$p_j = \frac{1 - (-1)^j}{2} = \begin{cases} 0 \ , & j \text{ even} \ , \\ 1 \ , & j \text{ odd} \ . \end{cases} \tag{5.19}$$

5.3.2 Classical picture of phases

In the limiting case $J^x = K = 0$, $J^z > 0$, the ground state is a ferromagnetic phase in the Z basis which breaks $\mathbb{Z}_3^x$, leading to a three-dimensional ground state manifold spanned by basis

$$\mathcal{B}_{z\mathrm{FM}} = \left\{ \bigotimes_j |0\rangle_j, \ \bigotimes_j |1\rangle_j, \ \bigotimes_j |2\rangle_j \right\} . \tag{5.20}$$

The ground states in the zFM phase are of course subject to quantum fluctuations but remain connected to this simple basis of product states.

Similarly, for $J^z = K = 0$, $J^x > 0$ the ground states exhibit ferromagnetic

order in the X eigenbasis (local basis states denoted $|0_x\rangle$, $|1_x\rangle$, $|2_x\rangle = |{-1_x}\rangle$):

$$\mathcal{B}_{x\mathrm{FM}} = \left\{ \bigotimes_j |0_x\rangle_j, \bigotimes_j |(1-2p_j)_x\rangle_j, \bigotimes_j |(2p_j-1)_x\rangle_j \right\}. \tag{5.21}$$

Setting $J^z = J^x = 0$, $K > 0$ recovers the Hamiltonian H_{bQ} of Eq. (5.8) which respects the full SU(3) symmetry. As described in Sec. 5.2.2, the ground state of this model is known to preserve SU(3) but spontaneously breaks the translation symmetry generator T_1 to $T_2 = (T_1)^2$, thus breaking a $\mathbb{Z}/2\mathbb{Z} = \mathbb{Z}_2$ symmetry and leading to twofold ground state degeneracy [4]. While the ground states at this point are finitely correlated, including additional terms discussed in Sec. 5.2.2 connects to a Majumdar–Ghosh-like point in the same phase. Thus we take the classical picture of the VBS phase to be spanned by

$$\mathcal{B}_{\mathrm{VBS}} = \left\{ \bigotimes_k |\psi_{\mathrm{s}}\rangle_{2k-1,2k}, \bigotimes_k |\psi_{\mathrm{s}}\rangle_{2k,2k+1} \right\}, \tag{5.22}$$

where $|\psi_{\mathrm{s}}\rangle_{j,j'} = \frac{1}{\sqrt{3}} \Big(|00\rangle_{j,j'} + |11\rangle_{j,j'} + |22\rangle_{j,j'} \Big)$.

Although every unit cell hosts a nontrivial projective representation, this system does not have an LSM anomaly [6–8], and it turns out that one can construct a gapped symmetric ground state. This symmetric phase is actually an SPT phase characterized by a fractionalized entanglement spectrum; as such, there is no simple classical picture of this state. In App. 5.A we develop an analytic MPS for this phase.

5.4 Results from uniform matrix product states

In order to reduce the three-dimensional parameter space of Eq. (5.11) to a two-dimensional phase diagram, we perform a change of variables to the anisotropy $\delta = \frac{J^z - J^x}{J^z + J^x}$; that is, $J^z = J(1+\delta)$ and $J^x = J(1-\delta)$, and we set $J = 1$. We find the phase diagram using the variational uniform matrix product state (VUMPS) numerical method [9]. We use an adiabatic protocol for determining the phase boundary, fully optimizing a trial state far away from the transition, then using this state as the initial condition for the variational procedure with a slightly perturbed Hamiltonian. In this way the state is tuned towards the phase transition but biased towards a particular symmetry-breaking order. Because at the mean-field level the phase transition is first-order, the energy landscape of the MPS close to the transition will develop two

local minima, with one being metastable on each side. The two choices of initial conditions, locating the trial states close to one or the other energy minimum, allow a comparison of trial energies which determines very precisely the exact location of the crossing for a given MPS bond dimension [2]. Scaling with bond dimension provides an estimate of the true location of the phase transition, based on the understanding of MPS as a dressed mean-field approximation [10].

For the purposes of data uniformity, we add a very small symmetry-breaking term to the Hamiltonian when preparing the initial variational states (i.e., at the very start of the adiabatic protocol scan inside each phase), so that all data are comparable across values of χ. In particular, in the state coming from the zFM side, we break g_x by biasing toward $\otimes_j |0\rangle_j$, as this ground state is invariant under the $\mathcal{C}$ symmetry generator. The symmetry-breaking term is removed during the rest of the adiabatic protocol scan. All scans are performed independently of one another.

5.4.1 Numerical phase diagram

As we will describe in Sec. 5.5.1, the point $(\delta, K) = (0, 0)$ maps under duality to two decoupled three-state clock models tuned to the self-dual point, supported on the two sublattices of the dual lattice. The critical theory describing each sublattice is the CFT for the three-state self-dual Potts model, the minimal model with $c = 4/5$. Accordingly, this point in the phase diagram is critical with $c = 8/5$. The K perturbation in this language has the form of an energy-energy term coupling the two clock models in a way that preserves self-duality. The corresponding field theory operator is RG relevant but is in fact integrable, known to lead to a massive fixed point [11] which presumably describes the VBS phase in our context. The δ term has support on the energy operator for each of the two Potts models and is strongly relevant, breaking self-duality and precluding a perturbative expansion about this point. (It is interesting that the model with only δ perturbation is also an integrable deformation of this CFT [12].)

Our numerical data, shown in Fig. 5.1, are consistent with a "wedge" shape; that is, at $\delta = 0$ the system is in the VBS phase for any finite $K > 0$. (For $K < 0$ we find a direct first-order transition between the zFM and xFM phases along $\delta = 0$.) The data are consistent with a second-order transition between

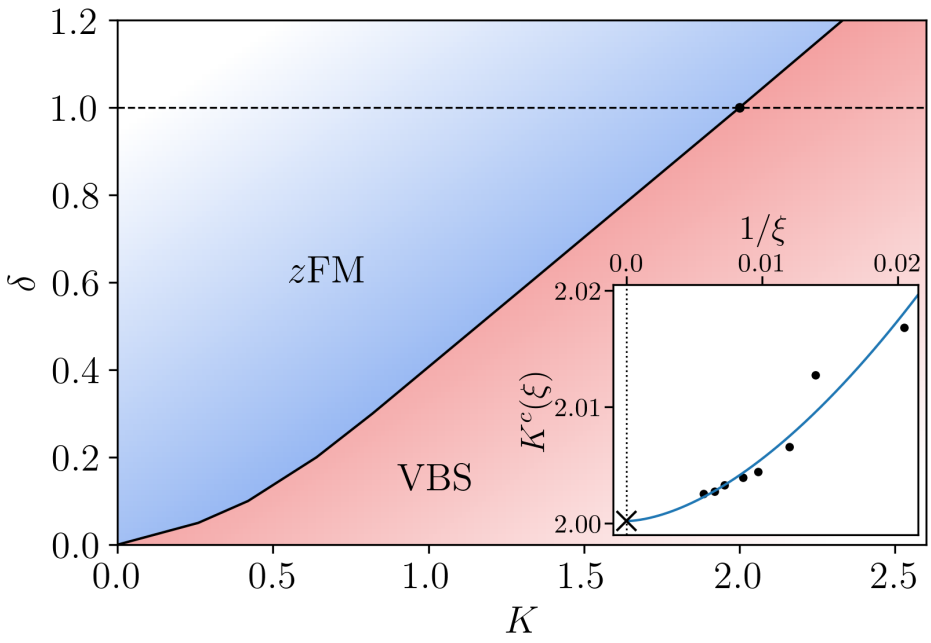

Figure 5.1: The phase diagram of $H[\delta, K]$ is determined from extrapolation in MPS correlation length of optimized variational MPS using an adiabatic protocol. The dashed line at $\delta = 1$ has an enhanced $\mathrm{U}(1) \times \mathrm{U}(1)$ onsite symmetry. The inset shows an example of the finite-entanglement process of approximating K^c. Each data point indicates a crossing of trial energies for states biased towards each symmetry-breaking order, which we scan along slices of constant δ. The data shown is for $\delta = 1$, with bond dimensions from 90 to 300 and correlation lengths between roughly 50 and 175 lattice spacings. The numerically extrapolated critical point is $K_c(\xi \to \infty) = 2.0002$. Evident in this data is a non-universal correction to the asymptotic scaling form, the magnitude of which is decreasing with $1/\xi$. We examine the $(\delta, K) = (1, 2)$ point in the phase diagram in detail in Secs. 5.6 and 5.7.

the zFM and VBS ordered phases, without continuously varying critical exponents. However, as we describe later, the situation turns out to be more complicated but also very interesting.

The slice $\delta = 1$ is indicated on Fig. 5.1, which in the original parameters of Eq. (5.11) sets $J^x = 0$ and $J^z = 2$. For $J^x = 0$ the Hamiltonian takes a simpler form:

$$H[J^x = 0, J^z, K] = -3 \sum_j \Big[J^z \sum_\alpha |\alpha\alpha\rangle\langle\alpha\alpha|_{j,j+1} + K \sum_{\alpha,\beta} |\alpha\alpha\rangle\langle\beta\beta|_{j,j+1} - (J^z + K) \Big]. \tag{5.23}$$

Along this line the global symmetry $\mathbb{Z}_3^z \times \mathbb{Z}_3^x$ is enhanced to $\mathrm{U}(1)^2 \rtimes \mathbb{Z}_3^x$, where

generators of the $\mathrm{U}(1) \times \mathrm{U}(1)$ symmetry can be constructed from any linearly independent combinations of Z and $Z^\dagger$.[1]

We represent the $\mathrm{U}(1) \times \mathrm{U}(1)$ symmetry generators by

$$\mathcal{N}_1 = \sum_j n_{1,j} = \sum_j (-1)^j |1\rangle\langle 1|_j \ , \tag{5.24}$$

$$\mathcal{N}_2 = \sum_j n_{2,j} = \sum_j (-1)^j |2\rangle\langle 2|_j \ . \tag{5.25}$$

A group element is written as

$$u(\varphi_1, \varphi_2) = e^{\mathrm{i}\,(\varphi_1 \mathcal{N}_1 + \varphi_2 \mathcal{N}_2)} = \prod_j e^{\mathrm{i}\,(\varphi_1 n_{1,j} + \varphi_2 n_{2,j})} \ , \tag{5.26}$$

and we have $g_z = u(-2\pi/3, 2\pi/3)$. The action of the other symmetry generators on $n_{a,j}$ $(a = 1, 2)$ is given by

$$g_x : \ n_{1,j} \mapsto n_{2,j}, \ n_{2,j} \mapsto (-1)^j - n_{1,j} - n_{2,j} \ , \tag{5.27}$$

$$\Theta : \ n_{a,j} \mapsto n_{a,j}, \ \mathrm{i} \mapsto -\mathrm{i} \ , \tag{5.28}$$

$$\mathcal{C} : \ n_{1,j} \mapsto n_{2,j}, \ n_{2,j} \mapsto n_{1,j} \ , \tag{5.29}$$

$$T_1 : \ n_{a,j} \mapsto -n_{a,j+1} \ , \tag{5.30}$$

$$\mathcal{I} : \ n_{a,j} \mapsto n_{a,-j} \ . \tag{5.31}$$

Note that the appearance of $(-1)^j$ in Eq. (5.27) indicates that each site forms a projective representation of the onsite symmetry group generated by g_x and $\mathcal{N}_{1,2}$. Furthermore, g_x commutes with $\mathcal{N}_{1,2}$ only in the $\mathcal{N}_1 = \mathcal{N}_2 = 0$ sector.

5.4.2 Central charge

Through a somewhat different protocol than was used to find the phase diagram, we are able to estimate the central charge at the phase transition. In this case we optimize MPS at the phase transition beginning from random initial states of small bond dimension; we then increase the bond dimension of the optimized state and re-converge. As a result, individual data points are not independent of one another, although the data for differing δ are independent. We do not explicitly break any symmetries in this scheme.

In Fig. 5.2 we show results for the central charge measured at the phase transition along cuts $\delta = 0.6, 1.0, 1.4$. In this figure we have used the extrapolated

[1] That is, the $\mathrm{U}(1)^2$ contains rotations about the generators of the Cartan subalgebra of $\mathfrak{su}(3)$. In general, in this way a q-state model can be written which is symmetric under a $\mathrm{U}(1)^{q-1}$ subgroup of $\mathrm{SU}(q)$.

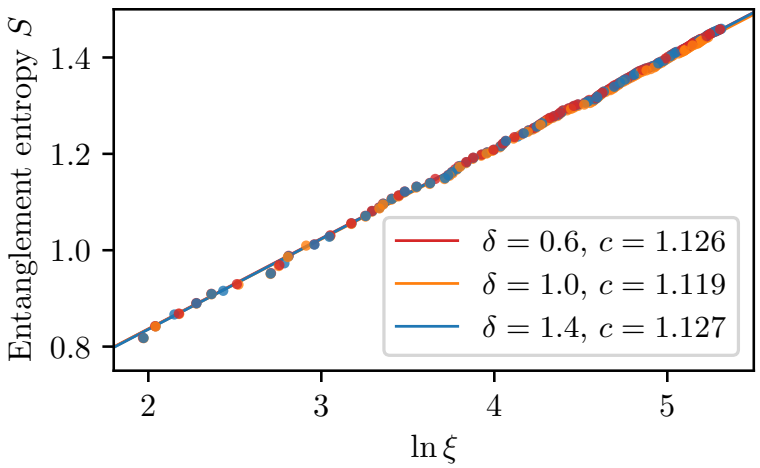

Figure 5.2: Entanglement scaling is shown at the precise phase transition for several values of δ. We draw data points in random order to emphasize consistency. Numerical c are obtained by fits to critical scaling of entanglement entropy $S = \frac{c}{6} \ln \xi$. States are optimized at the critical point but break g_x slightly. The best estimates for the exact locations of the phase transition are $(\delta, K^c) = (0.6, 1.327)$, $(1.0, 2.0)$, $(1.4, 2.664)$, which were determined by numerical extrapolations in the thermodynamic limit similar to inset in Fig. 5.1.

critical values $K^c(\delta)$ and generated MPS for these points over a large range of bond dimensions χ from 30 to 360, corresponding to ξ ranging from approximately 10 to 200. The entanglement entropy measurements are consistent with the expected critical scaling $S = \frac{c}{6} \ln \xi$, where ξ is the correlation length induced in the wavefunction by the finite MPS bond dimension.

We find nearly the same central charge at these fairly widely separated points on the phase boundary. This provides initial evidence that the phase boundary is controlled by a single fixed point. For values of δ close to 0 there is a crossover which interferes with the accurate scaling, but otherwise all results are consistent with a single fixed point.

5.4.3 Critical exponents

With optimized MPS ground states in hand describing the phase transition, measuring correlation functions of lattice operators with suitable symmetry properties allows for probing the universality based on critical indices. At a critical point various correlations display quasi-long-range order with asymptotic scaling given by $C_O(r) = \langle O^\dagger(0) O(r) \rangle - \langle O^\dagger(0) \rangle \langle O(r) \rangle \sim r^{-2\Delta_O}$ for a

local observable $O(r)$.

We focus on the line $\delta = 1$ and measure correlations at the phase transition, including of observable Z_j which carries g_x charge. We also consider $S^+_{1,j}$, which is charged under $\mathcal{N}_1$ but not $\mathcal{N}_2$:

$$S^+_{1,j} = \begin{bmatrix} 0 & p_j & 0 \\ 1-p_j & 0 & 0 \\ 0 & 0 & 0 \end{bmatrix} , \tag{5.32}$$

where p_j is the parity of j from Eq. (5.19).

We also consider the U(1) current with temporal part $n_{1,j}$ and spatial part $j_{1,j}$ derived from the conservation of $\mathcal{N}_1$. Explicitly,

$$j_{1,j} \sim (-1)^j \left(T^1_j T^2_{j+1} + T^2_j T^1_{j+1} - T^6_j T^7_{j+1} - T^7_j T^6_{j+1} \right) . \tag{5.33}$$

In order to extract long-wavelength correlations of the conserved currents, we measure

$$C_{n_1}(r = j' - j) \equiv \langle (n_{1,j} + n_{1,j+1})(n_{1,j'} + n_{1,j'+1}) \rangle \tag{5.34}$$

and similarly for $C_{j_1}(r)$.

The counterparts $S^+_{2,j}$, $n_{2,j}$, and $j_{2,j}$ are related to these operators by $\mathcal{C}$. These are all sensible for the transition at $\delta = 1$; away from this line definite charge under g_z is carried by X_j or $X^\dagger_j$, depending on p_j. However X_j and $X^\dagger_j$ are simply linear combinations of the $\mathrm{U}(1) \times \mathrm{U}(1)$ raising and lowering operators as well as other terms related by permutation symmetry, which we expect is respected at the critical point. So the critical exponent governing $S^+_{1,j}$ and $S^+_{2,j}$ will also determine the decay of correlations of X_j. We confirmed the symmetry numerically but do not show these results, instead summarizing this family of operators by $S^+_{1,j}$ only, and similarly for $n_{1,j}$ and $j_{1,j}$.

We also measure the 0-momentum and π-momentum components of the energy term $E_j = \overline{T}^a_j T^a_{j+1}$ which is invariant under the full internal symmetry group:

$$\epsilon^0_j = E_j + E_{j+1} , \tag{5.35}$$

$$\epsilon^\pi_j = E_j - E_{j+1} . \tag{5.36}$$

The operator ϵ^π_j is the natural lattice operator for VBS correlations, being in the singlet sector of all internal symmetries [actually the entire SU(3)] but odd under $\mathbb{Z}_2$ translation symmetry.

Finally, we wish to investigate the conjecture that the critical theory at the point $\delta = 1$ in fact controls the entire phase boundary. This would imply that the $\mathrm{U}(1) \times \mathrm{U}(1)$ symmetry of the line $\delta = 1$ is emergent at the transition for other values of δ; equivalently, terms breaking the symmetry are irrelevant at the transition for $\delta = 1$. We measure correlations of a term which carries charge under $\mathrm{U}(1)^2$ but preserves all symmetries of H in Eq. (5.11). Specifically, consider the following operator:

$$\mathcal{A} = \sum_j A_j \ , \tag{5.37}$$

with

$$A_j = \sum_{h \in S_3} \left(|h(1)\rangle\langle h(0)|_j \otimes |h(0)\rangle\langle h(2)|_{j+1} + \text{H.c.} \right) . \tag{5.38}$$

The sum is over elements of the permutation group, and the term corresponding to the identity element $e = (012)$ is $S^+_{1,j} S^+_{2,j+1} + S^-_{1,j} S^-_{2,j+1}$. It is easy to see that $\mathcal{A}$ respects g_z, g_x, $\mathcal{C}$, Θ, and lattice symmetries, while all terms in $\mathcal{A}$ break $\mathcal{N}_1$ and $\mathcal{N}_2$. We thus interpret $\mathcal{A}$ as a field-like term driving $\mathrm{U}(1) \times \mathrm{U}(1)$ symmetry breaking, hence maintaining criticality to leading order in the field.

Based on the above interpretation, we can predict the slope of the phase boundary in the phase diagram at $\delta = 1$ in Fig. 5.1. As mentioned there, the critical point H^* appears to be $(\delta, K) = (1, 2)$, where $J_z = K$. Now we suppose that $\mathcal{A}$ turns out to be the most relevant symmetry-breaking operator, and moreover that $H^* + \lambda \mathcal{A}$ remains critical to leading order in λ. Decomposing this term into the (δ, K) basis, which control terms $(X_j X_{j+1} - Z_j^\dagger Z_{j+1} + \text{H.c.})$ and $6\overline{T}^a_j T^a_{j+1}$, respectively, yields the unique solution

$$A_j = \left(X_j X_{j+1} + \frac{1}{3} Z_j^\dagger Z_{j+1} + \text{H.c.} \right) + 2\overline{T}^a_j T^a_{j+1} \tag{5.39}$$

$$= (X_j X_{j+1} - Z_j^\dagger Z_{j+1} + \text{H.c.}) + \frac{5}{3} \left(6\overline{T}^a_j T^a_{j+1} \right) + \frac{4}{3} \left((Z_j^\dagger Z_{j+1} + \text{H.c.}) - 6\overline{T}^a_j T^a_{j+1} \right) . \tag{5.40}$$

The final line in Eq. (5.40) simply changes the overall scale of H^*, allowing it to be removed from the perturbation term in this picture. So as a consequence of the conjectured irrelevance of this $\mathrm{U}(1)^2$ symmetry-breaking term, we predict that the critical manifold in these variables has slope $d\delta/dK = \frac{3}{5}$ at $(\delta, K) = (1, 2)$; this is highly consistent with the numerical data shown in Fig. 5.1.

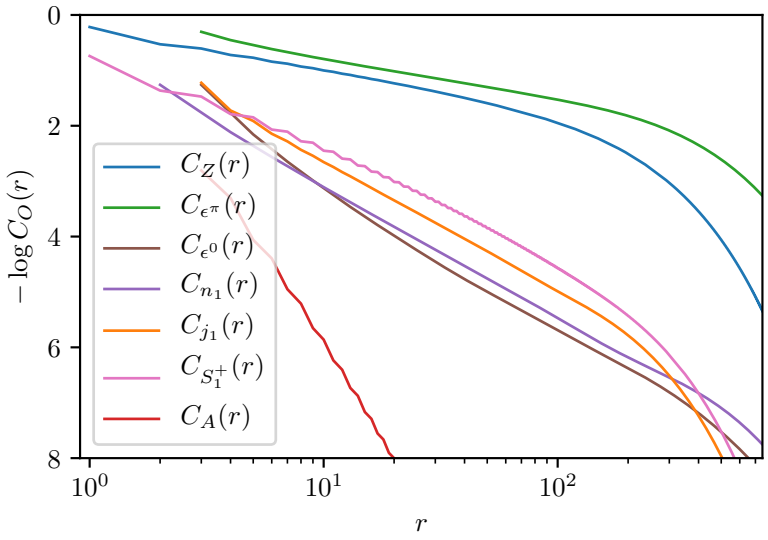

O	Z	ϵ^π	ϵ^0	n_1	j_1	S_1^+	A
Δ_O^d	0.36	0.37	1.15	1.17	1.17	0.89	3.77

Figure 5.3: Direct measurements of correlations are taken from an MPS of bond dimension $\chi = 300$ optimized for the phase transition at $\delta = 1$, with translation invariance; that is, biased towards breaking g_x. These operators are described in Sec. 5.4.3, and all correlations measure the connected component. In the trace of C_{ϵ^0} we include only odd separations r in the interest of visual clarity; the power law is unaffected.

Direct approach

The most straightforward approach to determining scaling dimensions is simply to measure the correlation function in real space and fit to a power law form. We refer to this as the "direct approach," following terminology used in Ref. [13]. This is very similar to the procedure used in Ref. [2] to fit critical indices for the transition between Ising FM and VBS. As was the case there, we determine a power law for the decay of correlations for a single bond dimension (usually the largest studied). However, in contrast to that work we will always use the connected correlations; accordingly, we will not obtain bounds on exponents as we did there but rather simple estimates. We suspect that this measurement will tend to overestimate operator scaling dimensions as a result of the finite length scale induced by the MPS bond dimension even at a critical point. In addition, the direct approach suffers from ambiguity in determining the appropriate intermediate power-law region between non-universal short-distance behavior and eventual exponential decay. We show

the results of these measurements in Fig. 5.3.

There is already an interesting observation visible in the raw data; namely, that the magnetic zFM and VBS observables have very similar power laws. This is suggestive of some enhanced symmetry unifying the two order parameters at the putative critical point, a characteristic property of DQCP.

Finite-entanglement scaling approach

As mentioned previously, finite-entanglement approximations necessarily induce a length scale; here the MPS correlation length ξ introduces some scaling function to the critical correlations which eventually decays exponentially. One technique to counteract this is referred to as "finite-entanglement scaling" (FES) [13], which is based on the observation that irrespective of the functional form of the correlations with a length scale, one finds that $C_O(s\xi) \sim (s\xi)^{-2\Delta_O}$. Here s is a dimensionless fraction which is kept fixed as one varies bond dimension (and hence ξ). We employ this more sophisticated strategy which incorporates data from multiple optimized MPS in Fig. 5.4, and provide a comparison with the direct results.

One sees that the direct approach tends to overestimate scaling dimensions as compared to FES, with the exception of the $S^+_{1,2}$ operators, whose raw data is not amenable to a power-law fit. Other results are qualitatively consistent with the direct approach, with highly relevant operators in the magnetic and translation symmetry–breaking sectors, along with other less-relevant operators charged under the U(1) symmetries and in the singlet sector. The expectation that the conserved space-time current components n_1 and j_1 have scaling dimension 1 is reasonably well satisfied. Additionally, the similarity between the zFM and VBS order parameters is maintained in this approach, albeit with slower power laws. The correlations C_A decay below the measurement error threshold too quickly to effectively treat with the FES method and are not shown.

From the scaling dimensions Δ_Z, Δ_{ϵ^π}, and Δ_{ϵ^0} measured in correlation functions we can provide numerical estimates of the critical indices characterizing the transition. The FES scaling dimensions generally depend on s, and there is no *a priori* best value of this parameter to choose. Fortunately our measurements do not vary widely, and for lack of a better option we will choose $s = 1$. These values are given in Fig. 5.4, and the reader is free to

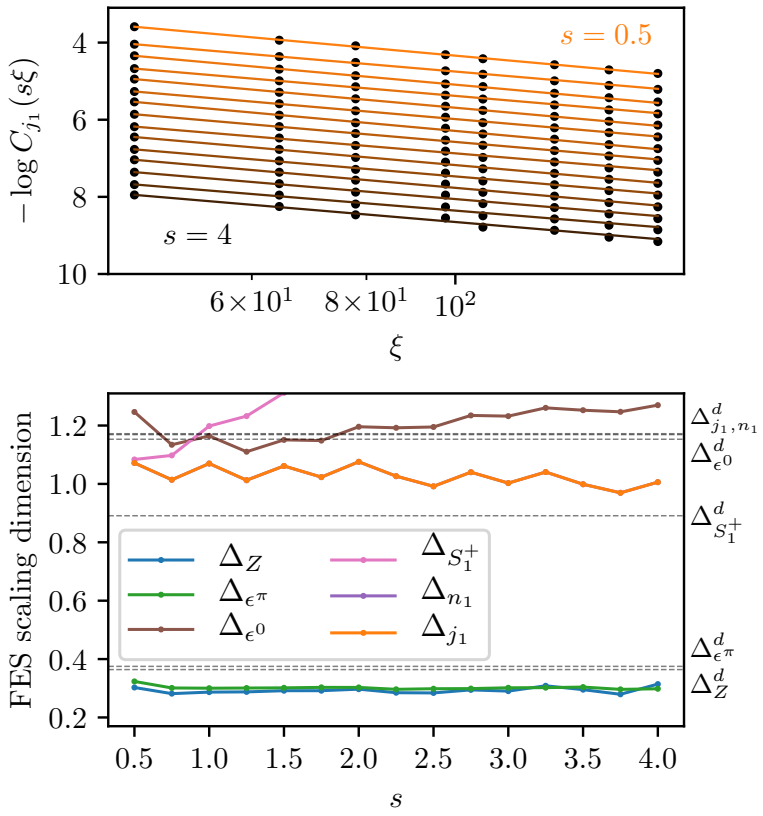

O	Z	ϵ^π	ϵ^0	n_1	j_1	S_1^+
$\Delta_O(s=1)$	0.29	0.30	1.16	1.07	1.07	1.20

Figure 5.4: In the FES approach we measure the correlations $C_O(s\xi)$ for a range of fixed dimensionless fractions s and varying ξ. The top panel shows data for the spatial part of the U(1) current $j_{1,j}$. For $s > 1$ the raw data is already in the exponential decay regime of Fig. 5.3, while this approach still exhibits consistent power law scaling; thus FES is indeed largely insensitive to the scaling function induced by finite MPS bond dimension. In the bottom panel we show scaling dimensions as a function of s. Δ_{j_1} and Δ_{n_1} are visually identical for all values of s. We do not include A, whose correlations decay too quickly to use this method. Horizontal lines marked Δ^d indicate values found by power-law fits in the direct approach in Fig. 5.3. In the table, we provide FES results at $s = 1$.

decide how seriously to take the numbers. The correlation length exponent we compute is $\nu = 1/(2 - \Delta_{\epsilon^0}) \approx 1.2$ and the order parameter exponents are $\beta_{z\mathrm{FM}} = \nu\Delta_Z \approx \beta_{\mathrm{VBS}} = \nu\Delta_{\epsilon^\pi} \approx 0.35$. Due to the strong irrelevance of the $\mathcal{A}$ perturbation breaking U(1) × U(1) symmetry, we predict that these critical indices describe an extended region of the phase boundary.

We revisit these measurements in Sec. 5.7 and compare with results from exact

diagonalization, identifying these operators with primary fields in a putative CFT where possible.

5.5 Theories of phase transition

5.5.1 Domain wall description

We write the standard duality mapping to $\mathbb{Z}_3$ domain wall variables on the dual lattice. Denote these operators by $\widetilde{Z}_{j+1/2}$ and $\widetilde{X}_{j+1/2}$:

$$\widetilde{X}_{j+1/2} = Z_j^\dagger Z_{j+1} \ , \tag{5.41}$$

$$\widetilde{Z}_{j+1/2} = \prod_{i\leq j} X_i \ , \tag{5.42}$$

$$\widetilde{Z}_{j-1/2}^\dagger \widetilde{Z}_{j+1/2} = X_j \ . \tag{5.43}$$

The dual operators satisfy $\widetilde{Z}\widetilde{X} = \omega \widetilde{X}\widetilde{Z}$. In these variables H is written (up to constant terms)

$$\begin{aligned}\widetilde{H} = -\sum_j \Big[& (J^x \widetilde{Z}_{j-1/2}^\dagger \widetilde{Z}_{j+3/2} + J^z \widetilde{X}_{j+1/2} + \text{H.c.}) \\ & + K(1 + \widetilde{Z}_{j-1/2}^\dagger \widetilde{Z}_{j+3/2} + \text{H.c.})(1 + \widetilde{X}_{j+1/2} + \text{H.c.}) \Big] \ ,\end{aligned} \tag{5.44}$$

and the generators of the $\mathbb{Z}_3^x \times \mathbb{Z}_3^z$ symmetry as

$$g_x = \prod_j \widetilde{Z}_{j-1/2}^\dagger \widetilde{Z}_{j+1/2} = 1 \ , \quad g_z = \prod_k \widetilde{X}_{2k+1/2} \ . \tag{5.45}$$

That on a periodic chain g_x appears trivial is a symptom of this duality failing to account for the global symmetry aspects of the model on such a chain. In App. 5.C, we formulate the duality on a periodic chain and account for all global aspects by using a dual $\mathbb{Z}_3$ gauge field. We can view the analysis in this section as being performed in a fixed gauge.

The action of the symmetries on the dual variables is

$$g_x : \ (\widetilde{X}_{j+1/2}, \widetilde{Z}_{j+1/2}) \mapsto (\widetilde{X}_{j+1/2}, \widetilde{Z}_{j+1/2}) \ , \tag{5.46}$$

$$g_z : \ (\widetilde{X}_{j+1/2}, \widetilde{Z}_{j+1/2}) \mapsto (\widetilde{X}_{j+1/2}, \omega^{p_j - 1} \widetilde{Z}_{j+1/2}) \ , \tag{5.47}$$

$$\Theta : \ (\widetilde{X}_{j+1/2}, \widetilde{Z}_{j+1/2}) \mapsto (\widetilde{X}_{j+1/2}^\dagger, \widetilde{Z}_{j+1/2}), \ \mathrm{i} \mapsto -\mathrm{i} \ , \tag{5.48}$$

$$\mathcal{C} : \ (\widetilde{X}_{j+1/2}, \widetilde{Z}_{j+1/2}) \mapsto (\widetilde{X}_{j+1/2}^\dagger, \widetilde{Z}_{j+1/2}^\dagger) \ , \tag{5.49}$$

$$T_1 : \ (\widetilde{X}_{j+1/2}, \widetilde{Z}_{j+1/2}) \mapsto (\widetilde{X}_{j+3/2}, \widetilde{Z}_{j+3/2}) \ , \tag{5.50}$$

$$\mathcal{I} : \ (\widetilde{X}_{j+1/2}, \widetilde{Z}_{j+1/2}) \mapsto (\widetilde{X}_{-(j+1/2)}, \widetilde{Z}_{-(j+1/2)}) \ . \tag{5.51}$$

The dual Hamiltonian Eq. (5.44) can be viewed as two individual 3-state clock models residing on the "even" and "odd" sublattices of the dual lattice (locations $2k + 1/2$ and $2k + 3/2$, $k \in \mathbb{Z}$, respectively), with energy-energy coupling between them. Physically, when all domain walls are gapped (that is, $\langle \widetilde{Z}_{\text{odd}} \rangle = \langle \widetilde{Z}_{\text{even}} \rangle = 0$), the zFM order is preserved. The threefold degeneracy of this phase is encoded in the gauge sector presented in full in App. 5.C.

Other phases can be obtained by various condensation patterns of the domain wall variables. For example, condensing $\langle \widetilde{Z}_{\text{odd}} \rangle = \langle \widetilde{Z}_{\text{even}} \rangle \neq 0$ breaks g_z but preserves g_x, $\mathcal{C}$, Θ, and T_1. We thus identify this with the particular classical state $\bigotimes_j |0_x\rangle_j$ in the xFM phase. The other classical states in this phase break $\mathcal{C}$ and T_1 but preserve $T_1\mathcal{C}$. These correspond to $\langle \widetilde{Z}_{\text{odd}} \rangle = \omega^{\pm 1} \langle \widetilde{Z}_{\text{even}} \rangle \neq 0$. It appears naively that there are a total of nine degenerate minima; however, when global symmetry aspects are accounted for, there are indeed only three degenerate ground states.

By instead condensing domain walls as $\langle \widetilde{Z}_{\text{odd}} \rangle \neq 0$ and $\langle \widetilde{Z}_{\text{even}} \rangle = 0$, or vice versa, one finds a phase which breaks translation symmetry and has twofold ground state degeneracy. We identify this condensate with the VBS phase in the lattice model. While this order parameter appears to transform nontrivially under g_z in the above equation, its value is not gauge-invariant, and this phase in fact respects the full internal symmetry group. From the perspective of the zFM in this language, the VBS is a particular Higgs phase, with the transition accomplished by condensing domain walls on only one sublattice of the dual lattice.

One can write a schematic theory of coarse-grained domain walls described by complex fields $w_A \sim \widetilde{Z}_{\text{odd}}$, $w_B \sim \widetilde{Z}_{\text{even}}$, transforming as

$$g_x : \ (w_A, w_B) \mapsto (w_A, w_B) \ , \tag{5.52}$$

$$g_z : \ (w_A, w_B) \mapsto (w_A, \omega^{-1} w_B) \ , \tag{5.53}$$

$$\Theta : \ (w_A, w_B) \mapsto (w_A, w_B), \ \mathrm{i} \mapsto -\mathrm{i} \ , \tag{5.54}$$

$$\mathcal{C} : \ (w_A, w_B) \mapsto (w_A^\dagger, w_B^\dagger) \ , \tag{5.55}$$

$$T_1 : \ (w_A, w_B) \mapsto (w_B, w_A) \ , \tag{5.56}$$

$$\mathcal{I} : \ (w_A, w_B) \mapsto (w_A, w_B) \ . \tag{5.57}$$

The associated Lagrangian reads

$$\mathcal{L} = \mathcal{L}_A + \mathcal{L}_B + \mathcal{L}_{AB} \ , \tag{5.58}$$

$$\mathcal{L}_\alpha = t|w_\alpha|^2 + u_3(w_\alpha^3 + c.c.) + u_4|w_\alpha|^4 + \cdots \ , \tag{5.59}$$

$$\mathcal{L}_{AB} = \lambda|w_A|^2|w_B|^2 + \cdots \ , \tag{5.60}$$

where $\mathcal{L}_\alpha$ is a schematic theory for the $\mathbb{Z}_3$ ordering transition on each sublattice. Gradient terms are omitted for simplicity. In addition to the usual mass term t and quartic term u_4, the symmetries allow the $\mathbb{Z}_3$ anisotropy term u_3, which energetically distinguishes three particular directions to capture the qualitative physics of the underlying $\mathbb{Z}_3$ clock variables $\widetilde{Z}_{\text{odd/even}}$.

In the absence of coupling between the two sublattices, the critical point (on each sublattice) is obtained by tuning the parameter t. Schematically, for "renormalized" $t_{\text{renorm}} > 0$ the fields w_A and w_B are both gapped, which for the original system corresponds to the zFM phase. In contrast, for $t_{\text{renorm}} < 0$ both fields condense; in the original system this corresponds to the xFM phase. This is not a tractable field theory for describing the $\mathbb{Z}_3$ criticality; instead, the actual critical properties are known from exact solutions of lattice models or study of the IR theory, which is a conformal minimal model. Nevertheless, this schematic writing simplifies the discussion of the domain wall theory.

$\mathcal{L}_{AB}$ represents coupling between the $\mathbb{Z}_3$ systems on the two sublattices. In our model, this has the form of energy-energy coupling, for which we write the most relevant term with amplitude λ.[2] It is known from the CFT description of the $\mathbb{Z}_3$ criticality that the energy-energy coupling is relevant at the decoupled point.

Consider now the full theory including $\mathcal{L}_{AB}$. By lowering t, one allows domain walls to proliferate and destroy the zFM order. Focusing on the quartic terms, if $\lambda < 2u_4$ both domain walls want to condense simultaneously, leading to the

[2]Additional terms in $\mathcal{L}_{AB}$ in Eq. (5.60) can be obtained, e.g., by forming symmetric combinations of products of terms in $\mathcal{L}_A$ and $\mathcal{L}_B$. The listed symmetries allow terms like $\kappa[(w_A w_B)^3 + \text{H.c.}]$ and $\kappa'[(w_A^\dagger w_B)^3 + \text{H.c.}]$ which individually are not energy-energy terms between the subsystems A and B. However, our specific lattice model in the dual formulation has an additional symmetry which acts like $\mathcal{C}$ on one sublattice only; that is, $\tilde{\mathcal{C}}_A : \tilde{Z}_{2k-1/2} \mapsto \tilde{Z}^\dagger_{2k-1/2}, \tilde{Z}_{2k+1/2} \mapsto \tilde{Z}_{2k+1/2}, w_A \mapsto w_A^\dagger, w_B \mapsto w_B$. This requires $\kappa = \kappa'$, and the combined term is an energy-energy term. This minor difference between general models with the defined symmetries and our specific model is not used in any essential way. The above additional symmetry of the lattice model which is manifest in the dual formulation is non-local in the original formulation.

xFM phase. (As described previously, the above Lagrangian does not include the dual $\mathbb{Z}_3$ gauge field needed to account for global symmetry aspects, which reduces the ground state degeneracy in this case to only three ground states.) If instead $\lambda > 2u_4$ it is energetically favorable for only one domain wall species to condense, with two possibilities: either $\langle w_A \rangle \neq 0$, $\langle w_B \rangle = 0$ or $\langle w_A \rangle = 0$, $\langle w_B \rangle \neq 0$, which correspond to the two degenerate ground states of the VBS phase.

In our lattice model, the above two regimes correspond to $K < 0$, where we find a transition from the zFM to the xFM phase, and to $K > 0$, where we find the VBS phase. Furthermore, along the $\delta = 0$ line we find a first-order zFM-xFM phase boundary for $K < 0$ while the VBS phase immediately opens up for $K > 0$. This is consistent with the relevance of the energy-energy coupling at the decoupled point $(\delta, K) = (0, 0)$, taken together with the above schematic energetics picture of the preferred domain wall condensation patterns for $K < 0$ and $K > 0$. Moreover, in our model along the line $\delta = 0$, the domain wall theory is invariant under a simultaneous duality transformation for each species A and B, treated as their own $\mathbb{Z}_3$ chains, which we interpret as maintaining the "thermal" variable $t_{\text{eff}} = 0$ and allowing only the energy-energy coupling to flow. The runaway flows are then interpreted as leading to coexistence of zFM and xFM on one side—having w_A and w_B both gapped or both condensed being energetically equal by the above self-duality—and the VBS phase on the other side.

We can now discuss the zFM-VBS phase boundary, which requires perturbing from the decoupled point in both t and λ directions in the field theory (both δ and K in our lattice model). In the low-energy theory at the decoupled point $(\delta, K) = (0, 0)$ both couplings t and λ are relevant, with scaling dimensions $4/5$ and $8/5$, respectively. The leading flow equations are $dt/d\ell = (6/5)t + \cdots$ and $d\lambda/d\ell = (2/5)\lambda + \cdots$; in particular, $t(\ell) \sim \lambda(\ell)^3$ along the flows near the decoupled point. To be on the phase boundary, the couplings t and λ must balance one another. Thus we predict that the phase boundary has the shape $\delta_c(K) \sim K^3$ near the decoupled point.

Unfortunately, we do not know the ultimate fate of this type of balanced flow of two relevant couplings. One possibility is that the flow leads to a new fixed point with only one relevant direction, which would then describe a generic continuous zFM-VBS transition. The alternative is that there is no such new

fixed point, and a runaway flow is interpreted as corresponding to a first-order zFM-VBS transition. The above "theory" does not provide a controlled way to study this question, but we hope that it will motivate more research in this problem.

5.5.2 Theory for $\mathrm{U}(1) \times \mathrm{U}(1)$-symmetric model

Bosonized variables

The apparently emergent $\mathrm{U}(1) \times \mathrm{U}(1)$ symmetry invites treatment via bosonization [14–16]. Consider the model along the $\delta = 1$ line where it has microscopic $\mathrm{U}(1) \times \mathrm{U}(1)$ symmetry. This model can be approximated by two coupled U(1) rotors with variables $(n_{a,j}, \phi_{a,j})$, $a = 1, 2$, defined by

$$(-1)^j |a\rangle\langle a| \sim n_{a,j} \ , \quad S^+_{a,j} \sim \mathrm{e}^{\mathrm{i}\,\phi_{a,j}} \ , \tag{5.61}$$

where $[n_{a,i}, \phi_{a',j}] = \mathrm{i}\,\delta_{aa'}\,\delta_{ij}$.

To begin writing the field theory description, we first determine the average filling in this system. The filling number is constrained by the action of g_x in Eq. (5.27); for a fully symmetric state we have

$$\langle n_{1,j} \rangle = \langle n_{2,j} \rangle = \frac{(-1)^j}{3} \ . \tag{5.62}$$

Next, to capture fluctuations $\delta n_a \equiv n_a - \langle n_a \rangle$ we introduce bond variables $\theta_{a,j+1/2}$, where

$$\delta n_{a,j} = \frac{1}{\pi} \left(\theta_{a,j+1/2} - \theta_{a,j-1/2} \right) \ . \tag{5.63}$$

We choose $\theta_{a,j+1/2}$ as follows:

$$\begin{aligned} \theta_{a,2k-1/2} &= \sum_{j' \le 2k-1} \pi\, n_{a,j'} \ , \\ \theta_{a,2k+1/2} &= \sum_{j' \le 2k} \pi\, n_{a,j'} + \frac{\pi}{3} \ . \end{aligned} \tag{5.64}$$

The commutator between θ_a and $\phi_{a'}$ is

$$[\theta_{a,j+1/2}, \phi_{a',j'}] = \mathrm{i}\,\pi\,\delta_{aa'}\,\Theta(j + 1/2 - j') \ , \tag{5.65}$$

where $\Theta(x)$ is the Heaviside step function.

To get to the low-energy theory, we define long-wavelength fields $\theta_{1,2}(x)$ and $\phi_{1,2}(x)$ in continuum space, where $\theta_{1,2}(x)$ are real-valued with periodicity π

and $\phi_{1,2}(x)$ have periodicity 2π. These fields satisfy

$$\left[\frac{\partial_x \theta_a(x)}{\pi}, \phi_{a'}(x')\right] = \mathrm{i}\,\delta_{aa'}\,\delta(x-x')\ . \tag{5.66}$$

The action of the symmetries on the fields can be deduced from their lattice operator counterparts in Eqs. (5.61) and (5.64):

$$u(\varphi_1,\varphi_2) : (\phi_1,\theta_1,\phi_2,\theta_2) \to \phi_1+\varphi_1, \theta_1, \phi_2+\varphi_2, \theta_2)\ , \tag{5.67}$$

$$g_x : (\phi_1,\theta_1,\phi_2,\theta_2) \to (-\phi_1+\phi_2, \theta_2, -\phi_1, -\theta_1-\theta_2)\ , \tag{5.68}$$

$$\Theta : (\phi_1,\theta_1,\phi_2,\theta_2) \to (-\phi_1, \theta_1, -\phi_2, \theta_2)\ ,\ \ \mathrm{i} \to -\mathrm{i}\ , \tag{5.69}$$

$$\mathcal{C} : (\phi_1,\theta_1,\phi_2,\theta_2) \to (\phi_2, \theta_2, \phi_1, \theta_1)\ , \tag{5.70}$$

$$T_1 : (\phi_1,\theta_1,\phi_2,\theta_2) \to \left(-\phi_1, -\theta_1+\frac{\pi}{3}, -\phi_2, -\theta_2+\frac{\pi}{3}\right)\ , \tag{5.71}$$

$$\mathcal{I} : (\phi_1(x),\theta_1(x),\phi_2(x),\theta_2(x)) \to \left(\phi_1(-x), -\theta_1(-x)+\frac{\pi}{3}, \phi_2(-x), -\theta_2(-x)+\frac{\pi}{3}\right). \tag{5.72}$$

We are now ready to write down the low-energy theory. The symmetry-allowed Gaussian part reads

$$\mathcal{L}_0 = \sum_{a=1}^{2}\left[\frac{\mathrm{i}}{\pi}\partial_\tau\phi_a\partial_x\theta_a + \frac{v}{2\pi}\left(g(\partial_x\phi_a)^2 + \frac{1}{g}(\partial_x\theta_a)^2\right)\right] + \frac{v}{2\pi}\left(-g\partial_x\phi_1\partial_x\phi_2 + \frac{1}{g}\partial_x\theta_1\partial_x\theta_2\right), \tag{5.73}$$

with a single tunable "Luttinger parameter" g and one "velocity parameter" v. There are two types of symmetric scattering terms:

1. Type I ($m \in \mathbb{Z}$):

$$\lambda_m^I\left[\cos\left(2m(\theta_1+\theta_2)-\frac{2m\pi}{3}\right)+\cos\left(2m\theta_1+\frac{2m\pi}{3}\right)+\cos\left(2m\theta_2+\frac{2m\pi}{3}\right)\right], \tag{5.74}$$

2. Type II ($m \in \mathbb{Z}$):

$$\lambda_m^{II}\left[\cos\left(2m(\theta_1-\theta_2)\right)+\cos\left(2m(\theta_1+2\theta_2)\right)+\cos\left(2m(2\theta_1+\theta_2)\right)\right]. \tag{5.75}$$

The scaling dimensions for generic exponentials of the fields at the Gaussian fixed point are given by [17]:

$$\dim\left[\exp(\mathrm{i}\,(2m_1\theta_1+2m_2\theta_2))\right]=\frac{2g}{\sqrt{3}}(m_1^2-m_1m_2+m_2^2), \tag{5.76}$$

$$\dim\left[\exp(\mathrm{i}\,(p_1\phi_1+p_2\phi_2))\right]=\frac{1}{2\sqrt{3}g}(p_1^2+p_1p_2+p_2^2). \tag{5.77}$$

We now list some important operators in this bosonized language (identified either microscopically or by using the symmetry transformations in Eqs. (5.67–5.72)) along with their scaling dimensions at the Gaussian fixed point.

- As discussed before, operators carrying unit charges under $\mathrm{U}(1)\times\mathrm{U}(1)$ are $S^+_{1,2}\sim\exp(\mathrm{i}\,\phi_{1,2})$, which have scaling dimensions $\dim[S^+_{1,2}]=\frac{1}{2\sqrt{3}g}$.
- The operator A defined in Eq. (5.38), which breaks $\mathrm{U}(1)\times\mathrm{U}(1)$ to $\mathbb{Z}_3^z$, reads

  $$A\sim\cos(\phi_1+\phi_2)+\cos(2\phi_1-\phi_2)+\cos(\phi_1-2\phi_2)\ , \tag{5.78}$$

  and $\dim[A]=\frac{\sqrt{3}}{2g}$.
- The zFM order parameter is given by

  $$O_{z\mathrm{FM}}\sim\cos\left(2\theta_1+2\theta_2-\frac{2\pi}{3}\right)+\mathrm{e}^{2\mathrm{i}\,\pi/3}\cos\left(2\theta_1+\frac{2\pi}{3}\right)+\mathrm{e}^{-2\mathrm{i}\,\pi/3}\cos\left(2\theta_2+\frac{2\pi}{3}\right)\ , \tag{5.79}$$

  and $\dim[O_{z\mathrm{FM}}]=\frac{2g}{\sqrt{3}}$.
- The VBS order parameter reads

  $$O_{\mathrm{VBS}}\sim\cos\left(2\theta_1+2\theta_2-\frac{\pi}{6}\right)+\cos\left(2\theta_1+\frac{\pi}{6}\right)+\cos\left(2\theta_2+\frac{\pi}{6}\right)\ , \tag{5.80}$$

  and $\dim[O_{\mathrm{VBS}}]=\frac{2g}{\sqrt{3}}$.

It is interesting to note that at the Gaussian fixed point, the zFM and VBS order parameters have the same scaling dimension, which also coincides with the scaling dimension of the leading allowed scattering term, given by Eq. (5.74) with $m=1$. Furthermore, we have the relation

$$\frac{\dim[S^+_a]}{\dim[A]}=\dim[S^+_a]\dim[O_{z\mathrm{FM}}]=\frac{1}{3}\ . \tag{5.81}$$

When $g > \sqrt{3}$, all allowed scattering terms are irrelevant and this system is in a stable gapless phase described by the Gaussian fixed point, with power law exponents as described above. This phase is stable as long as the $\mathrm{U}(1) \times \mathrm{U}(1)$ symmetry is present microscopically. Note, however, that we did not find this phase in our lattice model along the $\delta = 1$ line, but it would be interesting to look for it in some model deformations in the future. On the other hand, if the $\mathrm{U}(1) \times \mathrm{U}(1)$ symmetry is broken down to $\mathbb{Z}_3^z$ and the A term is allowed, one cannot simultaneously make this term and all scattering terms irrelevant and the gapless phase is unstable.

Gapped phases and "classical phase diagram" in the bosonized variables

We now develop the representation of various gapped phases in this theory. Different gapped quantum phases correspond to different patterns of $\langle \phi_{1,2} \rangle$ or $\langle \theta_{1,2} \rangle$. As a consequence of the Mermin–Wagner theorem, in the $\mathrm{U}(1) \times \mathrm{U}(1)$-symmetric model $\phi_{1,2}$ never condense and we always have $\langle \exp(\mathrm{i}\,\phi_1) \rangle = \langle \exp(\mathrm{i}\,\phi_2) \rangle = 0$.

For quantum states preserving T_1, we require $\langle \theta_{1,2} \rangle = \pi/6$ or $-\pi/3 \pmod{\pi}$. For quantum states preserving g_x, we require $\langle \theta_1 \rangle = \langle \theta_2 \rangle = 0$ or $\pm\pi/3 \pmod{\pi}$. We are then able to represent the gapped phases appearing in the previous sections as follows:

- $\langle \theta_1 \rangle = \langle \theta_2 \rangle = -\pi/3$ gives a fully symmetric phase. The detailed study of this SPT phase is presented in App. 5.A.2.
- $\langle \theta_1 \rangle = \langle \theta_2 \rangle = 0$ or $\pi/3$ gives the two degenerate ground states of the VBS phase.
- $(\langle \theta_1 \rangle, \langle \theta_2 \rangle) = (\pi/6, \pi/6), (\pi/6, -\pi/3), (-\pi/3, \pi/6)$ gives the three degenerate zFM ground states.

The classical phase diagram of this two-component Luttinger liquid theory is obtained by minimizing the energy of the scattering terms. We first consider the symmetric scattering term Eq. (5.74) with $m = 1$, which we label V_1^I. Its scaling dimension is $2g/\sqrt{3}$, the lowest among symmetric terms; it is relevant for $g < \sqrt{3}$. When $\lambda_1^I < 0$, V_1^I is minimized at $\theta_1 = \theta_2 = -\pi/3$, and thus gives the symmetric phase. When $\lambda_1^I > 0$, it is instead minimized at $\theta_1 = \theta_2 = 0$

or $\pi/3$, and thus gives the VBS phase. If we also have $g > 1/\sqrt{3}$ so that the next scattering term—Eq. (5.75) with $m = 1$—is irrelevant, the VBS to SPT transition is obtained when the single relevant coupling λ_1^I changes sign and is described by the Gaussian theory in Eq. (5.73). The correlation length exponent at this transition is set by the scaling dimension of V_1^I: $\nu = 1/(2 - 2g/\sqrt{3})$, while the power law correlations of various observables are governed by the scaling dimensions we have calculated. It is interesting that even though zFM order is not present on either side of the transition, its correlations decay with the same power law as the VBS order present on one side.

To describe the zFM phase and its transition to the VBS phase, we add the next scattering term (Eq. (5.75) with $m = 1$), labelled V_1^{II}. Thus the combined scattering term is

$$V = V_1^I + V_1^{II} \ . \tag{5.82}$$

When $g < 1/\sqrt{3}$, both V_1^I and V_1^{II} are relevant.

We parametrize $\lambda_1^{I,II}$ by λ and α, where $\lambda_1^I = \lambda \cos\alpha$ and $\lambda_1^{II} = \lambda \sin\alpha$. For each α, we identify all minima of Eq. (5.82), and associate classical phases with the minima by analysis of symmetry properties. The resulting phase diagram is shown in Fig. 5.5.

When $\arctan(1/8) < \alpha \leq \pi/4$, then $(\theta_1, \theta_2)_{\min} = (\pi/6, \pi/6)$, $(\pi/6, -\pi/3)$ or $(-\pi/3, \pi/6)$, which gives the zFM phase. We can also identify representative lattice wavefunctions for these three states by studying their transformation properties under $\mathcal{C}$ and g_x:

$$\left(\frac{\pi}{6}, \frac{\pi}{6}\right) \sim \bigotimes_j |0\rangle_j \ , \quad \left(\frac{\pi}{6}, -\frac{\pi}{3}\right) \sim \bigotimes_j |1\rangle_j \ , \quad \left(-\frac{\pi}{3}, \frac{\pi}{6}\right) \sim \bigotimes_j |2\rangle_j \ . \tag{5.83}$$

When $-\pi/2 < \alpha < \arctan(1/8)$, we find $(\theta_1, \theta_2)_{\min} = (0, 0)$ or $(\pi/3, \pi/3)$, which gives the VBS phase.

When $-\pi - \arctan(1/3) \leq \alpha < -\pi/2$, $(\theta_1, \theta_2)_{\min} = (-\pi/3, -\pi/3)$, and we find the symmetric phase.

When $\pi/4 < \alpha < \pi - \arctan(1/3)$, we get six degenerate minima, which can be parameterized by a single variable υ:

$$(\theta_1, \theta_2)_{\min} = \left(\frac{\pi}{6} \pm \upsilon, \frac{\pi}{6} \mp \upsilon\right), \ \left(\frac{\pi}{6} \mp \upsilon, -\frac{\pi}{3}\right), \ \left(-\frac{\pi}{3}, \frac{\pi}{6} \pm \upsilon\right). \tag{5.84}$$

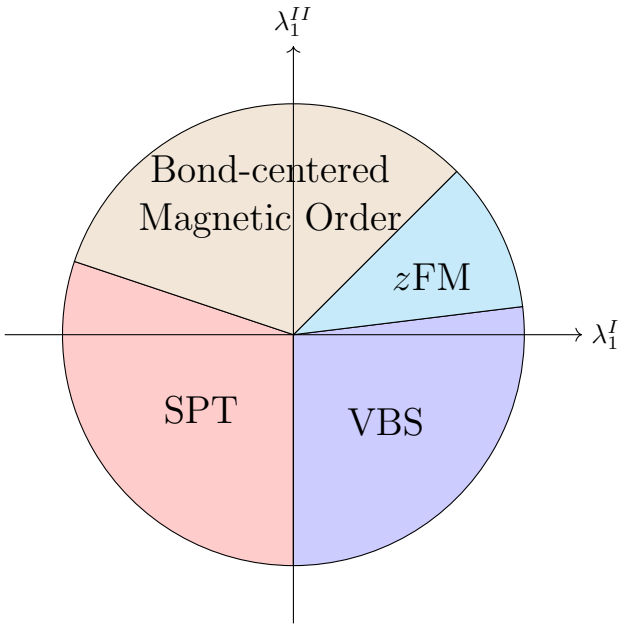

Figure 5.5: Four distinct phases appear in the classical phase diagram obtained by analyzing the minima of Eq. (5.82).

The physical picture of this phase can be obtained by analyzing the symmetries of these minima and their relation to nearby phases. Denoting the above minima as $\mathfrak{A}_\pm, \mathfrak{B}_\pm, \mathfrak{C}_\pm$, they transform in a 3-cycle way under $g_x : \mathfrak{A}_\pm \to \mathfrak{B}_\pm \to \mathfrak{C}_\pm \to \mathfrak{A}_\pm$, while they are exchanged pairwise under lattice translation T_1 and inversion about a site $\mathcal{I} : \mathfrak{A}_+ \leftrightarrow \mathfrak{A}_-, \mathfrak{B}_+ \leftrightarrow \mathfrak{B}_-, \mathfrak{C}_+ \leftrightarrow \mathfrak{C}_-$. Furthermore, $\mathfrak{A}_\pm/\mathfrak{B}_\pm/\mathfrak{C}_\pm$ are exchanged pairwise under symmetries $\mathcal{C}$, $g_x\mathcal{C}$, or $\mathcal{C}g_x$. At the point $\alpha = \pi/4$, the optimal $\upsilon = 0$ and these pairs merge to give the three ground states of the zFM phase in Eq. (5.83). We conclude that the phase with $\upsilon \neq 0$ also has magnetic order similar to zFM with additional translation and site inversion symmetry breaking (but preserves bond inversion symmetry). However, the lattice symmetry breaking is different from the VBS order: the VBS order parameter is zero in all these states for any υ, and, more directly, the VBS ground states are invariant under $\mathcal{C}$ and g_x, which is not the case here. According to the symmetry properties of this phase, we name it a "bond-centered magnetic order" phase.

We cannot write simple product states that would have the desired transformation properties for the bond-centered magnetic order states, including the expected quantum numbers under the $\mathrm{U}(1) \times \mathrm{U}(1)$. However, it is possible to write MPS wavefunctions for these ground states, by building upon the MPS

wavefunction for the neighboring SPT phase from App. 5.A.2, with which the present phase connects at $\alpha = \pi - \arctan(1/3)$, $\upsilon = \pi/2$, where all of the minima collapse to $(-\pi/3, -\pi/3)$ (remembering that the θ fields are defined modulo π). The MPS construction for this phase is presented in App. 5.A.3.

zFM-VBS transition in $\mathrm{U}(1) \times \mathrm{U}(1)$-symmetric theory

We can now discuss the phase transition between the zFM and VBS phases within this theory. In the above "classical" treatment of V_1^I and V_1^{II}, the phase transition occurs along the line $\lambda_1^{II} = \lambda_1^I/8$ with positive $\lambda_1^{I,II}$; this is a "level crossing" transition and is first order. This treatment is appropriate when both bare couplings λ_1^I and λ_1^{II} are large. On the other hand, we can consider starting from the Gaussian theory when these bare couplings are small. In the regime $g < 1/\sqrt{3}$, both couplings are relevant and start flowing to larger values. We may speculate that the (almost) continuous zFM to VBS transition observed in our numerical study occurs when these couplings during their flow balance each other in just the right way, but unfortunately we do not have a controlled means to study this.

Nevertheless, it is intriguing that some of the relations among the various scaling dimensions at the Gaussian fixed point appear to be approximately satisfied in our numerical study at the (pseudo-)critical point $(\delta, K) = (1, 2)$. Namely, we find numerically that the zFM and VBS order parameters have very close scaling dimensions, while they are equal in the Gaussian theory. We also find that Gaussian theory relations in Eq. (5.81) are approximately satisfied. The scaling dimensions are consistent with a naive estimate $g_{\text{eff}} \approx 0.25$. For such g_{eff}, both V_1^I and V_1^{II} would be relevant (in fact, one more scattering term with coefficient λ_2^I would also be relevant), consistent with these couplings flowing away from the Gaussian fixed point. For such a value of g_{eff}, the term A breaking the $\mathrm{U}(1) \times \mathrm{U}(1)$ symmetry down to g_z is irrelevant, which is consistent with the observed emergent $\mathrm{U}(1) \times \mathrm{U}(1)$ symmetry along the zFM-VBS phase boundary.

We remark that the above relations among various exponents in the Gaussian theory follow from the fact that there is a single Luttinger parameter in the theory, which in turn is dictated by the microscopic symmetries. It is possible that the corresponding approximate relations found in the numerical study of the (pseudo-)critical point are also primarily due to the symmetries rather

than proximity to the specific two-component Luttinger liquid theory. However, we do not know how to guess a better description, while the Luttinger liquid theory at least provides some framework for discussing observables and noticing these relations.

5.6 Connection to integrable statistical mechanics models

5.6.1 Classical model of non-intersecting strings

Focusing on the line of enhanced symmetry $\delta = 1$ which has significantly informed our study so far, one observes in Fig. 5.1 that this slice appears to intersect the phase boundary exactly at the point $(\delta, K) = (1, 2)$, at which $J^x = 0$ and $J^z = K$. Up to constants and an overall scale, this point is equivalent to

$$H^* = -\sum_j \Big((q-2) \sum_\alpha |\alpha\alpha\rangle\langle\alpha\alpha|_{j,j+1} + \sum_{\alpha,\beta} |\alpha\alpha\rangle\langle\beta\beta|_{j,j+1} \Big). \tag{5.85}$$

for $q = 3$. The above finding suggests that this Hamiltonian may be special, and in order to understand it we first return to another special instance of our Hamiltonian, namely, the point $J^x = J^z = 0$, which up to normalization and constants maps exactly to the pure biquadratic spin-1 Hamiltonian H_{bQ}, Eq. (5.8). This Hamiltonian is associated with the transfer operator of a particular 2d statistical mechanics model realizing "non-intersecting strings" (NIS).

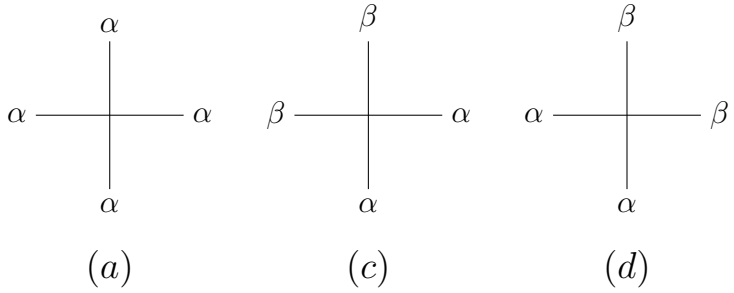

Figure 5.6: The three types of vertices shown here, with $\alpha \neq \beta$, are allowed in the vertex models we consider. We consider the model on the two-dimensional square lattice with vertex weights a, c, and d for the configurations (a), (c), and (d) respectively; see text for details.

These models are formulated with classical q-state degrees of freedom assigned to the edges of a graph—we have in mind the 2d square lattice—and weights assigned to the vertices according to their configurations. The only nonzero

vertices are those shown in Fig. 5.6; when accounting for the S_q permutation symmetry of the labels $\alpha, \beta = 1, \ldots, q$, there are $q(2q-1)$ allowed vertices. To simplify the notation, we write the weights as $w_{(a)} = a$, $w_{(c)} = c$, and $w_{(d)} = d$.[3] Solving the Yang–Baxter equation for the transfer matrix with S_q symmetry yields two integrable models for each value of q, satisfying the following conditions [19–21]:

$$\text{separable:} \quad a = c + d \ , \tag{5.86}$$

$$\text{non-separable:} \quad a^2 = a(c+d) + (q-2)cd \ . \tag{5.87}$$

We perform this calculation explicitly in App. 5.B.4 for the $q = 3$ transfer matrix. The solution Eq. (5.86) is commonly known as the separable NIS model, and we refer to that of Eq. (5.87) as the integrable non-separable case.

Schematically, under the separability condition Eq. (5.86), vertices of type (a) can be decomposed into both types (c) and (d) and thereby removed from the partition sum. Then one can map via a two-step duality to the self-dual point of the q^2-state Potts model [22]. The q^2-state Potts degrees of freedom reside on half of the plaquettes of the original square lattice (one color of a checkerboard pattern) and have generally anisotropic nearest-neighbor interactions in the $\hat{x} + \hat{y}$ and $\hat{x} - \hat{y}$ directions of the NIS lattice, with Boltzmann weights set by c/d and d/c. For any c and d the model is self-dual; the point $c = d$ corresponds to the isotropic self-dual model. We provide the explicit duality mapping from the separable q-state NIS model on the square lattice to the q^2-state Potts model, as well as further discussion, in App. 5.D using Hamiltonian language.

Both integrable NIS statistical mechanics models are exactly solvable for general q by the analytic Bethe ansatz [21, 23]. The structure is quite similar to the solution of the XXZ model using magnons, with the reference states of the method being the highest excited states (a manifold spanned by $|\alpha_1, \alpha_2, \ldots, \alpha_N\rangle$ with $\alpha_i \neq \alpha_{i+1}$). Although the solution for the eigenvalues was performed explicitly by De Vega et al. [24], we are not aware of how to access the low-energy subspace or ground state wavefunctions exactly.

[3] In choosing these vertex labels and weights, we follow the convention of Klümper [18].

5.6.2 Phases of NIS models

The weight of a single vertex can be written (with link variables labeled in the compass pattern S,W,N,E)

$$\begin{aligned} w(\alpha,\gamma,\beta,\rho) &= a\,\delta_{\alpha\gamma\beta\rho} + c\,(\delta_{\alpha\rho}\delta_{\beta\gamma} - \delta_{\alpha\gamma\beta\rho}) + d\,(\delta_{\alpha\gamma}\delta_{\beta\rho} - \delta_{\alpha\gamma\beta\rho}) \\ &= (a-c-d)\,\delta_{\alpha\gamma\beta\rho} + c\,\delta_{\alpha\rho}\delta_{\beta\gamma} + d\,\delta_{\alpha\gamma}\delta_{\beta\rho}\ . \end{aligned} \tag{5.88}$$

Since the overall scale of w does not change the probabilities, the vertex model has two independent parameters, which we are free to choose. We use c/d, which characterizes lattice anisotropy, as well as another parameter characterizing the relative weight of the (a)-type vertices compared to the (c)- and (d)-type vertices. One choice for such a parameter would be a^2/cd, but we will instead use a related quantity,

$$\Theta = \frac{a}{cd}(a-c-d) = \frac{a^2}{cd} - \frac{a}{\sqrt{cd}}\left(\sqrt{\frac{c}{d}} + \sqrt{\frac{d}{c}}\right)\ . \tag{5.89}$$

The parameter Θ is convenient in that the two integrable models correspond to $\Theta = 0$ and $\Theta = q-2$; for an explicit derivation we refer the reader to App. 5.B.4. At each of these special values of Θ, the NIS transfer matrices commute for any anisotropy parameter c/d; this is simply a restatement of Yang–Baxter solubility. In particular, the information encoded in the eigenvectors of the transfer matrices is independent of the "spectral variable" c/d. Accordingly, we can say that the physics is strictly independent of the anisotropy parameter. This conclusion does not hold at other values of $\Theta \neq 0, q-2$ and the quantitative details will depend on the anisotropy; however, we expect that the qualitative physics will still be independent.

Using the freedom afforded by the spectral variable, one can tune to the extreme anisotropic limit of the $\Theta = 0, q-2$ transfer matrices and take a logarithmic derivative to determine that these integrable models yield precisely the H_{bQ} and H^* quantum Hamiltonians, respectively, for the case $q = 3$ [18–20, 23, 25]. In this section we will allow Θ to vary and will argue that $\Theta < q-2$ realizes the same phase as the separable model $\Theta = 0$ which breaks the lattice translation symmetry, while $\Theta > q-2$ realizes a magnetically ordered phase. Hence, the integrable non-separable model $\Theta = q-2$ appears to be at the transition between these phases.

As suggested by its name, the NIS model partition sum can be rewritten in terms of nonlocal strings; these are "completely packed" on the square

lattice, with each edge containing a string segment. Every vertex can connect the segments on its adjoining edges in three different ways according to the pictures of (a)-, (c)-, and (d)-type vertices in Fig. 5.7. Ignoring boundaries, one sees that allowed string configurations take the form of loops lying along connected edges, all of which are in the same state within a single loop. These loops may self-intersect at (a)-type vertices but do not cross one another. The partition function can be rewritten independently of the q possibilities for the state of the edges comprising each loop, and the sum over flavors performed explicitly, obtaining a model in which q appears as a parameter and weights in the partition sum are determined entirely by loop geometry. The precise formulation in terms of unflavored strings is akin to a high-temperature expansion for a q-state Potts model. The utility of this formulation is that treating q as a parameter specifying a loop fugacity allows it to be varied continuously.

The weights of these vertices are read off from Eq. (5.88), so by substituting for Θ using Eq. (5.89) we write the general partition function in terms of the loops:

$$\begin{aligned} Z &= \sum_{\sigma} q^{\ell(\sigma)} (a-c-d)^{n_a(\sigma)} c^{n_c(\sigma)} d^{n_d(\sigma)} \\ &= (cd)^{\frac{N}{2}} \sum_{\sigma} q^{\ell(\sigma)} \left(\sqrt{\Theta + \gamma^2} - \gamma \right)^{n_a(\sigma)} \left(\frac{c}{d} \right)^{\frac{n_c(\sigma) - n_d(\sigma)}{2}} , \end{aligned} \tag{5.90}$$

where γ is determined from the anisotropy by

$$\gamma \equiv \frac{1}{2} \left(\sqrt{\frac{c}{d}} + \sqrt{\frac{d}{c}} \right) \geq 1 \; . \tag{5.91}$$

(The isotropic point with $\gamma = c/d = 1$ is a one-parameter loop model.) In the partition sum σ denotes a configuration of completely packed unflavored loops with connections at the vertices drawn from Fig. 5.7. Here $\ell(\sigma)$ is a nonlocal quantity, namely the number of loops in σ (more precisely, the number of connected components in the graph formed by the edges and their connections at the vertices), and n_a, n_c, and n_d are the numbers of vertices of each type in σ.

(We note parenthetically that a different variant of the NIS model also appears in the literature where it is defined on an oriented lattice with arrows pointing out of one sublattice and into the other; correspondingly, assignment

of weights for the two types of vertices becomes staggered compared to our unoriented-lattice model. The NIS model defined on the oriented lattice coincides with the model defined on the unoriented lattice for $c = d$; thus, the results about integrability still hold along this line, in agreement with the literature. However the staggered model with $c \neq d$ does not have commuting transfer matrices even for $\Theta = 0, q-2$ and is not integrable (this deformation corresponds to moving off self-duality and hence off criticality in the related q^2-state Potts model [22]).)

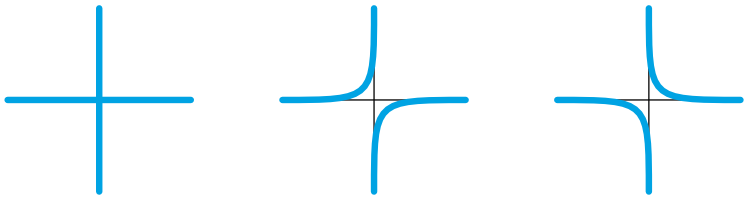

Figure 5.7: The vertex configurations of the loop model, which are unflavored, are shown. The weight of a configuration depends only on the geometric pattern of connections of the string segments assigned to the edges of the two-dimensional square lattice. The weight of each individual vertex type can be read off from Eq. (5.88); the partition sum in terms of such loops is specified in Eq. (5.90).

Consider first a regime in which the (a) vertex is suppressed at low energies. Setting $\Theta = 0$ enforces $n_a(\sigma) = 0$ identically. As mentioned earlier, this model is equivalent to the q^2-state Potts model, with anisotropic couplings if $c \neq d$, but such that self-duality is maintained. For $c = d$, the model is isotropic and for $q > 2$ is known to be at a first-order transition between the Potts ordered and disordered phases (and we expect this to be true also for $c \neq d$). In the NIS language, the ordered and disordered phases of the Potts model are known to correspond to short-loop states running predominantly around one or the other set of plaquettes [4, 21, 22].[4] This is a "checkerboard" phase of the loop model which spontaneously breaks the lattice symmetry, but is symmetric under S_q permutation of the labels. Presumably the short-loop checkerboard

[4]The most direct way to see that the ordered and disordered phases of the Potts model correspond to one or the other checkerboard pattern of NIS loops is to consider the isotropic NIS model and perturb it by staggered weights for the (c) and (d) vertices, oppositely for the two sublattices. In the NIS language this selects one of the checkerboard states, while under the duality to the q^2-state Potts model this moves the Potts model off self-duality and hence into one of the phases.

phase is stable under introducing some finite amount of Θ. (In the language of the related q^2-state Potts model with $q^2 > 4$, a small Θ perturbation moves along a first-order coexistence line.) This is the VBS phase of our spin model.

Conversely, in a regime with high weight on the (a) vertex, configurations at low energies include strings that extend across the whole system. In the language of the original vertex model degrees of freedom, such proliferation of strings corresponds to spontaneous breaking of the S_q permutation symmetry by choosing one of the q colors. Thus, the phase will display long-range correlations of a magnetic-type order parameter which measures whether distant links are connected by an unbroken string, whereas in the short-loop checkerboard phase correlations of this order parameter decay exponentially. In our spin model, the proliferated-loop phase is the zFM phase.

Now for an intermediate value of the parameter Θ there will be a transition between the extended phase and the short-loop checkerboard phase. Our finding that the VBS to zFM transition in the $q = 3$ model appears to be exactly at the integrable point corresponding to $\Theta = q - 2$ suggests that the completely packed loop model undergoes a transition between checkerboard short loops and the proliferated loop phase at exactly $\Theta = q-2$. A similar conjecture was made in Ref. [26] in the context of special completely packed O(n) loop models (which map precisely onto the above loop model with $q = n$) and was supported by transfer matrix studies for $n \geq 10$ and $n < 2$. As we discuss in the next subsection, the $\Theta = q - 2$ model actually has a finite correlation length, which however can be enormous for $q \gtrsim 2$, of which our spin model with $q = 3$ is an example. Our DMRG study reaching correlation lengths around 200 and locating the zFM-VBS transition very close to the point $\Theta = q - 2$ gives very strong support to this conjecture also in the vicinity of $q = 3$.

5.6.3 Walking description of phase transition

Summary of exact results for integrable models

There is a way to learn about the spectrum of the transfer matrix of the integrable NIS models without the need to construct eigenstates, through the so-called inversion trick introduced by Stroganov [27] and later used to study the six-vertex model by Baxter [28] and Baxter [29]. In its initial setting the inversion relation was actually developed specifically to compute the free energy per site of the two integrable $q = 3$ NIS models, before more was known

about their structure. An extended inversion relation was used by Klümper [18, 25] to compute subleading eigenvalues of the transfer matrix, exposing some details of the low-energy spectrum. In particular, he found that the dependence on q of the thermodynamic-limit energy gaps of both quantum Hamiltonians corresponding to the integrable NIS models (under some overall normalization) is governed by the function

$$\Delta = g(x) = \log x \prod_{n=1}^{\infty} \left(\frac{1 - x^{-n/2}}{1 + x^{-n/2}} \right)^2 , \tag{5.92}$$

and the correlation length by $\xi = f(x)$ [18, 30],

$$f(x) = -1/\log k(x) , \quad k(x) = \frac{4}{\sqrt{x}} \prod_{n=1}^{\infty} \left(\frac{1 + x^{-2n}}{1 + x^{-2n+1}} \right)^4 . \tag{5.93}$$

The two integrable models correspond to the following functional forms of the argument x:

$$x_{\rm sep}(q) = \frac{q + \sqrt{q^2 - 4}}{q - \sqrt{q^2 - 4}} , \tag{5.94}$$

$$x_{\rm ns}(q) = q - 1 . \tag{5.95}$$

One can draw some conclusions about these models from the equivalence between the separable q-state NIS model and the q^2-state self-dual Potts model. Because the self-dual Potts model transitions from critical to gapped at $Q_{\rm Potts} = 4$, then $\Delta^{\rm sep} = 0$ for $q \leq 2$ and $\Delta^{\rm sep} > 0$ for $q > 2$. Thus we can also determine the value q^c at which $\Delta^{\rm ns}$ experiences a transition from gapless to gapped. Because $x_{\rm sep}(q = 2) = 1 \equiv q^c - 1$, in fact the non-separable NIS model also experiences a transition from gapless to gapped at the value $q^c = 2$. In particular, using $q = 3$ and the normalization from Sec. 5.4.1, we exactly determine the energy gap of the Hamiltonian H^* to be $\Delta = 1.42 \times 10^{-4}$ and the correlation length $\xi = 190878$ lattice spacings. From the point of view of the functions $g(x)$ and $f(x)$, this is because the integrable non-separable lattice model has the gap and correlation length which correspond to the self-dual Potts model with $Q_{\rm Potts} = [x_{\rm sep}^{-1}(x_{\rm ns}(q = 3))]^2 = \frac{9}{2}$. The $Q_{\rm Potts} = 5$ model is known to already have a large correlation length of 3553 lattice spacings, and $Q_{\rm Potts} = \frac{9}{2}$ is even closer to the critical value $Q_{\rm Potts}^c = 4$.

To recapitulate the content of this section, the q-state separable integrable NIS model maps to the self-dual Potts model with $Q_{\rm Potts} = q^2$ states, and this

mapping is actually an equivalence of models in the bulk (that is, ignoring boundary effects). On the other hand, in the q-state non-separable integrable NIS model, the expression for the gap and correlation length are those which also apply to a Potts model at $Q_{\text{Potts}} = [x_{\text{sep}}^{-1}(x_{\text{ns}}(q))]^2 = q^2/(q-1)$, but we could not find any arguments for a stronger equivalence between these models.

Implications for renormalization group flow

Supposing that the $q = 3$ non-separable NIS model indeed describes the phase boundary, one concludes that the transition is *extremely* weakly first order. The emergence of such a length scale enormously greater than the lattice spacing presents a "hierarchy problem." Fortunately we can again look to the self-dual Potts model which provides a more familiar example of this phenomenon. In the preceding section we used exact results for the eigenvalues of the transfer matrix to contextualize the very small gap and long correlation length of H^* in terms of the Potts pseudo-criticality. A new understanding of the Potts case is due to a recent thorough treatment as an instance of "walking" of renormalization group flows [31, 32].

In brief, walking is the following proposal of an RG equation for a microscopic coupling λ:

$$\frac{d\lambda}{d\log L} = -\epsilon + \lambda^2 + \cdots \ . \tag{5.96}$$

For $\epsilon > 0$ the flow has fixed points $\lambda^* = \pm\sqrt{\epsilon}$, one of which is stable and the other unstable. (In the Potts case these are the critical and tricritical points existing at $Q_{\text{Potts}} < 4$; the system is assumed to be already tuned to the phase transition, e.g., by enforcing the self-duality, and λ is some remaining parameter in this manifold.) These fixed points merge upon tuning $\epsilon \to 0$, and "disappear" for $\epsilon < 0$. However in this regime solutions $\lambda^* = \pm i\sqrt{|\epsilon|}$ still exist, and represent a particular type of non-unitary theory. Quantities like central charge, scaling dimensions, and OPE coefficients at these complex fixed points generally have nonzero imaginary components, and the conformal data of the two fixed points are related by complex conjugation.

While the complex fixed points are inaccessible to RG flows in the unitary theory, they do control the physics at intermediate length scales. This is because the running of the coupling slows down considerably near $\lambda = 0$,[5]

[5]One can treat solutions λ^* with finite real part by simply removing it via a shift to $\lambda - \text{Re}[\lambda^*]$.

where it passes close to these "complex CFTs." The RG time required for λ to flow from -1 to $+1$ is found by integrating Eq. (5.96): the result is $t \sim \frac{\pi}{\sqrt{|\epsilon|}}$, corresponding to a length scale [31]

$$\xi = \xi_0 \exp \frac{\pi}{\sqrt{\epsilon}} \ . \tag{5.97}$$

For small values $|\epsilon| \ll 1$ this scale becomes very long; in this case the approximate conformal symmetry inherited from the complex CFTs looks nearly exact even for large finite systems. However, because the flow is not approaching a conformally symmetric fixed point, the conformal data measured in systems with a characteristic length will drift with the scale, displaying the eventual limiting behavior at a size comparable to ξ.

In the self-dual Potts model the form of Eq. (5.96) is well motivated by a long history of study, with parameter $\epsilon_{\text{Potts}} = \frac{1}{\pi^2}(4 - Q_{\text{Potts}})$ to leading order in the limit $Q_{\text{Potts}} \to 4$ [31]. By matching the characteristic walking behavior at $\epsilon = 0$ with the divergent parts of the exact results in the previous section we can write down ϵ also for the non-separable model. The function k defined in Eq. (5.93), an elliptic modulus, can equivalently be written $k(x) = (\vartheta_2(\widetilde{q})/\vartheta_3(\widetilde{q}))^2$, where $\vartheta_n(\widetilde{q})$ is the Jacobi theta function $\vartheta_n(z = 0, \widetilde{q} = 1/x)$. We emphasize that the usage of the letter $\widetilde{q} = 1/x$ in this way is an unfortunate coincidence arising from the conventions of elliptic functions.

To leading order as $\widetilde{q} \nearrow 1$ (that is, from the weakly first-order side), we expand

$$\frac{\vartheta_2(\widetilde{q})}{\vartheta_3(\widetilde{q})} \approx 1 - \frac{4}{2 + \exp\left[\frac{\pi^2}{1-\widetilde{q}}\right]} \ , \tag{5.98}$$

so $\log f(x) \sim \frac{\pi^2}{1-\widetilde{q}}$, and consequently

$$\log f(x_{\text{sep}}(q)) \sim \frac{\pi^2}{2\sqrt{q-2}} \ , \tag{5.99}$$

$$\log f(x_{\text{ns}}(q)) \sim \frac{\pi^2}{q-2} \ , \tag{5.100}$$

to leading order in the limit $q \to 2$. We therefore propose that in the RG equation for the integrable NIS models ϵ has the form

$$\epsilon_{\text{sep}} = -\frac{4}{\pi^2}(q-2) \ , \tag{5.101}$$

$$\epsilon_{\text{ns}} = -\frac{1}{\pi^2}(q-2)^2 \ , \ q \geq 2 \ . \tag{5.102}$$

These statements are strictly applicable only as $q \to 2$.[6] In this limit, Eq. (5.101) reproduces the known result for the self-dual Potts model with $Q_{\text{Potts}} = q^2 \approx 4+4(q-2)$; in particular, the complex fixed points separate as the square root of the deviation from the critical value of q: $\lambda^*_{\text{ns}} = \frac{2}{\pi}\sqrt{2-q}$. On the other hand, Eq. (5.102) indicates that the functional dependence on q is different in the non-separable case: the next correction to $\log f(q-1)$ is a constant, so $\frac{d\epsilon}{dq} = 0$ at $q = 2$ and $\lambda^* = \pm\frac{i}{\pi}(q-2)$ grows linearly with q. By taking these results seriously at $q = 3$—which is dubious based on the expansion but works well for the Potts model nonetheless; see Sec. 3.5 of Ref. [31]—from Eq. (5.97) one arrives at a value $\xi_0 \approx 9.9$ for H^*, which can be compared with the UV length scale $\xi_{0,\text{Potts}} \sim 0.19$ obtained for the weakly first-order Potts transition.

In order to follow the standard story of walking ϵ_{ns} should change sign at $q = 2$; it may indeed be the case that, for instance, an additional factor of $\text{sign}(q-2)$ is required in Eq. (5.102). However, we observe that close to the marginal value $q = 2$ the two—separable and non-separable—stories of walking we have been telling independently actually merge. In our spin model the former case lies inside the VBS phase with fairly large correlation length $\xi \approx 21$ for $q = 3$, diverging for $q \to 2$, while the latter resides on the VBS-zFM boundary and has a much larger correlation length with stronger divergence as $q \to 2$. It is interesting that both of these points occur in the same NIS model as Θ is varied, and it is intriguing to speculate that the walking parameter λ posited separately for each case may in fact be the same. If this is true, the complex CFTs discussed for the two models occur in the same larger parameter space which also contains the parameter Θ, and in principle a richer flow structure involving these fixed points is possible. It would be interesting to address this speculation with more concrete calculations and also to examine possible implications for crossovers in the physical spin problem.

5.7 Exact diagonalization study of CFT data for integrable model

In the walking picture the physics of our model in the approximately conformal regime is controlled by complex CFTs; accordingly, numerics are well suited to illuminate some of the properties of these theories. In order to do so we will study the lattice model using exact diagonalization (ED), where the details of the low-energy spectrum under periodic boundary conditions provide a reliable

[6] Specifically, the correspondences between the integrable $q = 3$ NIS models and the Potts models at $Q_{\text{Potts}} = 9$ and $\frac{9}{2}$ are not evident here due to the approximation.

way to identify CFT operators up to finite-size corrections [33]. Specifically, the energy E and lattice momentum P of an appropriate low-energy eigenstate are related to the scaling dimension Δ and conformal spin S of a CFT operator as

$$E_\alpha = \frac{2\pi}{Na}\left(\Delta_\alpha - \frac{c}{12}\right) + O(N^{-x}) \ , \quad P_\alpha = \frac{2\pi}{Na} S_\alpha \ , \tag{5.103}$$

under suitable normalization of the lattice Hamiltonian. The lattice spacing is denoted a and the number of sites N. Here $x > 1$ is a non-universal exponent controlling the finite-size scaling. In this way we can also compare ED data with some of the results of Sec. 5.4 by identifying the low-energy excitations associated with primary operators in the CFT. The application of this idea to lattice models was first worked out by Koo et al. [34] for Bethe-ansatz integrable models and later developed into a more general numerical technique [33].

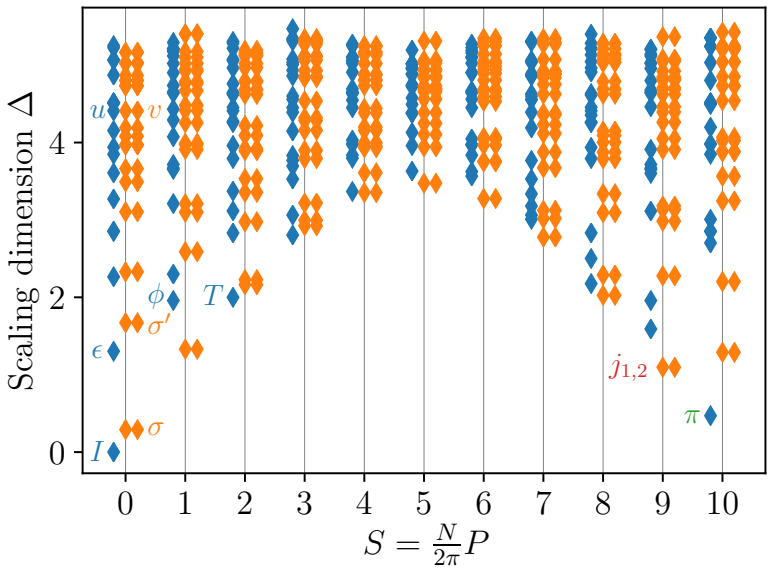

Figure 5.8: We show the low-energy spectrum of the integrable model $(\delta, K) = (1, 2)$ that resides on the zFM-VBS phase boundary with system size $N = 20$ in the $\mathcal{N}_1 = \mathcal{N}_2 = 0$ sector. Eigenvalues are organized based on conformal spin S and g_x quantum number, with $g_x = 1$ shown in blue and $g_x = \omega, \omega^2$ (which are related by $\mathcal{C}$) in orange. States are offset slightly from their quantized momenta for visual clarity. Scaling dimensions Δ are determined by normalization of the energy eigenvalue of the $|T\rangle$ state associated with the stress-energy tensor, as $\Delta_T = 2$. Highest-weight states identified using Fourier modes H_n are indicated by name. Quantum numbers of these states under symmetries $\mathcal{C}$ and $\mathcal{I}$ (where applicable) are not shown here but are listed in Table 5.1.

The fundamental idea is based on the observation that the Fourier modes of the Hamiltonian density in a CFT on a circle are linear combinations of the Virasoro generators:

$$H_n^{\mathrm{CFT}} = \frac{Na}{2\pi}\int_0^{Na} dx\, e^{inx\frac{2\pi}{Na}} h^{\mathrm{CFT}}(x) = L_n + \overline{L}_{-n},\ n \neq 0. \tag{5.104}$$

The action of a Virasoro (anti)chiral operator L_n ($\overline{L}_n$) is to decrease (increase) conformal spin by n and decrease conformal dimension by n. That is, H_n^{CFT} imparts conformal spin $-n$, connecting lattice momentum sectors $\frac{2\pi}{Na}S$ and $\frac{2\pi}{Na}(S-n)$. In a CFT, all states are grouped into conformal towers related by the Virasoso generators. Each tower descends from a unique highest-weight state, which is associated with a primary field by the state-operator correspondence. Because the energy of a state in the theory on a circle depends on the operator scaling dimension, the highest-weight states can be identified with those whose overlap with lower-energy states upon application of H_n vanishes or goes to 0 with increasing size. The numerical method is obtained by applying these statements about continuum fields to the lattice operators, in particular assuming that the relationship Eq. (5.104) also applies to Fourier modes of the lattice Hamiltonian and lattice counterparts of the Virasoro generators, up to finite-size corrections.

Based on the above, one does not need to construct lattice equivalents of the Virasoro generators; simply acting repeatedly with H_n, $n \in \{-2,-1,1,2\}$, on an eigenstate generates other states in the same conformal tower. By projecting the lattice Fourier modes H_n into the space of low-energy eigenstates, the structure of the conformal towers can be read off from the matrix elements, and those having zero matrix elements for all H_n with all eigenstates of lower energy will be the highest-weight states associated with primary fields in the CFT. We find in our data that for some eigenstates this sum of matrix elements on lower-energy states vanishes identically. In other cases an eigenstate may have a small matrix element which decreases with system size; if the spectrum does not contain another state from which this state could reasonably descend, we also label this state a primary and attribute the nonzero values of H_n to finite-size corrections. However, we are generally conservative and are not trying to exhaustively label all highest-weight states in the spectrum, but rather identify those that correspond to measurements made in previous sections, in addition to other obvious candidates.

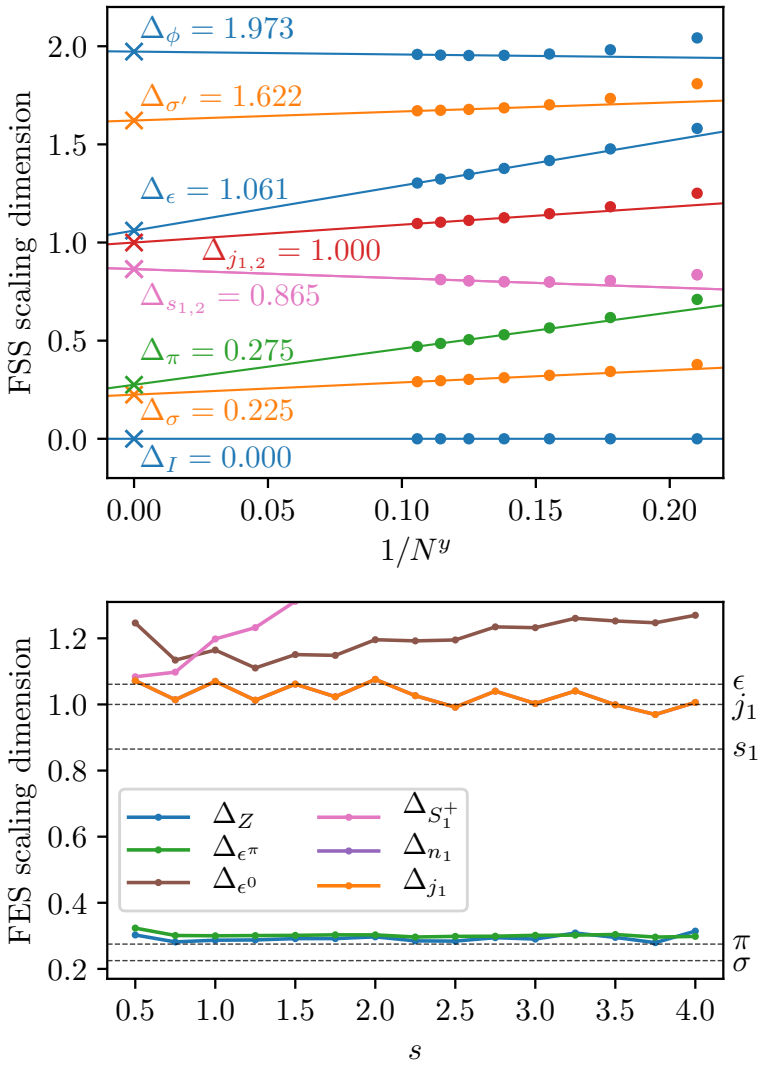

Figure 5.9: In the upper panel we show scaling dimensions of primary fields in the putative conformal fixed point obtained using finite-size scaling of the excitation energies of highest-weight states. We determine the exponent $y = 3/4$ numerically, by observation of finite-size corrections to the vanishing matrix elements of H_n with the state $|T\rangle$ used for normalization. We do not show the relatively heavy operators u, v, but these behave similarly. Scaling dimensions $\Delta_{s_{1,2}}$ of $S^+_{1,2}$ operators are extracted from ED data in the appropriate charged sectors different from that in Fig. 5.8 (not shown). For the fits we use only system sizes $N \geq 12$, though also show data for $N = 8, 10$. In the lower panel we repeat the plot containing data for the critical exponents obtained from the FES method, also shown in Fig. 5.4. Now the horizontal lines marked on the figure indicate the scaling dimension of the most relevant primary field in each associated symmetry sector as measured in ED.

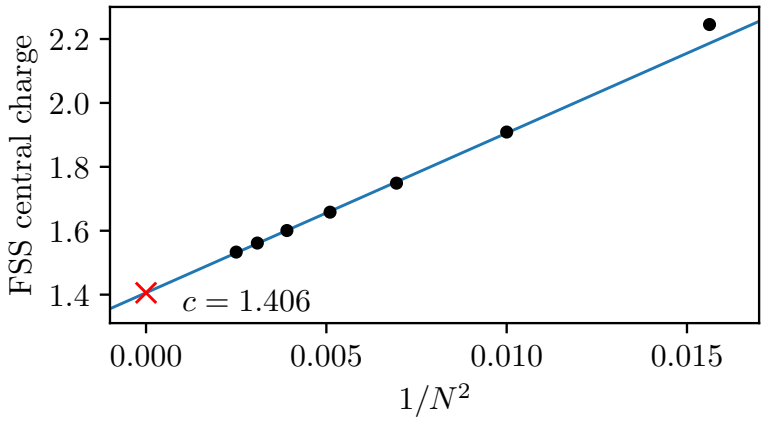

Figure 5.10: Finite-size scaling for the central charge is based on the matrix element $\langle T|H_{-2}|I\rangle$, where $|I\rangle$ is the ground state and $|T\rangle$ the state with conformal spin $S = 2$ associated with the stress-energy tensor in the field theory. This state has the lowest energy in its sector for all system sizes studied. The scaling with N^{-2} is used for other models [33], and visually appears to be appropriate. The fit excludes the first two data points $N = 8, 10$.

By finite-size scaling of the energy eigenvalues of highest-weight states we are straightforwardly able to estimate the scaling dimensions of primary operators in the CFT. Correct normalization of H is very important; to achieve this we follow Milsted et al. [33] and utilize the state related to the stress-energy tensor T, which is conserved and has known scaling dimension $\Delta_T = 2$. T is quasiprimary, related to the vacuum I by $\sqrt{\frac{c}{2}}|T\rangle = L_{-2}|I\rangle$ and can thus be readily identified in the $S = 2$ sector by calculating $H_{-2}|I\rangle$. This strategy allows us to avoid incorrectly identifying $|T\rangle$ for small sizes N, as described in Ref. [33]. So H is normalized by setting $\Delta_I = 0$ and $\Delta_T = 2$. The low-energy spectrum of the model for system size $N = 20$ is shown in Fig. 5.8 and the finite-size scaling results are shown in Fig. 5.9, where they are additionally compared with the finite-entanglement scaling results obtained previously from MPS.

Due to the appearance of the central charge c in the matrix element $\langle T|H_{-2}|I\rangle = \sqrt{\frac{c}{2}}$, we can also compare the finite-size scaling ED results for the central charge with those obtained from MPS. The finite-size scaling result $c \approx 1.4$ is shown in Fig. 5.10. While this number is not in agreement with the value obtained previously from scaling with MPS bond dimension, this is not unexpected, as the value of c will drift with system size at a pseudo-critical point,

Primary field	Re[Δ]	S	U(1)^2	g_x	$\mathcal{C}$	$\mathcal{I}$
I	0	0	0	0	$+$	$+$
$\sigma, \tilde{\sigma}$	0.225	0	0	± 1		$+$
π	0.275	$N/2$	0	0	$+$	$-$
s_1, s_2	0.865	$N/2$	$1_1, 1_2$			$+$
j_1, j_2	1.000	$N/2-1$	0			
ϵ	1.061	0	0	0	$+$	$+$
$\sigma', \tilde{\sigma}'$	1.622	0	0	± 1		$+$
$\phi, \overline{\phi}$	1.973	± 1	0	0	$-$	
u	5.025	0	0	0	$+$	$+$
$v, \tilde{v}$	5.025	0	0	± 1		$+$

Table 5.1: We identify and measure (the real parts of) several primary fields in the putative CFT for the integrable point at $(\delta, K) = (1, 2)$. Just as chiral primaries with $S \neq 0, N/2$ have an anti-chiral counterpart obtained by reflection (only $\overline{\phi}$ arises here), also primaries that do not commute with g_x have a counterpart with quantum number -1 related by time-reversal symmetry Θ; these are $\tilde{\sigma}$, $\tilde{\sigma}'$, and $\tilde{v}$. We also resolve charge conjugation $\mathcal{C}$ for states with $g_x = 0$ (these symmetries do not commute), as well as spatial inversion $\mathcal{I}$ in the 0- and π-momentum sectors. The operators above the line are those which we compare with finite-entanglement scaling results for correlations of lattice operators in the MPS study.

decreasing with increasing system size and eventually reaching $c = 0$ at very large sizes.

5.8 Summary of results

Motivated by the description of a DQCP in a spin-1/2 chain with rotation symmetry broken to $\mathbb{Z}_2 \times \mathbb{Z}_2$ in Refs. [1, 2], discussed in Ch. 4, we have probed the nature of a similar transition in a 1d model of local three-level systems forming projective representations of $\mathbb{Z}_3 \times \mathbb{Z}_3$. On one side of the transition is a ferromagnet phase with threefold ground state degeneracy, and on the other a twofold degenerate VBS phase which preserves onsite symmetries but breaks translation invariance. This is similar to the $\mathbb{Z}_2 \times \mathbb{Z}_2$-symmetric situation, however there an LSM theorem was important in prohibiting an intervening fully symmetric gapped phase; in the present case a featureless phase is allowed.

The above notwithstanding, our studies using an adiabatic protocol for optimized uniform MPS indicate that the phase diagram of the concrete Hamiltonian in Eq. (5.11) does indeed include a direct transition between zFM and VBS phases. Our numerical results are furthermore consistent with a continu-

ous phase transition with symmetry group enhanced to at least $\mathrm{U}(1) \times \mathrm{U}(1) \rtimes \mathbb{Z}_3$. In addition, the scaling dimensions of the two order parameters involved have nearly the same numerical value, possibly indicating a larger emergent symmetry or self-duality at the transition.

While we did not obtain a controlled low-energy theory of the transition using either $\mathbb{Z}_3$ domain wall fields or bosonization of the $\mathrm{U}(1)^2$-symmetric theory (which applies exactly on the lattice along a particular cut through the phase diagram), our numerical results suggest another strategy, by seemingly locating the special point H^*, Eq. (5.85), on the phase boundary. This quantum Hamiltonian is the counterpart to a two-dimensional solvable classical vertex model we term the non-separable integrable NIS model (see Sec. 5.6), and through a trick known as transfer matrix inversion one can use the analyticity properties of the eigenvalues to compute exact results about the spectrum. The surprising result of this method is that H^* is gapped, with very long but finite correlation length $\xi = 190878$ lattice spacings. Such a result is not incompatible with the numerics, which would not distinguish between such approximate conformal symmetry and a truly continuous transition.

The most natural conclusion would seem to be that this DQCP is extremely weakly first order, an intriguing result in light of the status of the SU(2)-symmetric DQCP in 2d, as discussed in the Introduction. As is true there, the most generic mechanism for generating a hierarchy is through RG walking, and exact results for H^* allow us to write an explicit form for the walking parameter, similar to the case for the self-dual Potts model but with different functional dependence on the continuous tunable parameter; see Eqs. (5.101) and (5.102). Based on this understanding, we interpret our numerical results as characterizing (the real parts of) the conformal data of the complex CFTs in the walking picture, and we use an ED method to identify some of the light primary fields of these theories.

5.A MPS for fully symmetric phase and proximate magnetic phase

5.A.1 SPT phase with $\mathbb{Z}_3^z \times \mathbb{Z}_3^x$ symmetry

A gapped fully symmetric ground state is allowed for Eq. (5.11), and one generically expects to encounter this phase as well. In fact, this phase has SPT order, since the entanglement spectrum and boundary states exhibit degeneracy due to the projective representation. A simple picture of the phase

can be written using an MPS wavefunction of bond dimension three:

$$|\psi_{\text{symm}}\rangle = \sum_{\{\alpha\}} \text{Tr}\left[\cdots A^{|\alpha_j\rangle} A^{|\alpha_{j+1}\rangle} \cdots\right] |\{\alpha\}\rangle \ . \tag{5.105}$$

We choose local tensors to be translationally invariant, so $T_1|\psi_{\text{symm}}\rangle = |\psi_{\text{symm}}\rangle$ automatically. We also require $A^{|\alpha\rangle} = (A^{|\alpha\rangle})^\top$, so that the state is symmetric under inversion.

In order to write a state that is invariant under the action of an onsite symmetry generator g, we require that local tensors satisfy the following symmetry condition:

$$A^{|\alpha_j\rangle} = W_{g,j} A_g^{|\alpha_j\rangle} W_{g,j+1}^{-1} \ , \tag{5.106}$$

where $A_g^{|\alpha_j\rangle} = g \circ A^{|\alpha_j\rangle}$ and $W_{g,j}$ is an invertible matrix implementing a gauge transformation acting on the left virtual leg of the local tensor at site j. The set of $\{W_{g,j}\}_g$ form a projective representation of the symmetry group generated by $\{g\}$. We choose the virtual legs to index a three-dimensional Hilbert space with basis $\{|0\rangle, |1\rangle, |2\rangle\}$. The gauge transformations are represented by

$$W_{g,j} = g_j \text{ for } g = g_z, g_x, \mathcal{C} \ ; \quad W_{\Theta,j} = 1 \ . \tag{5.107}$$

The virtual leg $(2k-1, 2k)$ hosts the projective representation [1], while the virtual leg $(2k, 2k+1)$ carries [2]. Thus, for each tensor one has $[l] + [p] = [r]$ mod 3, where $[l]$ ($[r]$) labels the projective representation on the left (right) virtual leg, and $[p]$ labels that of the physical leg.

The most general matrices consistent with invariance are

$$A^{|0\rangle} = \begin{bmatrix} \gamma & 0 & 0 \\ 0 & 0 & \delta \\ 0 & \delta & 0 \end{bmatrix} , \ A^{|1\rangle} = \begin{bmatrix} 0 & 0 & \delta \\ 0 & \gamma & 0 \\ \delta & 0 & 0 \end{bmatrix} , \ A^{|2\rangle} = \begin{bmatrix} 0 & \delta & 0 \\ \delta & 0 & 0 \\ 0 & 0 & \gamma \end{bmatrix} , \tag{5.108}$$

where $\gamma, \delta \in \mathbb{R}$. At the special point $\gamma \neq 0$, $\delta = 0$ the wavefunction reduces to the ground state of the zFM phase. Similarly, at another special point $\gamma = \delta \neq 0$ the wavefunction becomes the ground state of the xFM phase. For other parameter values this MPS represents an SPT state.

5.A.2 SPT phase with $\text{U}(1) \times \text{U}(1)$ symmetry

We now consider the case where $\mathbb{Z}_3^z$ is enlarged to $\text{U}(1) \times \text{U}(1)$. A basis for the legs (physical or virtual) can be labeled by particle numbers $|n_1, n_2\rangle$, which

are defined in Eqs. (5.24) and (5.25). For the $D = 3$ MPS we considered, the physical leg at site j and virtual leg $(j-1, j)$ share the same basis, defined to be

$$\left\{|0,0\rangle \equiv |0\rangle,\ |(-1)^j, 0\rangle \equiv |1\rangle,\ |0, (-1)^j\rangle \equiv |2\rangle\right\}\ . \tag{5.109}$$

The generic form for a local tensor at site j can be represented by a quantum state:

$$\hat{A}_j = \sum (A_j)^{n_1 n_2}_{l_1 l_2; r_1 r_2} |n_1, n_2\rangle_j \otimes |l_1, l_2\rangle_{(j-1,j)} \otimes \langle r_1, r_2|_{(j,j+1)}. \tag{5.110}$$

Translation T_1 acts as particle-hole symmetry on $\mathrm{U}(1) \times \mathrm{U}(1)$, which relates tensors at even sites $\hat{A}_\mathrm{e}$ and those at odd sites $\hat{A}_\mathrm{o}$ via

$$(A_\mathrm{o})^{n_1 n_2}_{l_1 l_2; r_1 r_2} = (A_\mathrm{e})^{-n_1, -n_2}_{-l_1, -l_2; -r_1, -r_2}\ . \tag{5.111}$$

For a $\mathrm{U}(1) \times \mathrm{U}(1)$ symmetric MPS, $\hat{A}_j$ in Eq. (5.110) should satisfy the particle number conservation condition

$$n_a + l_a = q_a + r_a\ , \quad \text{where } a = 1, 2\ . \tag{5.112}$$

Here, q_a is a site-dependent constant. On a periodic chain, this state has definite total particle numbers $\mathcal{N}_a \equiv \sum_j n_{a,j} = \sum_j q_{a,j}$, $a = 1, 2$.

By construction, a generic MPS in Eq. (5.108) breaks $\mathrm{U}(1) \times \mathrm{U}(1)$ symmetry to $\mathbb{Z}_3^z$. However, $\mathrm{U}(1) \times \mathrm{U}(1)$ symmetry can be restored by setting $\gamma = 0$. Indeed, in this case the local tensors can be written

$$\begin{aligned}\hat{A}_\mathrm{e} = {} & |0,0\rangle \otimes \big(|1,0\rangle\langle 0,-1| + |0,1\rangle\langle -1,0|\big) + |1,0\rangle \otimes \big(|0,1\rangle\langle 0,0| + |0,0\rangle\langle 0,-1|\big) \\ & + |0,1\rangle \otimes \big(|0,0\rangle\langle -1,0| + |1,0\rangle\langle 0,0|\big), \end{aligned} \tag{5.113}$$

$$\begin{aligned}\hat{A}_\mathrm{o} = {} & |0,0\rangle \otimes \big(|-1,0\rangle\langle 0,1| + |0,-1\rangle\langle 1,0|\big) + |-1,0\rangle \otimes \big(|0,-1\rangle\langle 0,0| + |0,0\rangle\langle 0,1|\big) \\ & + |0,-1\rangle \otimes \big(|0,0\rangle\langle 1,0| + |-1,0\rangle\langle 0,0|\big), \end{aligned} \tag{5.114}$$

where we have dropped the overall amplitude δ. One can check that these tensors indeed satisfy Eq. (5.112) with $q_a = 1$ (-1) for even (odd) sites. The other symmetries of the model, $\mathcal{I}$, Θ, g_x and $\mathcal{C}$, are also preserved by this MPS.

However, for the purpose of obtaining an MPS beyond the $D = 3$ case we can work out the symmetry constraints on A_j. Constraints from T_1 and

$\mathrm{U}(1)\times\mathrm{U}(1)$ are already listed in Eqs. (5.111) and (5.112). Time reversal Θ simply requires all tensor entries to be real numbers.

To be consistent with $\mathrm{U}(1)\times\mathrm{U}(1)$ symmetry in Eq. (5.112), inversion $\mathcal{I}$ acts with an additional particle-hole symmetry on the virtual legs, imposing the following constraint:

$$(A_j)^{n_1 n_2}_{l_1 l_2; r_1 r_2} = (A_j)^{n_1 n_2}_{-r_1,-r_2;-l_1,-l_2} \ . \tag{5.115}$$

$\mathcal{C}$ interchanges particles between the two species, thus

$$(A_j)^{n_1 n_2}_{l_1 l_2; r_1 r_2} = (A_j)^{n_2 n_1}_{l_2 l_1; r_2 r_1} \ . \tag{5.116}$$

On the physical leg at site j, g_x maps $|n_1, n_2\rangle_j$ to $|(-1)^j - n_1 - n_2, n_1\rangle_j$. On the left virtual leg $(j-1, j)$, the action of g_x is the same:

$$g_x : |l_1, l_2\rangle_{(j-1,j)} \to |(-1)^j - l_1 - l_2, l_1\rangle_{(j-1,j)} \ , \tag{5.117}$$

while on the right legs the fact that these are contracted with the left legs on the next tensor fixes the transformation to be

$$g_x : \langle r_1, r_2|_{(j,j+1)} \to \langle (-1)^{j+1} - r_1 - r_2, r_1|_{(j,j+1)} \ .$$

Thus, g_x imposes the constraint

$$(A_j)^{n_1 n_2}_{l_1 l_2; r_1, r_2} = (A_j)^{(-1)^j - n_1 - n_2, n_1}_{(-1)^j - l_1 - l_2, l_1; (-1)^{j+1} - r_1 - r_2, r_1} \ . \tag{5.118}$$

In summary, to construct a fully symmetric MPS with site tensor $\hat{A}_j$ defined in Eq. (5.110), tensor entries $(A_j)^{n_1 n_2}_{l_1 l_2; r_1 r_2}$ should be real numbers satisfying the symmetry conditions in Eqs. (5.111, 5.112, 5.115, 5.116, 5.118).

5.A.3 Bond-centered magnetic order phase

In this part, we present an MPS construction for the bond-centered magnetic order phase, which is the intermediate phase smoothly connecting the zFM and SPT phases in the classical phase diagram, as shown in Fig. 5.5 in Sec. 5.5.2. Although it is a spontaneously symmetry-breaking phase with six-fold ground state degeneracy, its ground states cannot be represented by direct product states.

We start from the MPS representation of the SPT phase with $\mathrm{U}(1)\times\mathrm{U}(1)$ symmetry. This MPS is constructed from a site tensor A in Eq. (5.108) with $\gamma = 0$. We can represent A as a quantum state as

$$\hat{A} = \sum_{a=0}^{2} |a\rangle \otimes (|a-1\rangle\langle a+1| + |a+1\rangle\langle a-1|) \ . \tag{5.119}$$

Let us insert additional bond tensors $B_{j,j+1}$ sitting between sites j and $j+1$. For the SPT phase, $B_{j,j+1}$ is the identity matrix, whose quantum state representation is

$$\hat{B}_{j,j+1} = \sum_{a=0}^{2} |a\rangle\langle a| \ . \tag{5.120}$$

We now break some symmetry by introducing a parameter κ into the bond tensors:

$$\begin{aligned} \hat{B}_{2k-1,2k} &= (1-\kappa)|0\rangle\langle 0| + (1-\kappa)|1\rangle\langle 1| + (1+\kappa)|2\rangle\langle 2| \ , \\ \hat{B}_{2k,2k+1} &= (1-\kappa)|0\rangle\langle 0| + (1+\kappa)|1\rangle\langle 1| + (1-\kappa)|2\rangle\langle 2| \ . \end{aligned} \tag{5.121}$$

where $0 \leq \kappa \leq 1$. We leave the site tensors unchanged. When $\kappa = 0$, we recover the SPT state. When $\kappa = 1$, $\hat{B}_{2k-1,2k} = 2|2\rangle\langle 2|$ and $\hat{B}_{2k,2k+1} = 2|1\rangle\langle 1|$, and by contracting all virtual legs, we get a zFM state $\bigotimes_j |0\rangle_j$ (up to a constant). Thus, the above state can indeed interpolate between the SPT and zFM phases.

We now analyze symmetry properties for the state with $0 < \kappa < 1$, based on the symmetry actions discussed in App. 5.A.2. It is straightforward to see that this state preserves $\mathrm{U}(1) \times \mathrm{U}(1)$ symmetry and breaks g_x, $\mathcal{C}$, T_1, and $\mathcal{I}$ symmetries. In fact, T_1, $\mathcal{I}$, and $\mathcal{C}$ act in the same way on this MPS, producing a state with even and odd bond tensors in Eq. (5.121) interchanged:

$$\begin{aligned} \hat{B}_{2k-1,2k} &= (1-\kappa)|0\rangle\langle 0| + (1+\kappa)|1\rangle\langle 1| + (1-\kappa)|2\rangle\langle 2| \ , \\ \hat{B}_{2k,2k+1} &= (1-\kappa)|0\rangle\langle 0| + (1-\kappa)|1\rangle\langle 1| + (1+\kappa)|2\rangle\langle 2| \ , \end{aligned} \tag{5.122}$$

We note that this pair of MPS share the same symmetry properties as states labeled by $(\pi/6 \pm \upsilon, \pi/6 \mp \upsilon)$ in Eq. (5.84). The MPS representation of the other two pairs of states in Eq. (5.84) can be generated by the action of g_x. Note that site tensors are invariant under g_x symmetry, and are given by Eq. (5.119). Bond tensors for the MPS states corresponding to $(\pi/6 \mp \upsilon, -\pi/3)$ are

$$\begin{aligned} \hat{B}_{2k-1,2k} &= (1 \pm \kappa)|0\rangle\langle 0| + (1-\kappa)|1\rangle\langle 1| + (1 \mp \kappa)|2\rangle\langle 2| \ , \\ \hat{B}_{2k,2k+1} &= (1 \mp \kappa)|0\rangle\langle 0| + (1-\kappa)|1\rangle\langle 1| + (1 \pm \kappa)|2\rangle\langle 2| \ , \end{aligned} \tag{5.123}$$

and the bond tensors for states corresponding to $(-\pi/3, \pi/6 \pm \upsilon)$ are

$$\begin{aligned} \hat{B}_{2k-1,2k} &= (1 \mp \kappa)|0\rangle\langle 0| + (1 \pm \kappa)|1\rangle\langle 1| + (1-\kappa)|2\rangle\langle 2| \ , \\ \hat{B}_{2k,2k+1} &= (1 \pm \kappa)|0\rangle\langle 0| + (1 \mp \kappa)|1\rangle\langle 1| + (1-\kappa)|2\rangle\langle 2| \ . \end{aligned} \tag{5.124}$$

5.B Integrability of 2d stat mech models

In this Appendix we provide the explicit solutions of the Yang-Baxter equation for the $q = 3$ case of the NIS models discussed in the text, in addition to the generators and relations defining the operator algebras for these models.

5.B.1 Separable NIS model

The $q = 3$ separable NIS model is realized in $H_{\rm NIS}$ at the point $J^z = 0$: (with equality up to constants)

$$H_{\rm sep} = 6K\, H_{\rm bQ} = 6K \sum_j \overline{T}^a_j T^a_{j+1} = -3K \sum_j \sum_{\alpha,\beta} |\alpha\alpha\rangle\langle\beta\beta|_{j,j+1} \equiv -3K \sum_j u_j. \tag{5.125}$$

The internal symmetry group of $H_{\rm sep}$ is expanded to the full SU(3), and its ground state is inside the VBS phase we encounter in the original model H. $H_{\rm bQ}$ refers to the pure biquadratic spin-1 Hamiltonian, which exactly maps to $H_{\rm sep}$. The local terms in the Hamiltonian satisfy

$$u_j^2 = 3\, u_j \tag{5.126}$$

$$u_j u_{j\pm1} u_j = u_j \tag{5.127}$$

$$u_j u_k = u_k u_j \ , \quad |k-j| > 1 \ . \tag{5.128}$$

This is the Temperley–Lieb operator algebra of the nine-state self-dual Potts model [29]. This operator algebra correspondence has led to extensive study of the separable case through its connection to the Potts model as well as to the XXZ model of spins at a particular anisotropy, with much work focused on application of the inversion relation [19–23, 25, 28]. Through the many connections to other models the correlation length can be calculated, as well as the value of the dimerization order parameter, confirming that $H_{\rm sep}$ describes a gapped phase breaking $\mathbb{Z}_2$ translation symmetry [3, 5].

5.B.2 Non-separable NIS model

The non-separable NIS model is attained by $H_{\rm NIS}$ at the point $J^z = K$: (equality up to constants)

$$H_{\rm ns} = -3K \sum_j \sum_{\alpha,\beta} (\delta_{\alpha\beta} + 1)\, |\alpha\alpha\rangle\langle\beta\beta|_{j,j+1} \tag{5.129}$$

$$= -3K \sum_j (u_j + v_j) \ , \ \text{where} \ \ v_j = \frac{1}{3}(Z_j^\dagger Z_{j+1} + Z_j Z_{j+1}^\dagger + 1) \ . \tag{5.130}$$

Here u_j is the Temperley–Lieb operator from the previous section. The non-separable NIS model does not appear to admit such useful equivalences as H_{sep}, and consequently is not as well understood. H_{ns} does exactly map onto one of the (rare) known solvable spin-1 Hamiltonians [35] and has in fact been exactly solved [24]. However, the Bethe ansatz solution is not immediately informative about properties of the eigenstates. The model of course satisfies the criteria for application of the inversion relation—which was the context in which it was first written down—and from this method the thermodynamic energy gap and correlation length are known [18], but nothing about the ground state degeneracy or symmetry-breaking order follows. It is distinguished from most of the $q+1$ different integrable q-state NIS models originally introduced by Schultz [19] in that it, along with the separable case, respects the S_q permutation symmetry of the edge labels.

Up to normalization the v_j operators are actually some of the $2L-1$ generators appearing in the three-state Potts representation of the Temperley–Lieb algebra. They satisfy

$$v_j^2 = v_j \tag{5.131}$$

$$v_j v_k = v_k v_j \text{ for any } j,k \tag{5.132}$$

as well as the following mixed relations

$$u_j v_j = v_j u_j = u_j \tag{5.133}$$

$$u_j v_{j\pm1} u_j = u_j \tag{5.134}$$

$$v_j u_{j\pm1} v_j = v_j v_{j\pm1} \tag{5.135}$$

$$v_j u_{j\pm1} u_j = v_j v_{j\pm1} u_j = v_{j\pm1} u_j \tag{5.136}$$

$$u_j u_{j\pm1} v_j = u_j v_{j\pm1} v_j = u_j v_{j\pm1} \tag{5.137}$$

$$u_j v_k = v_k u_j \ , \quad |k-j| > 1 \ . \tag{5.138}$$

Through application of these relations for the terms in the Hamiltonian, we find $h_j^2 = (u_j+v_j)^2 = 5u_j+v_j$, as well as $h_j h_{j\pm1} h_j = 2(u_j+v_j v_{j\pm1}+u_j v_{j\pm1}+v_j u_{j\pm1})$, but this doesn't seem to shed light on the integrability.

5.B.3 Parameterization by Klümper

We can take a further look at the results of Klümper [18], who applied the inversion relation [27, 28] to both separable and non-separable NIS models,

finding results for $q \geq 3$ (Stroganov [27] found the partition function per site for $q = 3$). The specific vertex model used there for the separable case is

$$w_{(d)}^{\text{sep}} = 1 \ , \quad w_{(l)}^{\text{sep}} = \frac{\omega z + 1 - \omega}{z+1} \ , \quad w_{(r)}^{\text{sep}} = 1 - w_{(l)}^{\text{sep}} = \frac{z(1-\omega)+\omega}{z+1} \ , \quad (5.139)$$

where $\omega = \frac{1}{2}\left(1 + \sqrt{\frac{q+2}{q-2}}\right)$, and $z = \alpha^v$, where $\alpha = (\frac{\omega}{\omega-1})^2$ and v is the spectral variable. The vertex model for non-separable NIS is

$$w_{(d)}^{\text{ns}} = 1 \ , \quad w_{(l)}^{\text{ns}} = \frac{z\sqrt{q-1}-1}{q-2} \ , \quad w_{(r)}^{\text{ns}} = \frac{z^{-1}\sqrt{q-1}-1}{q-2} \ , \quad (5.140)$$

where here $z = (q-1)^v$ and again v is the spectral parameter. In both cases $w_{(l)}$ and $w_{(r)}$ are exchanged by $v \mapsto -v$, which is important for the inversion relation.

For the non-separable case, Klümper's Hamiltonian convention is

$$H = -\frac{d}{dv} \log T\big|_{v=v_0} = -\sum_j h_j \ , \quad (5.141)$$

where

$$h_j = \frac{\log(q-1)}{q-2}[(q-2)\,\delta(\alpha_j\alpha_{j+1},\beta_j,\beta_{j+1}) + \delta(\alpha_j,\alpha_{j+1})\delta(\beta_j,\beta_{j+1}) - (q-1)\,\delta(\alpha_j,\beta_j)\delta(\alpha_{j+1},\beta_{j+1})] \ . \quad (5.142)$$

Because $\frac{\log(q-1)}{q-2}\big|_{q=2} = 1$, at this point we have $h_j = \delta(\alpha_j,\alpha_{j+1})\delta(\beta_j,\beta_{j+1}) - 1$. Up to a shift this is the local Temperley–Lieb operator that characterizes the separable NIS model. One sees also in the transfer matrices that at $q = 2$ the separable and non-separable models exactly coincide:

$$w_{(d)} = 1 \ , \quad w_{(l)} \to v + \frac{1}{2} \ , \quad w_{(r)} \to -v + \frac{1}{2} = 1 - w_{(l)} \ . \quad (5.143)$$

As a result, by extending $q \to 2$ we make contact between the non-separable NIS model, which is no longer distinct, and the critical four-state self-dual Potts model. By "deforming" with finite $\epsilon = q - 2$ the two models diverge, having different symmetry properties, but apparently the emergence of a finite gap is similar between the separable and non-separable cases. From this we conclude that the complex CFTs governing the DQCP are derived from the 4-state self-dual Potts conformal fixed point.

5.B.4 Yang–Baxter solution for the $q = 3$ transfer matrix

Following Baxter [29], designate the weights of the three vertex types (d), (l), and (r), as a, b, and c, respectively. Specializing the Yang–Baxter equation $R'_{j,j+1}R''_{j+1,j+2}R_{j,j+1} = R_{j+1,j+2}R''_{j,j+1}R'_{j+1,j+2}$ to $q = 3$ yields four independent relations between the vertex weights:

$$aa''b' + a'bc'' + bb'c'' = a'b''c \ , \tag{5.144}$$

$$a'a''b + ab'c'' + bb'c'' = ab''c' \ , \tag{5.145}$$

$$a''bb' + aa'c'' + bb'c'' = a''cc' \ , \tag{5.146}$$

$$a''bb' + a'bc'' + ab'c'' = b''cc' \ . \tag{5.147}$$

Treating a'', b'' and c'' as variables, the determinant of the coefficient matrix of Eqs. (5.144), (5.145), and (5.147) must vanish in order to have a solution for $a'', b'', c'' \neq 0$. This determinant is

$$\big(a'b + (a+b)b'\big)\big(ab'c'(a-b-c) - a'bc(a'-b'-c')\big) = 0 \ . \tag{5.148}$$

It is sufficient for either factor to vanish, but in order to satisfy the Yang–Baxter equation when $a' = a$, $b' = b$, and $c' = c$, we choose the second, which is symmetric in the primed and unprimed variables. Then

$$\frac{a}{bc}(a-b-c) = \frac{a'}{b'c'}(a-b'-c') \equiv \Theta \ . \tag{5.149}$$

Here Θ characterizes a family of commuting transfer matrices. Because the weights are unique up to ratios, this means that there is one free parameter for a given value of Θ. We eliminate c and c' by substitution in favor of Θ, and solve (5.144), (5.145), and (5.147) for a'', b'', and c'' up to an overall factor:

$$a'' = aa' + bb' + a'b\Theta + ab'\Theta \ , \tag{5.150}$$

$$b'' = \frac{(a'b + ab' + bb')(a + b\Theta)(a' + b'\Theta)}{aa'} \ , \tag{5.151}$$

$$c'' = aa' - a'b - ab' - bb'\Theta \ . \tag{5.152}$$

By substituting the preceding equations into (5.146) one finds that the only nontrivial solutions are $\Theta = 0, 1$. Indeed, clearly $\Theta = 0$ for the separable model, and the condition $\Theta = 1$ is a special case of the relationship already known for the non-separable model for general q [19, 22]:

$$a^2 = a(b+c) + (q-2)bc \ . \tag{5.153}$$

That is, $\Theta = q - 2 = 1$ for the $q = 3$ non-separable NIS model, which also reproduces Stroganov's $c = \frac{1-b}{1+b}$ for $a = 1$. So we find isolated integrable points rather than a continuous family, as was the case for the six-vertex model.

The unitarity condition can be written $R_{j,j+1}R'_{j,j+1} = \kappa\,\mathbb{I}_{j,j+1}$ for some κ. This simplifies to

$$aa' + 2bb' = \kappa \ , \tag{5.154}$$

$$a'b + (a+b)b' = 0 \ , \tag{5.155}$$

$$cc' = \kappa \ . \tag{5.156}$$

We make use of the Yang–Baxter solution to reduce to a condition on one free vertex weight, parametrized by the spectral variable u. Setting $a = a' = 1$ and eliminating c, c' in favor of Θ one finds that the condition is

$$bb'\Theta(\Theta - 1) = 0 \ . \tag{5.157}$$

That is, the nontrivial solutions for Θ arising from unitarity are the same as those that solve the Yang–Baxter equation. Typically we are able to parametrize the vertex weight by setting the spectral variable equal to the difference of "line variables" or rapidities associated with paths through a so-called Baxter (even-valent) lattice, subject to some sign convention. Then we will find that $b = b(v - w) \equiv b(u)$ and $b' = b(w - v) \equiv b(-u)$, where v and w are the appropriate line variables. Either value of Θ gives the same solution

$$b(-u) = \frac{-b(u)}{1 + b(u)} \ . \tag{5.158}$$

Finally, we also want to enforce the property that the vertex decouples lines with identical rapidities, or $R(u = 0) = \mathbb{I}$. This means $b(0) = 0$ and $c(0) = 1$. Recall Klümper's parametrization: in our notation,

$$a(u) = 1 \ , \tag{5.159}$$

$$b(u) = \frac{(q-1)^{\frac{1}{2}-u} - 1}{q-2} \xrightarrow{q=3} \sqrt{2}^{-u} - 1 \ , \tag{5.160}$$

$$c(u) = \frac{(q-1)^{\frac{1}{2}+u} - 1}{q-2} \xrightarrow{q=3} \sqrt{2}^{u} - 1 \ . \tag{5.161}$$

So while this parametrization can be seen to solve Yang–Baxter, it does not match the prescribed unitary form. Thus the variable u here cannot be interpreted as a difference of line variables.

5.C Domain wall duality mapping with $\mathbb{Z}_3$ gauge field

In this section we present the more precisely defined version of the duality mapping to domain walls on a periodic chain, which appear as matter fields on the dual lattice coupled to a $\mathbb{Z}_3$ gauge field. The purpose of the gauge field is essentially for bookkeeping, as it does not have its own dynamics. Instead, it will account for the differing global properties of the phases, the most important example in our case being ground state degeneracy [1].

In addition to the domain wall variables $\widetilde{X}_{j+1/2}$, $\widetilde{Z}_{j+1/2}$ which live on the sites of the dual lattice, we place gauge degrees of freedom ρ^x_j, ρ^z_j which form a [1] projective representation of $\mathbb{Z}_3\times\mathbb{Z}_3$ on the links of the dual lattice (equivalently, on the sites of the primal lattice). The duality mapping is then given by

$$\widetilde{X}_{j+1/2} = Z^\dagger_j Z_{j+1} \ , \tag{5.162}$$

$$\widetilde{Z}^\dagger_{j-1/2}\ \rho^{z\dagger}_j\ \widetilde{Z}_{j+1/2} = X_j \ , \tag{5.163}$$

$$\rho^x_j = Z_j \ . \tag{5.164}$$

The physical Hilbert space satisfies the gauge constraint

$$\widetilde{X}_{j+1/2} = \rho^{x\dagger}_j \rho^x_{j+1} \ . \tag{5.165}$$

The proof of the exact equivalence is similar to the Ising case in Ref. [1].

The Hamiltonian Eq. (5.11) translates to

$$\begin{aligned}\widetilde{H} = -\sum_j \Big[& (J^x \widetilde{Z}^\dagger_{j-1/2}\rho^{z\dagger}_j\rho^{z\dagger}_{j+1}\widetilde{Z}_{j+3/2} + J^z\widetilde{X}_{j+1/2} + \text{H.c.}) \\ & + K(1+\widetilde{Z}^\dagger_{j-1/2}\rho^{z\dagger}_j\rho^{z\dagger}_{j+1}\widetilde{Z}_{j+3/2} + \text{H.c.})(1+\widetilde{X}_{j+1/2}+\text{H.c.})\Big] \ .\end{aligned} \tag{5.166}$$

Using the dictionary above, and requiring equality to hold only in the physical sector, we can also rewrite the symmetry generators as

$$g_x = \prod_j \rho^{z\dagger}_j \ , \quad g_z = \prod_k \widetilde{X}_{2k+1/2} = \prod_k \rho^{x\dagger}_{2k}\rho^x_{2k+1} \ , \tag{5.167}$$

which are exact on a periodic system. One obtains the duality mapping presented in Sec. 5.5.1 by fixing the gauge $\rho^z_j = 1$.

The action of the symmetries on the gauge variables is

$$g_x: \ (\rho_j^x, \rho_j^z) \mapsto (\omega^{-1}\rho_j^x, \rho_j^z) \ , \tag{5.168}$$

$$g_z: \ (\rho_j^x, \rho_j^z) \mapsto (\rho_j^x, \omega^{1-2p_j}\rho_j^z) \ , \tag{5.169}$$

$$\Theta: \ (\rho_j^x, \rho_j^z) \mapsto (\rho_j^{x\dagger}, \rho_j^z) \ , \tag{5.170}$$

$$\mathcal{C}: \ (\rho_j^x, \rho_j^z) \mapsto (\rho_j^{x\dagger}, \rho_j^{z\dagger}) \ , \tag{5.171}$$

$$T_1: \ (\rho_j^x, \rho_j^z) \mapsto (\rho_{j+1}^x, \rho_{j+1}^z) \ , \tag{5.172}$$

$$\mathcal{I}: \ (\rho_j^x, \rho_j^z) \mapsto (\rho_{-j}^x, \rho_{-j}^z) \ . \tag{5.173}$$

Importantly, g_x acts non-trivially in this formulation. As in the main text, we designate the "even" and "odd" sublattices of the dual lattice as locations $2k + 1/2$ and $2k + 3/2$, $k \in \mathbb{Z}$, respectively.

We refer to this theory as having a $\mathbb{Z}_3^\rho$ gauge symmetry. Briefly, the pure gauge theory with physical constraint $\rho_j^{x\dagger}\rho_{j+1}^x = 1$ comprises three sectors, specified by $\rho_j^x = \omega^r$ for $r = 0, 1, 2$. These sectors are related by the symmetry generator $\prod_j \rho_j^{z\dagger} = g_x$, which is a symmetry of the Hamiltonian. Thus the appropriate sectors of the gauge symmetry are the linear combinations respecting g_x, namely with definite flux $\prod_j \rho_j^z$ taking values 1, ω, or ω^2. The instanton operator adding $\mathbb{Z}_3^\rho$ flux is ρ_j^x, which indeed transforms non-trivially under g_x.

5.C.1 Symmetry-breaking phases from the dual perspective

We can now revisit the phases described in Sec. 5.5.1. Consider first the case in which domain walls are gapped, so the low-energy properties are determined only by the gauge sector. In this case we have schematically $\langle \widetilde{Z}_{j+1/2} \rangle = 0$; this pattern is energetically favored in our model for J^z dominant. Because the instanton operator is not allowed in the Hamiltonian the three gauge flux sectors do not mix. From a formal perspective where we integrate out the gapped matter field $\widetilde{Z}$, the three states with different flux $\prod_j \rho_j^z$ can obtain slightly different energies but the energy splitting is exponentially small in the chain length. This corresponds to spontaneously breaking g_x and accounts for the threefold degeneracy of the ground state in the zFM phase.

The domain wall condensate having schematically $\langle \widetilde{Z}_{\text{odd}} \rangle \neq 0$, $\langle \widetilde{Z}_{\text{even}} \rangle \neq 0$ leads to a Higgs phase of the gauge field. Minimizing the energy of the J^x terms, it must be that $\prod_j \rho_j^z = 1$; i.e., a unique gauge flux is selected and hence the g_x symmetry is respected. Solving for classical ground states,

there are three gauge-inequivalent solutions with this flux, with representative states $\rho_j^z = 1, \widetilde{Z}_{\rm odd} = 1, \widetilde{Z}_{\rm even} = \omega^p$ everywhere on the chain, with $p = 0, \pm 1$. These solutions are distinguished by gauge-invariant observables $\widetilde{Z}^\dagger_{j-1/2}\rho_j^{z\dagger}\widetilde{Z}_{j+1/2}$, which are the same as the original X_j variables, and the resulting three different patterns in these correspond to the three xFM ground states in Eq. (5.21). We can thus see from the matter fields that g_z is broken but spatial symmetries are respected. All of these cases, which are favored at large values of J^x, make up the xFM phase with threefold degeneracy. That is to say, in the absence of the gauge field we would have separate $\mathbb{Z}_3$ symmetries associated with the "even" and "odd" sublattices of the dual lattice. Simultaneous condensation $\langle \widetilde{Z}_{\rm odd}\rangle \neq 0$, $\langle \widetilde{Z}_{\rm even}\rangle \neq 0$ would then produce nine ground states. However, the dual gauge field reduces the true number of ground states down to three via the Higgs mechanism.

We can also consider a condensate $\langle \widetilde{Z}_{\rm odd}\rangle \neq 0$ and $\langle \widetilde{Z}_{\rm even}\rangle = 0$, or vice versa. As was the case in the xFM phase, the Higgs mechanism here restores the g_x symmetry by selecting a unique flux sector $\prod_j \rho_j^z = 1$, but in contrast to the previous case, g_z and other internal symmetries are respected as well. (Schematically, the naive three-fold degeneracy from condensing $\widetilde{Z}$ on one sublattice is reduced down to one by the Higgs mechanism.) The state does break a $\mathbb{Z}_2$ translation symmetry however, and therefore is identified as the VBS phase. It is not evident from this analysis that this phase is energetically favored at large K in our model, but ample evidence of this fact is obtained from other sources.

5.C.2 SPT phase from the dual perspective

To obtain a fully symmetric phase, we condense a bound state of a domain wall on the odd sublattice and a domain wall on the even sublattice: schematically, $\langle \widetilde{Z}_{\rm odd}\widetilde{Z}_{\rm even}\rangle \neq 0$ while $\langle \widetilde{Z}_{\rm odd}\rangle = \langle \widetilde{Z}_{\rm even}\rangle = 0$. The g_x symmetry is restored because this bound state carries unit dual gauge charge: Indeed, keeping track of only the dual gauge charge, we have schematically $\widetilde{Z}^2 \sim \widetilde{Z}^{-1}$ (note that it is crucial that we have $\mathbb{Z}_N$ gauge field with odd N). Hence, the $\widetilde{Z}_{\rm odd}\widetilde{Z}_{\rm even}$ condensate completely Higgses out the dual gauge field ρ, which corresponds to the presence of the g_x symmetry. Since translation interchanges $\widetilde{Z}_{\rm odd}$ and $\widetilde{Z}_{\rm even}$, this condensate clearly preserves this symmetry. Under g_z action, $\widetilde{Z}_{\rm odd}\widetilde{Z}_{\rm even}$ obtains a phase factor ω^2; however, this is related to the fact that this schematic object is not gauge-invariant and the phase factor can be removed by a gauge

transformation. Any gauge-invariant local operator with non-zero expectation value will respect the g_z symmetry. Thus, we obtain a fully symmetric phase.

Another perspective on this condensate is that we condense bound states of a domain wall field in the g_x-symmetry-breaking order (i.e., $\widetilde{Z}$ field) and a g_z charge field (i.e., X field). Indeed, $\widetilde{Z}_{j-1/2}\widetilde{Z}_{j+1/2} = \widetilde{Z}^2_{j-1/2}\rho^z_j X_j \sim \widetilde{Z}^\dagger_{j-1/2} X_j$ (fixing the gauge $\rho^z_j = 1$). We expect that condensation of bound states of domain walls and charges leads to a non-trivial SPT phase.

5.D Duality of q-state separable model and q^2-state Potts model and generalization to non-separable model

In this Appendix, we perform a two-step duality that connects the q-state separable integrable model and $Q_{\text{Potts}} = q^2$-state Potts model. We will also follow the non-separable integrable model under the same mapping. The treatment here is in the Hamiltonian language and can be carried out for any integer q.

We begin with a q-state generalization of the $\mathrm{U}(1)^2$-symmetric $q = 3$ model from the main text. Consider the Hamiltonian

$$H = -\sum_j \left[J_z \sum_{\ell=0}^{q-1} \left(Z_j^\dagger Z_{j+1} \right)^\ell + K \sum_{\ell=0}^{q-1} \left(X_j X_{j+1} \right)^\ell \sum_{\ell=0}^{q-1} \left(Z_j^\dagger Z_{j+1} \right)^\ell \right]. \quad (5.174)$$

For $q = 3$ this reduces to the model in the main text, up to an additive constant. For general q the terms in the Hamiltonian have a simple form in bra-ket notation (see also Eq. (5.23)):

$$\sum_{\ell=0}^{q-1} \left(Z_j^\dagger Z_{j+1} \right)^\ell = q \sum_\alpha |\alpha,\alpha\rangle\langle\alpha,\alpha|_{j,j+1} \ ,$$
$$\sum_{\ell=0}^{q-1} \left(X_j X_{j+1} \right)^\ell \sum_{\ell=0}^{q-1} \left(Z_j^\dagger Z_{j+1} \right)^\ell = q \sum_{\alpha,\beta} |\beta,\beta\rangle\langle\alpha,\alpha|_{j,j+1} \ ,$$

from which it is easy to see that the model has continuous $\mathrm{U}(1)^{q-1}$ symmetry as well as S_q permutation symmetry. It has a trivial solvable point $J_z > 0, K = 0$ inside the zFM phase as well as two nontrivial integrable points: $J_z = 0, K > 0$ which is inside the VBS phase, and $J_z = K(q-2) > 0$ which we propose is at the transition between the zFM and VBS phases.

We first perform a formal duality transformation which is a straightforward

q-state generalization of the one in the main text:

$$X_j = \widetilde{Z}^\dagger_{j-1/2}\widetilde{Z}_{j+1/2} \ , \tag{5.175}$$

$$Z^\dagger_j Z_{j+1} = \widetilde{X}_{j+1/2} \ . \tag{5.176}$$

(For simplicity here and below, we do not exhibit dual gauge fields which would be necessary to account for global aspects in a periodic chain.) The dual Hamiltonian reads

$$\widetilde{H} = -\sum_j \left[J_z \sum_{\ell=0}^{q-1} \left(\widetilde{X}_{j+1/2}\right)^\ell + K \sum_{\ell=0}^{q-1} \left(\widetilde{Z}^\dagger_{j-1/2}\widetilde{Z}_{j+3/2}\right)^\ell \sum_{\ell=0}^{q-1} \left(\widetilde{X}_{j+1/2}\right)^\ell \right]. \tag{5.177}$$

Similarly to the main text, this can be viewed as two individually Potts-symmetric q-state systems residing on the "even" and "odd" sublattices of the dual lattice (locations $2k+1/2$ and $2k+3/2$, $k \in \mathbb{Z}$, respectively). The two systems have energy-energy coupling between them. In these variables, the zFM phase occurs when both $\widetilde{Z}_{2k+1/2}$ and $\widetilde{Z}_{2k+3/2}$ are gapped. On the other hand, the VBS phase occurs when only one species orders but not the other, which breaks the translation symmetry.

Let us now maintain the even sublattice variables $(\widetilde{Z}_{2k+1/2}, \widetilde{X}_{2k+1/2})$ and perform the above duality transformation on the odd sublattice variables $(\widetilde{Z}_{2k+3/2}, \widetilde{X}_{2k+3/2})$, treating this system as a 1d chain:

$$\widetilde{X}_{2k+3/2} = \widetilde{\widetilde{Z}}^\dagger_{2k+1/2}\widetilde{\widetilde{Z}}_{2k+5/2} \ , \tag{5.178}$$

$$\widetilde{Z}^\dagger_{2k-1/2}\widetilde{Z}_{2k+3/2} = \widetilde{\widetilde{X}}_{2k+1/2} \ . \tag{5.179}$$

Note that the variables dual to $(\widetilde{Z}_{2k+3/2}, \widetilde{X}_{2k+3/2})$ reside at the same locations as the even sublattice variables $(\widetilde{Z}_{2k+1/2}, \widetilde{X}_{2k+1/2})$, as indicated by the location indices of $(\widetilde{\widetilde{Z}}_{2k+1/2}, \widetilde{\widetilde{X}}_{2k+1/2})$. After this transformation, the Hamiltonian reads:

$$\begin{aligned}\widetilde{\widetilde{H}} = -\sum_{k\in\mathbb{Z}} \Bigg[& J_z \sum_{\ell=0}^{q-1} \left(\widetilde{X}_{2k+1/2}\right)^\ell + J_z \sum_{\ell=0}^{q-1} \left(\widetilde{\widetilde{Z}}^\dagger_{2k+1/2}\widetilde{\widetilde{Z}}_{2k+5/2}\right)^\ell \\ & + K \sum_{\ell=0}^{q-1} \left(\widetilde{\widetilde{X}}_{2k+1/2}\right)^\ell \sum_{\ell=0}^{q-1} \left(\widetilde{X}_{2k+1/2}\right)^\ell \\ & + K \sum_{\ell=0}^{q-1} \left(\widetilde{Z}^\dagger_{2k+1/2}\widetilde{Z}_{2k+5/2}\right)^\ell \sum_{\ell=0}^{q-1} \left(\widetilde{\widetilde{Z}}^\dagger_{2k+1/2}\widetilde{\widetilde{Z}}_{2k+5/2}\right)^\ell \Bigg]. \end{aligned} \tag{5.180}$$

In these variables, the zFM phase corresponds to gapped $\widetilde{Z}_{2k+1/2}$ variables and condensed $\widetilde{\widetilde{Z}}_{2k+1/2}$ variables. On the other hand, the VBS phase corresponds to either both $\widetilde{Z}_{2k+1/2}$ and $\widetilde{\widetilde{Z}}_{2k+1/2}$ being gapped or both condensed.

We can combine the tilded and double-tilded variables on each site $2k+1/2$ to form a q^2-state variable, $|A\rangle_{2k+1/2} \equiv |\widetilde{\alpha}\rangle_{2k+1/2} \otimes |\widetilde{\widetilde{\alpha}}\rangle_{2k+1/2}$, $\widetilde{\alpha}, \widetilde{\widetilde{\alpha}} = 1, \ldots, q$. The K terms become precisely the on-site and inter-site quantum Potts terms for these $Q_{\rm Potts} = q^2$-state variables:

$$\sum_{\ell=0}^{q-1} \left(\widetilde{X}_{2k+1/2}\right)^{\ell} \sum_{\ell=0}^{q-1} \left(\widetilde{\widetilde{X}}_{2k+1/2}\right)^{\ell} = \sum_{\widetilde{\alpha},\widetilde{\beta}} |\widetilde{\beta}\rangle\langle\widetilde{\alpha}|_{2k+1/2} \otimes \sum_{\widetilde{\widetilde{\alpha}},\widetilde{\widetilde{\beta}}} |\widetilde{\widetilde{\beta}}\rangle\langle\widetilde{\widetilde{\alpha}}|_{2k+1/2} \quad (5.181)$$

$$= \sum_{A,B} |B\rangle\langle A|_{2k+1/2} \equiv \sum_{\ell=0}^{q^2-1} \left(\mathcal{X}_{2k+1/2}\right)^{\ell}, \quad (5.182)$$

$$\sum_{\ell=0}^{q-1} \left(\widetilde{Z}^{\dagger}_{2k+1/2} \widetilde{Z}_{2k+5/2}\right)^{\ell} \sum_{\ell=0}^{q-1} \left(\widetilde{\widetilde{Z}}^{\dagger}_{2k+1/2}\ \widetilde{\widetilde{Z}}_{2k+5/2}\right)^{\ell}$$

$$= q \sum_{\widetilde{\alpha}} |\widetilde{\alpha},\widetilde{\alpha}\rangle\langle\widetilde{\alpha},\widetilde{\alpha}|_{2k+1/2,2k+5/2} \otimes q \sum_{\widetilde{\widetilde{\alpha}}} |\widetilde{\widetilde{\alpha}},\widetilde{\widetilde{\alpha}}\rangle\langle\widetilde{\widetilde{\alpha}},\widetilde{\widetilde{\alpha}}|_{2k+1/2,2k+5/2} \quad (5.183)$$

$$= q^2 \sum_{A} |A,A\rangle\langle A,A|_{2k+1/2,2k+5/2} \equiv \sum_{\ell=0}^{q^2-1} \left(\mathcal{Z}^{\dagger}_{2k+1/2} \mathcal{Z}_{2k+5/2}\right)^{\ell}, \quad (5.184)$$

where we have introduced standard operators $\mathcal{Z}_{2k+1/2}, \mathcal{X}_{2k+1/2}$ in the $Q_{\rm Potts} = q^2$-state Hilbert space on each site $2k+1/2$. Thus, in the absence of the J^z term we indeed obtain the self-dual q^2-state Potts model on the "even" sublattice of the dual lattice. This type of equivalence of the integrable model $H[J_x = 0, J_z = 0, K]$ to the self-dual q^2-state Potts model has been well known at least since Refs. [3, 4] where it was argued by comparing the Temperley–Lieb operator algebras in the two models. This is the quantum version of the equivalence between the classical separable integrable NIS and classical q^2-state Potts models mentioned in Sec. 5.6. By examining the origins of the two K terms in Eq. (5.180), it is also easy to see that staggering bond couplings in the original model corresponds to moving off self-duality in the Potts model.

The derivation here is of some interest in that it clearly demonstrates a non-local relation between the two models and also allows one to formulate the precise relation on periodic chains by carefully including the gauge fields appearing in the dualities to keep track of the global aspects, which for the sake

of simplicity we did not include. Of particular interest to us is that we can also write the J^z terms, which from Eq. (5.180) are

$$\sum_{\ell=0}^{q-1} \left(\widetilde{X}_{2k+1/2} \right)^{\ell} = \sum_{\ell=0}^{q-1} \left(\mathcal{X}_{2k+1/2} \right)^{\ell \cdot q} \ , \tag{5.185}$$

$$\sum_{\ell=0}^{q-1} \left(\widetilde{\widetilde{Z}}^{\dagger}_{2k+1/2} \widetilde{\widetilde{Z}}_{2k+5/2} \right)^{\ell} = \sum_{\ell=0}^{q-1} \left(\mathcal{Z}^{\dagger}_{2k+1/2} \mathcal{Z}_{2k+5/2} \right)^{\ell \cdot q} \ . \tag{5.186}$$

Note that the powers of operators summed on the right hand side are $\ell \cdot q$, which appear in the convention of the following ordering of the q^2 states $|A\rangle = |\widetilde{\alpha}\rangle \otimes |\widetilde{\widetilde{\alpha}}\rangle$:

$$A = (\widetilde{\alpha} - 1) \cdot q + \widetilde{\widetilde{\alpha}} \ , \tag{5.187}$$

$\widetilde{\alpha}, \widetilde{\widetilde{\alpha}} = 1, \ldots, q; A = 1, \ldots, q^2$. We can now see that the q^2-state model remains self-dual also in the presence of the J_z term, which however breaks the formal symmetry in these variables from S_{q^2} down to $S_q \times S_q$. Unfortunately, this formulation does not appear to inform us why $J_z = K(q-2)$ places the model precisely at the transition between the zFM and VBS phases. In the q^2-state Potts variables $\mathcal{Z}_{2k+1/2}$, the VBS phase corresponds to the first-order coexistence of the standard disordered and ordered Potts phases, while the zFM phase corresponds to a specific partial order. In this language, $J_z = K(q-2)$ appears to correspond to a special multi-critical point, and we are hopeful that this information may be useful for future elucidation of this transition.

BIBLIOGRAPHY

[1] S. Jiang and O. Motrunich, "Ising ferromagnet to valence bond solid transition in a one-dimensional spin chain: Analogies to deconfined quantum critical points", Physical Review B 99 (2019), 075103.

[2] B. Roberts, S. Jiang, and O. I. Motrunich, "Deconfined quantum critical point in one dimension", Physical Review B 99 (2019), 165143.

[3] M. N. Barber and M. T. Batchelor, "Spectrum of the biquadratic spin-1 antiferromagnetic chain", Physical Review B 40 (1989), 4621.

[4] I. Affleck, "Exact results on the dimerisation transition in SU(n) antiferromagnetic chains", Journal of Physics: Condensed Matter 2 (1990), 405.

[5] E. S. Sørensen and A. P. Young, "Correlation length of the biquadratic spin-1 chain", Physical Review B 42 (1990), 754.

[6] Z. Song, C. Fang, and Y. Qi, "Real-space recipes for general topological crystalline states", Nature Communications 11 (2020), 1.

[7] D. V. Else and R. Thorngren, "Topological theory of Lieb-Schultz-Mattis theorems in quantum spin systems", Physical Review B 101 (2020), 224437.

[8] S. Jiang et al., "Generalized Lieb-Schultz-Mattis theorem on bosonic symmetry protected topological phases", arXiv preprint arXiv:1907.08596 (2019).

[9] V. Zauner-Stauber et al., "Variational optimization algorithms for uniform matrix product states", Physical Review B 97 (2018), 045145.

[10] C. Liu et al., "Symmetry breaking and criticality in tensor-product states", Physical Review B 82 (2010), 060410.

[11] A. LeClair, A. Ludwig, and G. Mussardo, "Integrability of coupled conformal field theories", Nuclear Physics B 512 (1998), 523.

[12] A. Zamolodchikov, "Integrals of motion in scaling 3-state Potts model field theory", International Journal of Modern Physics A 3 (1988), 743.

[13] V. Stojevic et al., "Conformal data from finite entanglement scaling", Physical Review B 91 (2015), 035120.

[14] F. D. M. Haldane, "Effective Harmonic-Fluid Approach to Low-Energy Properties of One-Dimensional Quantum Fluids", Physical Review Letters 47 (1981), 1840.

[15] S. Sachdev, *Quantum Phase Transitions*, Second Edition, Cambridge University Press, 2011.

[16] T. Giamarchi, *Quantum Physics in One Dimension*, Clarendon Press, Oxford, 2004.

[17] C. Kane and M. P. Fisher, "Impurity scattering and transport of fractional quantum Hall edge states", Physical Review B 51 (1995), 13449.

[18] A. Klümper, "The spectra of q-state vertex models and related antiferromagnetic quantum spin chains", Journal of Physics A: Mathematical and General 23 (1990), 809.

[19] C. L. Schultz, "Solvable q-state models in lattice statistics and quantum field theory", Physical Review Letters 46 (1981), 629.

[20] J. H. Perk and C. L. Schultz, "New families of commuting transfer matrices in q-state vertex models", Physics Letters A 84 (1981), 407.

[21] J. Perk and F. Wu, "Graphical approach to the nonintersecting string model: star-triangle equation, inversion relation, and exact solution", Physica A: Statistical Mechanics and its Applications 138 (1986), 100.

[22] J. Perk and F. Wu, "Nonintersecting string model and graphical approach: equivalence with a Potts model", Journal of Statistical Physics 42 (1986), 727.

[23] J. Perk and C. Schultz, "Diagonalization of the transfer matrix of a nonintersecting string model", Physica A: Statistical Mechanics and its Applications 122 (1983), 50.

[24] H. De Vega and G. Giavarini, "Exact solution of the general non-intersecting string model", Nuclear Physics B 410 (1993), 550.

[25] A. Klümper, "New results for q-state vertex models and the pure biquadratic spin-1 Hamiltonian", EPL (Europhysics Letters) 9 (1989), 815.

[26] Y. Wang, W. Guo, and H. W. Blöte, "Completely packed O(n) loop models and their relation with exactly solved coloring models", Physical Review E 91 (2015), 032123.

[27] Y. G. Stroganov, "A new calculation method for partition functions in some lattice models", Physics Letters A 74 (1979), 116.

[28] R. Baxter, "The inversion relation method for some two-dimensional exactly solved models in lattice statistics", Journal of Statistical Physics 28 (1982), 1.

[29] R. J. Baxter, *Exactly solved models in statistical mechanics*, Elsevier, 1982.

[30] A. Klümper and J. Zittartz, "Eigenvalues of the eight-vertex model transfer matrix and the spectrum of the XYZ Hamiltonian", Zeitschrift für Physik B Condensed Matter 71 (1988), 495.

[31] V. Gorbenko, S. Rychkov, and B. Zan, "Walking, Weak first-order transitions, and Complex CFTs", Journal of High Energy Physics 2018 (2018), 108.

[32] V. Gorbenko, S. Rychkov, and B. Zan, "Walking, Weak first-order transitions, and Complex CFTs II. Two-dimensional Potts model at $Q > 4$", SciPost Physics 5 (2018), 050.

[33] A. Milsted and G. Vidal, "Extraction of conformal data in critical quantum spin chains using the Koo-Saleur formula", Physical Review B 96 (2017), 245105.

[34] W. Koo and H. Saleur, "Representations of the Virasoro algebra from lattice models", arXiv preprint hep-th/9312156 (1993).

[35] K.-H. Mutter and A. Schmitt, "Solvable spin-1 models in one dimension", Journal of Physics A: Mathematical and General 28 (1995), 2265.

Chapter 6

CONCLUSION

Based on the contents of the preceding chapters, a variety of future directions can be envisioned. I describe only a few here, in summary. From the numerical study in Ch. 3 it appears that RRG, whose performance is now competitive with DMRG, can indeed be a powerful tool for navigating challenging low-energy landscapes in 1d. As suggested by our usage (and also the experience of Ref. [1]), it could be seen as an algorithm for initial states which, already being located close to the global energy minimum, are quickly and accurately optimized to extreme precision by another method.

One potential generalization would be an "infinite RRG" for translation-invariant (TI) systems; in this case one would presumably specify some real-space coarse-graining protocol and track only a single viable set, looking for some indication of either scale invariance or trivial physics. Subsequent theoretical work on AGSP-based methods for the TI case has not yet surpassed the polynomial scaling in the system size of the full global AGSP, and moreover it has been demonstrated that computing local observables to arbitrary precision implies precise estimates of the ground state energy [2]. Consequently it is not easy to see how one would formally define a local AGSP construction applicable to TI Hamiltonians which allows sufficient control over the bond dimension.

In a different direction, it has been shown theoretically that in certain cases an AGSP method can be effective in 2d [3]. While this type of work is a highly nontrivial extension of the 1d result (for example, a naive attempt requires exponential scaling of the hyperparameter D with the RG scale), it is easy to see how the numerical RRG algorithm might be generalized to finite systems in higher dimensions, for example by using the 2d *projected entangled-pair states*, or PEPS, representation. There are many technical hurdles associated with this ansatz—for example, the challenges of contraction and defining canonical forms—but the relative lack of numerical methods in 2d may make this a worthwhile direction for future work. Perhaps, being an algorithm for finite systems, RRG could be useful in the study of boundary physics in this setting.

The picture of the critical line in the random XYZ spin chain which was

found using SBRG in Ref. [4] and expanded using RRG in Ch. 3 is very interesting: in many ways the full interacting theory is quite similar to our Hartree–Fock mean field and locally-correlated effective model. Though these non-interacting descriptions are only perturbatively correct and will not be descriptive of the tricritical point, it would seem to be the case that the model does not ultimately travel "too far" from the free-fermion fixed point. In the locally-correlated effective model we are able to use the analytic SDRG in its random-walk form to prove that critical exponents vary continuously along the line from the random XX model to the random XY model, a possibility originally raised by Fisher [5]. It may be the case that other properties or SDRG flows can be studied by similar methods using the random-walk formalism.

In our studies of DQCP in 1d in Chs. 4 and 5, we focused on static (i.e., equal-time) properties at the transition. It would be interesting to also study dynamical properties at the transition, both numerically and analytically, to see if they reveal more signatures of fractionalized excitations, in the spirit of the 2d study in Ref. [6]. In at least the $\mathbb{Z}_2 \times \mathbb{Z}_2$ case, we can calculate dynamical structure factors analytically at low frequencies using the effective field theory description, but we can also try to capture properties at high frequencies and high momenta using one of the microscopic parton descriptions in Ref. [7], for example using the fermionic parton mean field.

The results of Ch. 5 suggest that the picture of walking of RG flows is the appropriate way to think about the family of DQCP with $\mathbb{Z}_q \times \mathbb{Z}_q$ symmetry, where we find an extremely weakly first-order phase transition for $q = 3$, with correlation length $\chi = 190878$ lattice spacings. In Refs. [8, 9] the algebraic equivalence of the Potts model to the six-vertex model plays a crucial role, by allowing through the Coulomb gas formalism many explicit calculations which are then analytically continued into the weakly first-order regime. The operator algebra of the $\mathbb{Z}_q \times \mathbb{Z}_q$ DQCP model, written explicitly in Sec. 5.B for $q = 3$ and in Sec. 5.D for general q, is a generalization of the Temperley–Lieb algebra which to our knowledge has not yet demonstrated such equivalences. A representation theory study of this generalized algebra would be useful in determining whether there are other equivalent models which can illuminate the physics, possibly including a setting for analytic calculations in the ground state.

There is also the interesting possibility of qualitatively different walking behav-

iors arising from the coincidence of the separable and non-separable integrable NIS models at the marginal $q = 2$ point. If these multiple sets of complex CFT fixed points indeed exist in the same parameter space, then for small values of $(q - 2)$ one can imagine a rich structure for walking RG flows based on their interactions. Such a scenario would manifest in crossovers observable in the associated spin chains, and despite the very long length scales involved it is actually possible that quantum Monte Carlo simulations of the explicitly sign-problem-free Hamiltonian in Eq. (5.23) could probe this behavior, along the lines of Refs. [10, 11]. In addition, quantum Monte Carlo studies could be used to test the conjecture about the precise location of the DQCP for $q > 3$, and they could also be used to further examine emergence of the $\mathrm{U}(1)^2$ symmetry at intermediate scales in the original model Eq. (5.11) with only $\mathbb{Z}_3 \times \mathbb{Z}_3$ symmetry.

Finally, it is not clear what role duality plays in the story of the $\mathbb{Z}_q \times \mathbb{Z}_q$ DQCP in 1d, away from $q = 2$. It seems likely that the successes of duality approaches in developing descriptions of the DQCP transition in the $\mathbb{Z}_2 \times \mathbb{Z}_2$-symmetric model [12] are special to that model. However there are some hints in the $\mathbb{Z}_3 \times \mathbb{Z}_3$ model: chiefly, the close numerical correspondence of the zFM and VBS order parameters is not generally expected and may indicate that the DQCP supports an emergent symmetry or self-dual description. In addition, the lack of an intervening featureless phase without the help of an anomalous realization of the symmetry on the lattice could be attributable to an emergent anomaly resulting from enhanced symmetry at the transition, which would presumably achieve a "unification" of the two order parameters. It is our hope that further work on the type of 1d model we have studied here will lead to a more complete story of the behaviors of such fixed points in RG space, as well as to a better understanding of how each of these various components contributes to the DQCP phenomenology.

BIBLIOGRAPHY

[1] M. Block et al., "Performance of the rigorous renormalization group for first order phase transitions and topological phases", arXiv preprint arXiv:2010.15851 (2020).

[2] A. M. Dalzell and F. G. Brandão, "Locally accurate MPS approximations for ground states of one-dimensional gapped local Hamiltonians", Quantum 3 (2019), 187.

[3] N. Abrahamsen, "Sub-exponential algorithm for 2D frustration-free spin systems with gapped subsystems", arXiv preprint arXiv:2004.02850 (2020).

[4] K. Slagle, Y.-Z. You, and C. Xu, "Disordered XYZ spin chain simulations using the spectrum bifurcation renormalization group", Physical Review B 94 (2016), 014205.

[5] D. S. Fisher, "Random antiferromagnetic quantum spin chains", Physical Review B 50 (1994), 3799.

[6] N. Ma et al., "Dynamical signature of fractionalization at a deconfined quantum critical point", Physical Review B 98 (2018), 174421.

[7] S. Jiang and O. Motrunich, "Ising ferromagnet to valence bond solid transition in a one-dimensional spin chain: Analogies to deconfined quantum critical points", Physical Review B 99 (2019), 075103.

[8] V. Gorbenko, S. Rychkov, and B. Zan, "Walking, Weak first-order transitions, and Complex CFTs", Journal of High Energy Physics 2018 (2018), 108.

[9] V. Gorbenko, S. Rychkov, and B. Zan, "Walking, Weak first-order transitions, and Complex CFTs II. Two-dimensional Potts model at $Q > 4$", SciPost Physics 5 (2018), 050.

[10] N. Desai and R. K. Kaul, "Spin-S Designer Hamiltonians and the Square Lattice $S = 1$ Haldane Nematic", Physical Review Letters 123 (2019).

[11] G. Roose et al., *Lattice regularisation and entanglement structure of the Gross-Neveu model*, 2020.

[12] S. Jiang and O. Motrunich, "Ising ferromagnet to valence bond solid transition in a one-dimensional spin chain: Analogies to deconfined quantum critical points", Physical Review B 99 (2019), 075103.